



UNIVERSITY OF
BIRMINGHAM

DEVELOPMENT OF REFLECTIVE LOW CONCENTRATED PHOTOVOLTAIC/ THERMAL SYSTEM

By

Abdulmaged Omer ALGAREU

*A thesis submitted to the
University of Birmingham for the*

Degree of Doctor of Philosophy

Department of Mechanical Engineering

The University of Birmingham

February - 2017

UNIVERSITY OF
BIRMINGHAM

University of Birmingham Research Archive

e-theses repository

This unpublished thesis/dissertation is copyright of the author and/or third parties. The intellectual property rights of the author or third parties in respect of this work are as defined by The Copyright Designs and Patents Act 1988 or as modified by any successor legislation.

Any use made of information contained in this thesis/dissertation must be in accordance with that legislation and must be properly acknowledged. Further distribution or reproduction in any format is prohibited without the permission of the copyright holder.

ABSTRACT

Using concentrator photovoltaic (CPV) systems can contribute to lowering the system cost by replacing the relatively expensive PV materials with other cheaper (optical) materials that can be used to concentrate the sun light on smaller PV material area. Concentrators with low concentration ratios (ranging from 2 to 10) offer the advantage of light weight, small size and easy to install at reduced cost. The aim of this work is to investigate the performance of a new CPV/T system using 3D flat sided (3D V-trough) concentrators with different configurations named Squared (SAC), Hexagonal (HAC), Octagonal (OAC) and Circular (CAC) inlet and exit Aperture concentrators, with an effective cooling facility that keeps PV temperature within the normal operating range. Novel optical models were developed, for the HAC and OAC geometries using mathematical analysis and advanced ray tracing OptisWorks software, to calculate the geometrical concentration ratio (GCR), actual concentration ratio (ACR) and the optical performance. Results showed that the optimum concentrator side angles for GCR of 2, 4, 6, 8 and 10 are 35° , 30° , 20° , 20° and 15° , respectively for all investigated geometries. Optical efficiency is directly proportional to the concentrator surface reflectivity and inversely proportional to the gap distance between concentrator and receiver. SAC geometry offers the best uniformity among the four investigated geometries.

Using COMSOL Multi-physics software, U-type cooling duct design provides best performance, in which highest outlet cooling water temperature and lowest PV module average temperature among the modelled designs. Also COMSOL thermal modelling results, showed that the worst case is where no cooling, the ambient temperature (T_a) is 50°C and GCR 6, PV module temperature reached very high degree of average temperature exceeding 169°C that is about 130°C higher the Nominal Operating Cell Temperature range ($NOCT =$

42- 46 °C). While, using cooling water flow rate of 250 mL/min will lower the PV module temperature to lower than the NOCT. From indoor experimental results, a significant improvement was observed in small scale CPV system electrical conversion efficiency with the use of active cooling reaching up to 72%, and the electrical power gain by 362.85 % while PV cell material was reduced by 78.39 %, at GCR10. On the other hand, outdoor experimental results of large scale CPV/T system showed an improvement in both electrical and thermal power output with the increase of cooling water flow rate, consequently increasing the total power output. CPV/T with geometric concentration ratio of 2 has a total power output of about 180W (thermal and electrical), compared with a total power output of two modules of about 23W, consequently an increase of more than 8 times the flat PV module. While increasing the geometric concentration ratio to 6 will result in total power output of about 385 W, compared with the total power output of 6 flat PV modules of about 68W. The developed CPV/T system maximum total efficiency reached about 94.6 %, 88.1 % and 77.9 % with the use of SAC at different GCRs of 2, 4 and 6, at maximum used flow rates, respectively.

Optical, thermal and electrical investigation results highlighted that the developed CPV/T system is viable to be used for generating both enhanced electrical and thermal powers for domestic use, as one useful package of energy with high output compared with the flat PV modules which generate only electrical power and is affected by higher ambient temperature in the absence of effective cooling system.

ACKNOWLEDGEMENT

All praises are due to Allah (whom we praise Him, seek His help and ask for His forgiveness) for his guidance, blessing and helping me to complete this research project. May His Mercy and blessing be upon our noble Prophet Mohamed (SAWA) and his households and his companions.

My honest gratitude is to my supervisor Dr Raya Khalil Al-Dadah for her support, guidance and patience to accomplish this research project. I am really grateful for her precious suggestions, support, encouragement and revision of my work.

My honest gratitude is also to my second supervisor Dr Mahmoud, S. for his valuable suggestions and support in finalising this work. Many thanks to Mr Simon Rowan for his assistance in the experimental setup and solving of technical issues faced. My gratitude to all my friends and colleges in the department of Mechanical Engineering who helped me in this project such as Mr Suliman Alfarawi for helping me in using COMSOL Multi-physics and Dr Haider and Aydin for helping me in reflectivity and light source spectral measurements. Kind regards to staff in the Centre of Solar Energy Research Studies (CSERS) for their support with meteorological data of Libyan Cities.

My truthful appreciations go to my parents; Omer Algareu (May Allah has mercy on him) and Fatima Gansh, brothers and sisters for their love and support that encouraged me to reach this education stage. Many thanks my wife Somaia Amara who supported me in every piece of life and my children as well as my nieces, nephews for theirs prayers during my study.

I am grateful to all friends in Libya and Birmingham, such as Ezziddin Al-maloul and Dr Mohamed Oun, Mohamed Abosaf, Abdalqader Ahmad, Hassan Al-Werfully etc.

CONTENTS

ABSTRACT.....	I
ACKNOWLEDGEMENT	III
CONTENTS	IV
LIST OF FIGURES.....	VIII
LIST OF TABLES	XIV
ABBREVIATIONS.....	XV
NOMENCLATURE.....	XVI
LIST OF PUBLICATIONS	XVIII
DEDICATION	XXI
1. CHAPTER 1: INTRODUCTION	1
1.1. Background	1
1.2. Energy in Libya.....	2
1.3. Concentrator photovoltaic/ thermal system CPV/T	7
1.4. Aims and Objectives	9
1.5. Thesis Outline	10
2 CHAPTER 2: LITERATURE REVIEW	13
2.1. Introduction.....	13
2.2. Photovoltaic technology.....	13
2.2.1. Silicon PV cells	14
2.2.2. Thin Film PV cells	15
2.2.3. Multi-junction Cells	16
2.3. Reflective Low Concentrating Photovoltaic systems.....	17
2.3.1. 2D Reflective Low concentrating PV systems.....	18
2.3.2. 3D Reflective Low concentrating PV systems.....	34
2.3.3. Effect of non-uniformity on PV output	40
2.4. Methods of cooling low concentration photovoltaic systems	42
2.4.1. Air cooling for LCPV systems	42
2.4.2. Water cooling technique for CPV systems.....	45
2.5. Optical and thermal simulation tools	56
2.5.1. Optical ray tracing software	56
2.5.2. Thermal analysis software.....	59

2.6. Conclusion.....	61
3 CHAPTER 3: OPTICAL MODELLING OF CONCENTRATORS	63
3.1. Introduction:	63
3.2. Mathematical modelling of 3D concentrator with different aperture cross-sections	63
3.2.1. Number of reflections:	64
3.2.2. Width and height of the concentrator:	67
3.2.3. Concentration ratio of 3D square aperture concentrator:	68
3.2.4. Concentration ratio of 3D circular aperture concentrator.....	69
3.2.5. Concentration ratio of 3D hexagonal aperture concentrator	70
3.2.6. Concentration ratio of 3D octagonal aperture concentrator	72
3.2.7. Concentrator optical performance	73
3.3. Ray tracing optical simulation of 3D concentrator with different aperture cross-sections	76
3.4. Comparison of four concentrators.....	78
3.4.1. Mathematical modelling and ray tracing.....	80
3.4.2. Concentrator surface reflectivity	88
3.4.3. Gap distance between concentrator and receiver	89
3.4.4. Optical performance with incidence angle.....	90
3.4.5. Receiver flux distribution for various concentrators	94
3.5. Large concentrator for CPV system	97
3.6. Required concentrator material to build CPV with small and large SAC	102
3.7. Conclusions	104
4. CHAPTER 4: THERMAL MODELLING OF CPV/T SYSTEM	107
4.1. Introduction.....	107
4.2. Theory and governing equations	107
4.3. CPV/T system setup for thermal analysis	109
4.3.1. Cooling system configurations	109
4.3.2. CPV/T system geometry	111
4.3.3. CPV/T system Material properties	111
4.3.4. Flux distribution from OptisWorks	112
4.3.5. CPV/T system Meshing sensitivity	114
4.3.6. CPV/T thermal model assumptions.....	116
4.4. Results	117
4.4.1. Temperature distribution at different cooling system configurations	117

4.4.2. PV module average temperature	120
4.4.3. Average outlet temperature of cooling water under concentration	125
4.4.4. CPV/T system thermal power output at different operating conditions	126
4.4.5. Pumping power for different flow rates	128
4.5. Conclusions	129
5. CHAPTER 5: EXPERIMENTAL SETUP	131
5.1. Introduction	131
5.2. Classification of indoor radiation source	131
5.3. Indoor experiment setup	138
5.3.1. Small scale Concentrator/ PV test facility	138
5.3.2. Large scale concentrator PV/T testing	144
5.4. Outdoor experimental setup	146
5.5. Calibration of measuring devices	149
5.5.1. Calibration of thermocouples	149
5.5.2. Calibration of water flowmeter	153
5.6. Conclusions	156
6. CHAPTER 6: EXPERIMENTAL RESULTS AND VALIDATION	157
6.1. Introduction	157
6.2. Optical validation	157
6.2.1. Large scale SAC concentrator optical efficiency	158
6.2.2. SAC concentrator flux distribution	160
6.2.3. Small scale concentrators optical performance	162
6.3. Thermal validation of CPV/T system	165
6.4. Power output of CPV/T system under indoor conditions	167
6.4.1. Indoor power output of small scale CPV system	167
6.4.2. Indoor power output of CPV/T system	177
6.4.3. Indoor and outdoor PV module power output comparison	179
6.5. Power output of CPV/T system under outdoor testing conditions	181
6.5.1. CPV/T electrical power output	181
6.5.2. CPV/T thermal output	185
6.5.3. Total CPV/T output	188
6.5.4. CPV/T system power gain	189
6.6. Conclusion	195

7. CHAPTER 7: CONCLUSIONS AND RECOMMENDATIONS FOR FUTURE WORKS.....	197
7.1. Introduction.....	197
7.2. Theoretical and experimental investigation conclusions.....	199
7.2.1. Conclusions from optical modelling and experimental work.....	199
7.2.2. Conclusions from thermal modelling and experimental work	201
7.2.3. Conclusions from electrical experimental work.....	203
7.2.4. Total power output from experimental work using large scale SAC concentrator	204
7.3. Future works.....	205
References	207
APPENDIX-A.....	218
APPENDIX-B	234

LIST OF FIGURES

Figure 1-1 Libya energy supply and demand trend [9]	3
Figure 1-2 The estimated average solar energy in the Libya desert [11]	4
Figure 1-3 Energy installed capacity in: A- 2012 and B- 2025 [9]	4
Figure 1-4 Monthly average daily solar radiation on a horizontal surface of Sabha city (Lat. 27.02° N)6	
Figure 1-5 Monthly average daylight hours of Sabha city (Latitude: 27.02° N).	7
Figure 2-1 Structure of: A- silicon PV cell [23] and B- PV module with 1- tempered glass, 2- EVA, 3- PV cells, 4- EVA and 5- Back sheet	14
Figure 2-2 Global Installed Capacity and Average PV System Installed Costs, from 2013 to 2020 [28].	16
Figure 2-3 Spectral response of: a, silicon PV cell and b, multi-junction PV cell [30]	17
Figure 2-4 V-trough reflector: α , acceptance angle; ψ , trough angle; A, collector aperture width, B, receiver base width; H, reflector slant height [17].	19
Figure 2-5 A- Continuous Aluminium V-trough reflector and B- V-trough PV module and the Flat plate module I-V curves [40]	20
Figure 2-6 CPV/T system with a fixed bottom mounted on the metal support movable upper part enabling reflector tilting to 0 – 90 ° in relative to the horizontal plane [41].	21
Figure 2-7 A schematic and Experimental LCPV prototypes [43]	22
Figure 2-8 Photograph showing the ACPV system integrated with PCM [53]	24
Figure 2-9 Schematic diagram of CPC-PV/T system with CPC concentration ratio (1.5, 2, 2.5, and 3) and a U-type pipe as a collector [54].	24
Figure 2-10 CPV/T system with parabolic trough and photovoltaic cells attached to a thermal absorber [56]	25
Figure 2-11 Schematic and pictorial diagrams [57]	27
Figure 2-12 Side view of the BICPV–PCM system [58]	27
Figure 2-13 Three concentrating systems: A- ridge, B- Pseudo parallel and C- Pseudo vertical orientations [61]	29
Figure 2-14 Schematic diagrams for comparison of three different CPC with geometric concentration ratio of 2.5 [62]	30
Figure 2-15 A schematic diagram for the V-trough / CPC geometrical comparison [64]	31
Figure 2-16 Flux distribution comparison between V-trough and CPC concentrators: A, ray reflection schematic diagram and B, flux distribution profile on the receiver [65].	32
Figure 2-17 Generated energy by V-trough and CPC at different days and tilting angles [66]	33

Figure 2-18 3D conical flat sided concentrator used as CPVT system in Quincy, Massachusetts with multiple CPVT collectors [67].	34
Figure 2-19 Schematic design for reflective 3D crossed compound parabolic concentrator[68]	35
Figure 2-20 Comparison between square 3D and 2D CCPC with the same aperture area [71].	36
Figure 2-21 Schematic and geometry of MSDTIRC where (a) is the isometric view; (b) side 1; (c) side 2; (d) aerial, and (e) is the bottom view [72].	37
Figure 2-22 A schematic and pictorial of RACPC design [74].	37
Figure 2-23 Pictorial and schematic diagram for the SHE concentrator [76]	39
Figure 2-24 A pictorial 3D compound parabolic concentrator and array of 120 PV cells.	39
Figure 2-25 The effect of non uniform distribution on I-V curve characteristics of silicon cells at 65 °C [81].	41
Figure 2-26 Cooling pipe arrangements of series-connected solar cells [91]	44
Figure 2-27 Schematic design of CPV/T system with three CPC troughs and fins beneath the heat solar cells for heat transfer [92]	44
Figure 2-28 Schematic diagram for the PV/T collector cross section [41]	46
Figure 2-29 Schematic diagram of the CPC-based CPV/T system integrated with a heat pump [55]	47
Figure 2-30 CPC-based LCPVT system for building integration [97].	49
Figure 2-31 CPV/T solar window design [99]	51
Figure 2-32 CPV/T system with spherical PV module and PCM: 1. Squared aperture concentrator, 2. Spherical PV module filled with PCM, 3. Charge regulator and 4. Gel accumulator and fans [102].	52
Figure 3-1 2D illustration of ray multi-reflection in the internal surface of concentrators [64]	65
Figure 3-2 Method of image for determining the number of reflections to incident rays [177].	65
Figure 3-3 Concentrator side regions in terms of the numbers of reflections for: A- SAC, B- CAC, C- HAC and D- OAC	66
Figure 3-4 Flow chart of ray tracing simulation process for concentrators.	77
Figure 3-5 Concentrator optical efficiency and height with side angle at GCR=2 for: A- SAC, B- CAC, C- HAC and D- OAC.	82
Figure 3-6 Concentrator optical performance and height with side angle at GCR=4 for: A- SAC, B- CAC, C- HAC and D- OAC.	83
Figure 3-7 Concentrator optical performance and height with side angle at GCR=6 for: A- SAC, B- CAC, C- HAC and D- OAC.	84
Figure 3-8 Concentrator optical performance and height with side angle at GCR=8 for: A- SAC, B- CAC, C- HAC and D- OAC.	85

Figure 3-9 Concentrator optical performance and height with side angle at GCR=10 for: A- SAC, B- CAC, C- HAC and D- OAC.....	86
Figure 3-10 Effect of surface reflectivity on the optical performance of SAC, CAC, HAC and OAC at GCR = 6 and $\psi = 20^\circ$	88
Figure 3-11 Effect of distance between the concentrator and receiver on the optical performance	90
Figure 3-12 Incoming flux versus incidence angle	91
Figure 3-13 Change in flux distribution of SAC with GCR 6 at different incidence angles.....	92
Figure 3-14 Change in the optical performance with the increase of incidence angle (from 60° to -60°)	93
Figure 3-15 Effect of the incidence angle on the optical performance with different concentration ratios for the SAC.....	94
Figure 3-16 Received flux distribution and density (W/m ²) of A: SAC, B: CAC, C: HAC and D: OAC	96
Figure 3-17 Concentrator optical performance and height of large SAC with side angle and GCR: A - 2, B - 4 and C - 6	98
Figure 3-18 Optical efficiency of large SAC with GCRs of: A - 2, B - 4 and C - 6 with different side angles.....	100
Figure 3-19 Schematic diagram for SAC with long and short concentrator sides ($W/L < 1$)	101
Figure 3-20 Effect of incidence angle on the optical performance of SAC with W/L ratio	101
Figure 3-21 Schematic diagram with dimensions for the two CPV systems using: A – small and B – large SAC.	103
Figure 4-1 Cooling duct designs for CPV/T system: A-Flat inlet and out manifold (W=10 mm), B-Flat inlet and out manifold (W=30 mm), C-Slopped inlet and out manifold (W=30/10mm), D-Slopped inlet and flat outlet manifold and E- U-type duct.....	110
Figure 4-2 CPV/T system geometry.....	111
Figure 4-3 Flux distribution at the centre line of PV module: A- exported from OptisWorks software and B- imported to COMSOL software	113
Figure 4-4 Solving mesh used with CPV/T system thermal model	115
Figure 4-5 PV cells and outlet water temperatures with different mesh sizes	115
Figure 4-6 Temperature distribution cooling water using different designs of cooling duct at flow velocity of 0.09 m/s.....	118
Figure 4-7 Cooling water outlet temperature at the five duct configurations and flow velocities (0.01 – 0.09 m/s).....	119
Figure 4-8 PV cells temperature with the use of five duct configurations and flow velocities (0.01 – 0.09 m/s).....	120

Figure 4-9 PV module average temperature at different cooling water (20 °C inlet temperature) flow rates and ambient temperatures	121
Figure 4-10 PV module temperature with different concentration ratios and cooling flow rates (Ta = 50 °C)	123
Figure 4-11 CPV/T system temperature distribution under concentration and cooling effect (GCR = 2): A- no cooling, B- flow rate of 50mL/min, C- flow rate of 450mL/min and D- flow rate of 850mL/min (Ta = 25 °C)	124
Figure 4-12 Average cooling water outlet temperature with different concentration ratios	126
Figure 4-13 PV/T system power output at different flow rates and ambient temperatures.....	127
Figure 4-14 CPV/T system power output at different flow rates and ambient temperature values	128
Figure 4-15 Change of pressure drop and pumping power with flow rate.....	129
Figure 5-1 Spectral match test setup	132
Figure 5-2 Irradiance sampling with time at three different sampling times: 1 second, 100 milliseconds and 50 milliseconds.....	135
Figure 5-3 Measuring area for light intensity mapping.....	137
Figure 5-4 Experimental set-up for CPV system testing: A- schematic diagram, B- picture view.....	138
Figure 5-5 Concentrator development: A- SAC and B- HAC	140
Figure 5-6 A: SAC and B: HAC with exit aperture area of 25 cm ² and GCR =2-10.....	141
Figure 5-7 Schematic diagram of the system output measurements	142
Figure 5-8 schematic diagram for the cooling system	145
Figure 5-9 Parts of cooling facility, thermocouples positions and process of assembling with PV module.....	146
Figure 5-10 CPV/T outdoor test facility	147
Figure 5-11 Schematic diagram of CPV/T outdoor test facility	148
Figure 5-12 Calibration setup for thermocouples.....	149
Figure 5-13 Relation between thermometer and thermocouple readings.....	150
Figure 5-14 RTD ice temperature readings	152
Figure 5-15 Flow meter calibration setup	153
Figure 5-16 Relation between calculated flow rate using cylinder and flowmeter readings	154
Figure 6-1 SAC optical efficiency (reflectivity of 90.1 %).....	159
Figure 6-2 SAC actual concentration ratio.....	160
Figure 6-3 Simulated and experimentally measured flux distribution at geometric concentration ratios of 2, 4 and 6 with ± 20 % deviation.	161
Figure 6-4 Pictorial flux distribution from outdoor experiment (A) and simulated (B) flux distribution for large SAC with geometric concentration ratio of 2.	162

Figure 6-5 Validation for the effect of surface reflectivity on concentrator optical efficiency.....	163
Figure 6-6 HAC concentrator optical efficiency.....	164
Figure 6-7 Optical efficiency of HAC and SAC.....	164
Figure 6-8 Validation of the change in PV module temperature with water flow rate	165
Figure 6-9 Validation of the change in cooling water temperature at the outlet with flow rate.....	166
Figure 6-10 I-V curves for the PV cell under different cooling methods	167
Figure 6-11 PV output with concentration and no cooling	168
Figure 6-12 PV output with concentration and passive cooling	169
Figure 6-13 PV output with concentration and active cooling.....	169
Figure 6-14 PV cell temperature under various operating conditions.....	171
Figure 6-15 PV cell maximum power output at different operating conditions.....	172
Figure 6-16 PV cell electrical conversion efficiency	173
Figure 6-17 PV electrical efficiency improvement with cooling enhancement.....	174
Figure 6-18 Increase in power gain using SAC at various cooling methods	176
Figure 6-19 PV material reduction using SAC with cooling effect	177
Figure 6-20 Effect of concentration cooling on PV module power output	178
Figure 6-21 Change of CPV/T power output (large SAC with GCR2) with water cooling flow rate	179
Figure 6-22 Outdoor and indoor I-V curve experimental measurements.....	180
Figure 6-23 Outdoor and indoor P-V curve experimental measurements.....	181
Figure 6-24 Power output of CPV/T system at different Geometric concentration ratios (cooling and no cooling, and flux of 940 -995 W/m ²)	182
Figure 6-25 PV module temperature under no concentration and at different concentration ratios with and with no cooling (940 – 995 W/m ²)	183
Figure 6-26 Effect of flow rate on CPV/T system electrical power output and module temperature at GCR 2 and average flux of 980 W/m ²	184
Figure 6-27 Effect of flow rate on CPV/T system electrical power output and module temperature at GCR 4 and average flux of 956 W/m ²	184
Figure 6-28 Effect of flow rate on CPV/T system electrical power output and module temperature at GCR 6 and average flux of 941 W/m ²	185
Figure 6-29 CPV/T system outlet water temperature under different concentration ratios and flow rates (flux of 940 to 995 W/m ²)	186
Figure 6-30 CVP/T system thermal output power and temperature difference at different geometric concentration ratios	188
Figure 6-31 CVP/T system total output power at different geometric concentration ratios and flow rates (flux of 940 -995 W/m ²)	189

Figure 6-32 CPV/T system electrical power gain at different water flow rates: A- GCR2, B- GCR4 and C- GCR6 (940 – 995 W/m ²).....	190
Figure 6-33 CPV/T system thermal power gain at different water flow rates: A- GCR2, B- GCR4 and C- GCR6 (940 – 995 W/m ²).....	192
Figure 6-34 CPV/T system thermal power gain at different water flow rates and GCRs of 2, 4 and GCR6 (940 – 995 W/m ²).....	193
Figure 6-35 CPV/T system total efficiency (940 – 995 W/m ²).....	194

LIST OF TABLES

Table 1-1 PV systems in operation, under construction and planned projects in Libya [9].....	5
Table 2-1 V-trough research summery.....	22
Table 2-2 LCPVT-focused studies covered water cooling methods	55
Table 2-3 Applications designed using OptisWorks software	58
Table 2-4 Applications designed using COMSOL Multi-physics software	60
Table 3-1 Dimensions of SAC with the change of side angle at different concentration ratios.....	74
Table 3-2 Dimensions of CAC with the change of side angle at different concentration ratios.	74
Table 3-3 Dimensions of HAC with the change of side angle at different concentration ratios.	75
Table 3-4 Dimensions of OAC with the change of side angle at different concentration ratios.	75
Table 3-5 Maximum optical performance at optimum height and side angle for different geometric concentration ratios of SAC, CAC, HAC and OAC	87
Table 3-6 Average optical performance of SAC with different W/L ratios.....	102
Table 3-7 Concentrator dimensions and material needed for small and large SAC by unit area.....	104
Table 4-1 Thermal properties of the CPV/T system components	112
Table 5-1 ASTM E927 – 10 classifications of solar simulators for photovoltaics [197]	131
Table 5-2 Simulator Light spectrum distribution at the centre of the light spot and match with the standard spectrum distribution	133
Table 5-3 Simulator Light spectrum distribution at the middle and match with the standard spectrum distribution	133
Table 5-4 Simulator Light spectrum distribution at the edge of the light spot and match with the standard spectrum distribution	134
Table 5-5 Overall spectral match and classification of the simulator light	134
Table 5-6 Temporal instability of simulator light at three different test sampling times	136
Table 5-7 Spatial non-uniformity of the areas used in testing small and large concentrators.....	137
Table 5-8 SAC and HAC dimensions at different geometric concentration ratios	139
Table 5-9 Technical specifications of cooling element	144
Table 5-10 Technical specification of highly thermally conductive heat transfer paste HTSP	144
Table 5-11 PVA-1000S PV Analyzer Kit technical specifications.....	148
Table 5-12 Calculations of thermocouple reading uncertainty	151
Table 5-13 Curve fit equations and uncertainty calculation results of thermocouples	152
Table 5-14 Calculations of flow rate measurement uncertainty.....	155

ABBREVIATIONS

2D	Two Dimensional
3D	Three Dimensional
ACPPVC	Asymmetric Compound Parabolic Photovoltaic Concentrator
ACR	Actual Concentration Ratio
ASTM	American Society for Testing and Materials
BOS	Balance Of System
CAC	Circular Aperture Concentrator
CPC	Compound Parabolic Concentrator
CPV/T	Concentrating PhotoVoltaic Thermal system
CSERS	Centre of Solar Energy Research Studies

c-Si	single/ mono crystalline silicon
CV	Coefficient of Variation
DC	Direct Current
DHW	Domestic Hot Water
EVA	Ethylene Vinyl Acetate
EXP	Experiment
GCR	Geometric Concentration Ratio
GTM	Greentech Media
HAC	Hexagonal Aperture Concentrator
HP	Heat Pump
HTF	Heat Transfer Fluid
HTSP	Heat Transfer Compound Plus
LCPV	Low Concentrating PhotoVoltaic system
MaReCo	Maximum Reflector Collector
mc-Si	poly/multi - crystalline silicon
MSDTIRC	Mirror Symmetrical Dielectric Totally Internally Reflecting Concentrator
OAC	Octagonal Aperture Concentrator
PCM	Phase Change Materials PCM
RACPC	Rotationally Asymmetrical Compound Parabolic Concentrator
RADTIRC	Rotationally Asymmetrical Dielectric Totally Internally Reflecting Concentrator
RCREEE	Regional Centre for Renewable Energy and Energy Efficiency
REAOL	Renewable Energy Authority of Libya
RTD	Resistance Thermometer Detector
SAC	Squared Aperture Concentrator
SIM	Simulation
STC	Solar Thermal Collector

NOMENCLATURE

<i>Symbol</i>	<i>Description</i>	<i>Unit</i>
$U'_{\text{thermocouple}}$	Uncertainty of thermocouples	-
U'_{st}	Uncertainty of standard thermometer	-
$S_{\bar{x}}$	Standard deviation of the mean	-
$U'_{\text{curve-fit}}$	Uncertainty of curve fit	-
U'_{fm}	Uncertainty of the Platon flow meter	-

U'_{vc}	Uncertainty of the calibration method	-
V_f	Total collecting cylinder volume	mL
V_w	volume flow rate	m ³ /s
I_m	Current at maximum power point	A
I_{sc}	Short circuit current	A
P_{max}	Maximum power output	W
Q_{cond}	Conduction heat transfer	W
Q_{conv}	Convection heat transfer	W
$Q_{rad.}$	Radiation heat transfer	W
T_c	Cell temperature	°C
T_{in}	Inlet water temperature	°C
T_{out}	Outlet water temperature	°C
T_{ref}	PV reference temperature	K
V_m	Voltage at maximum power point	V
V_{oc}	Open circuit voltage	V
q_{heat}	Heat flux	W/m ²
q_{rad}	Radiation flux	W/m ²
ΔP	Pressure drop	Pa
A	Area	m ²
C_p	Specific heat capacity	J/kg.K
D_{in}	Inlet aperture diameter	m
H	Concentrator height	m
h	Convection heat transfer coefficient	W/(m ² .K)
k	Thermal conductivity	W/m.K
n	Number of reflections	-
n_a	Average number of reflections	-
Q	Thermal power output	W
r	Radius	
T	Temperature	°C
t	Time	s

T_a	Ambient temperature	°C
U	Flow velocity	m/s
W_{in}	Concentrator inlet aperture width	m
W_n	concentrator width after nth reflections	m
W_{out}	Concentrator exit aperture width	m
Dev	Deviation	%
σ	Standard deviation	

<i>Greek symbol</i>	<i>description</i>	<i>Unit</i>
β_{thermal}	Thermal coefficient of efficiency	-1/K
η_{opt}	Optical efficiency	%
η_{pv}	PV efficiency	%
η_e	Electrical efficiency	%
η_{ref}	PV efficiency at reference temperature	%
Δ	Difference	-
α	Acceptance angle	°
ε	Material emissivity	-
ρ	Density	kg/m ³
σ	Stefan-Boltzmann constant	kg/ m ² .K ⁴
ψ	Reflector side angle	°
θ	Incidence angle	°

LIST OF PUBLICATIONS

1. Algareu, A. O., Mahmoud, S., Al-Dadah, R. K. , Abdullahi, B. and Aldihani A.. **The Effect of Geometry on the Optical Efficiency of Small Scale Solar Concentrators.**
International Conference on Applied Energy ICAE, Pretoria, South Africa 2013

2. Aldihani, A., Algareu, A. O., Mahmoud, S. and Al-Dadah, R. K. . **The Effect of Sand on the Efficiency of PV Concentrators in Kuwait Environment.** International Conference on Applied Energy ICAE, Pretoria, South Africa 2013
3. Algareu, A. O., Mahmoud, S. and Al-Dadah, R. K. . **Optical Performance of Low Concentration Ratio Reflective and Refractive Concentrators for Photovoltaic Applications.** International Conference on Applied Energy ICAE, Taipei, Taiwan, 2014. Energy Procedia 61 (2014) 2375 – 2378.
4. Aldossary, A., Algareu, A. O., Mahmoud, S. and AL-Dadah, R. K. . **Performance of Multi Junction PV Cells With High Concentration Ratio in Saudi Arabia.** International Conference on Applied Energy ICAE, Taipei, Taiwan, 2014. Energy Procedia 61 (2014) 2258 – 2261.
5. Algareu, A. O., Aldossary, A., Mahmoud, S. and Al-Dadah, R. K. . **Optical Analysis of Flux Uniformity and Efficiency in Low Concentrating PV Systems.** 14th International Conference on Sustainable Energy Technologies SET 2015, Nottingham, UK, 2015.
6. Aldossary, A., Algareu, A. O., Mahmoud, S. and Al-Dadah, R. K. . **Improving Illumination and Temperature Distribution Uniformity in High Concentrating Solar Cells.** 14th International Conference on Sustainable Energy Technologies SET 2015, Nottingham, UK 2015.
7. Al-Shohani, W., Algareu, A. O., Mahmoud, S. and Al-Dadah, R.K. . **Ray-tracing Analysis of An Optical Filter for Photovoltaic/Thermal Module.** 31st European Photovoltaic Solar Energy Conference and Exhibition, EU PVSEC at Hamburg, Germany, 2015.

8. Al-Shohani, W., Algareu, A. O., Mahmoud, S. and Al-Dadah, R. K.. **Performance of a V-trough photovoltaic system.** International Conference on Renewable Energy Research and Applications ICRERA, At Birmingham, UK, 2016.
9. Al-Shohani, W., Al-Dadah, R.K., Mahmoud, S. and Algareu, A. O.. **Optimum design of V-trough concentrator for photovoltaic applications.** Solar Energy 140 (2016) 241–254.

DEDICATION

To the soul of my beloved father and

To my beloved mother

To my beloved wife, children and the whole family

CHAPTER 1: INTRODUCTION

1.1. Background

Since the dawn of civilization, energy is increasingly becoming essential to sustain human life and development. Due to growth in population and advances in industrialisation, and according to the World Energy Outlook 2016 a 30 % increase in global demand is expected by 2040. Most of world energy is generated from burning fossil fuels like coal, oil and gas, which have two main concerns: first is economical and related to the higher fuel cost and potential of its exhaustibility [1]. Second is related to the increase in air pollution, global warming and climatic change in the form of floods and storms that damage the environment and cause diseases and deaths of many lives.

Therefore, during the last few decades significant effort to utilise renewable energy sources including solar (electrical and thermal), wind, tides, geothermal and nuclear have been made. The power generated by renewable energy in 2040 is expected to be about 60% of total generated power, and about half of this energy comes from wind and solar photovoltaic (PV) systems [2]. The use of solar PV systems for producing electrical energy has increased significantly in the last decade [3]. According to the International Energy Agency report for 2014 the global capacity of PV technology exceeded 150 GW in the early 2014 and is expected to reach 4600 GW in 2050 [4]. This growth comes due to their advantages of no greenhouse gases emissions, long operating life (up to 25 years) with low maintenance and no noise. Some drawbacks are appearing in the presence of high temperature that affects system performance.

Due to the apparent reliability of PV systems made of traditional silicon, a remarkable presence for these renewable systems in today's market have been accomplished and

motivated by various programs in many countries for the advantages of clean energy [5]. However, in some areas that enjoy high level of direct solar radiation such as the Middle East and North African countries, according to the world bank data till 2012, the total electricity generated from renewable sources did not reach 4% of total electricity generated in this region [6] due to cost, and alternative cheaper sources like oil and natural gas available in this area.

1.2. Energy in Libya

Libya is a North African country, located between latitude of 20° and 33° N and longitude between 10° and 25° E. It is bordered by the Mediterranean Sea to the northern side, Egypt to the eastern side, Sudan to the southern east side, Chad and Niger to the southern side, and Algeria and Tunisia to the western side. It has a total area of $1,759,540 \text{ km}^2$ with the southern part of the country located in the Sahara desert and the northern part is on the Mediterranean Sea coast.

In the last years, the consumption of the electrical energy (kWh/capita) in Libya has increased, by over 111% in the period from 2000 to 2012 [7, 8]. This increase is due to the development in all sectors including transport, industry and living standards. This improvement is accompanied with increase in population in Libya, leading to an increase in energy demand. **Figure 1-1** shows the population growth and oil production, consumption and net exportation for the period from 1960 till the end of 2011[9]. It is clear that the population is significantly increased from about 1.3 million in 1960 to exceed 6 million at the end of 2011. Electricity production relies mostly on fossil fuel consumption resulting in significant greenhouse gases emissions [10].

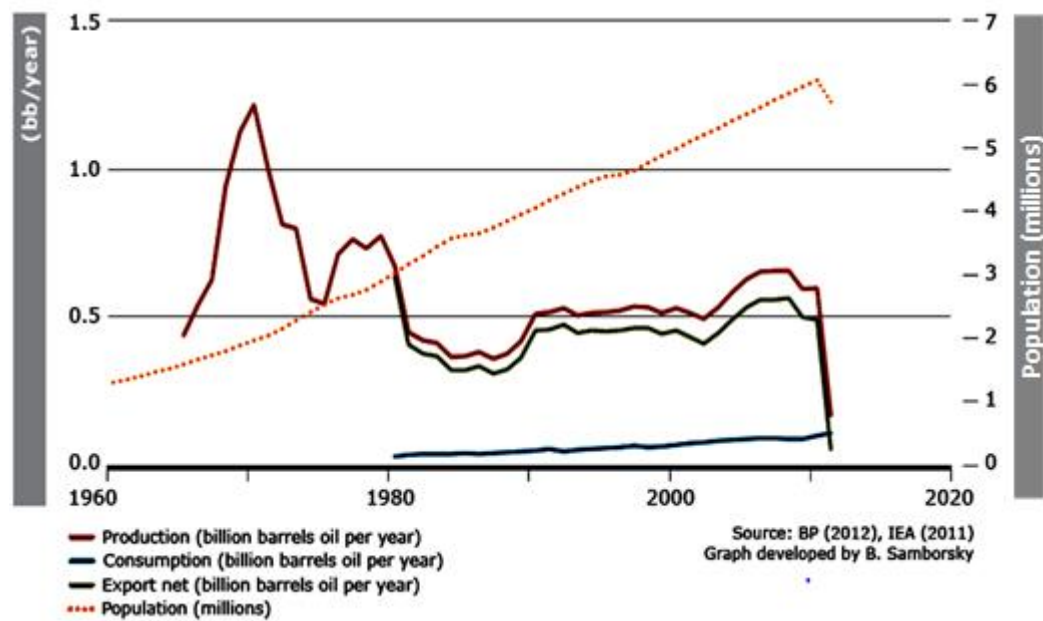


Figure 1-1 Libya energy supply and demand trend [9]

Consequently energy sector requires more investment in the power generation infrastructure of the country, such as renewal of power lines and constructing new power plants. Also, it is necessary to develop alternative electrical generation systems that could be spread geographically in Libya, especially renewable energy sources which are environment friendly such as solar energy.

Libya enjoys high rate of solar radiation with high beam component where a maximum average annual direct normal solar irradiance in the Libyan desert of about 3000 kW.h/m^2 per annum can be received as shown in **Figure 1-2** [11]. According to the Regional Centre for Renewable Energy and Energy Efficiency (RCREEE) [9], the 2012 installed capacity of renewable energy in Libya is only about 0.06 % of the total, while 99.94 % is for fossil fuel, as shown in **Figure 1-3**. Although there is a target for energy from renewables to reach about 10 % by 2025, but this target may not be achievable, for the reasons of war and no political stability till December 2016.

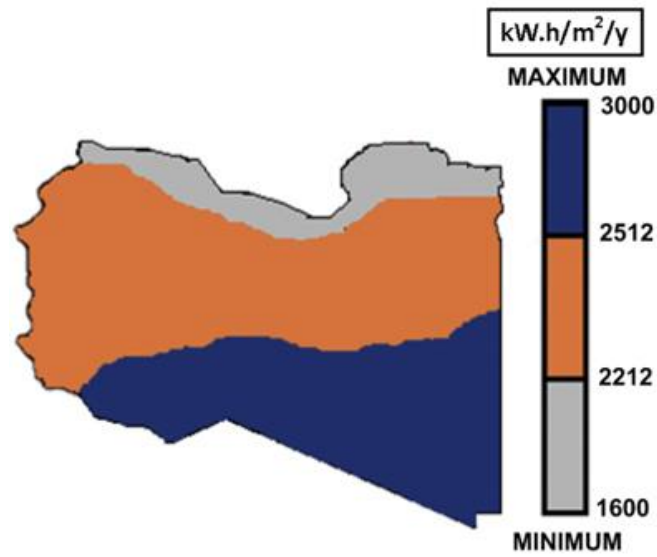


Figure 1-2 The estimated average solar energy in the Libya desert [11]

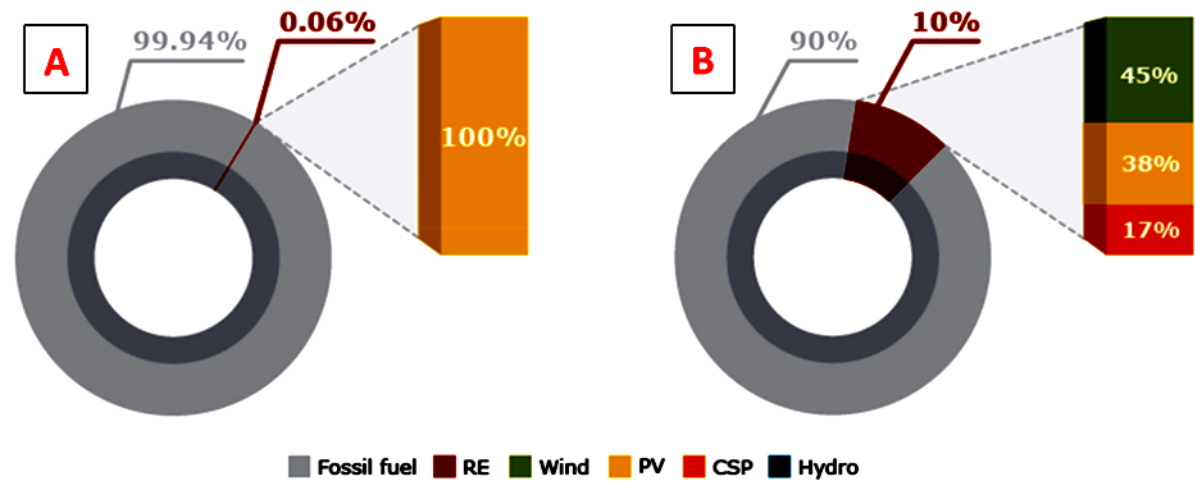


Figure 1-3 Energy installed capacity in: A- 2012 and B- 2025 [9]

Officially, establishment of the Solar Energy Research Centre and Renewable Energy Authority of Libya (REAOL) was in 1978 and 2007, respectively with the aim of research and development of renewable energy systems for various applications and promoting renewable energy in Libya. Although a general solar map for Libya exists based on satellite data, and the first large-scale PV Plant is under construction in Al-Jofra city with 14 MW, other projects are still in the planning stage and no real progress is made. **Table 1-1** lists all solar energy

projects in Libya including projects in operation, projects under construction and planned projects. In Sabha city, there is a plan for a solar PV project that should produce 40 MW and land is already assigned for this project by the Libyan government [9].

Table 1-1 PV systems in operation, under construction and planned projects in Libya [9]

Project	Capacity	Developer	Status
Wadi-Marsit Centralized PV System	67.2 kW	Public	In operation
PV water pumping system	120 kW	Public	
Communication repeater stations	950 kW	Public	
Grid connected small scale PV	42 kW	Public	
Rural electrification PV systems	725 kW	Public	
Street lighting PV systems	15 Systems × 75 kW	Public	
Mobile phones	1859 kW	Public	
PV Plant Al-Jofra	14 MW	Public	Under construction
PV Plant in Sabha	40 MW	Public	Planned
PV Plant South Green Mountain	50 MW	Private	
Rural electrification PV	2 MW	Public	
PV Plant Ghat	15 MW	Public	
PV Roof top systems	3 MW	Public	

The daily average of solar radiation on a horizontal plane in the coast region is (7.1kWh/m²/day) and in the southern region is (8.1kWh/m²/day) [12]. Sabha (Lat. 27.02° N) is one of the main cities of the southern region of Libya and mainly surrounded by

desserts. **Figure 1-4** shows the monthly average daily solar radiation on a horizontal surface in Sabha city showing that the beam radiation represents a significant component of solar radiation (75 % to 85 %).

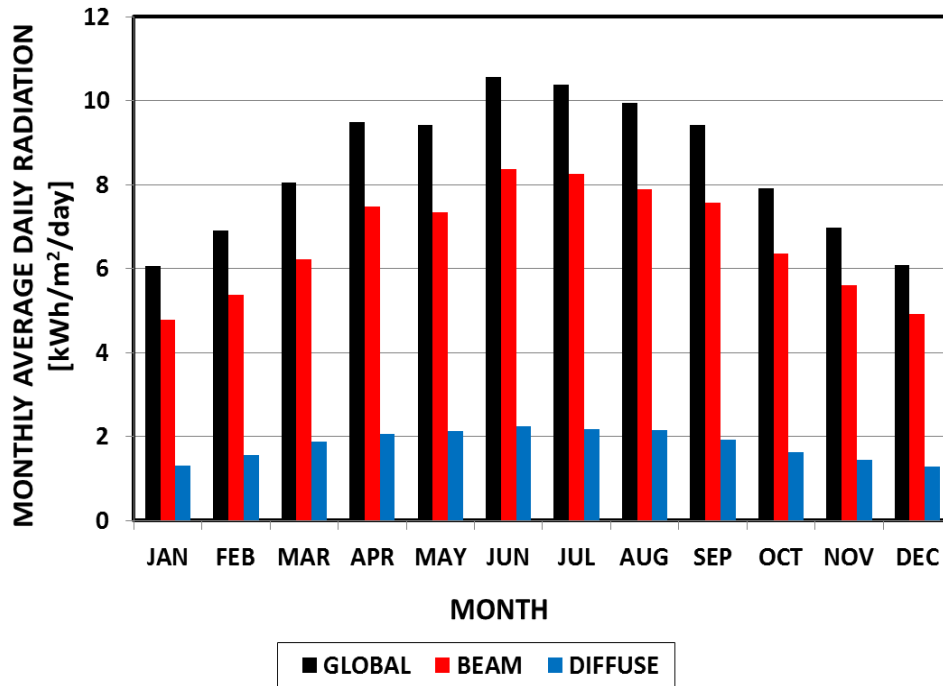


Figure 1-4 Monthly average daily solar radiation on a horizontal surface of Sabha city
(Lat. 27.02° N)

Figure 1-5 shows the monthly average daylight hours of Sabha city. It is clear that the city has high daylight hours during the year with the maximum exceeding 13 hours in May, June and July and minimum 10 hours in January, November and December months and annual average of 12 hours.

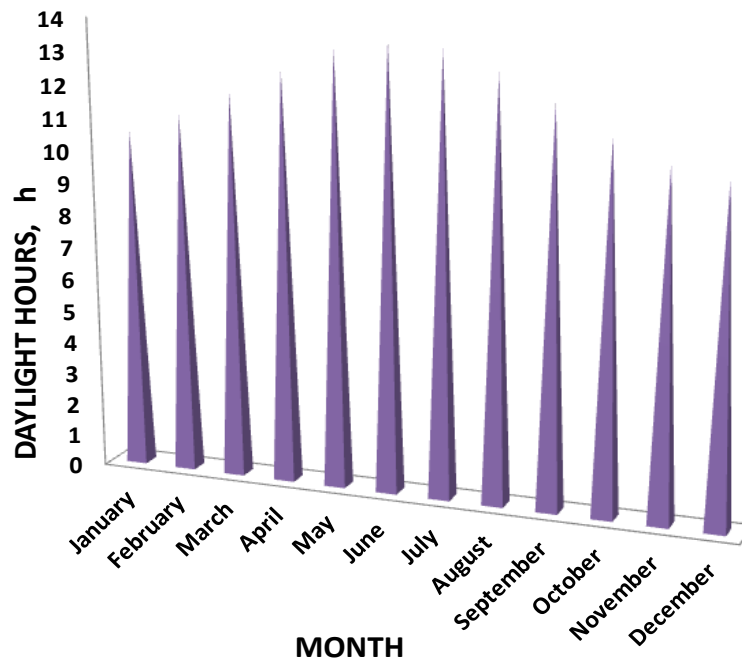


Figure 1-5 Monthly average daylight hours of Sabha city (Latitude: 27.02° N).

Due to the increasing energy demand and availability of desert area with abundant solar radiation, an urgent need to study the feasibility of solar energy in Libya using different solar systems (electrical and thermal). Decentralization of power production facility using solar power is one of the solutions that reduce the lack of energy and transmission losses which is about 19 % of output according to the World Bank especially in rural areas the need for hundreds of kilometres of electricity lines are needed. Also the use of heat generated by the CPV/T systems for cooling applications (such as adsorption systems) will contribute in reducing the direct electrical consumption.

1.3. Concentrator photovoltaic/ thermal system CPV/T

Using concentrator photovoltaic (CPV) systems can contribute to lowering the system cost by replacing the relatively expensive PV materials with other cheaper (optical) materials that can be used to concentrate the sun light on smaller PV material area [13, 14]. Concentrators with

low concentration ratios (ranging from 2 to 10) offer the advantage of light weight, small size and are easy to install at reduced cost [15, 16].

Solar concentrators can be classified into two main types, which are either reflective or refractive concentrators. Reflective concentrators include 2D concentrators like V-trough concentrators [17] and Compound Parabolic Concentrators (CPC) [18] or 3D concentrators like dish concentrator and other different concentrator configurations [19, 20]. Refractive concentrators include Fresnel lenses which can be classified as either Groove in or groove out Fresnel lens [21]. They are also classified as Point focus or Linear focus Fresnel lenses, which are either: Flat, Roof or curved [22].

Literature review has shown that huge amount of research has been reported on the performance improvement of concentrator photovoltaic and thermal systems, but it was neither on 3D flat sided (3D V-trough) concentrator (with any of designed geometries) with PV (CPV) system, nor with thermal extraction facility as a CPV/T system. An exhaustive research of 3D flat sided concentrator photovoltaic thermal (CPV/T) system that takes into consideration all the major parameters affecting system performance is needed. Therefore, this thesis describes a detailed investigation of such configuration for low concentration CPV/T system (2 - 10) with a consideration of all the factors affecting system performance, such as amount of radiation available, design parameters and system orientation. And from section 1.2, although the energy demand is increasing, in Libya and the abundant solar energy in this region, no concentrating photovoltaic thermal (CPV/T) systems, or CPV system in operation either at domestic or industrial level except few flat plate PV solar systems that do not satisfy domestic demand, especially in rural areas in the southern part of the country.

1.4. Aims and objectives

The aim of this work is to investigate the performance of a CPV/T system using 3D flat sided (3D V-trough) concentrators with different configurations named squared (SAC), Hexagonal (HAC), Octagonal (OAC) and Circular (CAC) inlet and exit apertures.

This investigation includes the following objectives:

- Optical optimisation using advanced ray tracing simulation (OptisWorks) and optical mathematical models for the suggested geometries, with a range of concentrator side angles. A comparison was made between the mathematical modelling and the optical simulation using OPTISWORKS software as well as, investigating the effect of gap distance between concentrator and receiver, concentrator reflectivity, incidence angle on concentrator optical performance and flux distribution.
- Thermal modelling of the whole CPV/T system, and the cooling system to evaluate the thermal performance; firstly for the suggested cooling duct configurations to select one for the CPV/T system, and secondly, the thermal performance of the whole system with the selected cooling duct.
- Testing and evaluating the performance of follow spot light to be used as a solar simulator in CPV/T indoor optical and thermal experiments.
- Constructing the selected geometries with optimised dimensions with small scale for preliminary testing with the indoor solar simulator under different operating conditions and large scale for outdoor testing, at different geometric concentration ratios.
- Conducting indoor and outdoor experiments to validate the optical and thermal simulation and testing the electrical and thermal performance of the developed CPV/T

system under different cooling flow rates, and evaluate the feasibility of this system for electrical and thermal energy demand in domestic applications.

1.5. Thesis outlines

This thesis provides detailed investigation of four different 3D flat sided reflective concentrator geometries (Square (SAC), Hexagonal (HAC), Octagonal (OAC) and Circular (CAC) inlet and exit apertures) with low geometric concentration ratio (2 - 10) to be used as a concentrator Photovoltaic cell thermal (CPV/T) system. The optical, electrical and thermal performance of the CPV/T system was investigated using air and water cooling approaches, and the total performance was evaluated.

The thesis begins with a critical literature review on the PV types, low concentrating photovoltaic systems and their cooling techniques including the design, performance enhancement and applications. Analysis was carried out for the solar radiation in Sabha City in the southern part of Libya using meteorological data. Experimental investigation was conducted using follow spot light, which was characterised according to the ASTM standard for indoor light source.

Detailed description of the development of the cooling system using COMSOL Multi-physics was conducted. Advanced ray tracing technique using OptisWorks software was extensively used in optimising the key parameters that affect the performance of the concentrators. Optical, electrical and thermal experimental work was conducted using the developed CPV/T system under different operating conditions. The total gain and system efficiency of the CPV/T system was analysed. The thesis content is briefly arranged as follows:

- **Chapter One** comprises a brief introduction to the energy issue in Libya including current and future status with the growth in population and increase in energy demand

trend as well as the potential of solar energy followed by an introduction on the reflective concentrators and the general thesis content.

- **Chapter Two** includes a critical literature review of published studies on the types of PV cells, experimental and numerical studies on low reflective concentrator PV systems in terms of electrical and thermal performance.
- **Chapter Three** describes the optical modelling of three dimensional (3D) concentrators of low concentration ratio (2-10). The investigation involves the actual concentration ratio and optical performance. A mathematical modelling was performed for four 3D concentrators with square, circular, hexagonal and octagonal inlet and exit apertures to be used as a concentrator photovoltaic (CPV/T) system. A ray tracing software (OptisWorks) was used to provide detailed flux distribution for the optimum designs in terms of optical performance.
- **Chapter Four** describes the thermal modelling of full CPV/T system assembly with SAC developed in chapter three at three different geometric concentration ratios using COMSOL Multi-physics software. Five different cooling system configurations were modelled to determine the best performing one in terms of the required pumping power.
- **Chapter Five** presents the experimental setup for indoor and outdoor optical, electrical and thermal investigation. Indoor setup was used to test a small scale CPV system with SAC having GCR values of 4, 6, 8, 10, large scale SAC with GCR values of 2 as well as, small scale Hexagonal Aperture concentrators (HAC). The testing facilities for the optical, electrical and thermal output of CPV/T system and instrument calibration were described in details.

- **Chapter Six** presents the indoor and outdoor experimental results for the designed CPV/T system. Results include the optical performance of SAC and HAC concentrators as well as the electrical and thermal output of the CPV/T using SAC concentrators with geometric concentration ratios of 2, 4 and 6 under different operating conditions. Also optical and thermal validation of the system performance is presented.
- **Chapter Seven** provides the conclusions obtained from the work conducted and recommendations for the future work.

CHAPTER 2: LITERATURE REVIEW

2.1. Introduction

In this chapter a literature review is carried out describing the different PV cell technologies for solar energy and the types of Concentrator Photovoltaic (CPV) systems, with particular focus on Low Concentration Photovoltaic (LCPV) systems, as this study is devoted to such type of concentrating systems. As a result of light concentration and the limitations of PV cells in converting solar radiation to electricity, heat is generated and need to be extracted by a cooling system that either dissipates the generated heat to the environment through the air or uses it for various applications by means of hot water. Thus the second part of the literature review is about the different cooling systems used with low concentration photovoltaic systems. The third part of this chapter is describing the optical and thermal simulation techniques used by researchers to simulate the optical and thermal characteristics of PV cells with low concentrating systems. Lastly, a determination of the research gap that should be filled by the researcher with a selection of the appropriate tools for design, evaluation and optimisation of the CPV/T system.

2.2. Photovoltaic technology

Solar cell is the electrical generator and is the most essential part in the solar PV system. It is a semiconductor solid state electrical device that converts the light photon energy into direct current (DC) electricity using the photovoltaic effect. The conversion of energy into electricity requires a material which absorbs the light photons, to raise electron energy to a higher energy form, enabling it to flow through an external circuit. Silicon is one of the most

commonly used semiconductor materials that use this process. A solar cell and panel structures are shown in **Figure 2-1**.

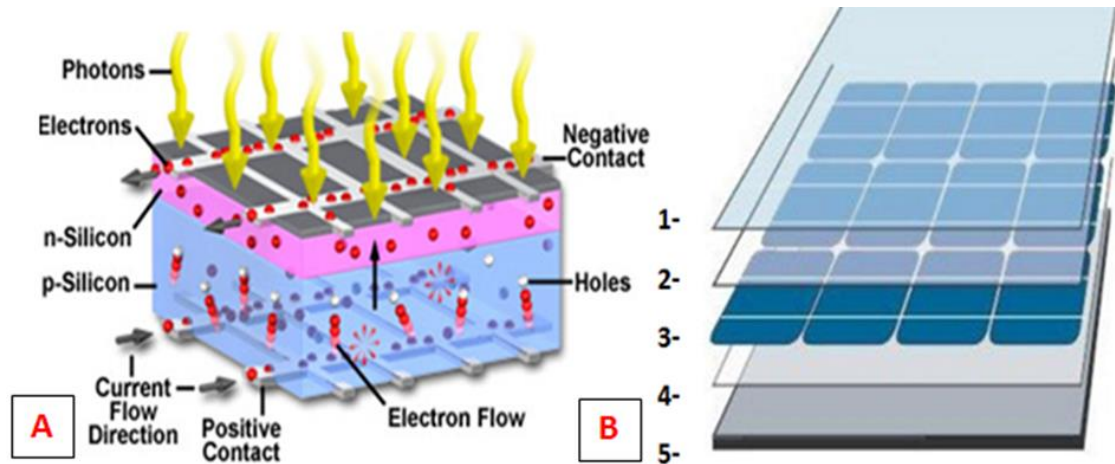


Figure 2-1 Structure of: A- silicon PV cell [23] and B- PV module with 1- tempered glass, 2- EVA, 3- PV cells, 4- EVA and 5- Back sheet

Different photovoltaic (PV) cells technologies are available in the market nowadays, with different conversion efficiencies. PV cells can be classified in three main categories: silicon PV cells which is the first generation of this technology, thin film PV cells (second generation) and multi junction PV cells (third and fourth generation). The following sections provide detailed information for the three main technologies.

2.2.1. Silicon PV cells

Silicon cells are the most commercially used solar cells which are built using silicon wafers. Crystalline silicon cells are of two types; single/ mono crystal (c-Si) and poly/multi - crystalline silicon (mc-Si/) the majority of which are based on a screen printing-based devices. The efficiency of commercial monocrystalline modules is between 14 % and 21 % [24], although new device technology by Panasonic has announced a HIT mono-crystal/ amorphous cell with efficiency of 25.6 %, and a module with 23.8 % efficiency at standard

testing conditions [25]. It is higher than that of Sunpower module efficiency (22.8 %). Monocrystalline PV technology accounts for about 23.9 % of the global annual production with 15.1 GW in 2015 [26]. The efficiency of commercial Multi-crystalline modules is between 12 % and 18 % [24] and the highest reported efficiency is about 20.8 % achieved by Trina Solar [25]. Multi-crystalline PV technology accounts for about 69.5 % of the global annual production with 43.9 GW in 2015 [26]. The efficiency of the silicon PV cells is affected by the light intensity. According to the theoretical and experimental results achieved by Khan et al. [27], at constant temperature (25 °C) the cell efficiency increases with the increase of light intensity ranging from 150 W/m² to about 600 W/m², then remains constant up to about 1000 W/m². While cell efficiency drops as the light intensity increases higher than 1000 W/m².

2.2.2. Thin film PV cells

The second-generation of PV cells are thin film PV cells which are based on the use of less material while maintaining the same efficiency of crystalline PV cells. As most of solar absorption occurs in the upper tens of microns, the rest of PV thickness (200 µm) has only mechanical support purpose. Thus the cost of PV cell will be less if the used material is reduced to the optimum thickness. This type of solar cells is made from amorphous-Si (a-Si), CuIn(Ga)Se₂ (CIGS), CdTe/CdS (CdTe) or polycrystalline-Si (p-Si) which are deposited on a glass substrate as a low cost material [28]. The efficiency of thin film ranges from 13.5 % to 21% for the size of 1 cm² and from 10.5 % to 18.6 % according to the highest lab results [26]. Thin film PV technology accounts for about 6.6 % of the global annual production by 4.2 GW in 2015 [26].

According to Greentech Media (GTM) Research's latest report in 2015 Technology Trends and Markets in the U.S. and Abroad, the PV market will show a reduction of PV balance of system (BOS) costs of about 40 % by the end of this decade (up to 2020) and installation capacity will increase to exceed 100 GW [29]. **Figure 2-2** illustrates the installed capacity growth and cost reduction trend between 2013 and 2020 expectations.

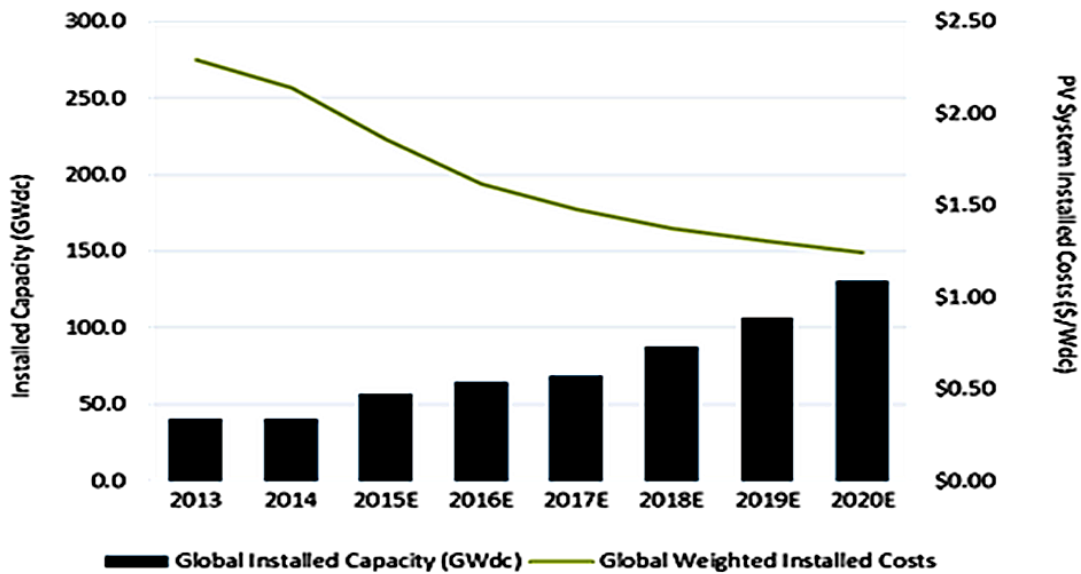


Figure 2-2 Global Installed Capacity and Average PV System Installed Costs, from 2013 to 2020 [29].

2.2.3. Multi-junction cells

As research effort is focusing at increasing the total system efficiency at all levels from cell to module, the third generation of PV cells which has higher conversion efficiency include multi-junction PV cells. Multi-junction solar cells consist of three or more layers of single-junction solar cells stacked over each other. These single junction cells have different bandgaps arranged by the material which has larger bandgap on the top and getting smaller and smaller to the bottom material that has the smallest bandgap. This variety of bandgap allows converting the photons that have energies greater than the bandgap of certain layer and

less than the bandgap of the higher layer [30]. Increasing the number of junctions and widening the bandgaps should widen the range of spectrum absorbed consequently higher conversion efficiency is achieved [31], as clearly illustrated by the comparison of silicon PV cell and multi-junction PV cells light absorption shown in **Figure 2-3**. The typical triple-junction PV cell structure includes three n-p junctions of gallium indium phosphide (GaInP), gallium indium arsenide (GaInAs) and germanium (Ge) stacked on top of each other to form series connection [32].

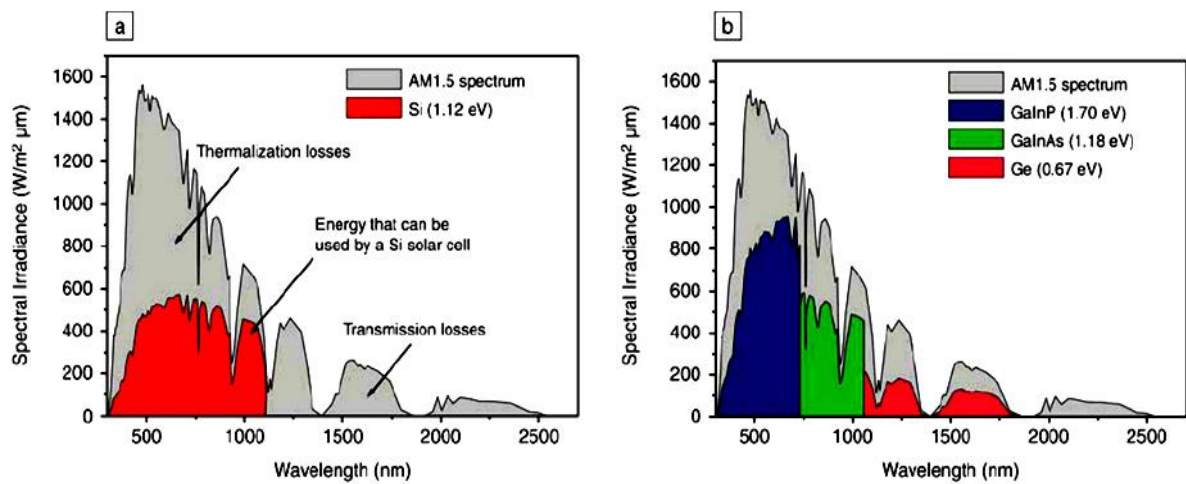


Figure 2-3 Spectral response of: a, silicon PV cell and b, multi-junction PV cell [31]

The laboratory conversion efficiency of multi-junction PV cell with four-junctions (GaInP/GaAs//GaInAsP/GaInAs) has reached 46.0 % [33-35], which exceeds double the efficiency of silicon cells, while with concentrator technology, module efficiencies reached 38.9 % [35].

2.3. Reflective low concentrating photovoltaic systems

In reflective Low Concentrator Photovoltaic LCPV systems, concentrators can be classified 2D or 3D concentrators. The following is a detailed explanation of the available LCPV systems based on the classification mentioned above.

2.3.1. 2D reflective low concentrating PV systems

2D V-Troughs or compound parabolic concentrators (2D-CPC) were used with silicon PV cells. V-trough is an attractive low concentrating option for reducing the price of the PV electrical power [17], and one of the simplest designs for a maximum concentration ratio of 3 [36-39]. Sangani and Solanki in 2006 [17] designed and manufactured three different V-trough concentrators depending on the tracking system (seasonal, one axis and two axes) using mirror and anodized aluminium with a reflectivity of 79% and 85%, respectively. These designs have been experimentally tested on three different commercially available monocrystalline and polycrystalline PV modules to evaluate the cost of PV power output (\$/W). **Figure 2-4** shows the system construction and the angles of V-trough reflector. Experimental results showed that the PV illumination is more uniform using V- trough design with an angle of 30° but less power output compared to the one with an angle of 15° which gives non-uniform illumination and requires larger reflector area but higher power gain. Also concentrated PV modules produced higher output power and lower series resistance PV modules. The power gain was increased by over 40 % from flat PV systems, and the cost/ unit watt decreased by 24 %.

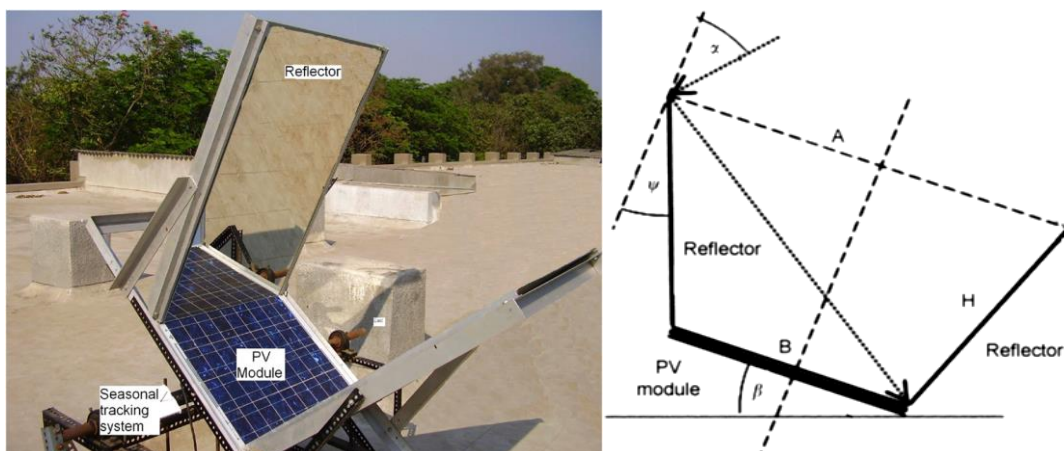


Figure 2-4 V-trough reflector: α , acceptance angle; ψ , trough angle; A, collector aperture width, B, receiver base width; H, reflector slant height [17].

Maiti, et al [40] investigated the effect of reflector angular variation on the optical efficiency and spatial distribution for V-troughs made of anodized Aluminium reflectors with specular reflectivity of 70 % and a system area of $9.64 \text{ m} \times 0.55 \text{ m}$. Ray tracing results predicted a maximum optical efficiency of 85.9 % can be achieved and results were validated with an average error of $\pm 10\%$. In 2008, Solanki et al [41] have designed a 2 sun concentrator PV system shown in **Figure 2-5-A** with V-trough reflector, made of a continuous Aluminium sheet (used to enhance heat dissipation) for six PV module strips. Each strip was integrated with 6 monocrystalline Si cells and the system has the advantages of concentrating sun light and dissipating the generated heat simultaneously. Outdoor measurements showed an increase in generated current and voltage, consequently higher power output compared with the flat plate module as shown in **Figure 2-5-B**. Improvement in current and voltage is a result of concentration and heat dissipation by V-trough design, respectively (cell temperature decreased from 80°C to 60°C under 750 W/m^2).

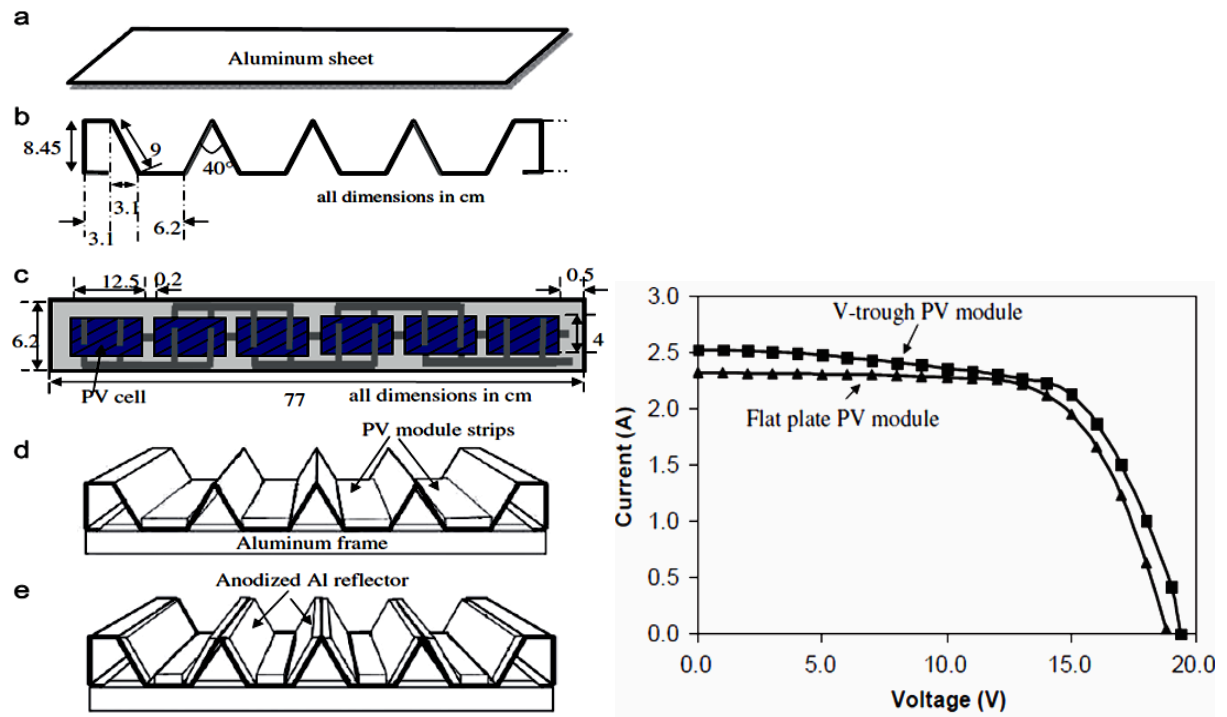


Figure 2-5 A- Continuous Aluminium V-trough reflector and **B-** V-trough PV module and the Flat plate module I-V curves [41]

Kostic et al [42] studied the influence of reflectance and reflector side position on the optical efficiency of V-trough used as CPV/T system. The system was used with two different reflective materials (Al sheet and Al foil), single-crystalline silicon PV module and has a fixed bottom part mounted on a metal support and movable trough sides enabling reflector tilting from 0° to 90° , aiming to determine the best position as shown in **Figure 2-6**.

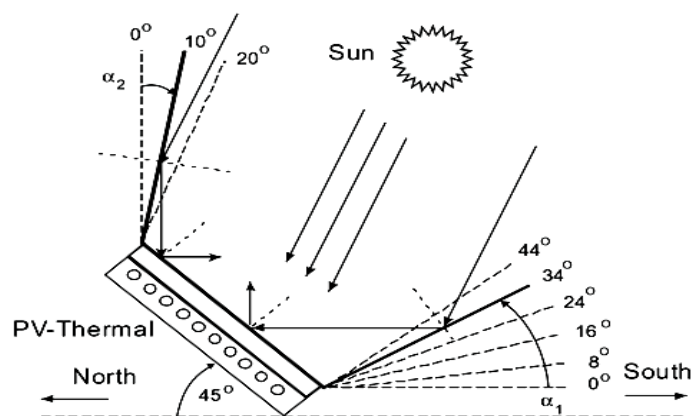


Figure 2-6 CPV/T system with a fixed bottom mounted on the metal support movable upper part enabling reflector tilting to $0 - 90^\circ$ in relative to the horizontal plane [42].

Measurements showed that the total reflectance for Al sheet and Al foil are almost the same, but specular reflectance for the Al foil resulted in higher concentration ratio, consequently higher total energy generated by the system where an energy gain of about 35% and 50% for PV/Thermal collector with concentrators made of Al sheet and Al foil, respectively compared to the PV/Thermal collector without concentrators. Also Shaltout et al. [43] designed a V-trough concentrator to be used with two axis tracking system to increase the PV performance. Two different PV cells were used with the concentrator namely polycrystalline and amorphous silicon cells. Comparing the concentrated system performance with the same PV cells without concentrator, results showed an increase in solar radiation gain for concentrated system by 58% more than normal radiation, while further increase of 23% using full tracking with the concentrated system. Response of PV cells was different where amorphous silicon cells achieved an increase in output by 40% with concentration higher than without while polycrystalline silicon cells achieved less than that. Increasing amorphous silicon cell temperature by $15 - 20^\circ\text{C}$ produced a drop in voltage by 4 % around the noon time. On the other hand, increasing polycrystalline cell temperature by $3 - 7^\circ\text{C}$ resulted in a drop in voltage by 6 %. Butler et al. [44] designed, built and evaluated the optical and electrical efficiency of a LCPV system using linear trough with four facets producing a geometrical concentration ratio of 3, and Multi-crystalline silicon cells attached to heatsink, as shown in **Figure 2-7**. Modelling and experimental results showed an actual concentration ratio of 2.68 and 2.49, respectively.

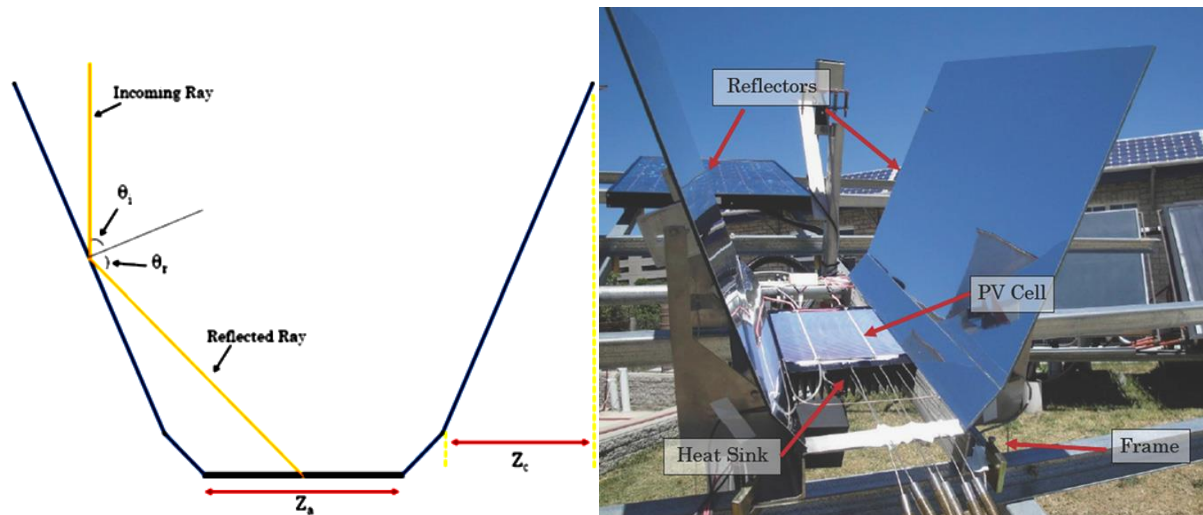


Figure 2-7 A schematic and Experimental LCPV prototypes [44]

Table 2-1 summarizes some of V-trough research references for photovoltaic application including concentration ratio, reflectivity and system gain.

Table 2-1 V-trough research summery

Reference	application	CR	Reflectivity %	Increase in power %
[45]	solar water purification and electricity generation	2.34	82.1	100 %
[46]	electricity generation (PCM cooling)	1.55	-	55%
[47]	photovoltaic V-trough pumping systems	1.6	80	48%
[48]	electricity generation	1.81	90	34 %

[49]	Electricity and thermal power generation	2.36	67	25 %
[50]	Photovoltaic-electrolyser with V-trough	1.9	55	-
[51]	Optical analysis	2	-	95%
[52]	Electricity generation	2	79	54.3 %
[53]	Electricity generation	1.5 and 2	83	20 and 50

Different designs of compound parabolic concentrators, CPC were investigated with different configurations by many researchers. Wu [54] has designed an Asymmetric Compound Parabolic Photovoltaic Concentrator (ACPPVC) shown in **Figure 2-8** with a concentration ratio of 2, integrated with a Phase Change Materials (PCM) at the rear for cooling purpose for a building façade. Indoor experimental results showed a 1.8 times output increase compared to that of the flat plate PV system with the same PV cell area.

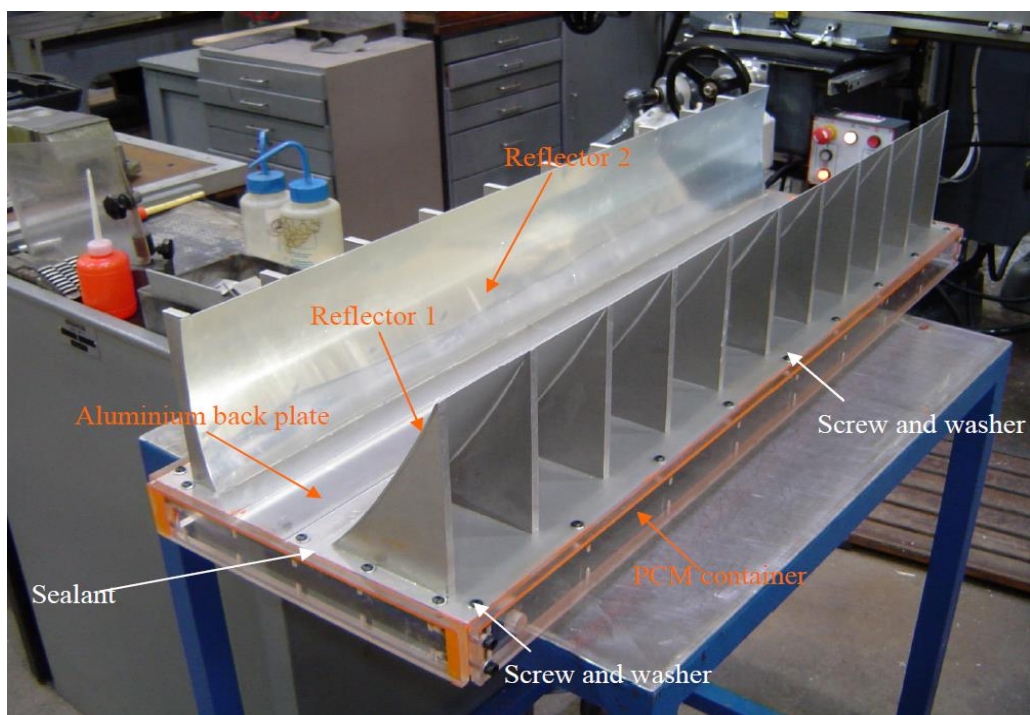


Figure 2-8 Photograph showing the ACPVVC system integrated with PCM [54]

Guiqiang et al. [55] developed a mathematical algorithm to study CPC-PV/T system with single crystalline PV cells using different CPC concentration ratios (1.5, 2, 2.5, and 3), and compared the results with experimental results of flat PV system and CPV/T system in terms of overall performance. A schematic diagram of CPC-PV/T system is shown in **Figure 2-9**. Results demonstrated that a maximum total system efficiency of 78 %, at concentration ratio of 3, recognizing the suitability of the CPCs with CR below 3 for building integrated systems, as well as increasing the overall thermal and electrical efficiencies.

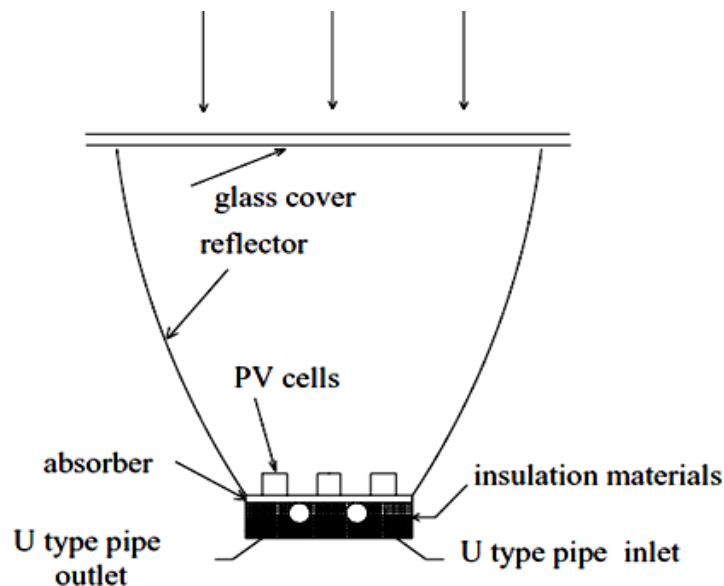


Figure 2-9 Schematic diagram of CPC-PV/T system with CPC concentration ratio (1.5, 2, 2.5, and 3) and a U-type pipe as a collector [55]

Xu et al. [56] designed low concentrating photovoltaic thermal system integrated with a heat pump, LCPV/T-HP. This system used compound parabolic concentrator made of mirror finished Aluminium sheet with reflectivity of 0.88 and geometric concentration ratio of 2.44. The system used the evaporator of the heat pump where refrigerant R134a flows through Aluminium tubes fitted underneath the solar cells to extract the generated heat. Results

demonstrated an actual concentration ratio of 1.6, while comparing the LCPV/T-HP with LCPV alone, the electrical efficiency has increased from 12.9% to 17.5%, which is 1.36 times that of the LCPV without cooling. Bernardo et al. [57] exemplified a particular case of comparison of output per unit area between a hybrid CPV/T system with parabolic trough and a north-south tracking system and separate PV module and flat plate collector. PV cells in the CPV/T system are laminated to one side of the triangular cross-section thermal absorber along the concentrator as shown in **Figure 2-10**.

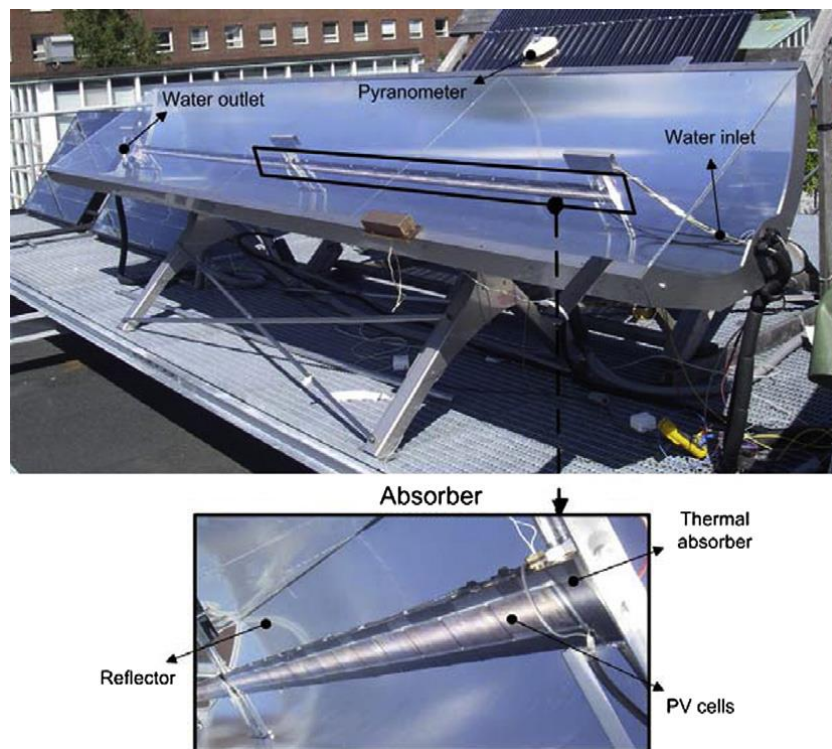


Figure 2-10 CPV/T system with parabolic trough and photovoltaic cells attached to a thermal absorber [57]

Based on systems electrical and thermal efficiency, CPV/T system showed an electrical efficiency of 6.4% in the electrical efficiency and 45% in optical efficiency, compared with the standard PV module (16 %) and flat plate collector (80%). Moreover, the hybrid system has 20-40% lower beam radiation incident on the north-south axis tracking surface than the

global radiation on a fixed surface at optimal tilt, as they highlighted that the hybrid CPV/T system is not a good alternative to conventional PV modules and flat plate collectors. Sarmah et al. [58] designed and indoor tested a 170mm X 150 mm prototype of photovoltaic module for building integration with concentration ratio of 2.8 as shown in **Figure 2-11** schematically and pictorially. Their experimental optical results showed an 80.5% optical efficiency. This increased the maximum power by 2.27 times compared to the module without concentration, and an average electrical efficiency of 9.43% and maximum of 12.1%. Cost analysis demonstrated a reduction of 20% per unit power output.

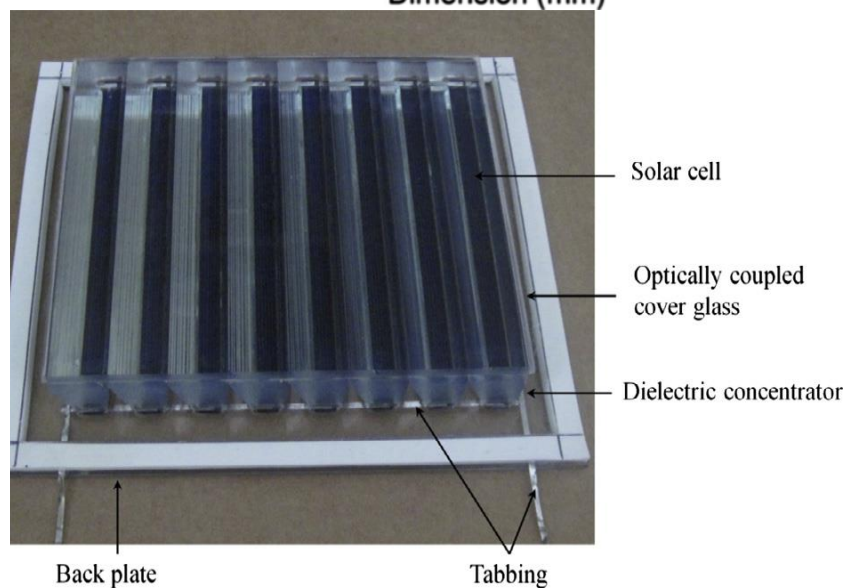
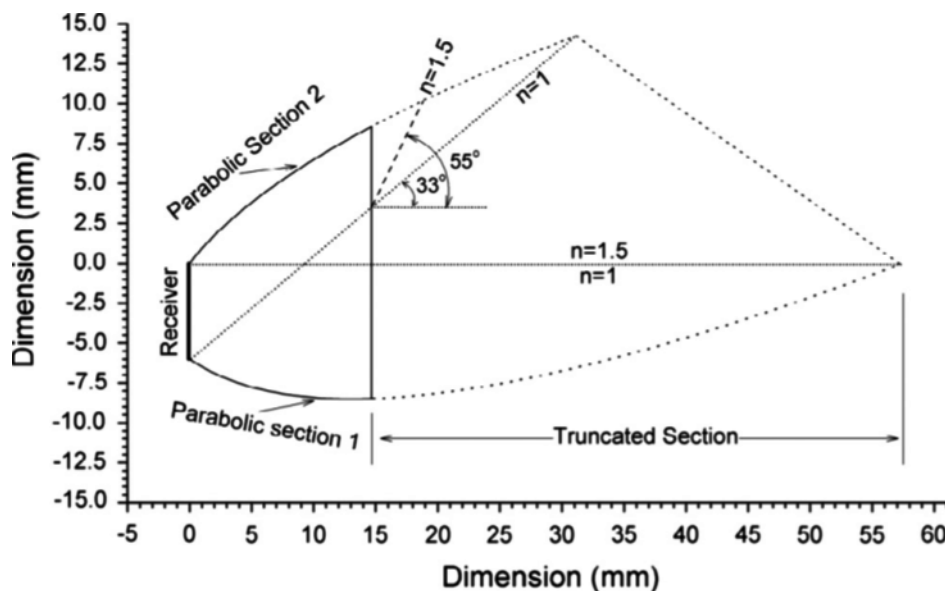
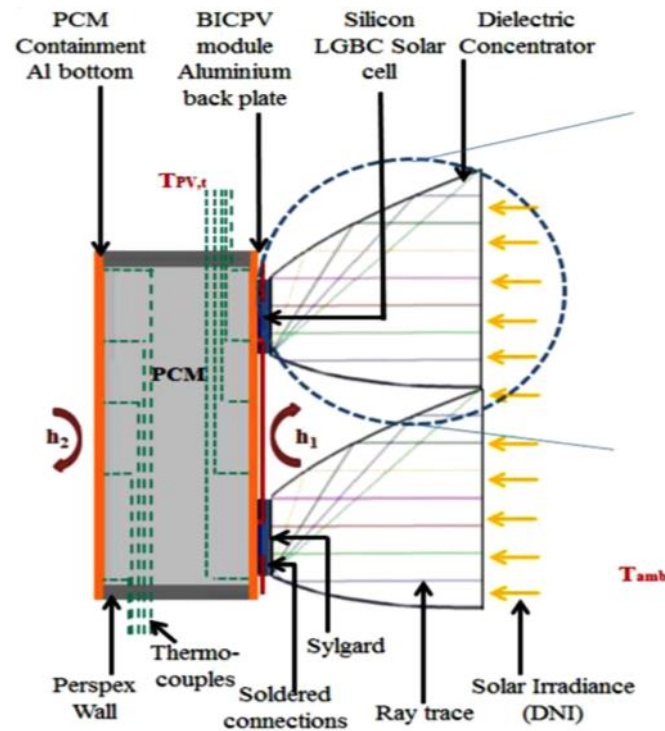


Figure 2-11 Schematic and pictorial diagrams [58]

Sharma et al. [59] experimentally tested the performance of BICPV system, which is adapted from reference [58] with cooling enhancement using phase change material, PCM **Figure 2-12**. At irradiance of 1000 W/m^2 , their results showed that PCM incorporation reduced the temperature by 3.8°C at the module centre compared to the module without PCM. This relatively improved the open circuit voltage by 4.4% and electrical efficiency by 7.7%.

**Figure 2-12** Side view of the BICPV–PCM system [59]

Also, in another study, Sarmah and Mallick [60] introduced an outdoor experimental evaluation of a larger prototype (300mm X 300mm) to the CPV mentioned in reference [58] and results showed the same maximum power ratio of 2.27 compared to the flat plate module. Another design of CPC-based LCPVT for building integration purpose was developed and simulated by Nilsson et al. [61] and named the Maximum Reflector Collector (MaReCo) in Lund University. System

performance was evaluated using MINSUN simulation software. MaReCo is an asymmetrically truncated CPC with monocrystalline PV cells attached to a dark coloured aluminium receiver to improve receiver heat absorption. The geometric concentration ratios of the front and back reflectors are 3.5 and 2.5, respectively, and a combined acceptance of 20–65°. Three different MaReCo arrangements were investigated; namely the MaReCo 1, 2 and 3 having 2, 12 and no cells facing the back reflector, respectively, and 3, no cells and cells facing the front reflector, respectively. MaReCo 1 and 3 used anodized aluminium, while MaReCo 2 uses steel with an aluminium coating. Results showed that low incidence angle has a positive effect on back reflector radiation collection while the front reflector collects most of the radiation at high incidence angle. The thermal energy estimated at heat transfer fluid temperature of 50 °C for MaReCo 3 is 145 kWh/m², while Electrical evaluation results show that the optimum position is when PV cells face the front reflector which generate about 49 % output increase compared with PV cells output of 23 % increase when they face the back reflector.

Poulek et al [62] evaluated the energy gain of bifacial silicon PV panels with three different concentrating systems. The systems are: Ridge concentrator that collects the energy from both the front and ground reflected energy and Pseudo parabolic concentrator with two different PV fixing orientations, one was fixed parallel with the concentrator axis that collects energy directly by the side facing the sun and concentrated energy by the rear face, while the other was fixed vertical with concentrator axis and collects the concentrated energy by the two PV faces (**Figure 2-13**). The geometric concentration ratios used are 1.5, 4.1 and 3.6, respectively. Energy gain results showed an increase in total energy production by 172 %, 267 % and 214 % for the three mentioned systems, respectively.

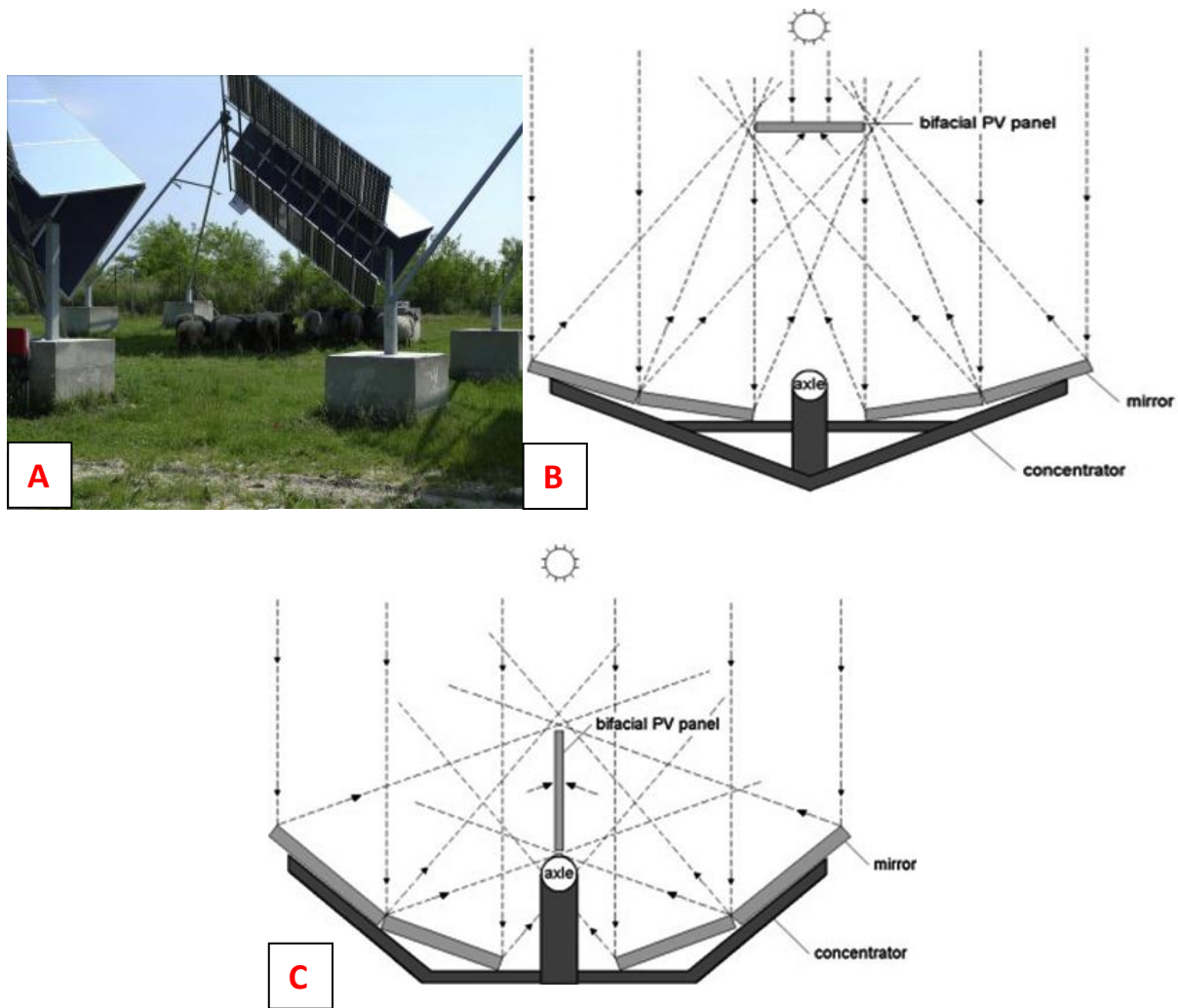


Figure 2-13 Three concentrating systems: A- ridge, B- Pseudo parallel and C- Pseudo vertical orientations [62]

Su et al. [63, 64] presented a comparative analysis to the annual solar energy collection of three different CPC designs, namely: Lens-walled CPC, mirror CPC and solid CPC using commercial optical analysis software (PHOTOPIA). CPCs are with geometrical concentration ratio of 2.5, 10 mm base width and 39.9 mm height. The mirror CPC surface reflectance used was 0.95, and the lens- wall CPC material refractive index was 1.5 and transmissivity of 0.95. Schematic diagrams shown in **Figure 2-14** illustrate the reflection principles through the three designs with the incidence angles. Depending on the optical efficiency predicted by ray

tracing simulation, it is stated that the Lens-walled CPC has a larger acceptance angle compared to the mirror and solid CPCs. This makes Lens-walled CPC reach about 80% of solid CPC efficiency with lighter weight, and 20-30% more than mirror CPC, hence Lens-walled CPCs can be a good alternative to solid CPCs.

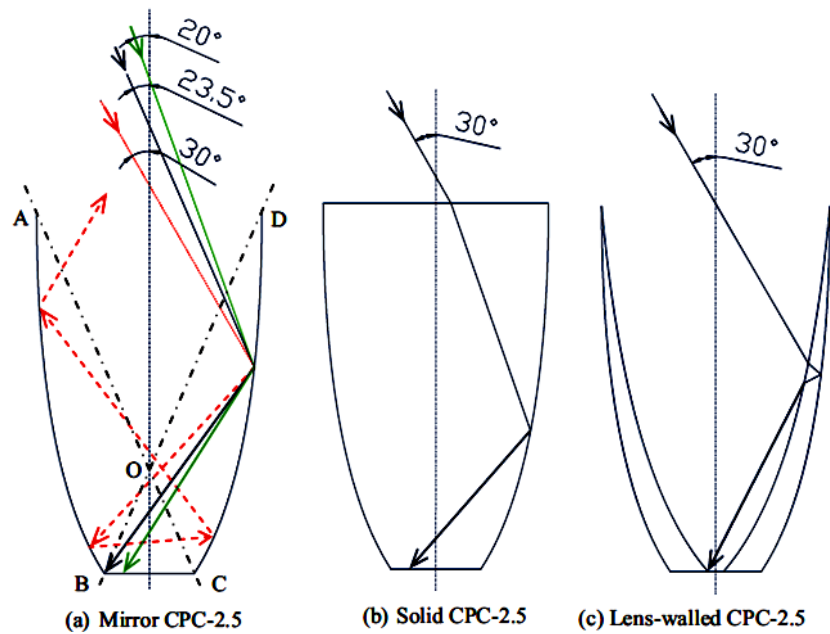


Figure 2-14 Schematic diagrams for comparison of three different CPC with geometric concentration ratio of 2.5 [63]

A geometrical comparison between compound parabolic concentrator and V-trough has been made by Irshid and Othman [65], with the same Apex angle and concentration ratio. Results showed that V-trough concentrator has the advantage of less height than the CPC concentrator; consequently less material is needed to build the concentrator, as shown in Figure 2-15.

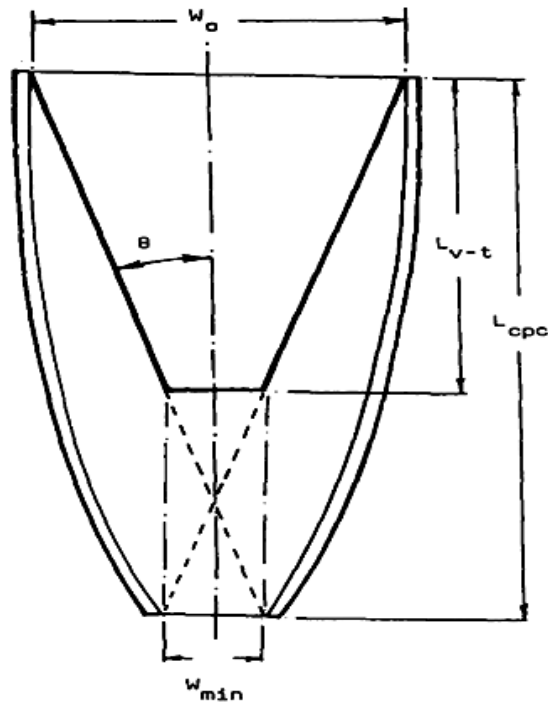


Figure 2-15 A schematic diagram for the V-trough / CPC geometrical comparison [65]

Another comparison was conducted by Paul [66] between V-trough and CPC received flux distribution with the same concentration ratio of 1.96. Simulation results showed that as part of the incident radiation reaches the receiver uniformly without reflection, the other part reaches with one or more reflections and then concentrated on a part of the receiver. The more uniformly distributed flux on the receiver the better flux distribution is received. Based on this, better received flux distribution can be obtained from V-trough than the CPC concentrator at the 0° incidence angle where the incoming rays are perpendicular to the concentrator receiver as shown in **Figure 2-16**.

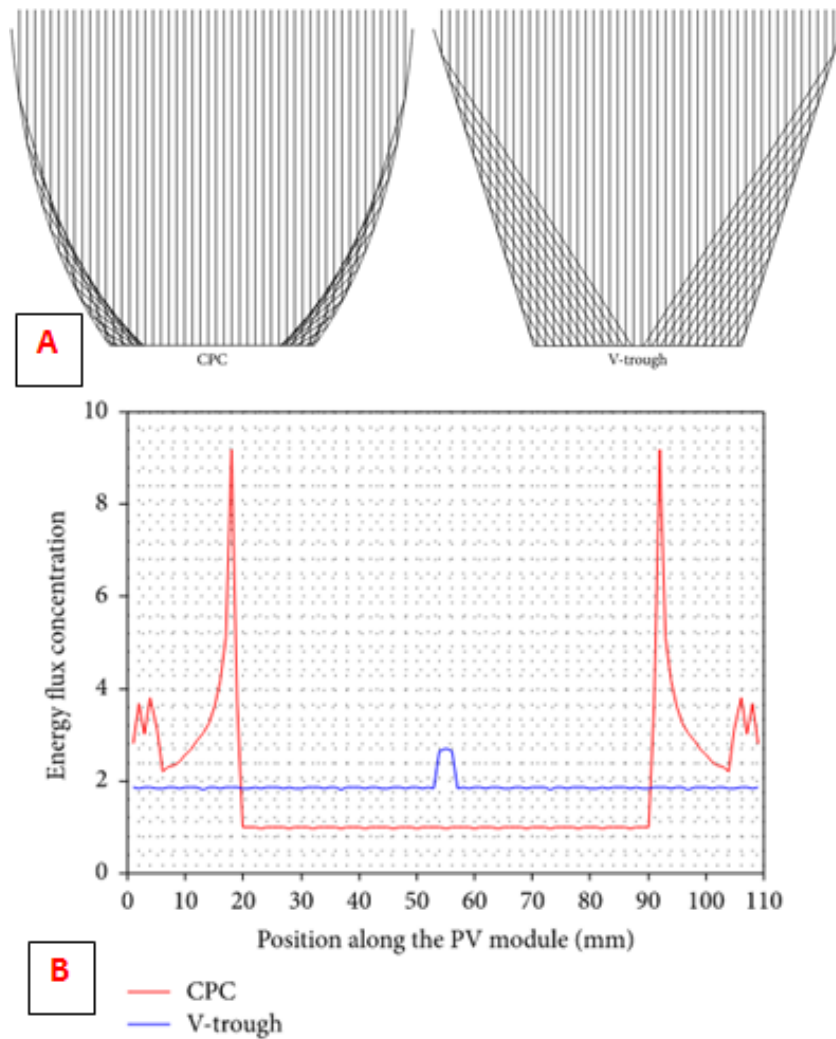


Figure 2-16 Flux distribution comparison between V-trough and CPC concentrators: A, ray reflection schematic diagram and B, flux distribution profile on the receiver [66]

An experimental investigation was made by Singh et al [67] to compare compound parabolic concentrators, CPC with V-troughs with the same geometric concentration ratio of 2.2, in terms of system performance. The electrical energy generated by the two systems is shown in **Figure 2-17**. The energy generated by the V-trough is more than that of CPC at all tilting angles used.

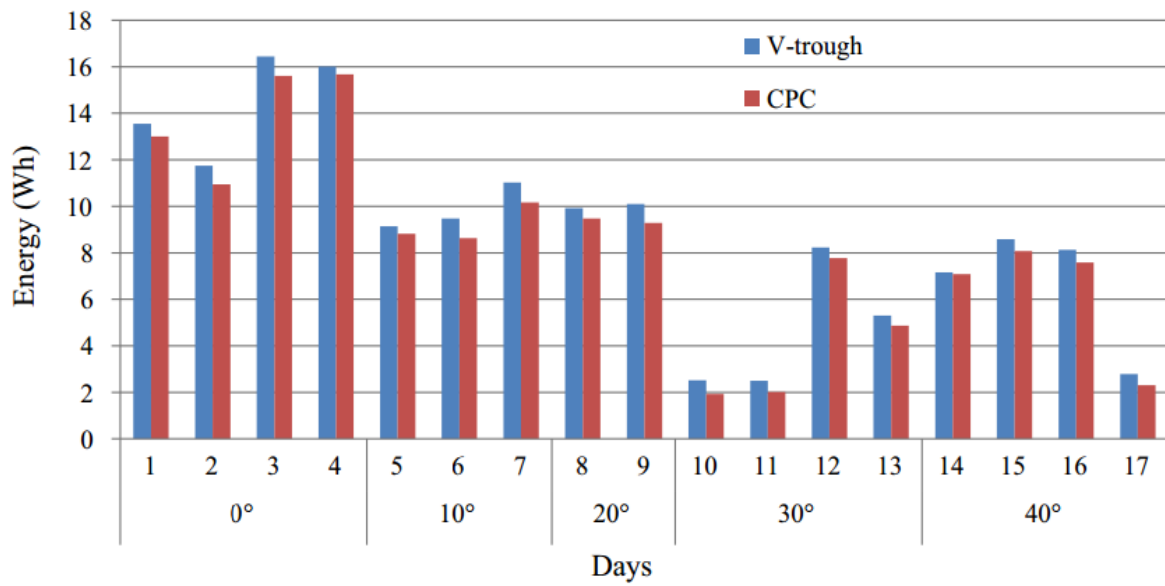


Figure 2-17 Generated energy by V-trough and CPC at different days and tilting angles [67]

Moreover, thermal results showed that the PV module temperature reached 110 °C using V-trough which is higher than the temperature of the module with the CPC by 11.1 %. Although this increase in PV module temperature has a negative effect on system power output, it offers the opportunity to extract more thermal energy from the system and enhance the power output using cooling.

For the above described literature, it can be concluded that V-trough concentrators produce better uniformity with higher energy output, less design height, consequently less material needed and simplicity of geometry as well as the flat side profile does not need advanced manufacturing technology to produce compared with CPC side profile. But in contrast, V-troughs have the disadvantage of low concentration ratio that does not exceed 3X limitations due to the increase in height with increasing the concentration ratio. This limitation can be alleviated if a 3D flat sided V-trough concentrator is used instead of 2D concentrator, that decreases the height needed for a certain geometrical concentration ratio.

2.3.2. 3D reflective low concentrating PV systems

3D concentrators with different configurations have been studied by few researchers. One of the early developed and installed designs of 3D flat sided concentrators was by Strong et al. [68] who used the design as a low concentration CPV/T system in 1979. The CPV/T system's design is based on a flat-sided conical aluminium concentrator with concentration ratio of 5, a circular monocrystalline silicon PV cell and a one-axis step tracking system. The one -axis azimuth tracker used a three step sequence that places the system at 25° east of solar noon, at solar noon, or at 25° west of solar noon, controlled using three PV cells oriented at the three mentioned tracking positions. The CPV/T system units were organised in rows and columns inside aluminium casing, as shown in **Figure 2-18**.

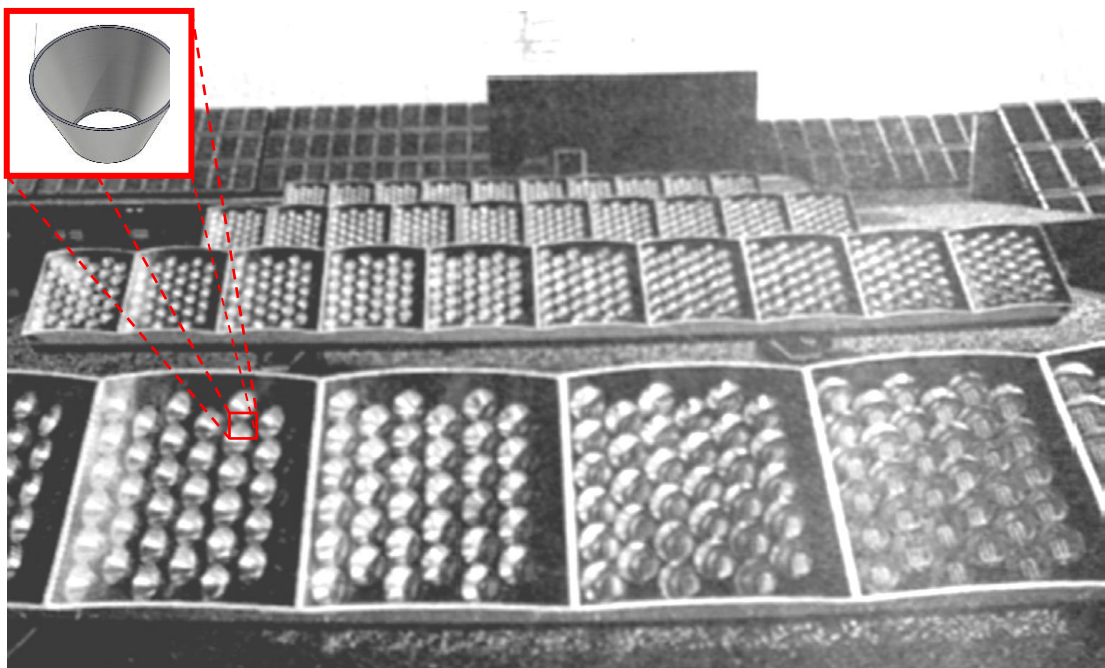


Figure 2-18 3D conical flat sided concentrator used as CPVT system in Quincy, Massachusetts with multiple CPVT collectors [68].

The system was successfully installed in a number of domestic and commercial spaces to provide power, space heating, and domestic hot water (DHW). This includes two private

houses, two banks, and a 40 CPV/T modules for a housing complex with 270 units to produce electrical output of 3kW.

Mammo et al. [69] designed and tested electrically and optically the performance of reflective 3D cross compound parabolic concentrator (3DCCPC) for building integrated photovoltaic applications. The design geometric concentration ratio was 3.6X, as shown in **Figure 2-19**. A maximum output power achieved was 3.0X compared with the same non-concentrating PV module. Good agreement was reported between MATLAB simulation code for electrical efficiency of 14 %, and 3D ray tracing for optical efficiency of 94.6 % with a deviation of 19.4 % from the experimental optical efficiency. Increasing module temperature to 50 °C caused maximum output power drop by 0.014 W/°C.

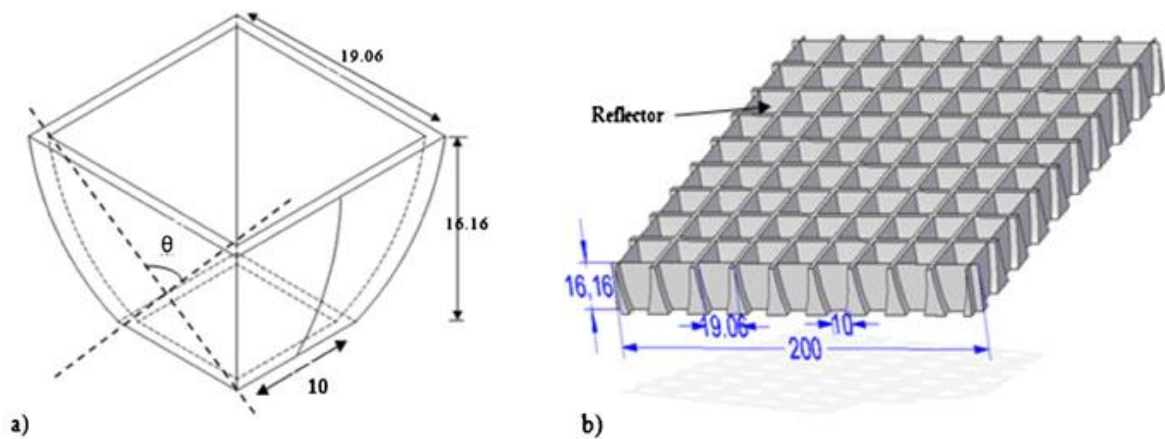


Figure 2-19 Schematic design for reflective 3D crossed compound parabolic concentrator[69]

The same design and geometric concentration ratio of 3.6 was tested by Baig et al [70], but as a clear Dielectric 3DCCPC for building integrated application, and used with a 1cm²silicon cell. Results showed a 73.4% optical efficiency and a maximum power ratio of 2.67 compared with non-concentrating counterpart. The non-uniform illumination effect caused a drop in short circuit current by 2.2%, while cell temperature increased to 332 °K leading to an overall drop in power production of 14.6%. Baig et al [71] studied the light losses of 3DCCPC in

reference [70] by the encapsulant spillage at the bottom of concentrator with and without adding a reflective film to that area. By applying different incidence angles, results showed a complete management of these losses using the reflective film and the maximum power ratio increased from 2.56 to 2.73. On the other hand, the short circuit current has increased by 8.5% and no significant increase in open circuit voltage. MatLab software was used by Sillami and Mallick [72] to study the optical efficiency of 3DCCPC to be used with PV cell at different angles of incidence. 3DCCPC concentrator doubles the concentration ratio of the 2D CPC concentrator and reduces the PV cell material as shown in **Figure 2-20**. The maximum optical efficiency obtained was 95 % with a deviation of 12 % from the experimental results.

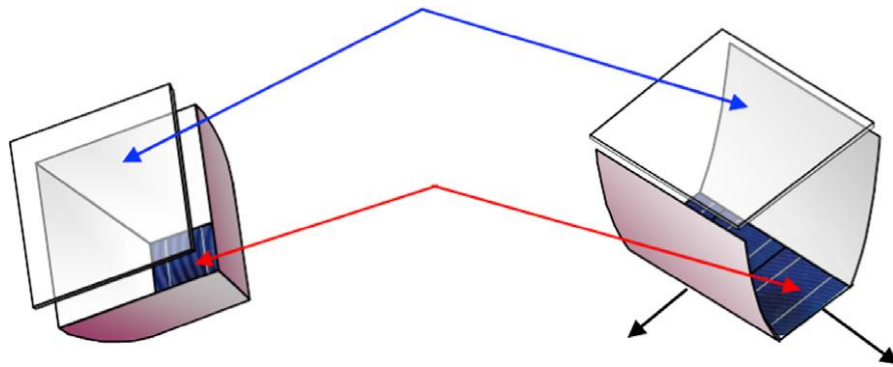


Figure 2-20 Comparison between square 3D and 2D CCPC with the same aperture area [72]

Muhammad-Sukki et al. [73] designed and experimentally tested what is so called mirror symmetrical dielectric totally internally reflecting concentrator, MSDTIRC for building integrated PV systems as shown in **Figure 2-21**. Different configurations were simulated and simulation results showed a maximum optical concentration of 13.54 can be gained, while for geometric concentration ratio of 4.91 simulation results showed an actual optical concentration ratio of 4.59 and experimentally was 4.17.

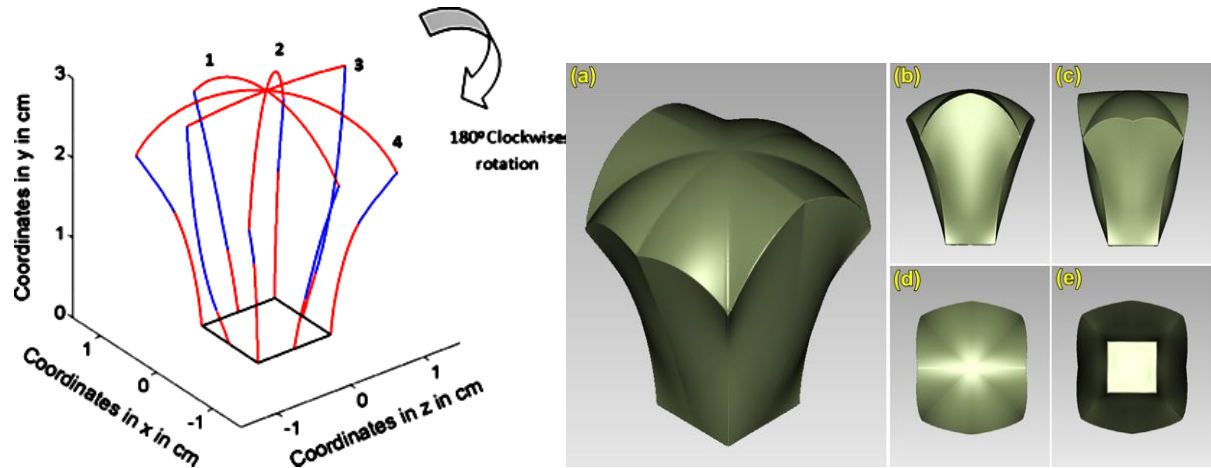


Figure 2-21 Schematic and geometry of MSDTIRC where (a) is the isometric view; (b) side 1; (c) side 2; (d) aerial, and (e) is the bottom view [73]

Abu-Bakar et al. [74] designed a Rotationally Asymmetrical Compound Parabolic Concentrator, RACPC for building integrated applications with geometric concentration ratio ranging from 1.73 to 6.59. The optical efficiency predicted by the simulation ranged between 94% and 98%. **Figure 2-22** shows schematic and pictorial diagrams of RACPC design

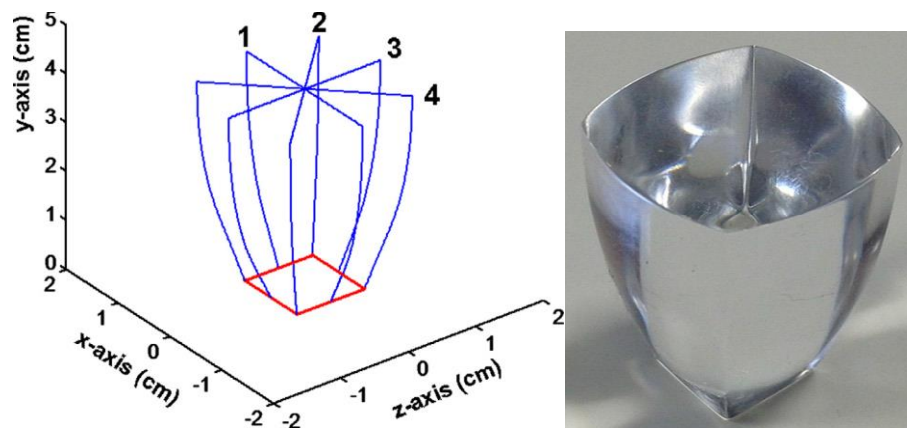


Figure 2-22 A schematic and pictorial of RACPC design [75]

Abu-Bakar et al [75] experimentally evaluated the performance of RACPC [74] with geometric concentration ratio of 3.6675, integrated with monocrystalline solar cell of an area of 1 cm^2 . Results showed an optical efficiency of 92% with an increase in short circuit current

by 3.01X and a maximum power ratio of 3.3X, while the cell temperature increased to 57 °C with concentration compared to 25 °C without concentration. This increase caused a drop in maximum voltage from 0.51 V to 0.44 V and in maximum power from 0.051 W to 0.044 W. The determined voltage, current and power coefficients are: 2.1875 mV/°C, 0.000 mA/°C and 0.2188 mW/°C. Also Abu-Bakar et al [76] tested a small double glazing window with a Rotationally Asymmetrical Dielectric Totally Internally Reflecting Concentrator, RADTIRC developed in reference [73] with a geometric concentration ratio of 4.91 for building integrated PV application. Their indoor and outdoor experimental results showed an increase in short circuit current by 4.13 and a maximum power of 4.8 times more than the non-concentrated. On the other hand, fill factor decreased from 81% to 79% and the cell temperature increased from 25 °C to 69 °C causing a drop in voltage from 6.12V to 5.2V and in maximum system power output by 27%.

Sellami and Mallick [77] designed and tested Square Elliptical Hyperboloid, SEH concentrator with three different heights ($H_1 = 10\text{mm}$, $H_{1.5} = 15\text{mm}$ and $H_2 = 20\text{mm}$), to be used as integrated CPV window with geometric concentration ratio of 4 as shown in **Figure 2-23**. Simulation and experimental results showed an optical efficiency of 40% and optical concentration ratio of 1.6 for H_1 , only 12% lower efficiency with incidence angle range used -60° to $+60^\circ$. While $H_{1.5}$ and H_2 concentrators have higher optical efficiencies at 0° , of 47% and 60%, respectively, but higher drop in optical efficiency reaching 46% and 66% of the optical efficiency at 0° , with the same incidence angle range.

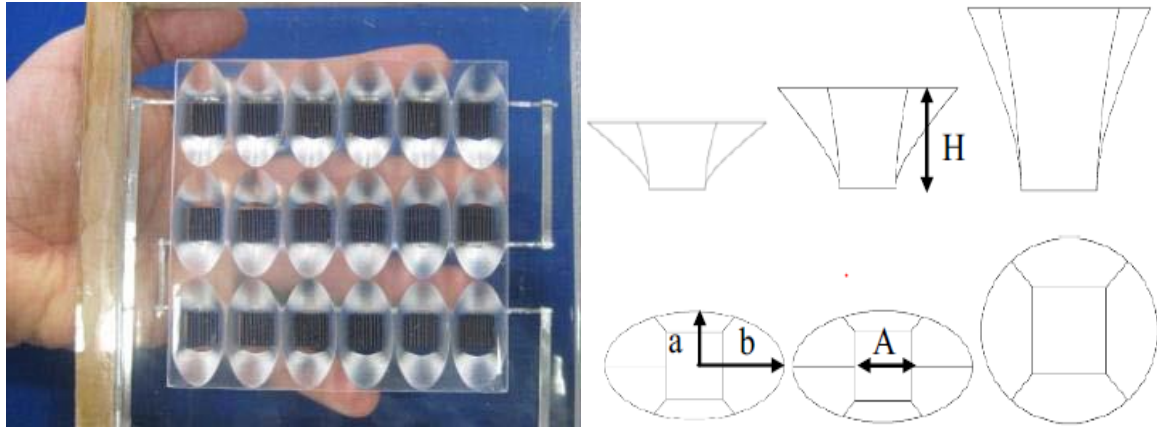


Figure 2-23 Pictorial and schematic diagram for the SHE concentrator [77]

Schuetz et al [78] designed and tested the performance of a prototype of 120 cells (10mmX 12mm) array using 3D asymmetric compound parabolic concentrator shown in **Figure 2-24** with geometric concentration ratio of 7 fabricated using aluminium acrylic mirror. The system is used with single tracking device. Finite element analysis was used to simulate a heat sink for passive cooling of the PV cell with a goal of temperature difference not exceeding 10 °C from ambient.



Figure 2-24 A pictorial 3D compound parabolic concentrator and array of 120 PV cells.

Performance analysis results showed an increase in short circuit current by 5.4X (0.45 A to 2.53 A), while open circuit voltage has increased from 0.566 V to 0.626 V, and fill factor increased from 66.8 % to 69.6 %, but a drop in total efficiency of the unit from 15 % without CPC to 7.9 %. Thermal simulation results showed a temperature difference between PV cell ambient temperature did not exceed 6 °C, which is less than the expected difference (10 °C). Validation results showed that 3DCPC demonstrated an optical efficiency variation of about 9.68 % between simulation and experiments.

The limited theoretical and experimental work on the optical performance of 3D flat sided reflective concentrators and even less work on the electrical performance of PV cells integrated with such concentrators is clearly seen in the review of 3D concentrators. Moreover, aperture configurations such as hexagonal and octagonal flat sided geometries have not been evaluated even theoretically, as well as the feasibility of these configurations as a tool of higher radiation intensity and thermal energy that can be extracted from such CPV/T system has not been evaluated

2.3.3. Effect of non-uniformity on PV output

Flux distribution and the nonuniformity effect have been studied by researchers for its importance as one of the parameters affecting the PV performance [79-81]. Apart from the high temperature negative effect on open circuit voltage, non uniform distribution for both flux and temperature causes a decrease in open circuit voltage as the irradiance increases as shown by Franklin and Coventry [82]. In their study of the I-V curve characteristics of the Si cells (**Figure 2-25**), they clarified the flux and temperature distribution effects on the open circuit voltage.

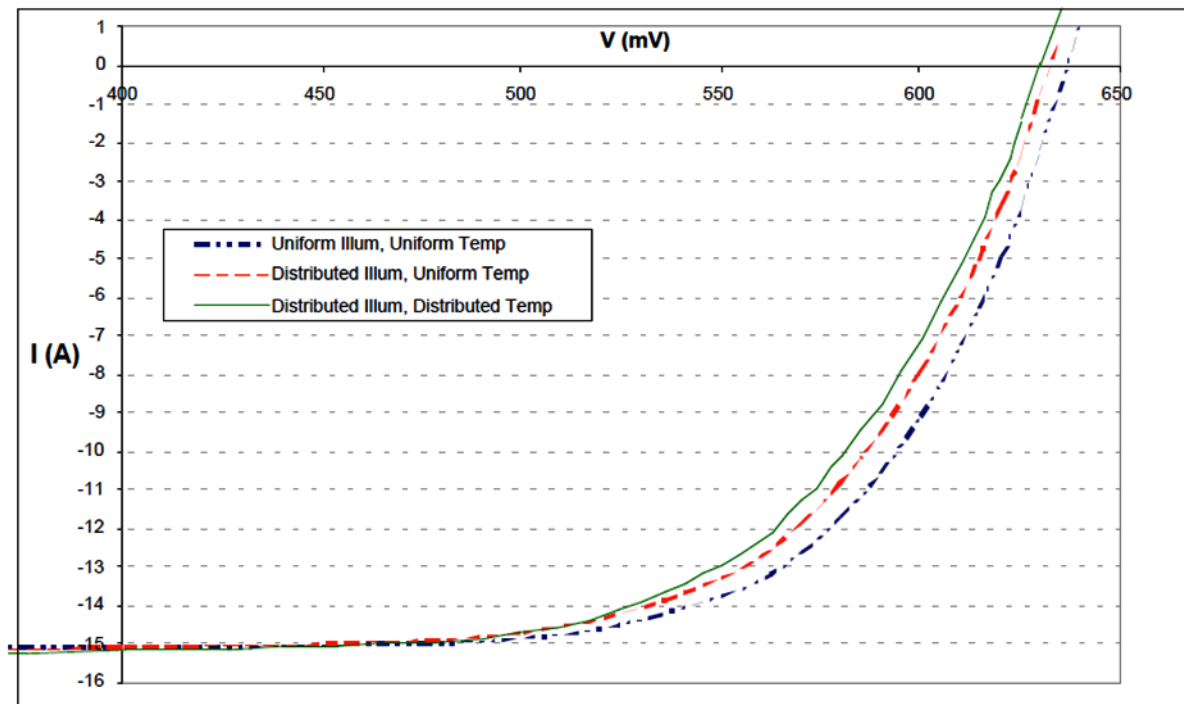


Figure 2-25 The effect of non uniform distribution on I-V curve characteristics of silicon cells at 65 °C [82]

On the other hand, Chong et al. [83] studied the effect of different concentrating mirror dielectric material thicknesses (3mm to 6 mm) on the flux distribution profile at the receiver. The uniformity comparison was made using a statistical calculation of the ratio of standard deviation to the average solar irradiance known as coefficient of variation, CV. This statistical tool is normally used when the comparison is made between two or more values of standard deviation having different average values [84], as the standard is not comparable when average values are different. An optical scanner was developed for this purpose and two samples were measured for each mirror thickness. Scanning results for the two samples showed that the thicker the mirror dielectric material, the higher the losses due to absorption. This can be seen from the drop in average solar concentration ratio from 0.955 at 3 mm thickness to 0.804 at 6 mm. On the other hand, mirror with less thickness has higher slope errors caused by the surface deformation due to less physical support to mirror material

surface, which affected the two sample average value of the irradiance. This caused a reduction of standard deviation to average ratio from 0.113 at 3 mm to 0.091 at 6 mm, and the optimum thickness is 5 mm with standard deviation to average ratio of 0.083.

2.4. Methods of cooling low concentration photovoltaic systems

The increase in PV temperature is one of the disadvantages of CPV systems leading to lower power output and PV operational life. With higher irradiance values the cell temperature of CPV system is expected to be higher than 100°C [85], and the cooling system should satisfy the cooling needs in order to reduce cell temperature and enhance system efficiency. Different cooling techniques have been investigated to extract the heat generated by concentration. Cooling methods can be divided according to the fluid used into two: air cooling systems that use air to extract heat from the PV using a heatsink attached to it, or by cooling duct fitted underneath the CPV, and water or other coolants flowing in a channel underneath the PV [86] or over the PV cell [87, 88] so that infrared and ultraviolet radiation could be absorbed before reaching the cell and only the visible light is received.

2.4.1. Air cooling for LCPV systems

Air cooling techniques were investigated by many researchers either with flat plate PV panel or low concentrating photovoltaic LCPV systems in order to reduce PV cell's temperature and increase the power output. Sheyda et al. [89] used a wind driven ventilator to reduce polycrystalline PV module temperature from 63.5 °C to 48.7 °C thus increasing the module power output by 46.54%. Rahimi et al. [85] designed a conic wind-collecting tunnel to cool down a polycrystalline PV cell with a conversion efficiency of 16% and their results showed a reduction in cell temperature from 85.25 °C to 60 °C and an increased power output from the system by about 36 %. Under concentration ratio of 10 and different ambient temperatures,

Natarajan et al. [90] numerically investigated cell temperature using fins as passive cooling arrangement with various numbers of fins. Their results demonstrated a reduction in the PV temperature with the increase of fin height and recommended four number of fins for the studied cell size. Solanki et al [41] have designed a 2 sun concentrator PV system with an enhanced heat dissipation using V-trough reflector, made of a continuous Aluminium sheet for six PV module strips. Outdoor measurements showed that cell temperature with heat dissipater remained close to the temperature of a cell in a flat plate (60 °C), while without it reached 80 °C under 750 W/m². Also using fins and air velocity of 1.1 m/s with CPV/T system, Jian and Mingheng [91] reduced cell temperature by 30 K from the case of fins at 0 m/s to reach about 58 °C, which is similar to that of the cell under ambient temperature. This CPV system has doubled the short circuit current compared to the panel system. Using heatsink and concentration ratio of 3, Butler et al. [44] kept PV cell temperature at 41.7 °C which is close to the temperature of normal operating conditions.

Tarabsheh et al. [92] used different arrangements of air cooling ducts as shown in **Figure 2-26**, which are fitted beneath the PV module and with series electrically connected solar cells. A non-uniform PV module cooling due to the temperature difference of the cooling fluid between the inlet and outlet as a result of heat exchange between the backside of the module and pipes, and therefore a gradually increased pipe temperature from the inlet to the outlet is resulted. This affects each PV cell operating temperature in the module leading to different electrical characteristics for each cell.

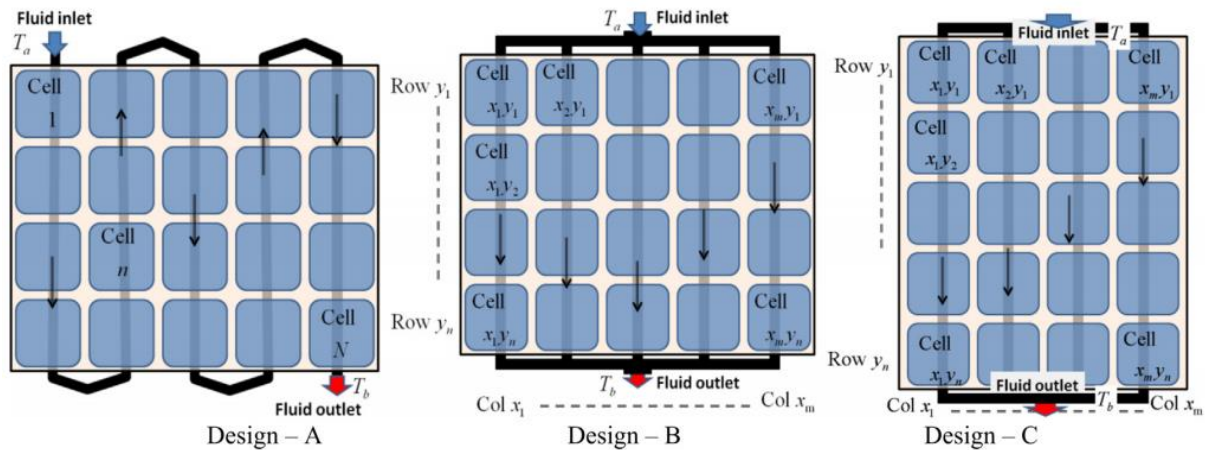


Figure 2-26 Cooling pipe arrangements of series-connected solar cells [92]

Results showed that the method of cooling underneath each PV string improves the electrical efficiencies of PV cells, as cells are not much heated compared with using one pipe for all PV cells.

A numerical model developed by Sun and Shi [93] to evaluate the electrical and thermal performance of a CPC based CPV/T system using air as cooling fluid and finned absorber panel to which solar cells are attached in-series. The absorber panel with the back plate form the air passage and the upper low-iron glass cover with the absorber form an enclosure to the CPC and PV cells, and the whole CPV/T system is surrounded by an insulator. **Figure 2-27** shows a schematic diagram of the CPV/T system with cooling facility beneath the PV cells.

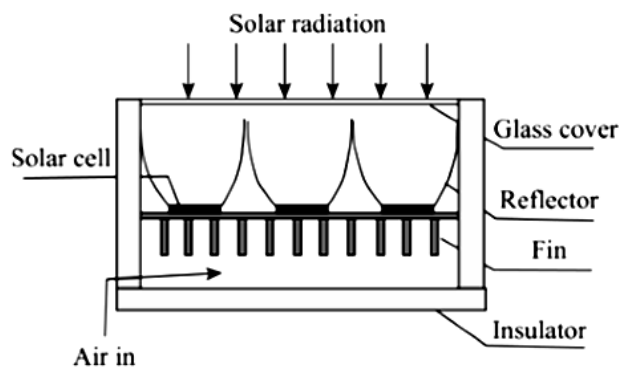


Figure 2-27 Schematic design of CPV/T system with three CPC troughs and fins beneath the heat solar cells for heat transfer [93]

System modelling results for concentration ratio of two showed that the total efficiency of the system is about 75 %, a thermal efficiency of about 66%, an electrical efficiency of about 9 % and outlet temperature of about 89 °C.

A comparison was carried out for the CPV/T system introduced by Strong et al. [68] between air and water cooling techniques. First, the PV cell was fixed on an aluminium extrusion at 1cm gap beneath the concentrator. This gap between the concentrator and cell surface was to allow the air to circulate in a horizontal channel as a heat removal method. The other cooling method is to let water flow in water channels fitted to the rear of the aluminium extrusions. Results showed an increase in the air temperature by about 6–8 K, and water temperature was raised by about 8–10 °C, while both cooling techniques maintained the PV cells temperature at 60–65 °C.

From a thermal management viewpoint, the thermal properties of air makes it not as efficient a coolant as water, and so it is not as suitable to extract the thermal energy from the PV system like water coolant [94].

2.4.2. Water cooling technique for CPV systems

Water cooling is an active cooling method which has the advantages of more efficient cooling technique than the air cooling and the heat extracted from the system can be used for various applications. Different water cooling systems configurations were investigated by researchers. Guiqiang et al. [55] studied a CPVT system fitted with U-type channel for cooling PV cells and providing hot water. Results showed that the thermal and electrical efficiencies decreased with the increase of outlet water temperature, due to increased heat losses and higher PV cell temperature. At concentration ratio of 3 and water temperature of 60 °C, the CPV/T system thermal efficiency has reached 62.2% simultaneously with electrical efficiency of 10.4%,

while water temperature of 30 °C at the same concentration ratio showed a thermal and electrical efficiencies of 67.6 % and 12.6 %, respectively.

The CPV/T system designed by Kostic et al [42], and experimentally tested has used a sheet-and-tube design that produced by NISSAL Co., Niš, Serbia to cool the PV module.

Figure 2-28 shows a schematic diagram for the PV/T collector cross section. It consists of an anodized aluminium box, a mineral wool thermal insulation, a thermal absorber and a front glass protected PV module. The thermal absorber is composed of Aluminium sheets and copper tubes fixed at the bottom of the PV module. Results showed a total daily thermal energy of 39 % and 55 % with concentrators made of Al sheet and Al foil, respectively higher than that generated by PV/T flat collector.

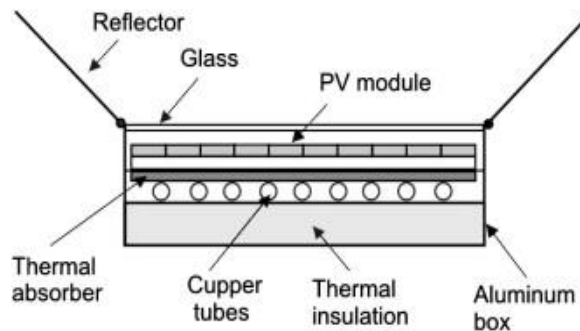


Figure 2-28 Schematic diagram for the PV/T collector cross section [42]

The CPC-based LCPV/T system constructed and experimentally tested by Xu et al. [56] is a heat pump cycle developed to cool the PV cells and produce hot water for domestic use. The thermal receiver works as an evaporator of the heat transfer fluid R 134a and at the same time as a cooler for the PV cells. Each CPVT unit has involves six modules and PVT receivers. CPC was truncated, and 88% reflectance mirror-finished aluminium was surrounding the PVT receiver both sides. The PVT receiver consists of an array with six glass-laminated PV cells stuck to a thermal receiver with conductive glue. R-134a flows through multi-port aluminium tubes inside each thermal receiver where it vaporises by absorbing the thermal energy, and then it is compressed in a rotary compressor. R134a is then condensed in a tube-in-tube heat

exchanger, transferring the thermal energy collected to water producing hot water for domestic use. The heat transfer fluid is then passed through an expansion valve to the evaporator, and repeats the cycle. **Figure 2-29** shows a schematic diagram of the CPC-based CPV/T system integrated with a heat pump.

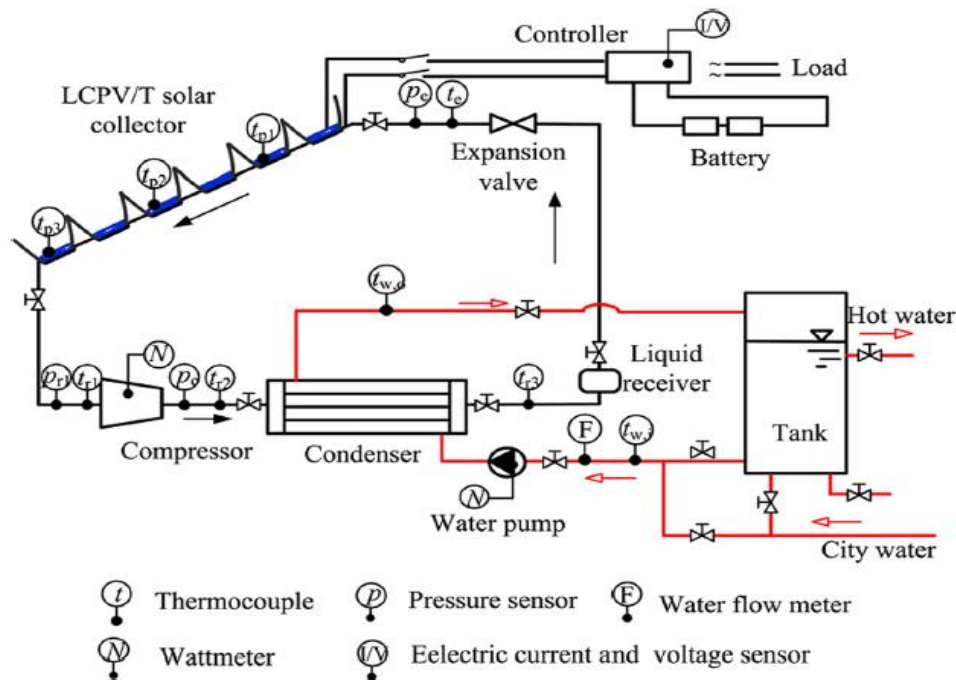


Figure 2-29 Schematic diagram of the CPC-based CPV/T system integrated with a heat pump [56]

The outdoor experimental results showed that a remarkable improvement in the electrical efficiency from 12.9 % for the case of a CPV without cooling facility to 17.5 % for the CPVT system with cooling. The cell base plate temperature of the system with cooling varied between 20 °C and 30 °C, while for the LCPV increased up to 85 °C without cooling. As mentioned, the system is capable of producing hot water of temperature 50 °C for domestic use.

A theoretical study was conducted by Xuetao et al. [95] to develop an electrical and thermal model to evaluate the performance of a CPC-based CPVT system. The cooling water is assumed to flow through a channel beneath the PV cells to cool and collect the thermal energy. The PV cell consists of a glass layer for protection, a p–n junction, and a substrate that is surrounded by the CPC from the two sides. The CPVT system output is based on the maximum power point tracking and generates both electrical power and hot water. Results showed that the total efficiency of the system was about 87 %, the electrical efficiency was 16 %, and the thermal efficiency was 71 % at a concentration ratio of 6, while the temperature of the outlet water reached 50 °C. With the assumption of 9 hours in operation under irradiance of 1000 W/m², the system would produce about 3264 W and 917 W of the thermal and electrical output, respectively.

A theoretical evaluation of thermal and electrical performance was carried out by Hedayatizadeh et al. [96] for a CPV/T system. The CPV/T system consists of a CPC that has a reflectance of 85 %, and concentration ratio of 2, equipped to PV/T water collector. Simulation results were then compared with Huang et al. [97] experimental results for a PV/T system in 2001. Simulation results showed a good agreement with the experimental results. It was concluded that the use of CPC reflectors can enhance the thermal and electrical performance of the system with an increase of cooling mass flow rate as this increase will enhance the heat removal from the PV system consequently increasing the system electrical and thermal efficiencies. Wind speed has a positive effect on system electrical efficiency and a negative effect on the system thermal efficiency, due to heat dissipated from the system to the ambient and therefore increases system heat loss.

A stationary LCPVT system CPC-based for building integration was developed by Brogren et al. [98] An optical analysis was conducted to predict the CPVT system performance

including the CPC with the glazing, and PV cell as well as the electrical and thermal performance. The CPVT system shown in **Figure 2-30** has a concentration ratio of 4 and involves three rows with four series- connected PV strings. Each string contains 12 monocrystalline cells laminated to an aluminium profile and the total aperture area is 7.2 m^2 with acceptance half-angle of 12° . The CPCs are truncated at a height of 0.45 m and made of bright anodized aluminium coated by anti-reflecting material and a surface reflectance of 81%, and system inclination need to be changed four times a year. The cooling facility is cooling fins with water tubes attached to the back of the modules with water flowing through.

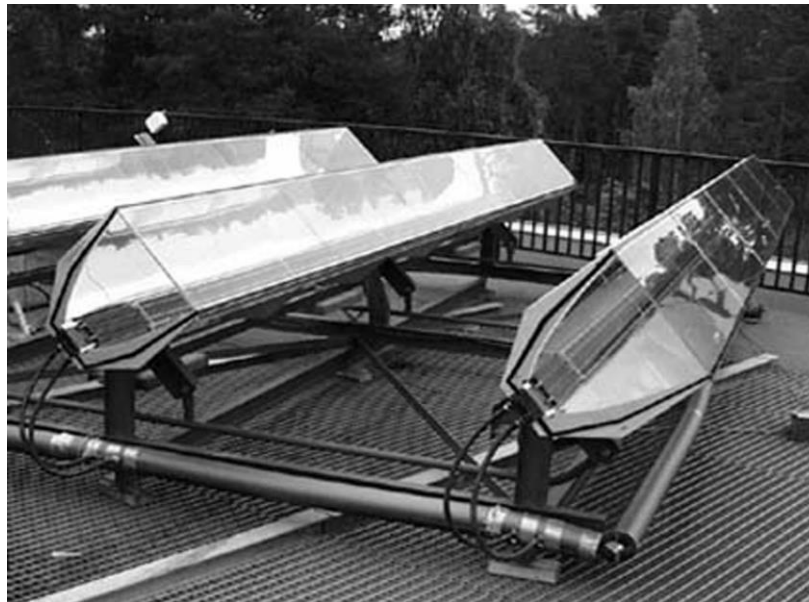


Figure 2-30 CPC-based LCPVT system for building integration [98]

Results showed a 71% optical efficiency, while the assessment of the thermal and electrical performance has shown a peak thermal output of 3500 W and electrical output of and 500W. The comparison of the CPV/T system with the conventional PV module having the same area showed a CPVT system total power output increased of about 18 times than the PV module power output, showing the feasibility of proposed CPVT system for producing energy.

In another work, Brogren and Karlsson [99] have designed and assessed the performance of two other CPC-based LCPVT systems with different configurations. The first design is for domestic façade integration and the second is for the domestic ground mounting application. The first design uses stationary aluminium CPCs with a concentration ratio of 3 covered with acrylic front cover, while the second design uses stationary asymmetrically-truncated CPCs made from either anodized aluminium sheets or laminated aluminium foils oriented in an east-west location and has a concentration ratio of 4.3 and an acceptance half-angle of 22.5° . Results showed an optical efficiency for the 3X design of about 60 %, the electrical output was 200 kWh/m^2 per year, the thermal output was 510 kWh/m^2 per year and the cooling water outlet temperature was 50°C . The 4.3X design generated about 200 kWh/m^2 per year and 800 kWh/m^2 per year of electrical and thermal outputs, respectively, recommending thicker thermal receiver fins, while using two tubes will produce much higher heat transfer between the PV cells and the HTF than one tube. The proposed CPV/T systems can offer about twice the electric output of conventional PV systems designed for building integration application, and with additional thermal energy at water outlet temperature of 50° .

Another façade-integrated CPV/T system was developed by Davidsson et al. [100] at Lund University with booster reflectors, to provide electricity and domestic hot water (DHW). The CPV/T should be integrated into standard windows for the purpose of sharing the glazing and the frame, shown in **Figure 2-31**. The CPV/T system consists of PV cells laminated to a thermal receiver with a packing factor of 0.8 simultaneously with the booster reflectors made of anodized aluminium placed next to the thermal receiver. Within the thermal receiver, tubes are embedded where water flows in. When the reflectors are tilted to a vertical/closed position, the radiation is directed to the receiver, and when they are titled to the horizontal/open position, the radiation passes to the building in a passive heating mode.

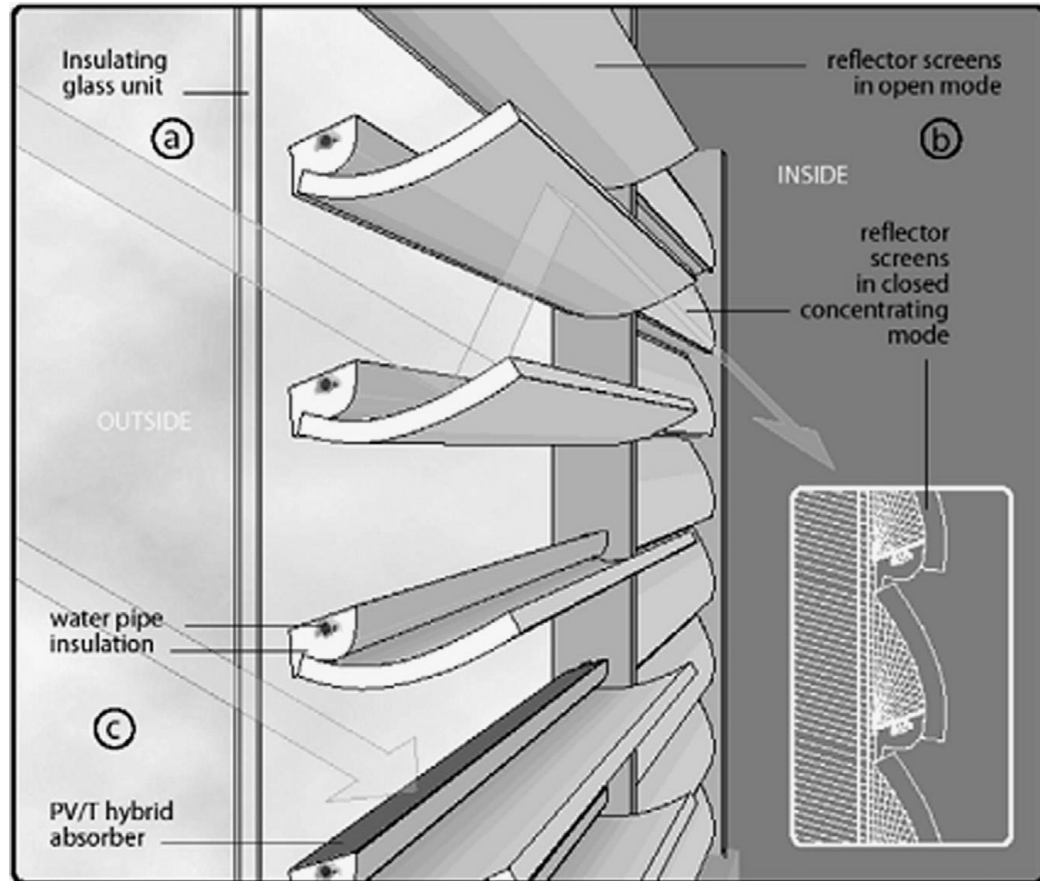


Figure 2-31 CPV/T solar window design [100]

Two prototypes were tested that harvest all beam, diffuse, and reflected radiation for energy generation; a laboratory prototype, which involves five PV modules, with 8 series connected PV cells and an aperture area of 1.2 m^2 . While the other is house prototype which involves four units including eight PV modules per unit, having 8 series connected PV cells per module and a total aperture area of 16 m^2 . The CPV/T window is double-glazing with a geometrical concentration ratio of 2.45. The theoretical results compared with the measured results showed excellent agreement while the reflectors contributed about 30–50 % of the generated electrical output during periods with low solar radiation. Comparing the CPV/T system with two conventional PV modules with different mounting methods (wall and roof mounted) with the same efficiencies and areas, the CPV/T system generated annual electric

energy of about 35 % higher than the wall mounted PV module while about 20 % less than the roof-mounted PV module. Also, to achieve the same annual thermal output from the designed CPV/T, wall-integrated solar thermal collector (STC), and roof-integrated STC, need areas of 16 m², 8.3 m² and 6.0 m², respectively. Loss analysis showed that an increase of 23 % in the annual electrical output can be achieved with the removal of glazing and increase of 19 % if shading is avoided.

Phase Change material (PCM) is one of the cooling methods used to maintain the PV cell temperature at lower levels [59, 101-103]. An LCPV/T system that uses Paraffin wax (PCM) as heat storage was designed and tested by Ceylan et al [103]. The solar panel was manufactured in a shape of sphere from PV cells. The paraffin wax was used to maintain lower temperature of the PV cells that should increase with the concentration effect through concentrator. The PV cells output is used to operate the fans in a greenhouse, which in turn is used in an application of drying Spinach leaves. System is shown in **Figure 2-32**.

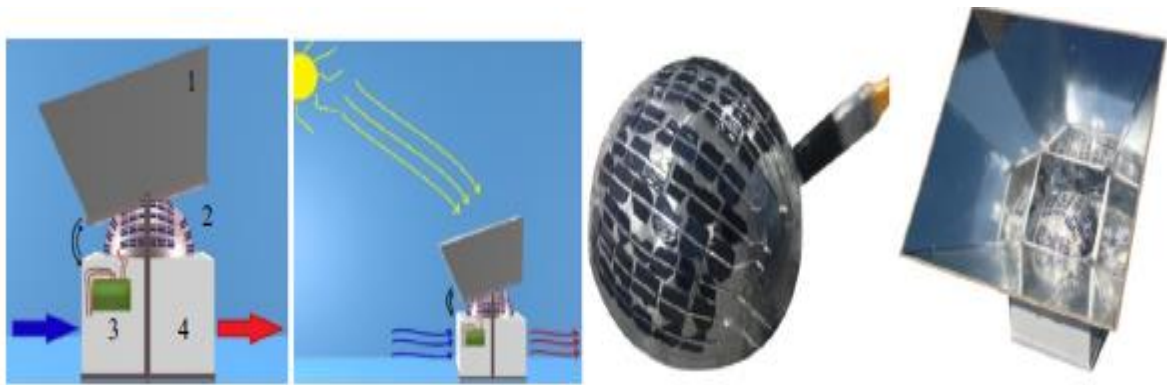


Figure 2-32 CPV/T system with spherical PV module and PCM: 1. Squared aperture concentrator, 2. Spherical PV module filled with PCM, 3. Charge regulator and 4. Gel accumulator and fans [103].

Results showed that radiation intensity was increased with the use of concentrator to about 2x and electrical power gain was increased. Thermal and electrical power outputs of the system were compared with non-concentrated panel. The maximum PV panel temperature at the back was 37 °C and the PV panel efficiency was 11% at an average radiation intensity of about 2000 W/m².

For the effect of temperature gradient on PV performance, Tina et al. [104] in a bibliographical study, have analysed the effects of the temperature gradient and maximum temperature on the PV panel performances with the use of water cooling system. The PV cells temperature gradient depends on various parameters (G, Ta, and Va), water circulation type (parallel, serpentine or spiral), flow rate and PVT collector design. Results showed that PV cell temperature gradient takes the same water temperature gradient, with higher PV cell temperature that can reach more than 70°C. On the other hand, the effect of temperature gradient is negligible on series connected PV cells efficiency, but a significant effect on parallel connected PV cells efficiency. For instance, the power output of two cells connected in two ways (series and parallel) was investigated in two cases; first at temperatures gradient from 0 °C to 100°C and second at uniform temperature of 50°C. Both cells connections produces the same powers of 12.2 W and voltage of 0.49 V when working under uniform temperature, while with the presence of gradient, the power produced with series and parallel connections are 12.1 W and 10.1 W, respectively. this drop in power is as a result of voltage drop with parallel connection from 0.49 to 0.43 V (variation of 17.2% in power and 12.2% in voltage).

This also was proved by Smiths et al [105] when they measured the effect of non-homogeneity of temperature on the performance of series connected PV cells and found no significant effect, while Lambariski [106] has mentioned a very small effect of the temperature on series

connection ($<1\%$) , and a large effect on parallel connection of about 17% efficiency loss, concluding series strings can be represented by their average temperature and can work at different temperatures. Temperature effect on series connected PV cells was also evaluated numerically by De Vries [107] for three temperature differences (20, 40 and 60 °C) at ranges of 298 – 318 K, 298- 338 K and 298- 358 K and no effect for the temperature gradient on PV efficiency was found. According to Guiqiang et al. (2012) [55] U-type pipe avoids the temperature gradient on the system absorber and allows PV cells to produce electricity effectively. **Table 2-2** summarizes studies related to water cooling under low concentration.

Table 2-2 LCPVT-focused studies covered water cooling methods

Ref.	Study	CR	Outlet temperature °C	Thermal efficiency %	Electrical efficiency %
[108]	CPC-PV/T with water flowing through a channel below the PV cell (P)	6	50	71	16
[109]	Optimization of water circulation (below and above the PV cell)	8	196	40	7.3
[110]	Water flows through a rectangular channel at PV cells bottom side	5	27	-	8.5
[111]	Water flows through copper pipe attached to PV cells by copper receiver	1.35	-	80	13
[112]	Water flows through copper pipes attached to PV cells by an Aluminum	2.1	70	33.5	3.35
[113]	Water flows through the receiver from both sides	1.5	25	-	13.9
[114]	Water flows through tubes within an absorber collecting heat from PV cells	3	28	70	10.7
[115]	Water flows through pipes attached to PV cells by an Aluminum	10	40	39.4	14.1
[116]	Water flows at the back of Aluminium absorber	3	-	78	14

2.5. Optical and thermal simulation tools

Many computational analysis software have been used to design, evaluate and optimize concentrated photovoltaic / thermal systems for different applications. The following are some of the most commonly used software in the field of CPV/T systems' optical and thermal design and evaluation process

2.5.1. Optical ray tracing software

Optical simulation starts with building geometries that previously selected to be tested or optimized using one of the available simulation software. Building geometries is normally done using specialized software like: GeoMagic [117], AutoCAD [118], Solidworks [119], Solid-Edge [120] etc. software that are widely used to generate 2d and 3D shapes [75] [73]. On the other hand, ray-tracing technique is a computational method to virtualize the solar light source, system incoming flux, after concentration received flux distribution, concentrating element, inclination, material properties (reflectivity, absorbance and transmittance). It is used to optimize concentrated photovoltaic and thermal systems with different configurations [121], in addition to the analyses of materials used in solar applications [122]. Many software and codes are specialized in ray tracing investigation. Some of these ray tracing software are: Trace Pro [78], MINSUN [61], MatLab [72], APEX [71], Tiesol [122] tracer [123], Spray (MIRVAL) [124], SOLFAST [125], Tonatiuh [126], STRAL [127], ISOS [128], HFLCAL [129], CRS4 [130], HFLD [131], Biomemtic [132], ASAP [133], OptiCAD [134], OSLO [135], ZEMAX [73-76, 136], DELSOL [137], UHC [138], HFLCAL [129], FIAT LUX [139], SolTrace [40, 140, 141] which is a public ray tracing software, OptisWorks [142]. The available ray tracing software is OptisWorks, which is one of the efficient ray tracing software that is capable of providing a simulation environment for optical optimization of solar concentrators as well as exporting close to real

concentrated flux distribution taking consideration of all parameters affecting the optical performance. Also, OptisWorks allows concentrator designers to deal with the optical textures of PV solar cells [72]. In addition, results of experimental work based on this software has achieved an acceptable agreement with a variation of about 5% [143] and has been used by many researchers to virtualize, evaluate, and optimise the optical performance for different solar applications and systems designs. Some of these applications can be seen in the literature review given in **Table 2-3**.

Table 2-3 Applications designed using OptisWorks software

Reference	Concentrator design	Application	Exp. Dev.
[144]	Luminescent Solar Concentrator	Photovoltaic	5 %
[145]	Compound Parabolic Concentrator	Thermal	-
[146]	Reflective Parabolic Concentrator	Photovoltaic	-
[147]	Ring Array Concentrator (RAC)	Thermal	-
[148]	Crossed Compound Parabolic Concentrator (CCPC)	Photovoltaic	5 %
[149]	V-through Concentrator	Photovoltaic	2 %
[150]	Circular Miniature Concentrator (CMC)	Photovoltaic	-
[150]	Squared Miniature Concentrator (SMC)	Photovoltaic	-
[150]	Hexagonal Miniature Concentrator (HMC)	Photovoltaic	-
[150]	Point-focus Fresnel Lens (PFL)	Photovoltaic	-
[150]	Modified Fresnel Lens (MFL)	Photovoltaic	-
[151]	Circular Conical Concentrator (CCC)	Thermal	-
[151], [152], [153]	Circular Hyperboloid Concentrator (CHC)	Thermal	-
[77], [143], [154]	Square Elliptical Hyperboloid	Photovoltaic	5 %
[155], [156], [157]	Parabolic Dish with Cavity Receiver	Thermal	4.5-7 %
[158]	Lens-Taper-Fibre system	Photovoltaic	-
[159]	Fresnel Lens	Photovoltaic	-

2.5.2. Thermal analysis software

Apart from electrical performance, Wenguang Li studied the thermal performance of the 3D CCPC with solar cell, which was experimentally tested in references [69, 72] with the use of ANSYS CFX 15.0. A good agreement between simulation results and experimental results was reported. ANSYS CFX software was also used by Natarajan et al. [160] for thermal modelling of an early prototype [90] of CPV system to predict the temperature of two PV systems. Experimental validation of the systems showed a deviation of 3.8 % to 11.1 % from the simulation results.

TRaNsient SYstems Simulation, TRNSYS is a program developed by University of Wisconsin and University of Colorado in 1975 [161]. The latest version (17.1) contains a modular structure that recognizes a description language for systems where the user identifies their components and the operating conditions. TRNSYS library contains various components that are usually available in both thermal and electrical energy systems [161]. TRNSYS software has been used by many researchers in the field of solar energy to investigate the CPV/T systems [162]. Buonomano et al. [163] investigated the Solar heating and cooling systems by CPVT and evacuated tube solar collectors using TRNSYS software and validation results showed less than 10 % difference between simulation and measured thermal output of the system.

Winsun is a TRNSYS based software which was developed by Bengt Perers to estimate the thermal and electrical energy [57]. TRANSOL is also developed by TRNSYS, and it is one of the computational tools used to design and predict the installations behaviour of solar thermal energy, using dynamic simulations [164]. COMSOL Multi-physics was also used to thermally model various CPV/T systems [165]. **Table 2-4** lists some of the research papers that used COMSOL Multi-physics as a thermal analysis tool. As it is widely used and has the advantage

of importing the flux distribution from other optical modelling software such as OptisWorks, it was decided to use it in this research project.

Table 2-4 Applications designed using COMSOL Multi-physics software

Reference	Main investigation	Application	Exp. Dev.
[165]	Modeling Thermal Fatigue in CPV assembly	photovoltaic	-
[166]	CPV heat transfer	photovoltaic	-
[167]	CPV heat transfer	photovoltaic	-
[168]	Heatsink air cooling	photovoltaic	-
[169]	CPV air cooling	photovoltaic	-
[170]	PV water cooling	photovoltaic	-
[94]	HCPV water cooling	photovoltaic	-
[171]	PCM for PV cooling	photovoltaic	-
[172]	CPV air and water cooling	photovoltaic	5 %
[173]	PV water cooling	photovoltaic	-
[174]	CPV thermal and electrical	photovoltaic	11 %
[175]	CPV air cooling	photovoltaic	Good agreement
[176]	CPV water cooling	photovoltaic	Good agreement
[177]	PV thermal behaviour	photovoltaic	Good agreement

2.6. Conclusion

From the literature review of different low concentrator photovoltaic systems, the following summary points are concluded:

- Most of the past research involves two main reflective concentrating element categories; 2D concentrators or 3D concentrator. 2D also can be classified into two, V-troughs which are flat sided linear concentrators or CPCs that are curved sided linear concentrators. V-trough concentrator has the advantage of, better uniformity, higher energy output with less design height, and consequently less material needed and simplicity of geometry manufacturing that the flat side profile does not need high technology to produce it compared with CPC side profile. However, V-trough concentrator has the disadvantage of low concentration ratio limitations due to the increase in height as the concentration ratio increases; hence it is not suitable for concentration ratios higher than 3X. This limitation can be widened to some extent if a 3D flat sided V-trough concentrator is used instead of 2D concentrator, that decreases the height needed for a certain geometrical concentration ratio. Limited theoretical and experimental work on the optical performance of 3D flat sided reflective concentrators and even less work on the electrical performance of PV cells integrated with such 3D flat sided reflective concentrators has been reported in the literature. Also other aperture configurations such as hexagonal and octagonal flat sided geometries have not been evaluated even theoretically in the literature review.
- Also the feasibility of these configurations as a tool of higher radiation intensity and thermal energy that can be extracted from such CPV/T system has not been evaluated. Therefore this project will theoretically and experimentally investigate the optical performance of 3D flat sided concentrators with low geometric concentration ratio (2 -

10) and four different aperture configurations as a selective study to build a high performance low concentration photovoltaic/ thermal (LCPV/T) system using commercial polycrystalline PV technology as electrical generator of the system with a well-designed active water cooling facility that improves the electrical output and extracts the thermal energy for domestic application use.

- The optical ray tracing software OptisWorks will be used in investigating the concentrators optical performance and COMSOL Multi-physics will be used in the thermal investigation of the CPV/T system.

CHAPTER 3: OPTICAL MODELLING OF CONCENTRATORS

3.1. Introduction:

This chapter aims to investigate the optical potential of using three dimensional concentrators of low concentration ratio (2-10) for concentrated photovoltaic cells. The investigation involves the actual concentration ratio and optical performance in terms of efficiencies and flux distribution. A mathematical modelling was performed using four 3D concentrators with square, circular, hexagonal and octagonal inlet and exit apertures to be used as a concentrator for photovoltaic system (CPV). The geometrical concentration ratio and the optical performance were determined for the concentrator geometries at side angles, ψ ranging from 10° to 45° with interval of 5° and targeted geometrical concentration ratios. This is to determine the optimum concentrator geometry with best optical performance at different concentration ratios. A ray tracing software (OptisWorks) was used to compare the mathematical modelling results, as well as the flux distribution for the optimum concentrator in terms of optical performance was investigated.

3.2. Mathematical modelling of 3D concentrator with different aperture cross-sections

This type of concentrator is 3D flat sided and has either reflective sides with square (SAC), circular (CAC), hexagonal (HAC), and octagonal (OAC) inlet and outlet apertures with the sides inclined with respect to the concentrator axis at an angle, ψ [65]. As part of the incident radiation reaches the concentrator exit aperture without reflection, the rest of the radiation

strikes on the concentrator reflective sides and changes its direction with an angle equal to the angle of incidence. Rays keep changing depending on the number of reflections through the ray's path to the exit aperture (receiver).

3.2.1. Number of reflections:

The extremal ray shown in **Figure 3-1** is incident on the concentrator inlet aperture and parallel to the concentrator axis ($\Theta = 0^\circ$) before reflecting on the inclined concentrator side. After the first reflection it makes an angle of 2ψ , 4ψ after the second reflection and $2n\psi$ after the n th reflection. This reflection happens through the ray path to the exit aperture unless the ray angle reaches 90° , otherwise it will be reflected back to the inlet aperture. On the other hand, the maximum number of reflections, n_{max} that allows the incident ray to reach the exit aperture can be determined by the following equation [65]:

$$2n_{max}\psi < 90^\circ \quad (3.1)$$

From equation 3.1, to have a single reflection, ψ should not be more than 45° , and the side angle, ψ range can be determined by [37]:

$$\frac{90^\circ}{2(n_{max}+1)} \leq \psi < \frac{90^\circ}{2n_{max}} \quad (3.2)$$

The number of reflections can be determined by using the image ray method shown in **Figure 3-2**. Extending rays by the dashed line shows whether the ray has one reflection, two reflections or more by the number of intersections with the side images till reaching the concentrator exit aperture [178]. The number of reflections varies from zero reflection at the middle region with the width equal to the width of exit aperture to the maximum number of reflection at the point of extremal incident ray, as shown in **Figure 3-3**.

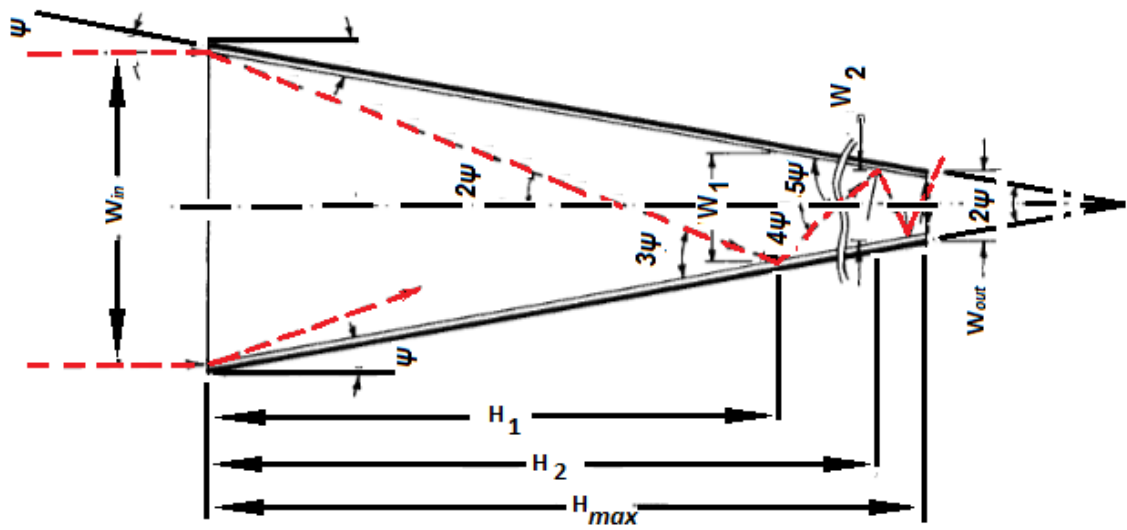


Figure 3-1 2D illustration of ray multi-reflection in the internal surface of concentrators [65]

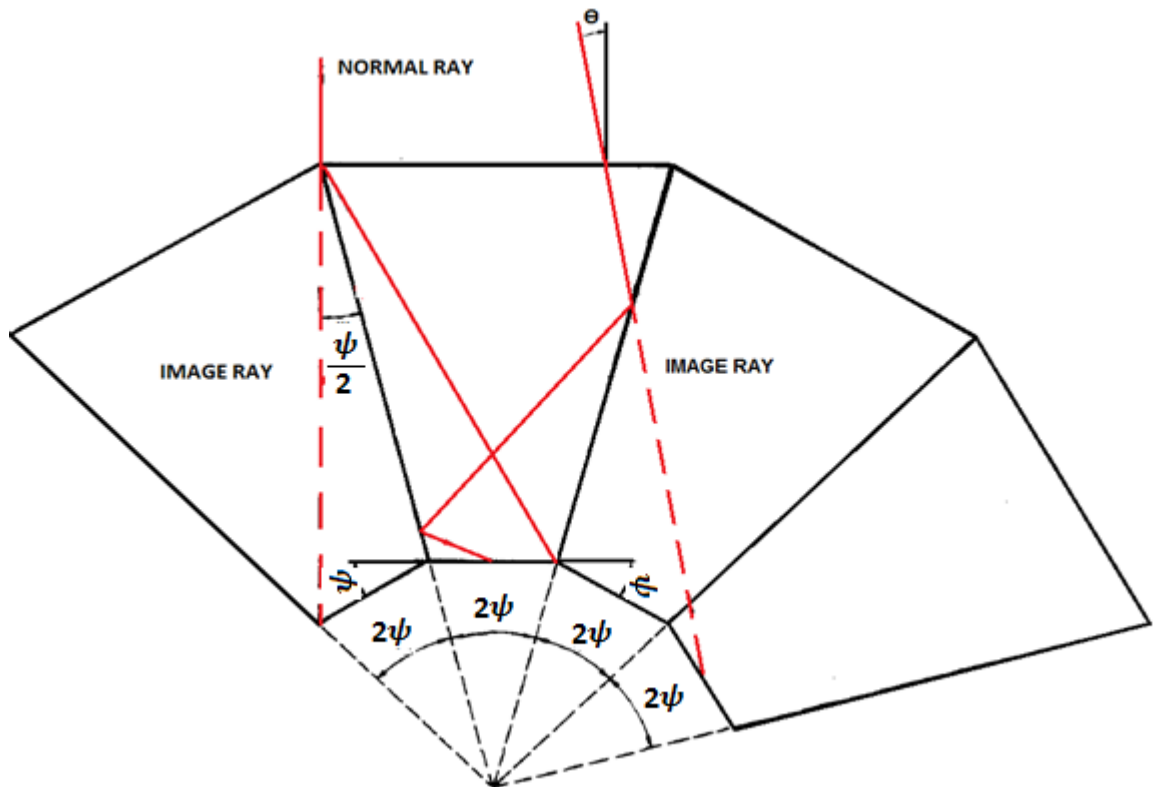


Figure 3-2 Method of image for determining the number of reflections to incident rays [178].

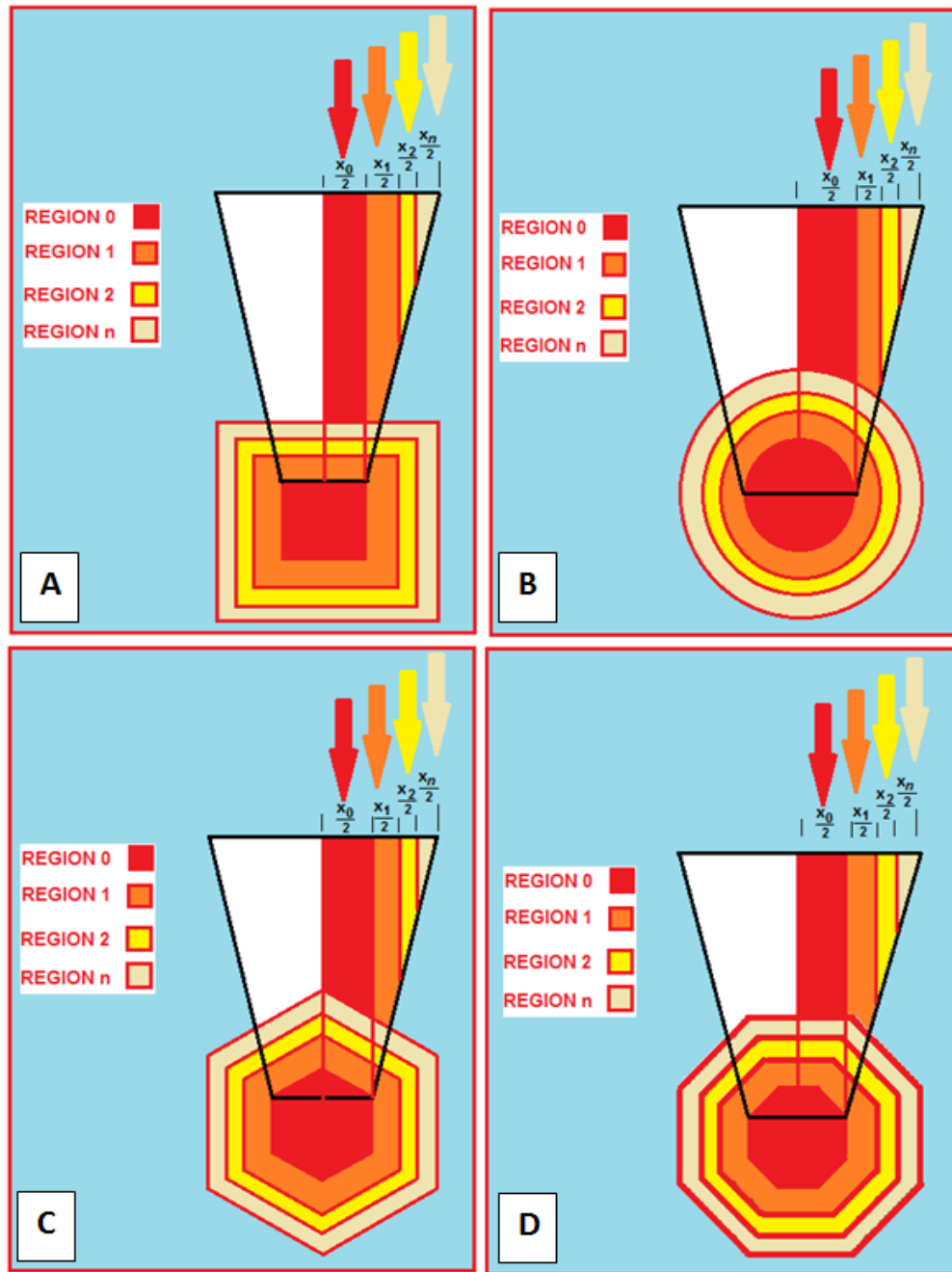


Figure 3-3 Concentrator side regions in terms of the numbers of reflections for: A- SAC, B- CAC, C- HAC and D- OAC

Generally, the closer the incident ray to the concentrator axis the lower the number of reflections the ray experiences before reaching the exit aperture, as the normal incident rays on a region of area equal to the area of exit aperture have no reflection at all [179].

Using diurnal (two axis) tracking system, radiation incident on concentrator is expected to be at normal with inlet aperture, therefore the incident angle, Θ is equal to zero [17]. This will give the advantage of maximum concentration ratio at minimum concentrator material, even though concentration ratio drops with $\Theta < 0^\circ$ it still high for several angles less than the concentrator side angle, ψ [180].

3.2.2. Width and height of the concentrator:

Using the law of reflection, concentrator width after n th reflections W_n can be calculated in terms of inlet aperture width W_{in} , as:

$$W_n = W_{in} \frac{\sin\psi}{\sin(2n+1)\psi} \quad (3.3)$$

The height of the concentrator, H between the inlet aperture and the exit aperture is calculated by:

$$H = \frac{1}{2} (W_{in} - W_{out}) * \cot\psi \quad (3.4)$$

For the average number of reflection for incident rays, W_{in} can be divided into regions according to the number of reflections occurring at the region, starting from zero reflection region with a width X_0 , one reflection region with width X_1 ,...up to n reflection region with width X_n , as shown in **Figure 3-3**. The width of the region is calculated by [65]:

$$X_n = W_{n-1} - W_n \quad (3.5)$$

Where W_n is the width after n th number of reflections. The average number of reflections n_a will be:

$$n_a = \frac{0X_0 + 1X_1 + 2X_2 + \dots + n_{max} X_{n_{max}}}{W_{in}} \quad (3.6)$$

Substituting X from eqn. (3.5), eqn. (3.6) can be rewritten as:

$$n_a = 1 + \frac{W_1}{W_{in}} + \frac{W_2}{W_{in}} + \dots + \frac{W_{n_{max}-1}}{W_{in}} - n_{max} \frac{W_{n_{max}}}{W_{in}} \quad (3.7)$$

Also substituting W_n from eqn. (3.3), eqn. (3.7) is written as:

$$n_a = \sin\psi \left[\left(\sum_{k=0}^{n_{max}-1} \frac{1}{\sin(2k+1)\psi} \right) - \frac{n_{max}}{\sin(2n_{max}+1)\psi} \right] \quad (3.8)$$

3.2.3. Concentration ratio of 3D square aperture concentrator:

The concentrator main parameter is the concentration ratio, which is the amount of radiation reaching the exit aperture (receiver) to the amount of radiation coming through the inlet aperture. Neglecting the losses due to the concentrator surface reflectivity, the two amounts should be of the same value [65]. Therefore, the concentration ratio is the ratio of inlet to the exit apertures, which is also called the geometrical concentration ratio [181]. For 2D square aperture concentrator (V-trough like) the concentration ratio is calculated using the following equation [180]:

$$GCR_{2DS} = \frac{A_{in}}{A_{out}} = \frac{W_{in}}{W_{out}} = \frac{\sin(2n+1)\psi}{\sin\psi} \quad (3.9)$$

Where W_{in} is the width of the inlet aperture and W_{out} is the width of the exit aperture

The geometrical concentration ratio of the 3D square aperture concentrator, SAC is the square of GCR_{2D} [65], as:

$$GCR_{SAC} = (GCR_{2D})^2 = \left\{ \frac{W_{in}}{W_{out}} \right\}^2 = \left\{ \frac{\sin(2n+1)\psi}{\sin\psi} \right\}^2 \quad (3.10)$$

The actual concentration ratio should be less than the geometrical concentration ratio as the concentrator material does not have an ideal surface reflectivity ($\rho = 1$) consequently, losses in radiation due to reflections exist. The level of ray absorption is function of surface

reflectivity that is if the surface reflectivity is 0.95, this means that 95% of the rays will be reflected and 5% of the rays will be absorbed after the first reflection. In this case, concentration ratio is defined as the ratio of the total irradiance (W/m^2) reaching the exit aperture to the irradiance coming through the inlet aperture. Taking into account the different number of reflections along the concentrator sides, the 2D actual concentration ratio can be calculated by:

$$ACR_{2D} = \frac{X_0 + \rho X_1 + \rho^2 X_2 + \dots + \rho^{n_{max}} X_{n_{max}}}{W_{n_{max}}} \quad (3.11)$$

Also, for the 3D square aperture, SAC the actual concentration ratio is the square of ACR_{2D} [65], then it will be:

$$ACR_{SAC} = \left\{ \frac{X_0 + \rho X_1 + \rho^2 X_2 + \dots + \rho^{n_{max}} X_{n_{max}}}{W_{n_{max}}} \right\}^2 \quad (3.12)$$

3.2.4. Concentration ratio of 3D circular aperture concentrator

3D circular aperture concentrator, CAC also called conical concentrator is a truncated hollow cone with highly reflective internal surface and an angle, ψ with the concentrator cone axis line. As in SAC, part of the incident radiation reaches the concentrator exit aperture without reflection, while the remaining rays reflect on the concentrator internal surface at an angle equal to the ray incident angle on the cone surface and changing with the number of reflections occurring through the ray's path to exit aperture [182]. Regions in Figure 3-3-B represent the incident rays going through the circular inlet aperture at a diameter, D_{in} with a number of reflections n on the concentrator surface before reaching exit aperture at a diameter, D_{out} . The areas of these regions can be calculated by [182]:

Region 0 $A_0 = \pi r_0^2$

Where r_0 is the radius of region 0 ($r_0 = \frac{x_0}{2}$) and equal to radius of the exit aperture, r_{out} .

So $A_0 = A_{out}$.

Region1

$$A_1 = \pi r_1^2 - A_0$$

And r_1 is the radius of the region1 ($r_1 = r_0 + \frac{x_1}{2}$).

Region 2

$$A_2 = \pi r_2^2 - (A_0 + A_1)$$

Region n

$$A_n = \pi \left(r_0 + \sum_{k=1}^n \frac{x_k}{2} \right)^2 - \sum_{k=1}^{n-1} A_k \quad n = 0, 1, 2 \dots n_i \quad (3.13)$$

The geometrical concentration ratio of the circular aperture concentrator is calculated by:

$$GCR_{CAC} = \frac{A_{in}}{A_{out}} = \frac{A_0 + A_1 + A_2 + \dots + A_n}{A_{out}} \quad (3.14)$$

With concentrator surface reflectivity, ρ , the actual concentration ratio of the circular aperture concentrator is written as:

$$ACR_{CAC} = \frac{A_0 + \rho A_1 + \rho^2 A_2 + \dots + \rho^{n_{max}} A_{n_{max}}}{A_{out}} \quad (3.15)$$

3.2.5. Concentration ratio of 3D hexagonal aperture concentrator

Hexagonal aperture concentrator, HAC is a truncated hollow hexagonal pyramid consisting of six identical sides with reflective internal surfaces. Each side is inclined at an angle, ψ to the concentrator axis line. Inlet aperture has a width, W_{in} (twice the apothem) and the exit aperture has a width, W_{out} . Also part of the incident radiation reaches the concentrator exit

aperture without reflection, and the remaining rays reflect from concentrator opposing sides and change direction with an angle equal to ray incident angle with the concentrator side angle, ψ , and continue to change direction depending on the number of reflections. Hexagonal ring like regions in Figure 3-3-C represent the number of reflections n taken by incident ray on concentrator sides before reaching exit aperture, and the areas of these regions with respect to hexagonal width, W can be calculated by:

Region 0
$$A_0 = \frac{\sqrt{3}}{2} W_0^2$$

Where W_0 is the width of the hexagonal region 0 ($W_0 = X_0$) and equal to the width of exit aperture, W_{out} , consequently $A_0 = A_{out}$.

Region 1

$$A_1 = \frac{\sqrt{3}}{2} W_1^2 - A_0$$

Where W_1 is the width of the region 1 ($W_1 = W_0 + X_1$).

Region 2

$$A_2 = \frac{\sqrt{3}}{2} W_2^2 - (A_0 + A_1)$$

Region n

$$A_n = \frac{\sqrt{3}}{2} (W_0 + \sum_{k=1}^n X_k)^2 - \sum_{k=1}^{n-1} A_k \quad n = 0, 1, 2 \dots n_i \quad (3.16)$$

The geometrical concentration ratio of the hexagonal aperture concentrator can be written as:

$$GCR_{HAC} = \frac{A_0 + A_1 + A_2 + \dots + A_n}{A_{out}} \quad (3.17)$$

With concentrator surface reflectivity ρ , the actual concentration ratio of the hexagonal aperture concentrator is written as:

$$ACR_{HAC} = \frac{A_0 + \rho A_1 + \rho^2 A_2 + \dots + \rho^{n_{max}} A_{n_{max}}}{A_{out}} \quad (3.18)$$

3.2.6. Concentration ratio of 3D octagonal aperture concentrator

Octagonal aperture concentrator, OAC is a truncated hollow octagonal pyramid consisting of eight identical sides. Similar to HAC, the side is inclined at an angle, ψ to the concentrator axis line. Part of the incident radiation reaches the octagonal exit aperture without reflection. The remaining of radiation rays strike on the concentrator opposing sides and change direction with an angle equal to the ray incident angle with respect to the concentrator side angle, ψ . Changing the direction is dependent on the number of reflections taken by the ray. Figure 3-3-D shows an octagonal ring like regions where the incident rays go through inlet aperture with a number of reflections n before reaching the exit aperture. The inlet aperture has a width, W_{in} (distance between two opposing sides at the inlet), and the exit aperture has a width, W_{out} (distance between two opposing sides at the exit). The areas of these regions in terms of octagonal configuration width W can be calculated by:

Region 0
$$A_0 = 2(\sqrt{2}-1) W_0^2$$

Where W_0 is the width of the octagonal region 0 ($W_0 = X_0$) and equal to the width of exit aperture W_{out} , and $A_0 = A_{out}$.

Region 1

$$A_1 = 2(\sqrt{2}-1) W_1^2 - A_0$$

Where W_1 is the width of the region1 ($W_1 = W_0 + X_1$).

Region 2

$$A_2 = 2(\sqrt{2}-1) W_2^2 - (A_0 + A_1)$$

Region n

$$A_n = 2(\sqrt{2} - 1)(W_0 + \sum_{k=1}^n X_n)^2 - \sum_{k=1}^{n-1} A_k \quad n = 0, 1, 2 \dots n_i \quad (3.19)$$

The geometrical concentration ratio of the octagonal aperture concentrator can be written as:

$$GCR_{OAC} = \frac{A_0 + A_1 + A_2 + \dots + A_n}{A_{out}} \quad (3.20)$$

With the concentrator surface reflectivity ρ , the actual concentration ratio of the octagonal aperture concentrator is written as:

$$ACR_{OAC} = \frac{A_0 + \rho A_1 + \rho^2 A_2 + \dots + \rho^{n_{max}} A_{n_{max}}}{A_{out}} \quad (3.21)$$

3.2.7. Concentrator optical performance

The optical efficiency η_{opt} of all concentrator geometries (SAC, CAC, HAC and OAC) is the ratio of the power (W) at the exit aperture to the incoming power through the inlet aperture [21]. It can also be calculated by dividing the actual concentration ratio of the concentrator by the geometrical concentration ratio as [65]:

$$\eta_{opt}(\%) = \frac{ACR_{3D}}{GCR_{3D}} \times 100 \% \quad (3.22)$$

Different concentrator side angles were investigated mathematically to determine the optimum concentrator side angle and other dimensions, as well as the number of reflections in each region.

Table 3-1-4 present concentrator dimensions of exit aperture and height at different side angles, and various concentration ratios of the four configurations.

Table 3-1 Dimensions of SAC with the change of side angle at different concentration ratios.

GCR_{SAC}	2	4	6	8	10
$A_{out} [mm^2]$	2500	2500	2500	2500	2500
Side angle, ψ	Height, H	Height, H	Height, H	Height, H	Height, H
45	10.36	25	36.2	45.71	54.06
40	12.34	29.79	43.14	54.48	64.42
35	14.79	35.70	51.70	65.28	77.20
30	17.94	43.30	62.703	79.17	93.63
25	22.21	53.61	77.63	98.03	115.92
20	28.45	68.69	99.46	125.60	148.51
15	38.65	93.30	135.10	170.59	201.74
10	58.73	141.78	205.30	259.23	306.56

Table 3-2 Dimensions of CAC with the change of side angle at different concentration ratios.

GCR_{CAC}	2	4	6	8	10
$A_{out} [mm^2]$	2500	2500	2500	2500	2500
Side angle, ψ	Height, H	Height, H	Height, H	Height, H	Height, H
45	11.68	28.21	40.89	51.58	61
40	13.92	33.62	48.73	61.47	72.69
35	16.68	40.29	58.40	73.66	87.11
30	20.23	48.86	70.82	89.34	105.65
25	25.05	60.50	87.69	110.61	130.80
20	32.09	77.51	112.34	141.71	167.58
15	43.59	105.28	152.60	192.50	227.64
10	66.24	159.99	231.90	292.52	345.92

Table 3-3 Dimensions of HAC with the change of side angle at different concentration ratios.

GCR_{HAC}	2	4	6	8	10
$A_{out} [mm^2]$	2500	2500	2500	2500	2500
Side angle, ψ	Height, H	Height, H	Height, H	Height, H	Height, H
45	11.13	26.86	38.94	49.12	58.09
40	13.26	32.01	46.41	58.54	69.23
35	15.89	38.37	55.61	70.15	82.96
30	19.27	46.53	67.45	85.08	100.61
25	23.86	57.61	83.51	105.34	124.57
20	30.57	73.81	106.99	134.95	159.59
15	41.53	100.26	145.33	183.31	216.78
10	63.10	152.35	220.84	278.56	329.43

Table 3-4 Dimensions of OAC with the change of side angle at different concentration ratios.

GCR_{OAC}	2	4	6	8	10
$A_{out} [mm^2]$	2500	2500	2500	2500	2500
Side angle, ψ	Height, H	Height, H	Height, H	Height, H	Height, H
45	11.38	27.47	39.8	50.22	59.39
40	13.56	32.73	47.45	59.85	70.78
35	16.25	39.23	56.86	71.73	84.82
30	19.71	47.57	68.96	86.99	102.87
25	24.40	58.90	85.38	107.70	127.37
20	31.26	75.47	109.39	137.98	163.18
15	42.46	102.51	148.59	187.43	221.65
10	64.52	155.77	225.79	284.82	336.83

From **Table 3-1-4**, it is clear that increasing concentrator side angles decreases concentrator height, and increasing concentration ratio increases concentrator height. Also, it is noticed that

increasing the number of concentrator sides, increases the concentrator height, where at side angle 10° the heights of the SAC, HAC, OAC and CAC are 58.73 mm, 63.10 mm, 64.52 mm and 66.24 mm, respectively. CAC is taller than other shapes because the sides are closer due to the area of a circle being more contained than other shapes.

3.3. Ray tracing optical simulation of 3D concentrator with different aperture cross-sections

Ray tracing technique predicts the received irradiance at the receiver for a given input taking into account the geometry and surface properties of the concentrator. In order to maximize concentrator optical performance, geometry and surface properties have to be modified to minimize the reflected rays away from receiver and eliminate absorption by concentrator reflective surfaces. OptisWorks, an advanced ray tracing software was used to predict the actual concentration ratio, ACR and optical efficiency of the four 3D concentrator geometries mentioned above, as well as the received flux distribution at concentrator exit. This ray tracing software can be used to predict the optical performance of concentrator systems at different solar incident angles, solar flux, and concentrator material properties.

Ray tracing simulation process follows five major steps (**Figure 3-4**) including building the concentrators, building the light source, defining concentrator's boundary conditions (material properties and surface reflectivity), defining the incoming and receiver detectors and running the simulation.

The light source is defined as the real sun or the lightening lamp used in solar simulators. The definition includes defining the flux (W), emittance (uniform or variable), intensity type (Lambertian, Cos or Gaussian), spectrum (Monochromatic or blackbody), temperature and the number of rays, with ray tracing colour (true or false).

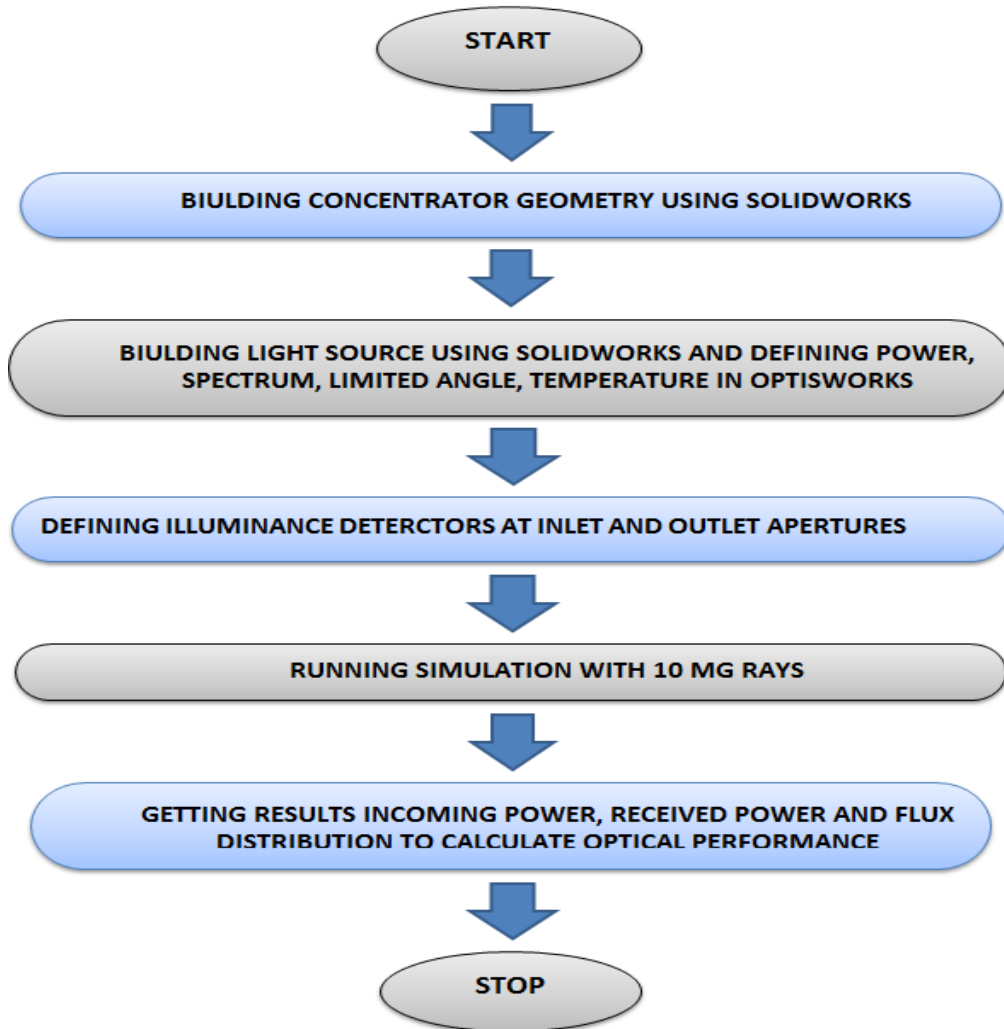


Figure 3-4 Flow chart of ray tracing simulation process for concentrators

The simulation was carried out under an average solar irradiance of the mean day of June (792 W/m^2 , at 162 n day of year) for Sabha city in the southern part of Libya. A generation of 10 Mega rays, Lambertian intensity type (normal to the concentrator aperture) was set to the source as planar with a size larger than the concentrator inlet aperture area, to guarantee rays to cover concentrator inlet aperture.

The value of surface reflectivity used in both the mathematical model and the ray tracing software boundary conditions is 90.1 %, which is for high reflective material (MIRO-SUN® PV weatherproof reflective) [183] to predict the actual concentration ratio and the optical

performance of the four concentrators. The analysis was carried out for geometric concentration ratios of 2, 4, 6, 8 and 10.

3.4. Comparison of four concentrators

The results of the optical performance of SAC, CAC, HAC and OAC, obtained by the mathematical modelling, were compared with results obtained using the ray tracing software (OptisWorks) at different side angles, ψ starting from 45° to 10° with interval of 5° , and different geometric concentration ratios.

The difference in optical performance of the two methods (mathematical modelling and ray tracing) is calculated for all cases by taking the absolute value using the following equation:

$$Difference_{opt.} = \left| \frac{\eta_{ray} - \eta_{mod.}}{\eta_{ray}} \right| * 100 \quad (3.23)$$

The effect of concentrator surface reflectivity on optical performance was investigated using OptisWorks software with three different actual reflectivity values of three different materials. The materials are: Polished stainless steel 316 with measured reflectivity of 57.35%, Pilkington Optimirror with measured reflectivity of 72.95 % and high reflective material (MIRO-SUN®PV weatherproof reflective) with reflectivity of 90.1 % taken from manufacturer product datasheet [183]. The effect of gap distance between concentrator and receiver on the optical performance was also investigated by changing the gap distance from 0 (no gap) to 10 mm with an interval of 2 mm using the four concentrator geometries.

The effect of incidence angle, θ on the optical performance was investigated using OptisWorks software at different incidence angles, taking into account two cases: first, the system is considered static during the day, and θ ranges from -75° to 75° with an interval of 15° . Every 15° represents 1 hour and $\theta = 0^\circ$ represents noon time (at Zenith) based on real

time. Also the change in flux distribution with the incidence angle is investigated for the four geometries are at the same concentration ration (GCR = 6).

In the second case, the system was considered to use diurnal tracking system, but an error or inaccuracy in tracking may occur, leading to a drop in system output [184]. Θ used in this case ranges from -15° to 15° with an interval of 1° , and the total Θ represent 1 hour before and after Zenith time. This second investigation was caried out using the SAC, but with larger size to be used as part of CPV system with three different GCRs (2, 4 and 6) and three different side angles ψ of each concentrator that give maximum performance at $\Theta = 0^\circ$. This is to determine which side angle makes the concentrator flexible enough with tracking system error and no significant loss in optical performance. The effect of incident angle on the radiation flux entering the concentrator was also investigated at GCR 6. The effect of incidence angle on the optical performance in terms of geometry width to length ratio, W/L ratio is investigated for the large concentrator. The comparison was made for the whole expected optical performance with W/L of 1, 0.75, 0.50 and 0.25, under different incidence angles ranging from -75° to 75° .

A comparison was made to the flux distribution on the receiver, for all geometries at GCR=6. Received flux distribution on the receiver at $\Theta = 0^\circ$ was investigated at GCR = 6. The uniformity was calculated to the received flux for each case at $\Theta = 0^\circ$ using standard deviation, σ and coefficient of variation, CV. Standard deviation is one of the statistical tools used to quantify the variation from the flux average (mean) value [185]. Not always smaller flux standard deviation means better uniformity with different average values [83]. Coefficient of variation measures the amount of variation relative to the average value, and is defined as the ratio of standard deviation to the average value. It can be used to compare values with different flux average values [186]. In this work it is applied to the received flux

of concentrator geometry, where every distribution has its own average and standard deviation.

3.4.1. Mathematical modelling and ray tracing

Figure 3-5 to **Figure 3-9** show the effect of side angle, ψ on the optical efficiency and concentrator height of the four concentrator geometries for geometrical concentration ratios of 2, 4, 6, 8 and 10, respectively. It is clear that the optical efficiency of all concentrator geometries with different GCRs increases as the side angle, ψ decreases. In **Figure 3-5**, all concentrator geometries with GCR=2 the optical efficiency decreases to about 50% at $\psi = 45^\circ$ achieving ACR of only 1 where the only rays reaching the exit aperture are the ones with no reflection while all other rays reaching the concentrator sides are reflected out. On the other hand, the maximum optical efficiency exceeds 94% at an angle $\psi = 35^\circ$ and no further increase occurs with reducing the angle below 35° . As for the concentrator height, H, it increases significantly from 15 – 16 mm at an angle $\psi = 35^\circ$ to 59- 66 mm at an angle $\psi = 10^\circ$ with no significant increase in optical efficiency.

Figure 3-6 shows that the maximum optical efficiency for concentrators with GCR =4 reaches about 90.6 % for SAC and about 92.5 % for the other three geometries at angle of 30° , and no increase with angles lower than 30° . For concentrators with GCR = 4, the side height increases from 43.3 – 48.9 mm at an angle $\psi = 30^\circ$ to 142- 160 mm at an angle $\psi = 10^\circ$. In **Figure 3-7**, the maximum optical efficiency of the four geometries at GCR = 6 stays close to concentrator efficiency at GCR = 4 but with smaller ψ (20°), except in SAC the efficiency is lower by about 2%. While concentrator height increases from about 100mm – 112 mm at $\psi = 20^\circ$ to 205 – 232 mm at $\psi = 10^\circ$. At GCR =8 (**Figure 3-8**), the maximum optical efficiency is about 86 % for SAC and OAC , and 90 % for CAC and HAC, achieved at ψ of 20° the same as in GCR =6. The concentrator height increases from about 126 mm – 142 mm at $\psi = 20^\circ$ to

259 – 292 mm at $\psi = 10^\circ$. At GCR =10 (**Figure 3-9**) the concentrator optical efficiency increases from 85% for SAC to 87 % for OAC to 89 % for CAC to 89 % for HAC at $\psi = 15^\circ$. The concentrator height increases from about 202 mm – 228 mm at $\psi = 15^\circ$ to 307 – 346 mm at $\psi = 10^\circ$ with no increase in concentrator optical efficiency.

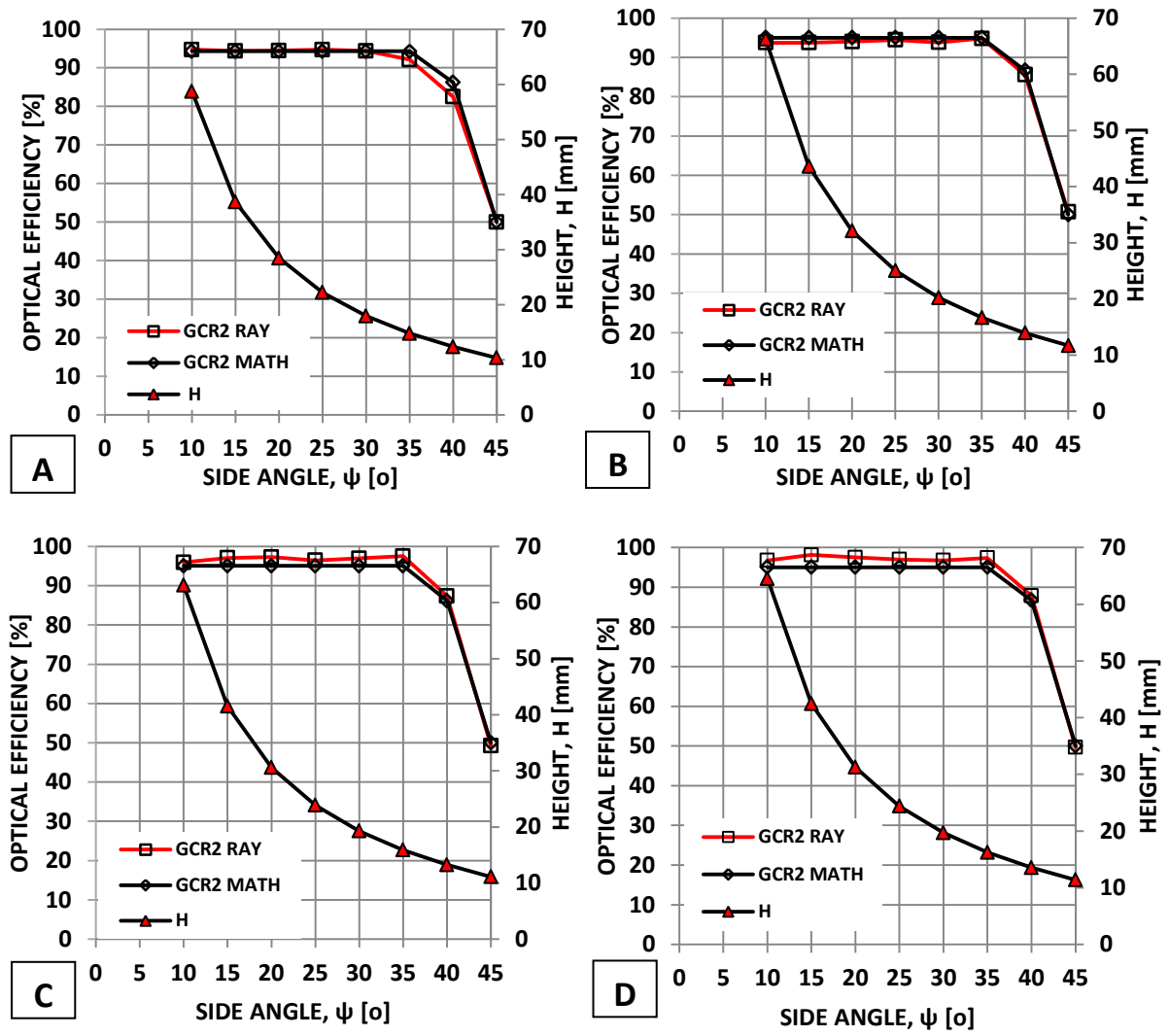


Figure 3-5 Concentrator optical efficiency and height with side angle at GCR=2 for: A- SAC, B- CAC, C- HAC and D- OAC

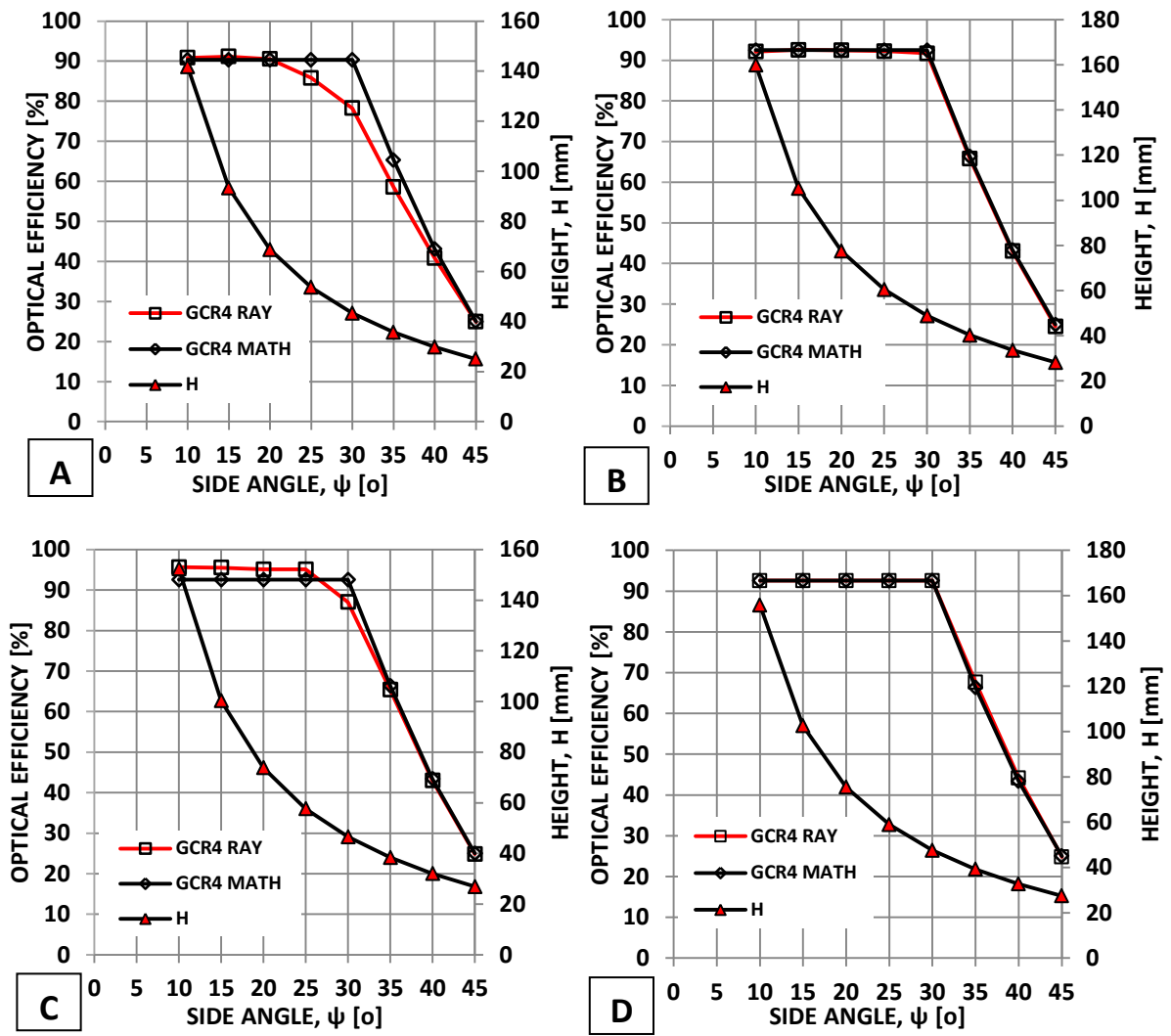


Figure 3-6 Concentrator optical performance and height with side angle at GCR=4 for: A- SAC, B- CAC, C- HAC and D- OAC

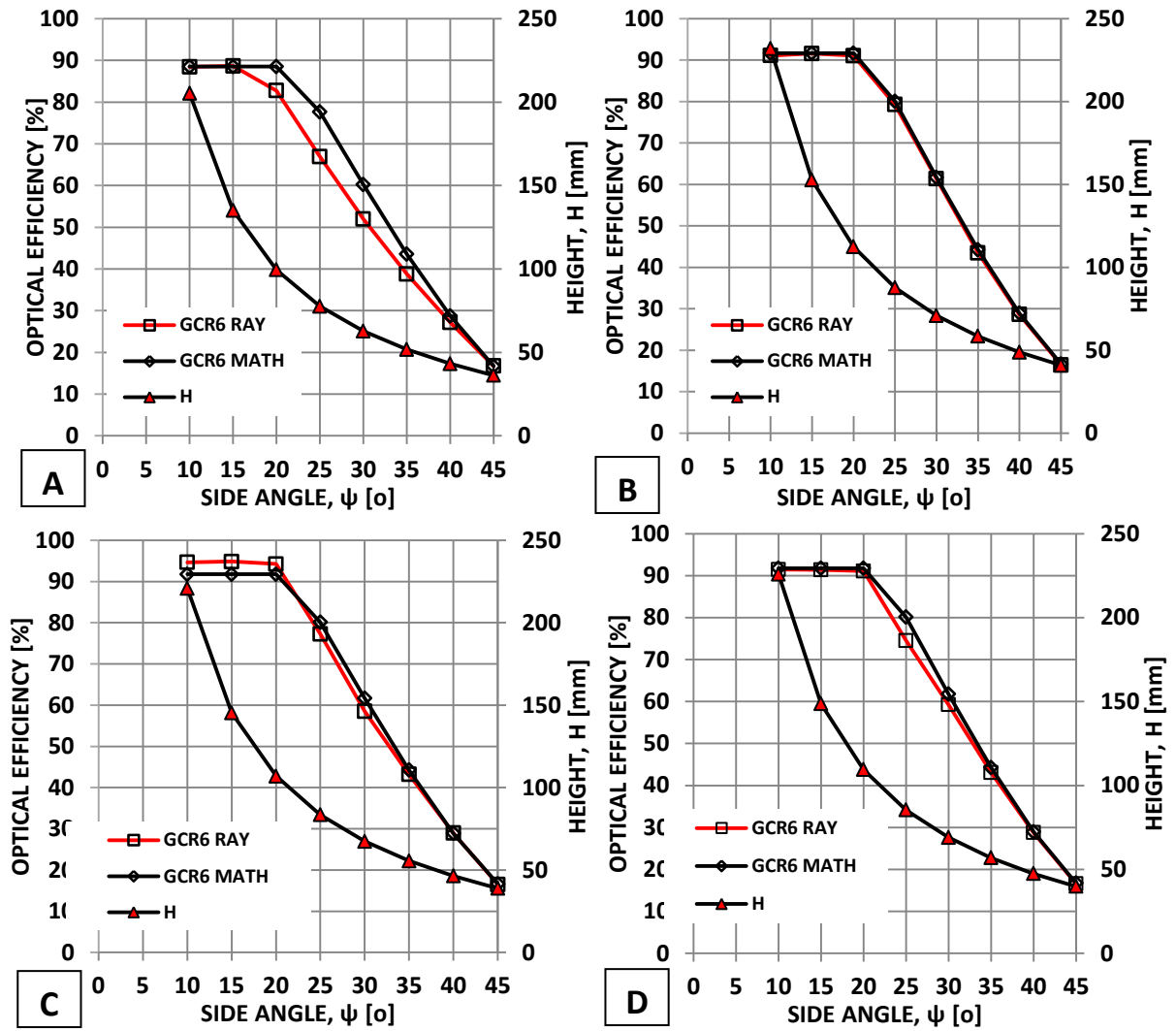


Figure 3-7 Concentrator optical performance and height with side angle at GCR=6 for: A- SAC, B- CAC, C- HAC and D- OAC

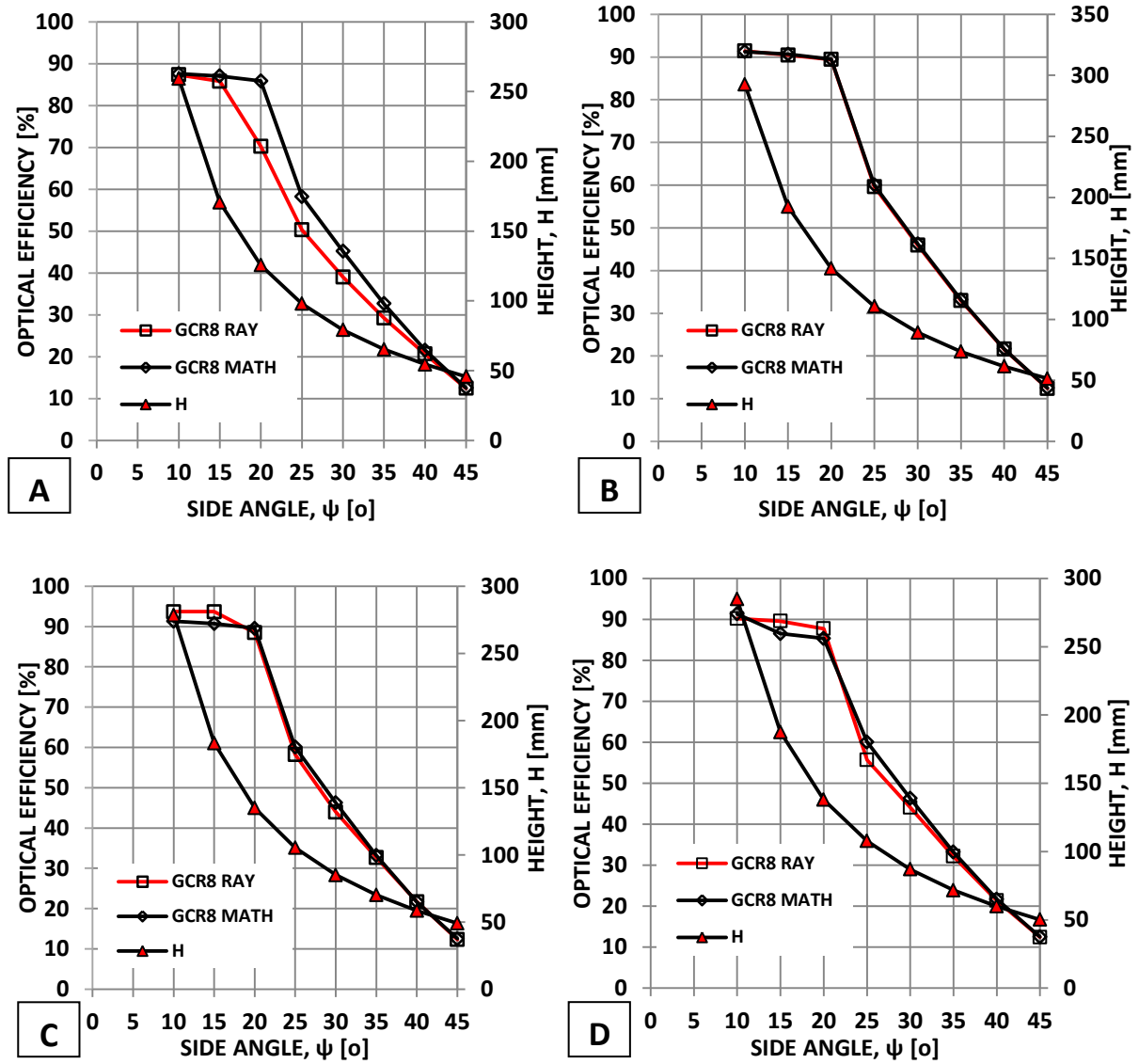


Figure 3-8 Concentrator optical performance and height with side angle at GCR=8 for: A- SAC, B- CAC, C- HAC and D- OAC

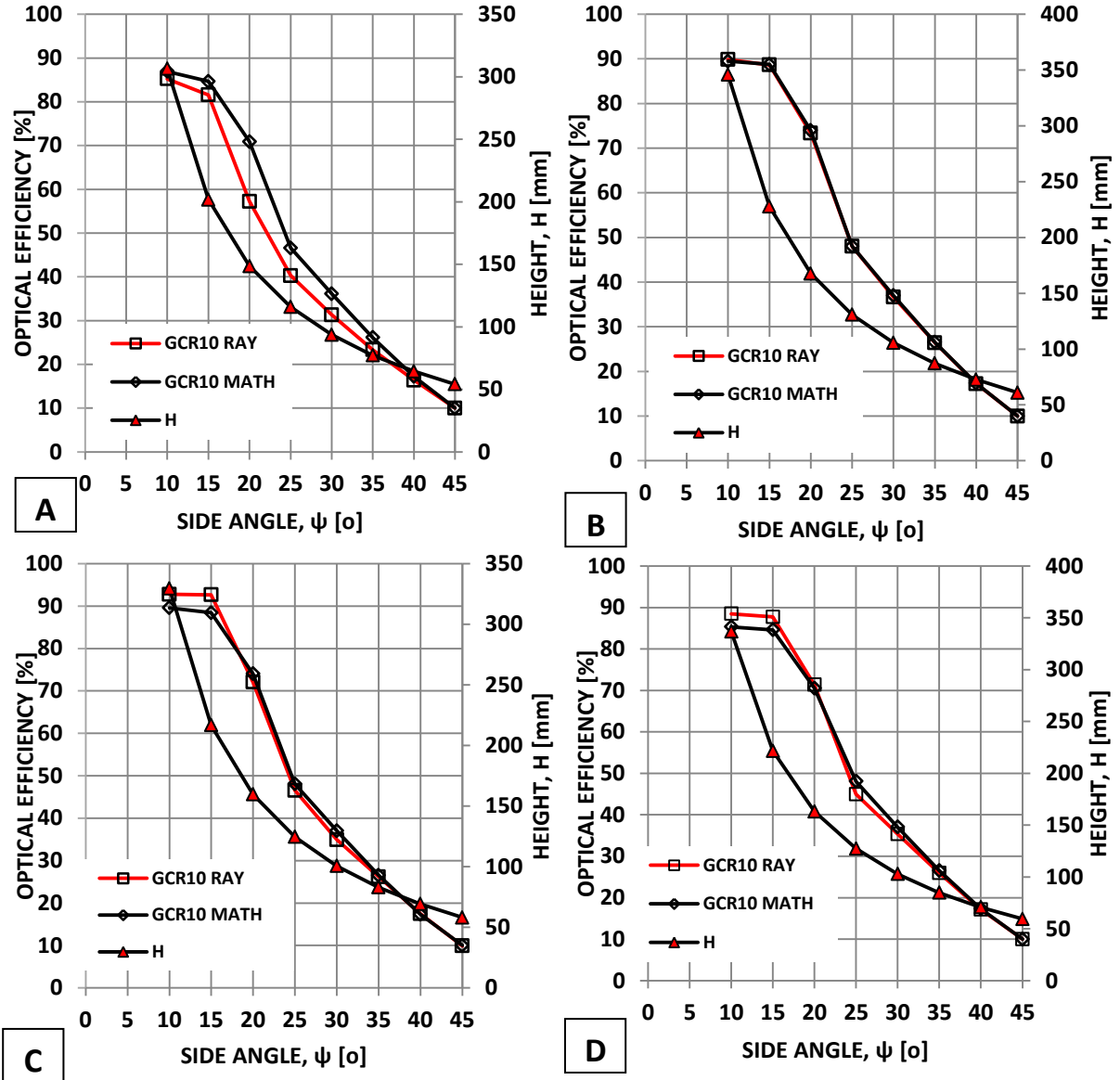


Figure 3-9 Concentrator optical performance and height with side angle at GCR=10 for: A- SAC, B- CAC, C- HAC and D- OAC

It is clear from **Figure 3-5** to **Figure 3-9** that there is good agreement in optical efficiency between the mathematical model and the ray tracing with an average difference of 5 % for the side angles investigated. The maximum difference is 19 % occurring with the SAC at GCR=10 and $\psi = 20^\circ$, which is larger than the optimum angle listed in **Table 3-5** (15°). On the other hand, the average difference in optical efficiency between the new derived mathematical model and the ray tracing results for HAC concentrator is only 2.4 %, while the maximum

difference is 6 % with GCR =4 and $\psi = 30^\circ$, which is the optimum angle of the concentrator. For OAC concentrator, the average difference between the new derived mathematical model and the ray tracing results is 2.1 %, and the maximum difference is 7 % occurring at GCR =8 and $\psi = 25^\circ$ that is not the optimum angle ($\psi = 20^\circ$) of this geometry.

Table 3-5 shows the side angle, height and optical efficiency at optimum performance of the various concentrator geometries at different geometric concentration ratios. The optimum performance is taken when the concentrator has maximum optical efficiency and lowest height. It can be seen that for all concentrator geometries the side angle at which the maximum optical efficiency occurs decreases with the increase of the concentration ratio. Also for the same concentration ratio, all concentrator geometries achieved their maximum optical efficiency at the same side angle. For instance, $\psi = 35^\circ$ gives the maximum optical efficiency for concentrator with GCR =2, while changing the GCR to 10, at least $\psi = 15^\circ$ is needed to obtain the maximum optical efficiency.

Table 3-5 Maximum optical performance at optimum height and side angle for different geometric concentration ratios of SAC, CAC, HAC and OAC

Geometry	SAC			CAC			HAC			OAC		
GCR	ψ , [°]	H, [mm]	η , [%]	ψ , [°]	H, [mm]	η , [%]	ψ , [°]	H, [mm]	η , [%]	ψ , [°]	H, [mm]	η , [%]
2	35	14.8	94.3	35	16.7	95	35	15.9	95	35	16.2	95
4	30	43.3	90.6	30	48.9	92.5	30	46.5	92.6	30	47.6	92.6
6	20	99.5	88.5	20	112.3	91.7	20	107	91.8	20	109.4	91.7
8	20	125.6	85.9	20	141.7	89.5	20	135	89.6	20	138	85.3
10	15	201.7	84.7	15	227.6	88.7	15	216.8	88.4	15	221.7	84.6

3.4.2. Concentrator surface reflectivity

In order to investigate the effect of concentrator surface reflectivity on the optical performance of the small scale concentrators, reflectivity values of three different commercially available materials were used. Ray tracing simulations were carried out to predict the effect of surface reflectivity on the concentrator optical performance, with no gap between the receiver and concentrator. The materials are: Polished stainless steel 316 with measured reflectivity of 57 %, Pilkington Optimirror with measured reflectivity of 73 % and high reflective material (MIRO-SUN®PV weatherproof reflective) with reflectivity of 90 % taken from manufacturer product datasheet [183]. **Figure 3-10** shows the variation of optical efficiency with the concentrator surface reflectivity for SAC, CAC, HAC and OAC at GCR = 6 and $\psi = 20^\circ$.

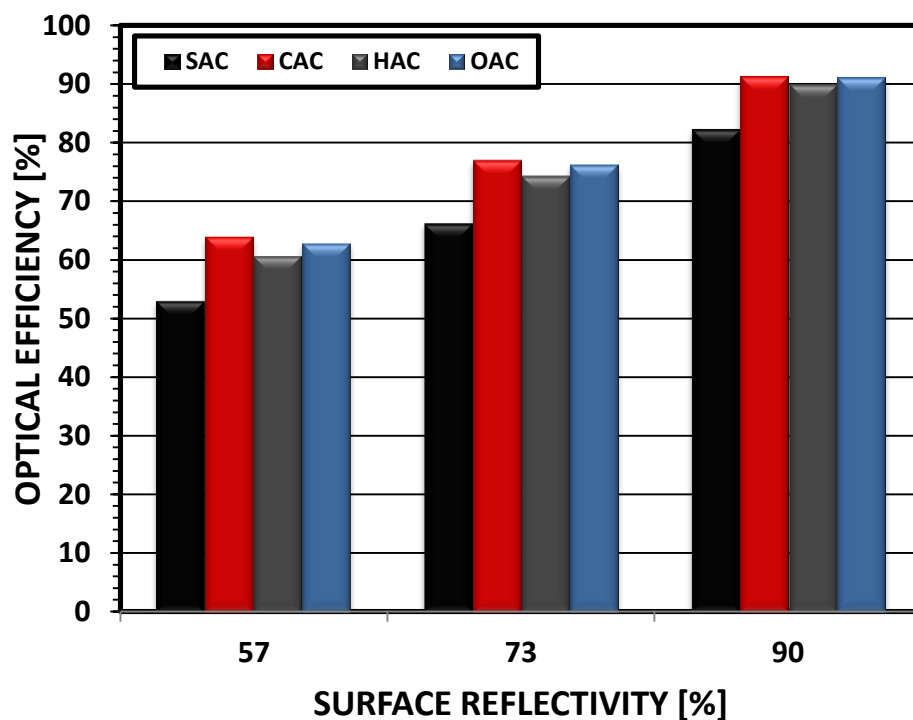


Figure 3-10 Effect of surface reflectivity on the optical performance of SAC, CAC, HAC and OAC at GCR = 6 and $\psi = 20^\circ$

It can be seen that the optical efficiency decreases with the decrease in concentrator surface reflectivity with the lowest efficiency achieved by the SAC and highest efficiency achieved by the CAC at all efficiency values. For example, the optical efficiency of SAC changes from 54 % with reflectivity of 57.354 % to 66 % with reflectivity of 72.95 % to 82 % with reflectivity of 90.1 %. For CAC, the optical efficiency is 65 %, 77 %, 91 % for reflectivity values of 57.354 %, 72.95 %, 90.1 %, respectively. It is worth noting that CAC, HAC and OAC have similar optical efficiency values with maximum difference of 5 %.

3.4.3. Gap distance between concentrator and receiver

The effect of gap distance between the concentrator and the receiver on the optical performance was investigated with distance changing from 0 (no gap) to 10 mm with an interval of 2 mm using the four concentrator geometries at $GCR = 6$ and $\psi = 20^\circ$. It is clear from **Figure 3-11** that the gap distance has a significant effect on concentrator optical performance. The SAC receiver is the most sensitive to the gap distance where the effect can be seen immediately after moving the concentrator 2mm above the receiver with the optical efficiency decreased by about 3 %. The CAC, HAC and OAC have shown higher performance compared to that of the SAC and lower rate of drop in efficiency up to 6 mm gap distance (by about 1 % with 2 mm interval), then decreasing by about 3 % with 2 mm interval similar to CAC.

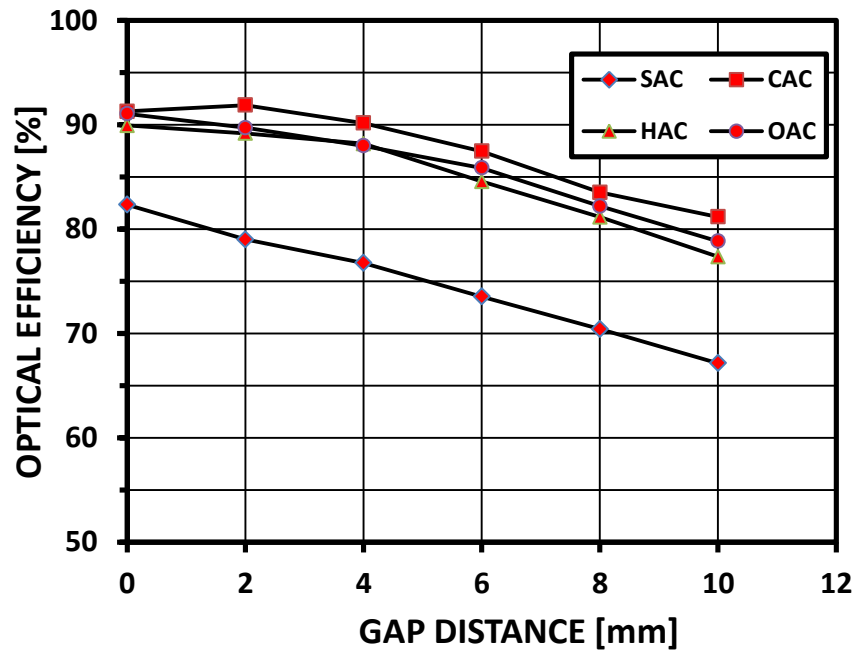


Figure 3-11 Effect of distance between the concentrator and receiver on the optical performance

3.4.4. Optical performance with incidence angle

The effect of incidence angle on the optical performance was investigated using ray tracing simulation at different incident angles ranging from -75° to 75° with an interval of 15° (every 15° represents 1 hour and 0 represents 12:00 noon (at Zenith)). Generally, the incoming flux on the concentrator aperture depends on the incidence angle. **Figure 3-12** shows the variation of the incoming flux with the incidence angle on the SAC aperture with GCR 6. It is clear that maximum incoming flux on the aperture occurs at zero degree and the flux decreased with the increase of the incident angle.

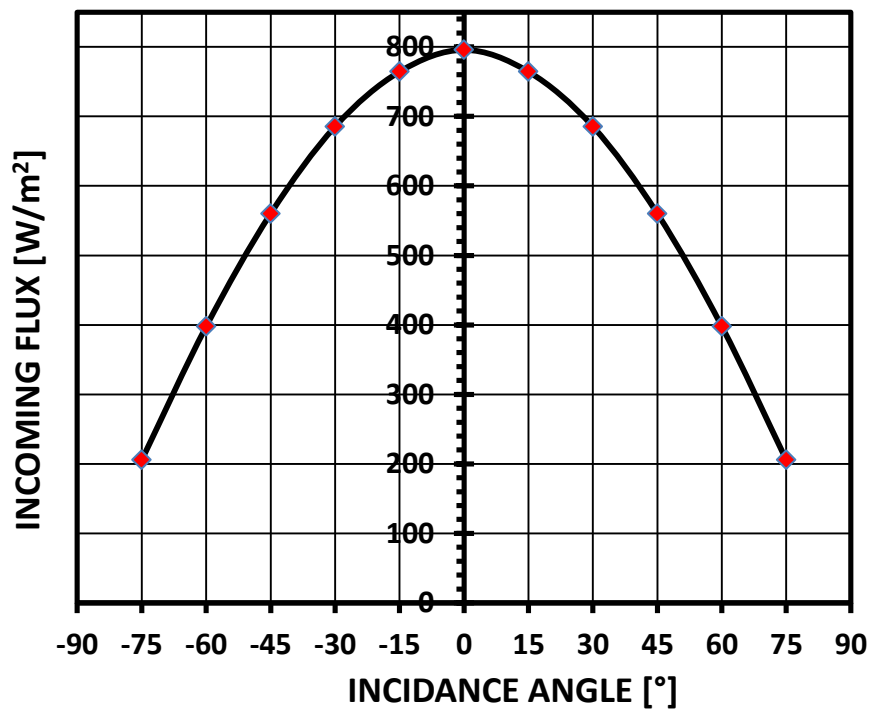


Figure 3-12 Incoming flux versus incidence angle

Figure 3-13 shows the change in flux distribution for the SAC (as an example) at the concentrator receiver. The colour scale shows the highest intensity with the red colour and the lowest with blue colour where no flux is received. The flux distribution is changing and the illuminated area on the receiver decreased as the incidence angle, θ increased. **Figure 3-13-D** shows that at $\theta = 45^\circ$ all incoming flux is reflected outside and the concentrator becomes ineffective. Also, it is shown that any two opposite incidence angles give symmetrical flux distribution on the receiver as happens with 30° and -30° angles (**Figure 3-13-C and E**).

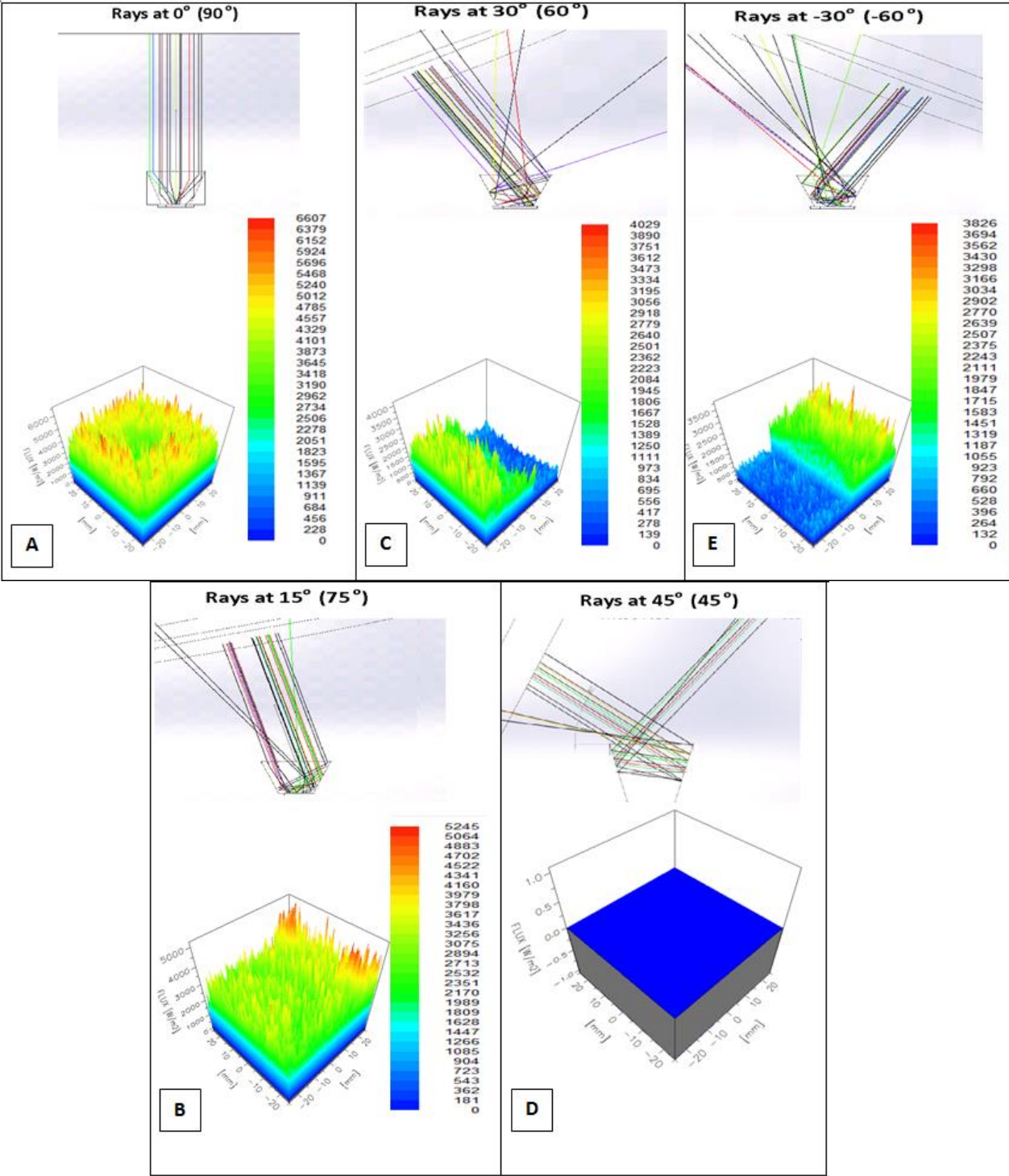


Figure 3-13 Change in flux distribution of SAC with GCR 6 at different incidence angles

Figure 3-14 shows the effect of incidence angle on the optical efficiency of different geometries with GCR 6 and the same side angle of 20°. It is clear that the CAC, HAC and

OAC have higher optical efficiency than SAC with about 90% at Zenith (0°) for the three concentrators and about 82 % for SAC throughout the range of incident angles investigated. The decrease in efficiency of SAC could be attributed to the number of reflections occur to the incoming rays before reaching the exit aperture compared to the other shapes. But for the other incidence angles all concentrators including SAC have similar optical efficiency.

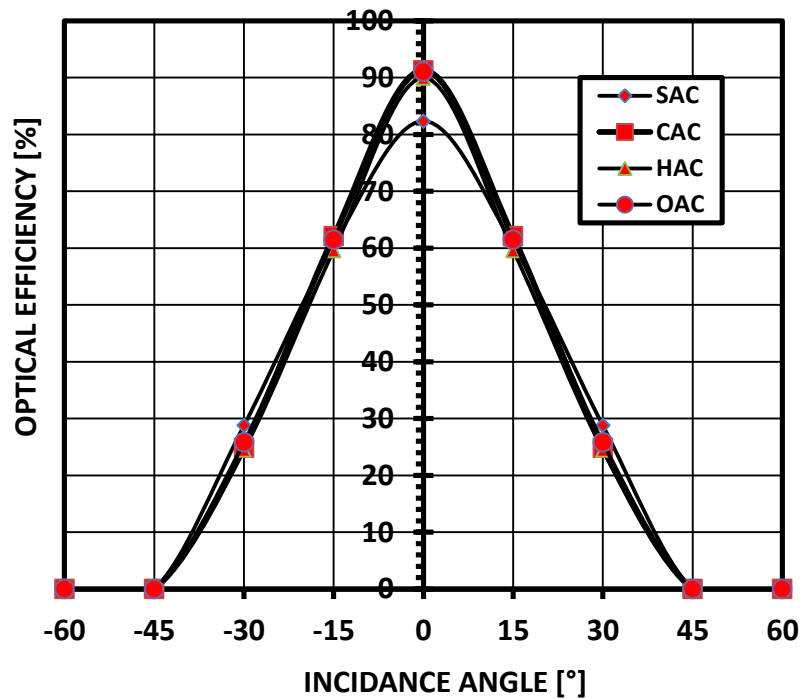


Figure 3-14 Change in the optical performance with the increase of incidence angle (from 60° to -60°)

The effect of incidence angle on concentrator optical efficiency was investigated with different concentration ratios for the SAC at the optimum angle of each concentration ratio, as shown in **Figure 3-15**. It can be seen that as the concentration ratio increases, the concentrator accepts less radiation with the change of incidence angle, consequently less concentrator working hours during the day (in case of static). For example, SAC with GCR2 accepts radiation for incidence angles from -75° to 75° while SAC with GCR6 accepts radiation only

for incidence angles less than -45° to 45° . The highest efficiency was about 92 % at GCR2, while the lowest was about 82% at GCR4.

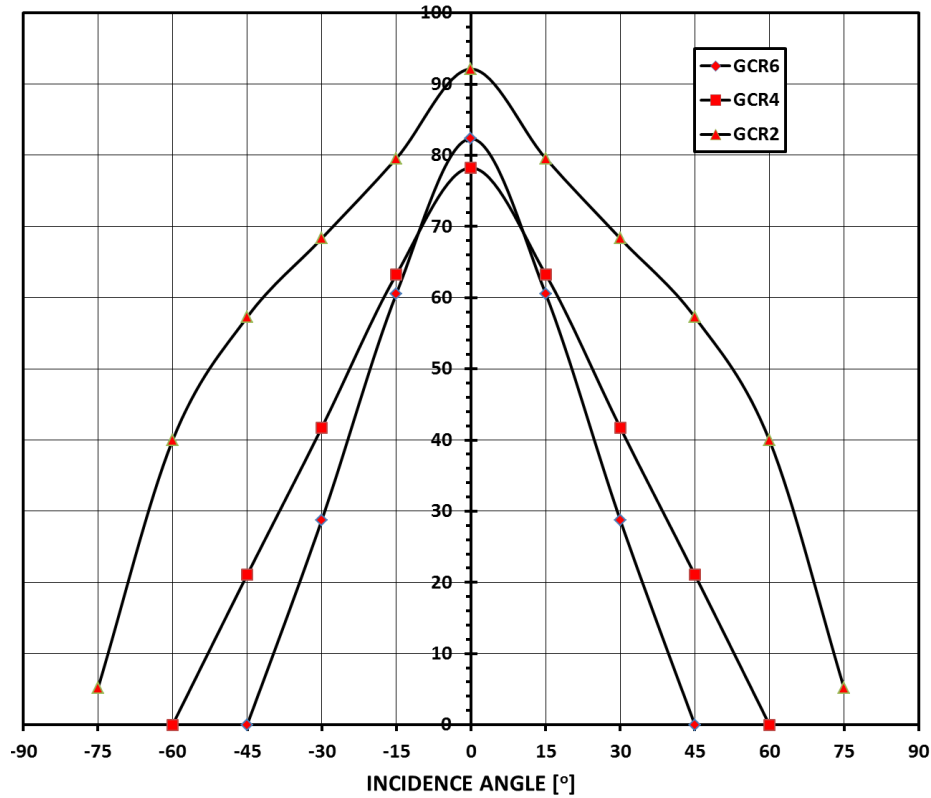


Figure 3-15 Effect of the incidence angle on the optical performance with different concentration ratios for the SAC

3.4.5. Receiver flux distribution for various concentrators

Figure 3-16 shows the flux distribution at the receivers of the four investigated concentrators at gap distance of 0 mm, surface reflectivity of 90.1% and incident angle of 0° and GCR6. It can be seen from **Figure 3-16-A** that the flux distribution in the SAC receiver is more concentrated in a ring like shape with less density at the centre line and overall average flux of about 3903 W/m^2 . In the CAC (**Figure 3-16-B**), it is clear that all concentration takes place at the central spot (region with diameter of about 6 mm) with an average flux of around $35 \times 10^3 \text{ W/m}^2$, while the overall flux average is about 4208 W/m^2 . In the HAC (**Figure 3-16-C**), the

concentration has moved to a hexagonal frame connecting the centre to the corners of the hexagon but with less concentration at the centre of the receiver and average flux of about 4266 W/m^2 . As for the OAC (**Figure 3-16-D**), it can be seen that the concentration in the areas connecting the centre to the corners is reduced and more concentration is at the central part of the receiver and average flux is about 4225 W/m^2 . The circular spot at the centre of CAC receiver demonstrates the point focus concentration property with maximum flux value of many times greater than that of other concentrator geometries. Similar flux distribution has been reported by Ali et al. [187] for 3-D Elliptical Hyperboloid Concentrator (EHC) with $a/b = 1$ (circular inlet and exit apertures).

Standard deviation (σ) and coefficient of variation (CV) results for received flux showed the best uniformity was obtained using SAC with σ value of 629 W/m^2 and CV of 0.16, followed by HAC with σ value of 1246 W/m^2 , CV of 0.29 then OAC with σ value of 1418 W/m^2 and CV of 0.34. While the worst case was the CAC with σ value of 4582 W/m^2 and CV of 1.1, due to the highly concentrated flux at the centre and little flux is distributed on the rest of receiver area.

It is clear from **Figure 3-16** and uniformity analysis that flux distribution at the receiver can vary depending on the configuration of the concentrator. Therefore the geometry should be carefully selected to suit the application. For example, the CAC will not be suitable for the PV systems due to its high local concentration.

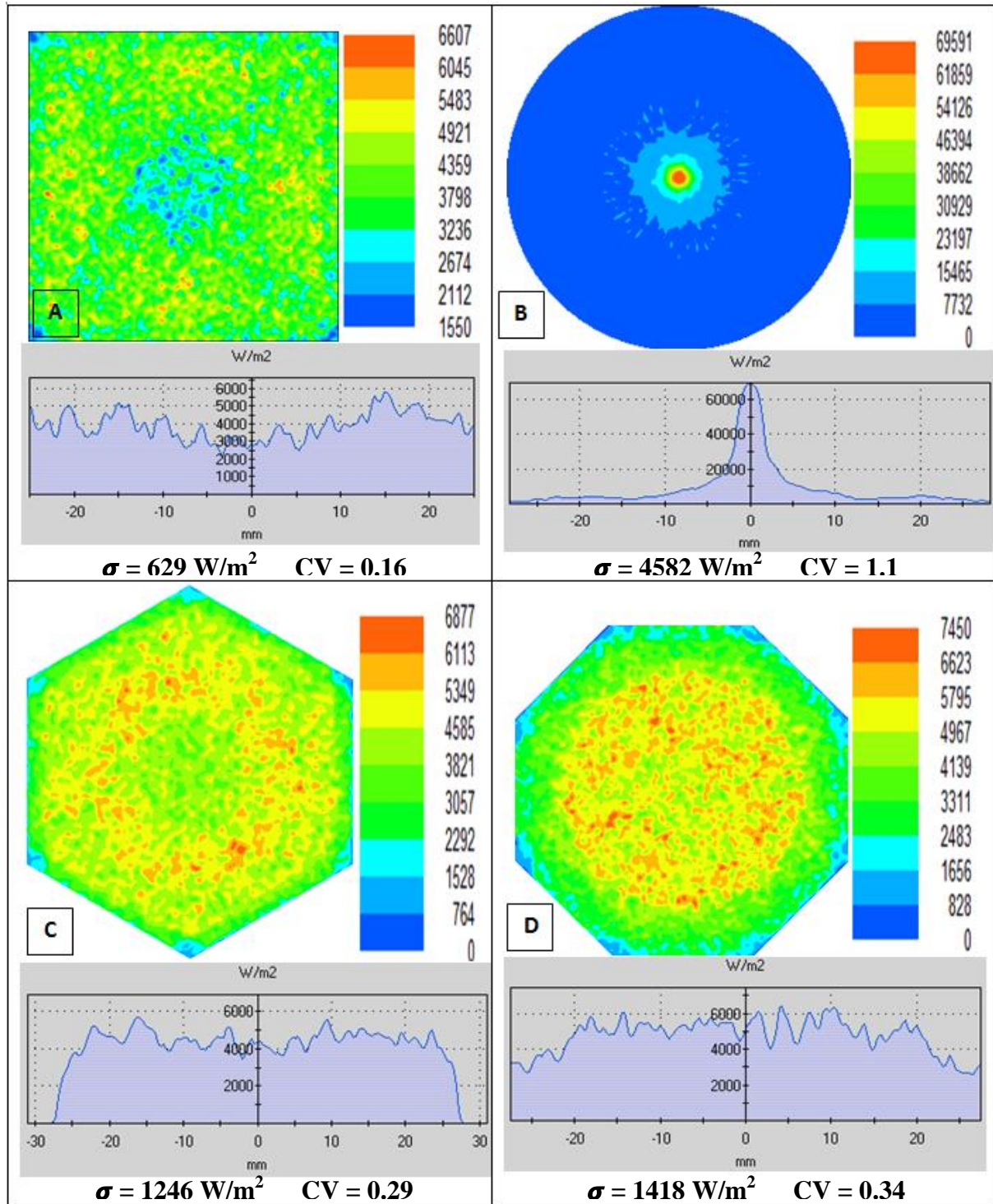


Figure 3-16 Received flux distribution and density (W/m²) of A: SAC, B: CAC, C: HAC and D: OAC

3.5. Large concentrator for CPV system

Concentrators for larger PV modules have less installation costs and more suitable to the available PV module sizes than PV cells with an area of 50 mm X 50 mm. The optical performance of a concentrator for a PV module of 315 mm X 315 mm consisting of four 156 mm X 156mm Polycrystalline PV cells was investigated. **Figure 3-17** shows the optical performance and concentrator height of the large SAC with GCR 2, 4 and 6, respectively at different side angles (see **Figure 3-5** to **Figure 3-7**). By comparing the large SAC with small SAC, the optical performance has no significant difference for all GCRs, but the height has increased. For instance, the height of SAC has increased from 14.79 mm to 93.17 mm at the same ($\psi=35^\circ$) and GCR = 2. Also for all GCRs at $\psi= 45^\circ$ what reaches the receiver is only about 50%, 25% and 16% for GCRs 2, 4 and 6 respectively, producing maximum ACR of 1. The maximum optical efficiency reaches 94%, 90% and 88.63% at side angles ψ of 35° , 30° and 20° respectively, and no increase with smaller angles, although a significant increase in concentrator height. For instance, at GCR of 2 the concentrator height increased from about 93 mm at angle of 35° to 370 mm at an angle $\psi= 10^\circ$.

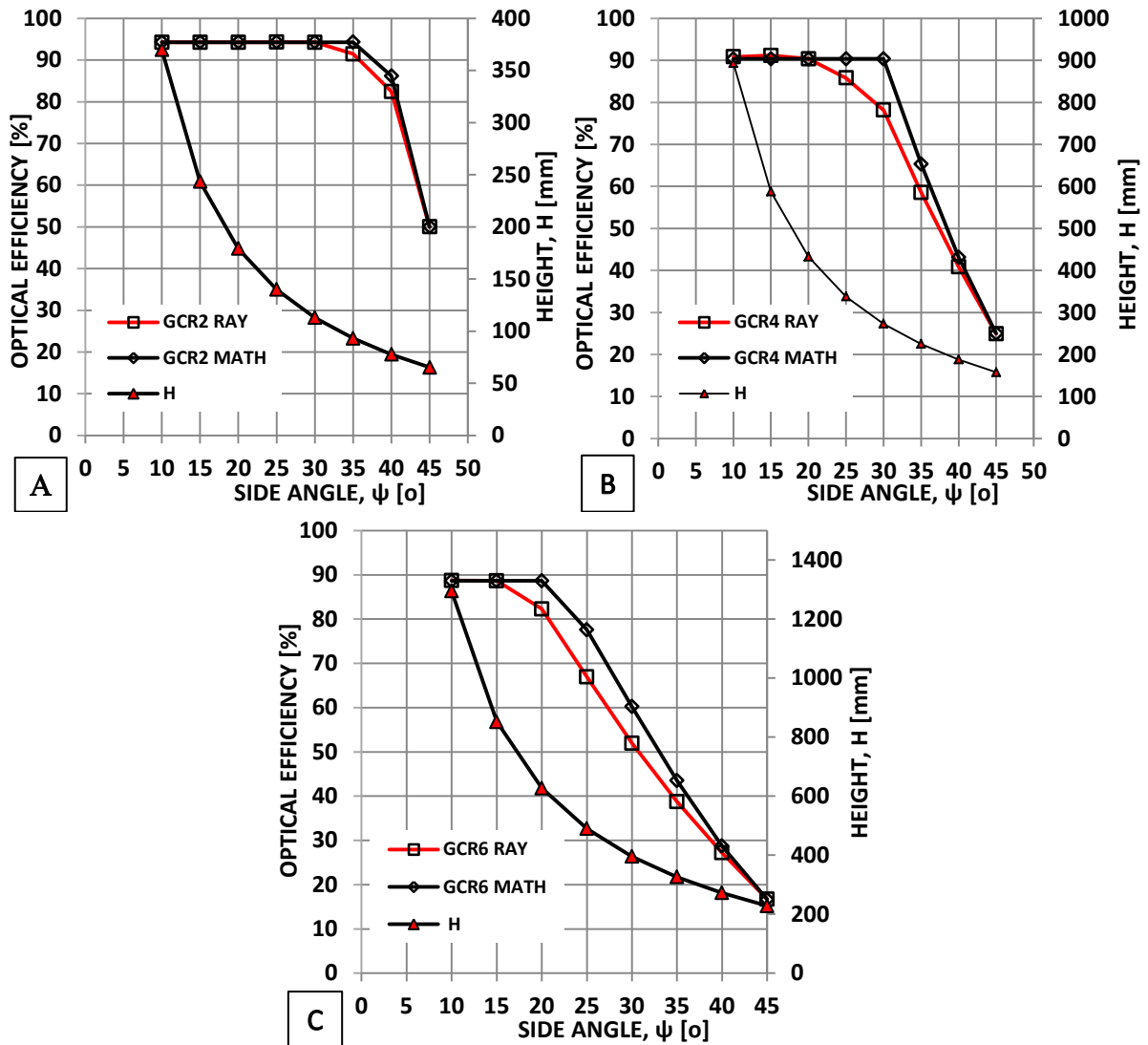


Figure 3-17 Concentrator optical performance and height of large SAC with side angle and GCR: A - 2, B - 4 and C - 6

The optical efficiency was also analysed using OptisWorks software in terms of the effect of incidence angle on concentrator flexibility with tracking. **Figure 3-18** shows the optical efficiency of large SAC with GCRs of 2, 4 and 6 at three different side angles and incidence angle ranging from -15° to $+15^\circ$ after the 0° angle. From **Figure 3-18**, as ψ decreases more stability in optical efficiency is achieved where for GCR 2 (**Figure 3-18-A**), the highest optical efficiency is at $\psi=25^\circ$ with values remaining above 93% for θ ranging from -15° to

+15°, while at $\psi=35^\circ$ the efficiency drop occurs after $\Theta = 5^\circ$ from about 91% to below 80%. On the other hand, the concentrator height has increased from about 93mm at $\psi=35^\circ$ to 140mm at $\psi=25^\circ$, respectively. At GCR 4 (**Figure 3-18-B**), the efficiency drops by about 15% with incidence angle changing from 0° to $\pm 15^\circ$ for all three side angles. But at $\psi=20^\circ$ performance drops significantly after $\Theta = 5^\circ$ while at $\psi=25^\circ$ it drops after $\Theta = 3^\circ$ and at $\psi=30^\circ$ the drop occurs after $\Theta = 0^\circ$ respectively, the worst case with lowest optical efficiency values that could be attributed to the larger side angle causing more ray reflected out before reaching the exit aperture. On the other hand, a significant increase in concentrator height occurred with GCR 4 where it increased from 273 mm at $\psi=30^\circ$ to 433 mm at $\psi=20^\circ$, respectively.

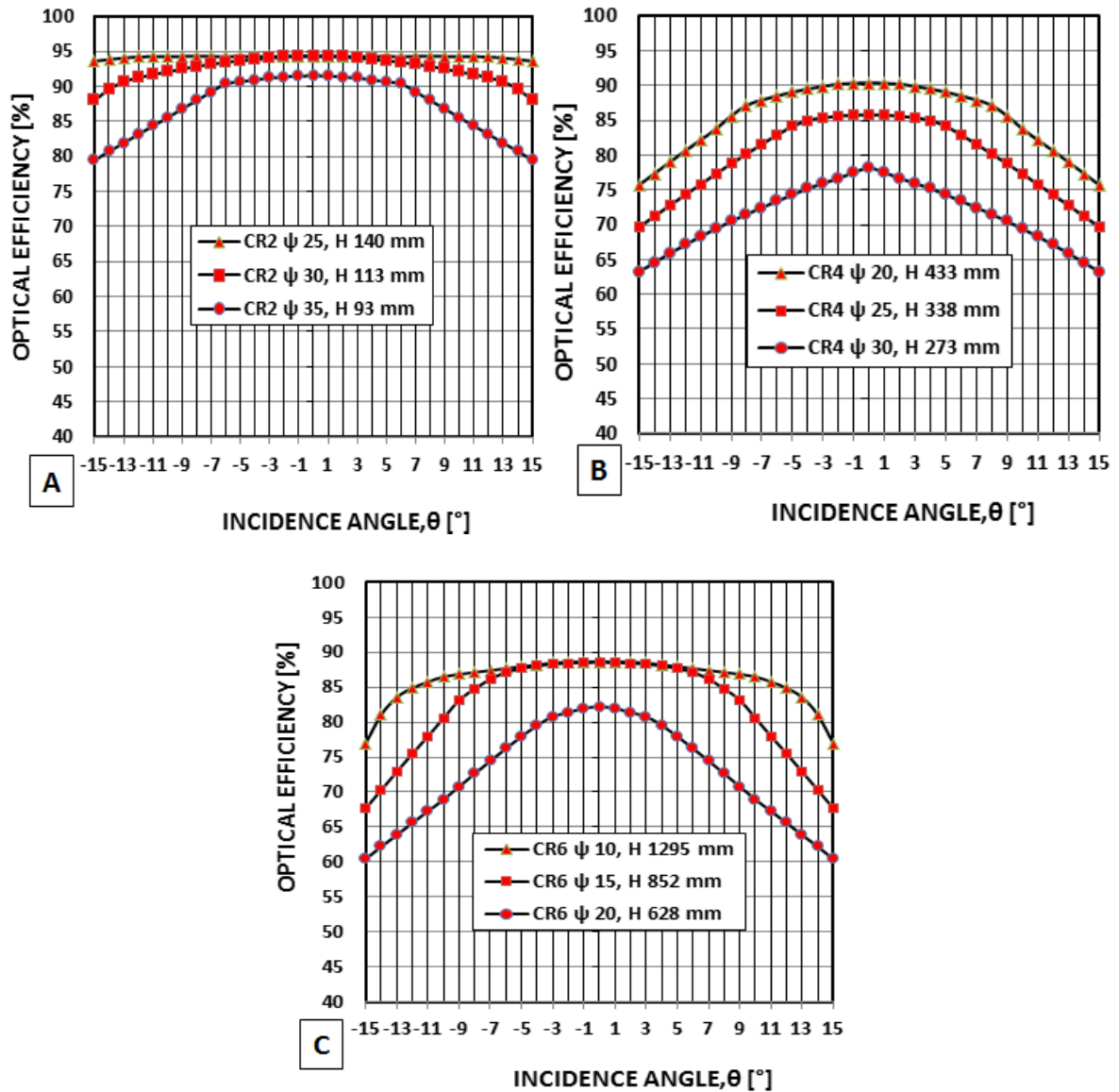


Figure 3-18 Optical efficiency of large SAC with GCRs of: A - 2, B - 4 and C - 6 with different side angles

At GCR 6 (**Figure 3-18-C**), the optical efficiency at $\psi=10^\circ$ drops after $\theta = 9^\circ$ by about 8% while at $\psi=15^\circ$ it drops after $\theta = 5^\circ$ by about 20%. At $\psi=20^\circ$ the efficiency drops after $\theta = 0^\circ$ by about 22% representing the worst case at this concentration ratio. Concentrator height has increased from 628mm at $\psi=20^\circ$ to 1295mm at $\psi=10^\circ$ (increased by 106%). It is clear that better optical performance and more concentrator flexibility with tracking system can be

gained with lower concentration ratio, smaller side angle and consequently higher concentrator height.

Figure 3-20 shows the effect of incidence angle on the optical performance of the large SAC with $GCR = 2$ and $\psi = 35^\circ$ for various geometry width to length ratios, W/L . When W/L changes to lower than 1, the side angles also change to different values, where the shorter sides have an angle greater than that of the longer sides (**Figure 3-19**). Thus, two cases were investigated: the first is that short sides with $\psi_{short} = 35^\circ$, while the second is for long sides with $\psi_{Long} = 35^\circ$. In **Figure 3-20**, a comparison was made for the optical efficiency with W/L of 1, 0.75, 0.50 and 0.25.

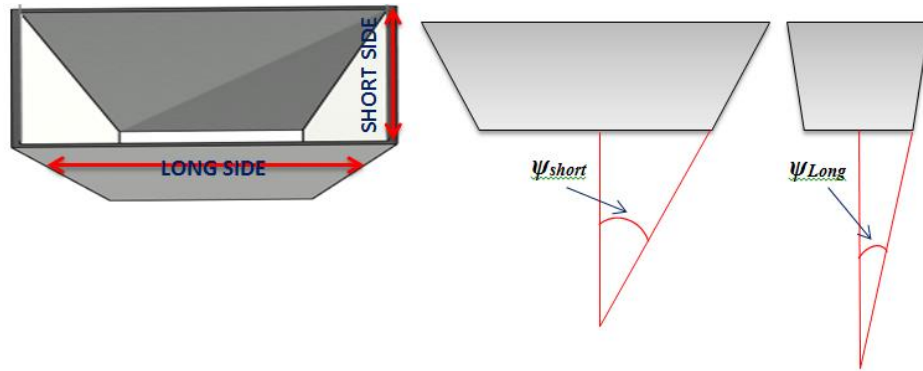


Figure 3-19 Schematic diagram for SAC with long and short concentrator sides ($W/L < 1$)

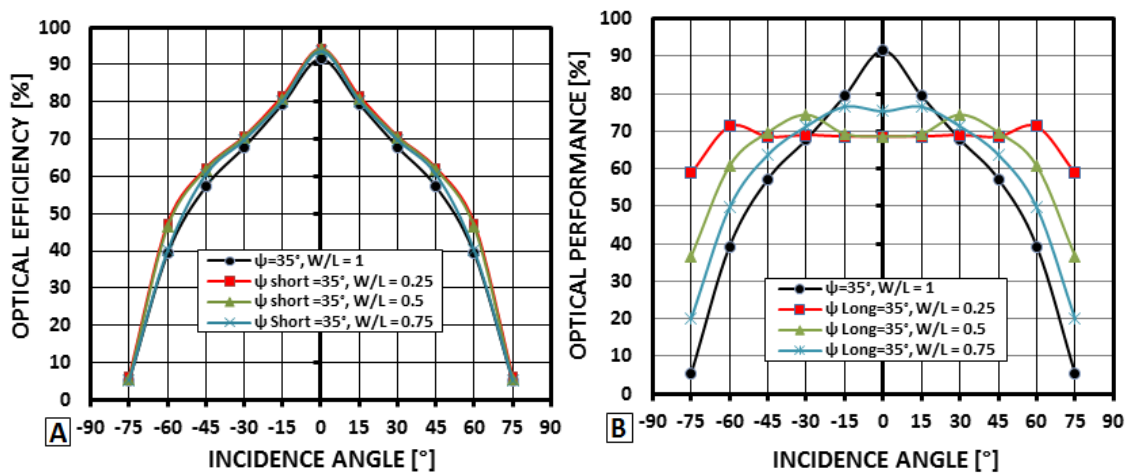


Figure 3-20 Effect of incidence angle on the optical performance of SAC with W/L ratio

Results in **Figure 3-20** also show that the optical efficiency decreases with the increase of incidence angle, but with smaller W/L ratio the concentrators accept rays in wider incidence angles. W/L = 0.25 demonstrates higher average optical efficiency of 57.39 % and 67.41% for the two cases of ψ_{short} and ψ_{Long} , respectively, compared with W/L = 1 with average efficiency of 53.61 %. Although the case of ψ_{Long} has optical efficiency significantly lower than the case of ψ_{short} at $\theta = 0^\circ$, it demonstrates higher average performance by about 10% for the range of incidence angles (-75° to $+75^\circ$) used in the investigation. Also a significant reduction in concentrator height, H in the case ψ_{Long} , especially at W/L = 0.25 with H = 46.59 mm compared with the case of ψ_{short} where H = 186.34 mm.

Table 3-6 shows the average of optical efficiency and concentrator height of SAC with different W/L ratios, for the two cases of ψ_{Long} and ψ_{short} , respectively.

Table 3-6 Average optical performance of SAC with different W/L ratios.

SAC	W/L =1		W/L = 0.75		W/L = 0.50		W/L = 0.25	
	$\eta_{opt. [\%]}$	H [mm]	$\eta_{opt. [\%]}$	H [mm]	$\eta_{opt. [\%]}$	H [mm]	$\eta_{opt. [\%]}$	H [mm]
$\psi_{short} [\%]$	53.61	93.17	55.03	107.58	56.78	131.75	57.39	186.34
$\psi_{Long} [\%]$	53.61	93.17	57.98	80.69	62.77	65.88	67.41	46.59

3.6. Required concentrator material to build CPV with small and large

SAC

The material required to build a CPV system with two different receiver sizes has been calculated to a PV area of (640 mm X 640 mm). The CPV with small concentrator consists of

169 (N) concentrators with a receiver area of 50 mm X 50 mm each, while the CPV with large concentrator consists of 4 concentrators with a receiver area of 315 mm X 315 mm each. The two concentrator sizes have the same concentration ratio ($GCR = 2$) and side angle ($\psi = 35^\circ$).

Figure 3-21 shows schematic diagram with dimensions for the two CPV systems using small and large SAC.

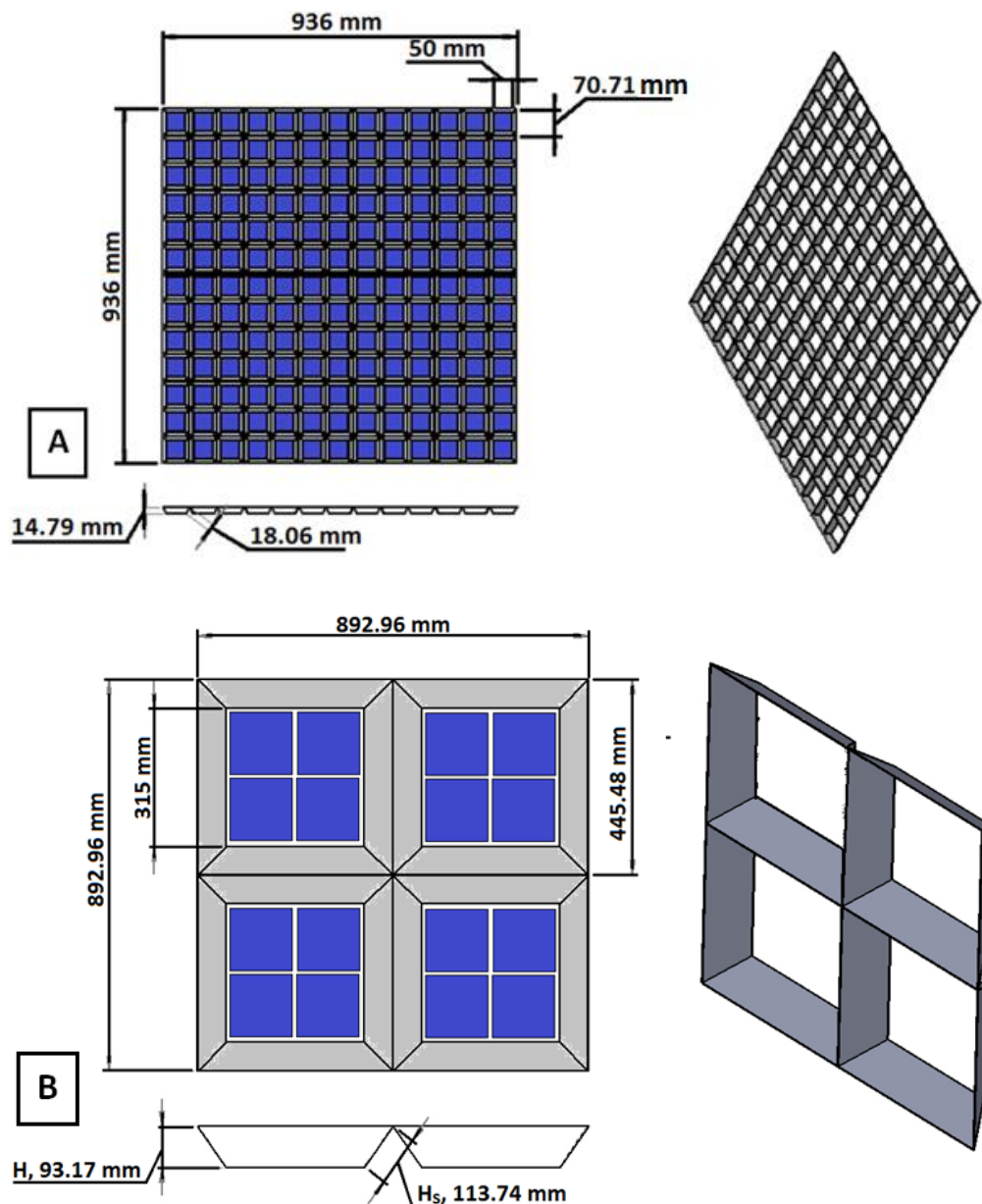


Figure 3-21 Schematic diagram with dimensions for the two CPV systems using: A – small and B – large SAC.

Table 3-7 lists the concentrator dimensions and material needed for small and large SAC by unit area. From **Table 3-7**, although large SAC is relatively higher than the small SAC, the total reflective material required to build such CPV using large SAC is less than that when using small SAC.

Table 3-7 Concentrator dimensions and material needed for small and large SAC by unit area.

SAC	Small [N=169]	Large [N=4]
Receiver Area	0.05m X 0.05 m	0.315 m X 0.315 m
Inlet Aperture Area	0.071 X 0.071	0.445 X 0.445 m
Concentrator Height, H	0.01479 m	0.09317 m
Concentrator Slant Height, H_s	0.01806 m	0.11374 m
Side Area, A_{SIDE}	0,00109 m ²	0.0432 m ²
Concentrator Area, A_{CONC.} (A _{SIDE} X 4)	0.00436 m ²	0.173 m ²
CPV concentrator area, (A _{CONC.} X N)	0.73684 m ²	0.690 m ²

3.7. Conclusions

Mathematical modelling of optical performance was performed using small scale 3D flat sided concentrators with four different inlet and exit aperture configurations, followed by a comparison with OptisWorks ray tracing software. The four geometries are: Square Aperture Concentrator, SAC, Circular Aperture Concentrator, CAC Hexagonal Aperture Concentrator, HAC and Octagonal Aperture Concentrator OAC. Good agreement was obtained between the mathematical model and ray tracing software results.

Results of surface reflectivity effect on concentrator optical performance showed an increase in the optical efficiency using materials with higher reflectivity for all geometries

investigated. On the other hand, investigating the effect of gap distance between the receiver and the concentrator has shown that increasing the gap decreases the optical performance, but CAC seem to have less sensitivity to gap for the dimensions used until 4 mm.

Incidence angle has an effect on the optical performance of all geometries with the same trend, in which the optical efficiency decreases with the increase of the rays' incidence angle. But this effect varies with concentration ratio where lower GCR accepts wider range of incidence angles. For instance, concentrator with GCR 2 accepts rays with incidence angles up to 75° , making it more suitable to systems without tracking, while concentrator with GCR6 accepts rays only with incidence angles up to 30° , which should work better with tracking system.

Flux distribution analysis at GCR6 showed that SAC has best uniformity among other geometries with received flux σ value of 629 W/m^2 and CV of 0.16, followed by HAC with σ value of 1246 W/m^2 and CV of 0.29 then OAC with σ value of 1418 W/m^2 and CV of 0.34. While the worst case was the CAC with σ value of 4582 W/m^2 and CV of 1.1, due to the highly concentrated flux at the centre and little flux is distributed on the rest of receiver area.

SAC geometry was chosen for larger scale concentrator among other geometries for the following reasons: Good optical performance although other geometries have higher efficiency at the same side angle, but performance can be increased by using smaller side angle as shown in results presented in section 3.4.1. Better flux uniformity depending on the results of standard deviation among the other geometries, and easier in fabrication than other geometries which are more complicated and may need special equipment.

Large SAC analysis of incidence angle showed concentrator with smaller side angle is more flexible to tracking system, but with greater height and consequently more concentrator

material needed. On the other hand, concentrator with smaller W/L ratio is less effected by the incidence angle and a significant reduction in concentrator height, H in the case ψ_{Long} , specially at W/L = 0.25 with H = 46.59 mm compared with the case of ψ_{short} that H = 186.34 mm.

CHAPTER 4: THERMAL MODELLING OF CPV/T SYSTEM

4.1. Introduction

In this chapter, CPV/T system is thermally evaluated using COMSOL Multiphysics FEA software. A full CPV/T system assembly with SAC developed in chapter three is modelled at three different geometric concentration ratios of 2, 4 and 6. An aluminium cooling duct was modelled in COMSOL with five different flow arrangements and various water inlet temperature. These duct designs were analysed in terms of module temperature and outlet water temperature as well as temperature distribution to determine the impact of flow arrangement on CPV/T system. As this study investigates active cooling using water as the coolant fluid, a number of water flow velocities are used to investigate the effect of flow velocity/rate on maintaining the module at the desired operating temperature range. Moreover, the pumping power needed for the investigated flow velocities/rates is considered.

4.2. Theory and governing equations

In modelling CPV/T system, all modes of heat transfer are considered including conduction, convection and radiation. Conduction heat transfer occurs through the PV module structure from the top surface of the PV module to the inner surface of the cooling duct. Convection heat transfer is from the CPV/T system to the surroundings by natural convection and the cooling fluid by forced convection. On the other hand, a long-wave radiation heat transfer is from the PV module surface to the surroundings [188]. Steady state conduction heat transfer through CPV/T system solid structure is given by the fourier's law [189], as:

$$Q_{cond} = -k. A. \frac{\Delta T}{\Delta x} \quad (W) \quad (4.1)$$

Where k is the thermal conductivity (W/(m.K)) of the material, A is the cross-sectional area (m^2), $\Delta T/\Delta x$ is temperature (K) gradient through the material thickness (m).

Part of the solar energy transformed in the PV cells to heat is dissipated from the external CPV/T system to the environment through surfaces, by natural or forced convection heat transfer as given by Newton's law of cooling [190]:

$$Q_{conv.} = h. A. \Delta T \quad (4.2)$$

Where, $Q_{conv.}$, is the convection heat transfer rate in Watts, h is the convection heat transfer coefficient, A is the external surface area of the CPV/T system exposed to the ambient, ΔT is the temperature difference between PV module and the ambient air.

Radiation heat transfer to the environment is given by the following equation [188, 191]:

$$Q_{rad.} = \varepsilon. \sigma. (T_c^4 - T_a^4) \quad (4.3)$$

Where, $Q_{rad.}$ is the radiation heat transfer rate in Watts, ε is the emissivity of material and σ the Stefan–Boltzmann constant, T_c is module temperature and T_a is the ambient temperature.

COMSOL Multiphysics solves numerically heat transfer using the above correlations to all surfaces at any position (vertical, horizontal or inclined), together with Navier-Stokes equations (that govern the fluid motion) as conjugate heat transfer model.

For incompressible fluid flow and constant cross-sectional area, the continuity (4.4), momentum (4.5), and total energy flux (4.6) equations are as follows [192]:

$$\nabla. (\rho u) = 0 \quad (4.4)$$

$$\rho u \cdot \nabla u = -\nabla p + \nabla \cdot (\mu(\nabla u + (\nabla u)^T)) \quad (4.5)$$

$$e_{tot} = \rho u E_0 - k \nabla T + q_{rad} - \sigma u \quad (4.6)$$

Where, ∇ , ρ , u , p , μ , E_0 are vector differential operator, density, vector velocity, pressure, dynamic viscosity, total internal energy and σu is the convective stress energy, respectively.

In the case of stationary study, the energy equation is written as:

$$\int_{\partial\Omega} e_{tot} \cdot n dS = \int_{\Omega} Q_{ext} dV \quad (4.7)$$

The conduction – convection heat transfer for water cooling of the CPV/T system is solved by the following equation (4.8) [193]:

$$\rho C_p u \cdot \nabla T = \nabla \cdot (k \nabla T) \quad (4.8)$$

4.3. CPV/T system setup for thermal analysis

4.3.1. Cooling system configurations

Figure 4-1 shows five different cooling system configurations with size of 330x330x10mm that have been thermally simulated using COMSOL Multi-physics software in order to develop an effective cooling system for the CPV/T system. The cooling system consists of 11 Aluminium rectangular channels with 30 mm × 10 mm × 330 mm as width, height and length and 1.5 mm wall thickness. These channels are fitted with inlet and outlet headers to distribute the water flow to the channels. Five different flow arrangements were modelled including: 1- flat inlet and outlet manifold duct with 10 mm width (W), 2- flat inlet and outlet manifold

duct with 30 mm width, 3- slopped inlet and outlet manifold duct (30/10 width), 4- slopped inlet (30/10 width) flat outlet manifold (30 mm width) and 5- U- type duct.

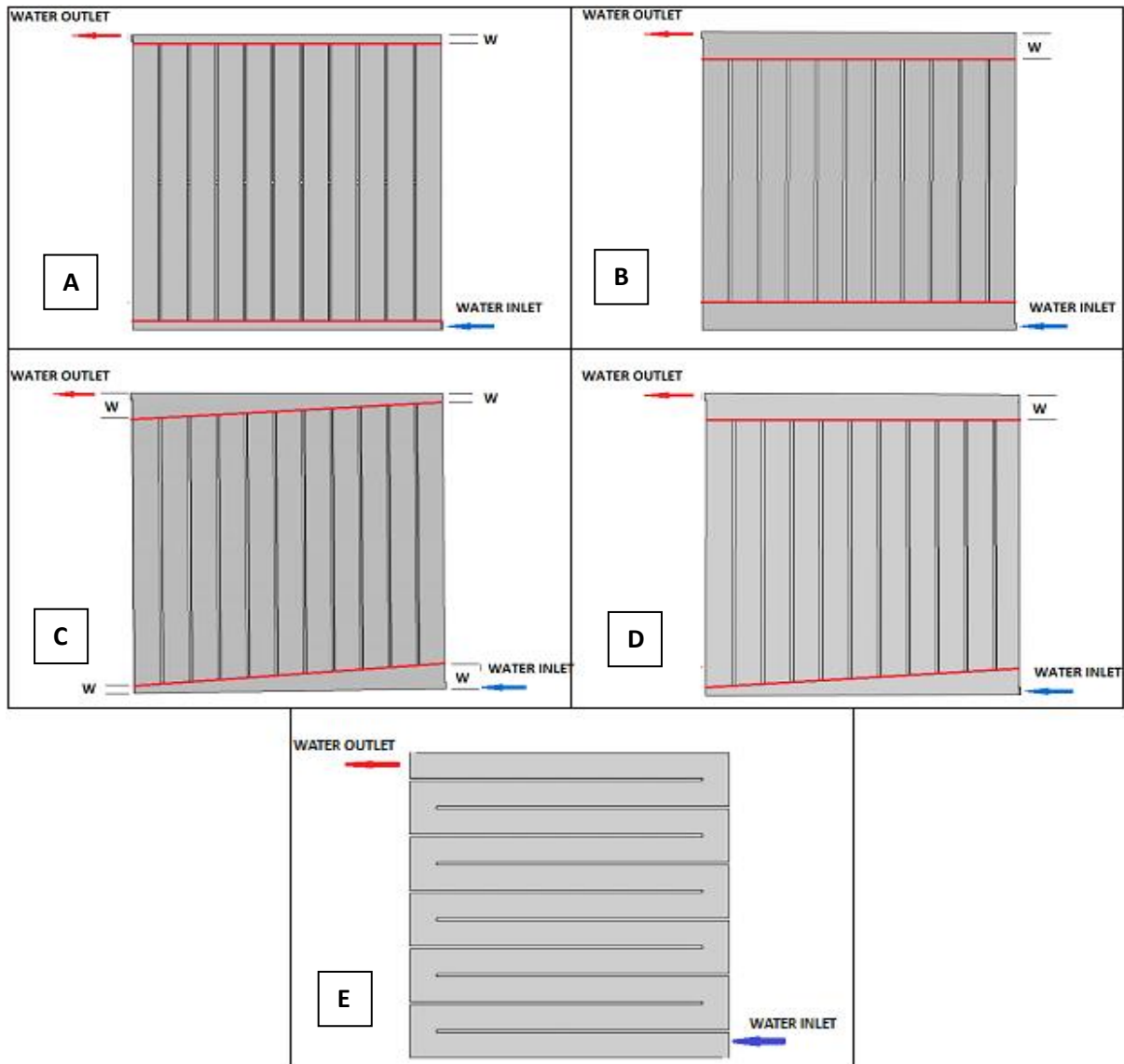


Figure 4-1 Cooling duct designs for CPV/T system: A-Flat inlet and out manifold (W=10 mm), B-Flat inlet and out manifold (W=30 mm), C-Slopped inlet and out manifold (W=30/10mm), D-Slopped inlet and flat outlet manifold and E- U-type duct.

4.3.2. CPV/T system geometry

CPV/T system geometry shown in **Figure 4-2** was drawn using Solidworks software. It consists of cooling system (including water domain), SAC concentrator (aluminium based) and PV module. PV module consists of (330 x 330 x 4 mm) PV glass front laminates which were divided into 21 divisions (15.714 x 330 x 4mm) in order to get more detailed flux distribution on the PV module surface and close to the imported flux distribution from OPTISWORKS software. The encapsulation ($t \approx 1\text{mm}$) includes 4 square polycrystalline 156mm x 156mm x 0.2mm, (IM156B3 from MOTECH) embedded in EVA (ETIMEX® - EVA film VISTASOLAR® - fast cure, transparent) and a back sheet (AKASOL® PVL 2-1000V) is attached to the PV module from the back.

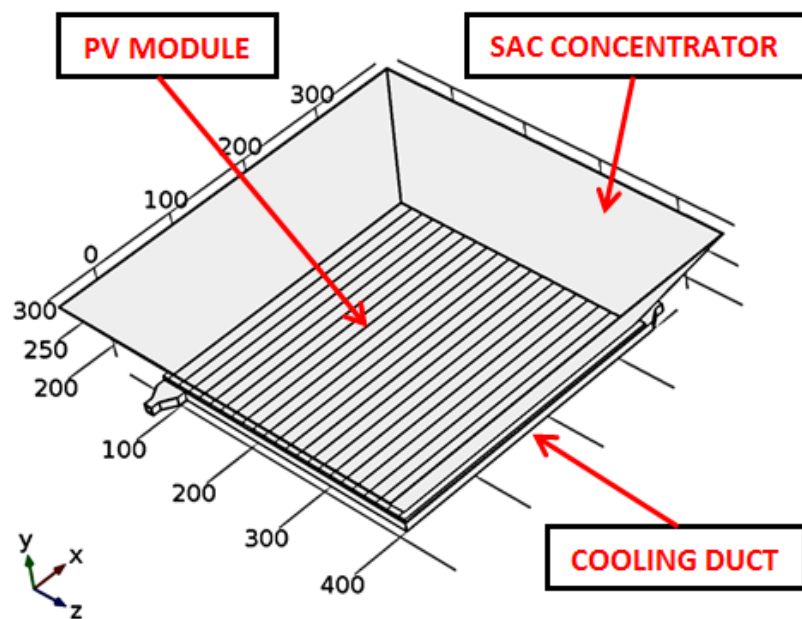


Figure 4-2 CPV/T system geometry

4.3.3. CPV/T system material properties

Material properties of each system component were defined in Comsol multi-physics in order to match the real CPV/T system. Cooling duct and SAC concentrator materials were defined

as Aluminium 6063-T83, water domain as water and PV glass as Quartz, PV cells as Poly silicon from the material library, while other materials such as Ethylene-vinyl acetate (EVA) and BACK sheet material were imported to Comsol software. **Table 4-1** lists the main thermal properties of the CPV/T system components.

Table 4-1 Thermal properties of the CPV/T system components

Component	Emissivity	Thermal conductivity (K) [W/(m*K)]	Heat capacity (C_p) [J/(kg*K)]	Density (ρ) [kg/m ³]	Thickness (t) [mm]
Cooling duct (Al 6063-T83)	0.09	201	900	2700	10
Thermal paste (HTSP)	0.9	3	1000	3000	0.6
PV glass (quartz)	0.91	1.1	480	2200	4
EVA	0.9	0.34	1400	950	0.3
PV cell (poly)	0.85	130	700	2329	0.2
EVA	0.9	0.34	1400	950	0.3
Back sheet	0.9	0.2	1250	1200	0.5

4.3.4. Flux distribution from OptisWorks

The radiation flux (q_{rad}) values (W/m²) were exported from OptisWorks software for PV module results for every 15.714 mm distance on the receiver, and imported to COMSOL software for every section. **Figure 4-3** shows flux distribution for GCR 2 from OptisWorks software and the imported to COMSOL at the centre of the PV module.

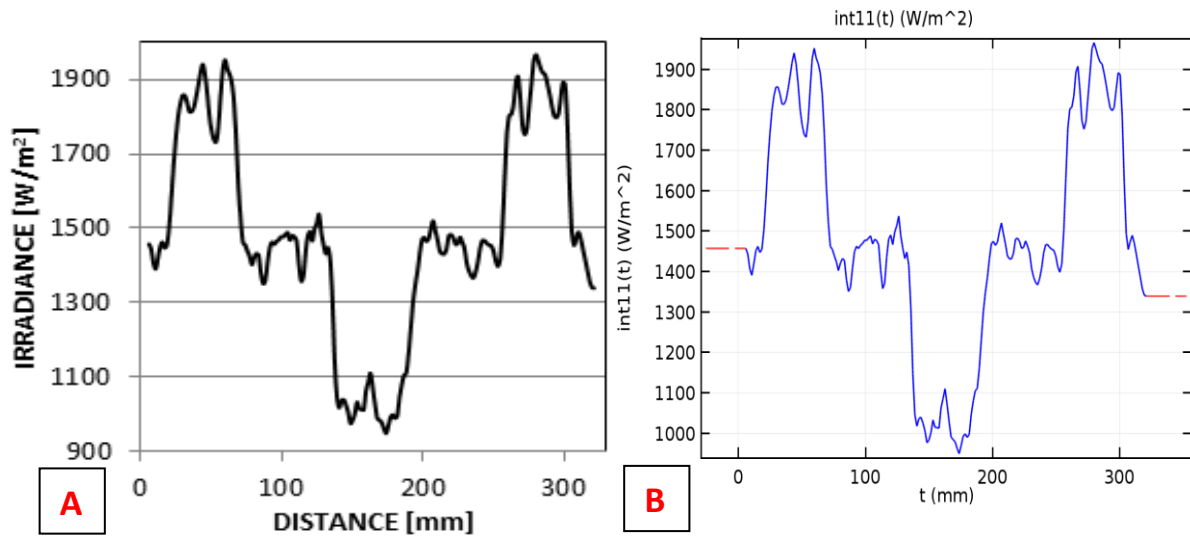


Figure 4-3 Flux distribution at the centre line of PV module: A- exported from OptisWorks software and B- imported to COMSOL software

On the other hand, the amount of flux converted by the PV cell/module into electrical energy is taken into account. This is done either: by using PV module electrical conversion efficiency from experimental test or by calculating the PV cell/module electric conversion efficiency at different cell/module temperatures, and then subtracting it from the radiation flux, which is exported from OPTISWORKS software to get the net heat flux (q_{heat}). PV electrical conversion efficiency is calculated using the following equation [172, 194]:

$$\eta_{\text{pv}} = \eta_{\text{ref}} - [\beta_{\text{thermal}}(T_c - T_{\text{ref}})] \quad (4.9)$$

Where η_{pv} is the PV electrical conversion efficiency as a function of thermal coefficient, β_{thermal} , which is either taken directly from PV panel datasheet, or calculated from the maximum power output at two different temperature values, T_{ref} is the reference temperature (298.15 °K) and T_c is the PV cell/module surface temperature which is taken from COMSOL software. Then, heat flux (q_{heat}) is calculated by the following equation [195]:

$$q_{\text{heat}} = q_{\text{rad}} \times (1 - \eta_{\text{pv}}) \cdot \text{ACR} \quad (4.10)$$

Where, q_{rad} is the radiation flux and ACR is the actual concentration ratio of the concentrator.

4.3.5. CPV/T system meshing sensitivity

Different mesh sizes were investigated for mesh sensitivity on thermal results normal, fine and finer mesh sizes and PV module average temperature (T_c) was compared. Mesh shown in Figure 4-4 is a finer element size, Physical-controlled finer mesh size was chosen for the thermal paste layer and PV module, which consists of Tedlar (back sheet), EVA layers, PV cells in the CPV/T system assembly for the reason, that larger size was not working and smaller will take longer time. For the remaining parts of the system (cooling duct, water domain and the top glass of the PV), a run for three different mesh sizes was carried out to determine the effect of mesh size on the results. The number of elements for each mesh is 2681867, 2723328 and 3694621 for normal, fine and finer meshing sizes, respectively.

As seen in **Figure 4-5** that no significant difference in thermal results with the change of meshing size from normal to finer. Thus normal mesh size was used in investigating the PV module and cooling water outlet temperatures of the CPV/T system parts including water domain, cooling duct, and top glass.

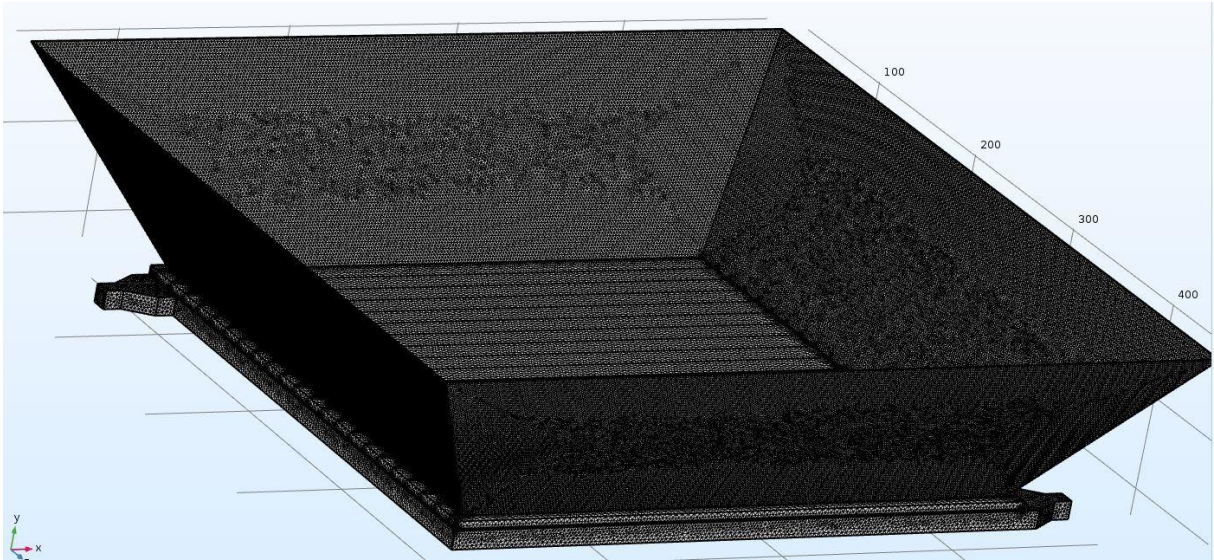


Figure 4-4 Solving mesh used with CPV/T system thermal model

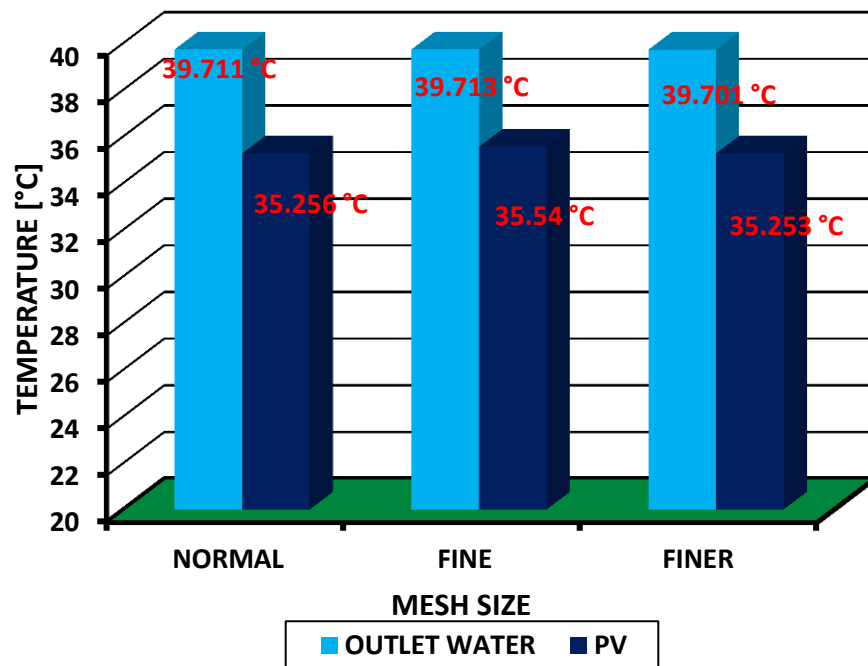


Figure 4-5 PV cells and outlet water temperatures with different mesh sizes

The solver type was kept as default where in solving general linear systems COMSOL will automatically detect the best solver without the need for the user input [196]. Relative tolerance value of stationary solver was set to default value 0.001. Pictorial figures are shown

in **Appendix A** for the conjugate heat transfer thermal model setup, which is a setup for steady state (stationary) heat transfer model with laminar flow type in COMSOL version 5.2a.

4.3.6. CPV/T thermal model assumptions

1. The solar flux imparted on the top active area of CPV/T system, which is the area of the four PV cells including the cells spacing (315mm×315mm).
2. The cooling system is simulated with a uniform flux distribution of 800 W/m^2 (Libya average solar irradiance of the mean day of June), for design comparison, while water flow velocity range is between 0.01 m/s and 0.09 m/s.
3. The solar flux is considered to be imported to the system with its real distribution as it is exported from OptisWorks software after concentration effect with an average of $1000 \text{ W/m}^2 \times \text{ACR}$.
4. All solar flux is converted into heat excluding the amount of flux converted into electricity.
5. CPV/T system is clean and no dust/dirt is on the top surface of CPV/T system affecting the solar flux absorption.
6. Uniform cooling water temperature (20 °C) at the inlet of cooling duct.
7. For the selected tube cross-sectional area and the range of flow rates, the flow is considered fully developed, laminar and incompressible for the cooling water through the cooling duct.
8. CPV/T system surroundings have an ambient temperature ranging from 15 °C to 50°C.
9. CPV/T system is simulated with a range of flow rate from 50 mL/min to 850 mL/min, applied to the cooling water throughout the cooling duct.

10. Normal PV module construction materials are considered and highly conductive thermal paste between the PV module and the cooling duct for good contact purposes.

4.4. Results

4.4.1. Temperature distribution at different cooling system configurations

A primary PV system was attached to the cooling ducts while testing water flow inside the cooling ducts and its effect on temperature distribution. PV system consists of four polycrystalline PV cell, stuck to the cooling duct, using thermal paste (**Table 4-1**). Cooling water flow simulation was carried out using water flow velocity (u) ranging from (0.01 to 0.09 m/s) and irradiance 800 W/m^2 at the top of four PV cells. **Figure 4-6** shows temperature distribution of cooling water domain, with different cooling duct designs and flow velocity of 0.09 m/s. **Figure 4-6-A** shows, the highest cooling water temperature is localised close to the centre of the cooling duct and forming a hotspot, while water with lower temperature goes through the duct outlet. In **Figure 4-6-B** and **C** the hot spot moves up towards the outlet of cooling duct, but still higher temperature is localised opposite the water outlet. In **Figure 4-6-D** the hot spot is close to the cooling duct water outlet. In **Figure 4-6-E**, no hot spot is formed and water temperature uniformly and gradually increases as it goes through duct channels, and reaches its maximum at the duct outlet.

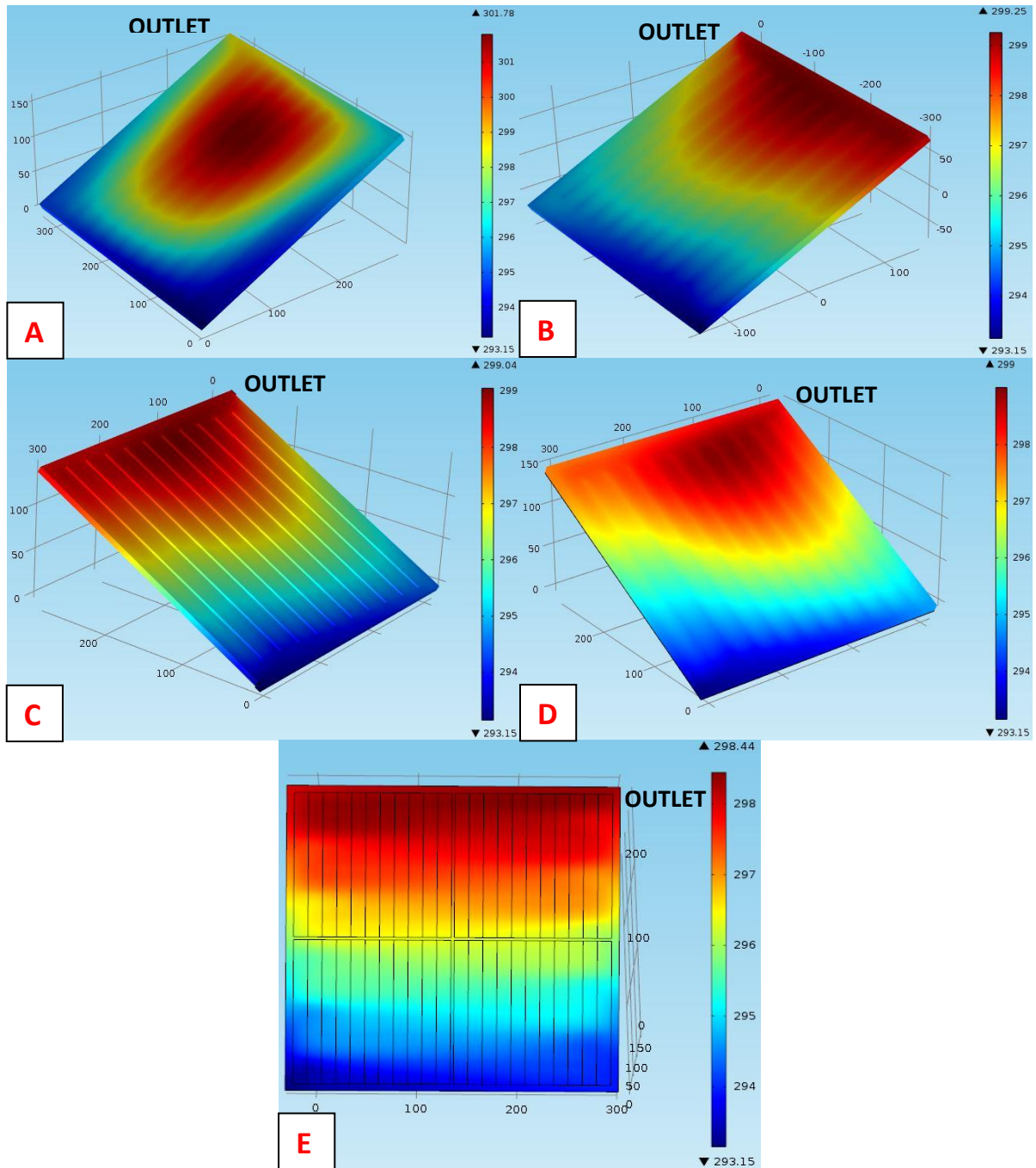


Figure 4-6 Temperature distribution cooling water using different designs of cooling duct at flow velocity of 0.09 m/s. A-Flat inlet and out manifold (W=10 mm), B-Flat inlet and out manifold (W=30 mm), C-Slopped inlet and out manifold (W=30/10mm), D-Slopped inlet and flat outlet manifold and E- U-type duct.

Figure 4-7 shows the outlet temperature of cooling water for the five duct configurations, at different flow velocities ranging from 0.01 to 0.09 m/s. With all configurations, water outlet temperature decreases with the increase of flow velocity, but U-type cooling duct (**E**) has the highest water temperature among other configurations. This means the highest extracted heat from system occurs with U-type design through different flow velocities, where water temperature difference from other designs gets higher with the increase of flow velocity.

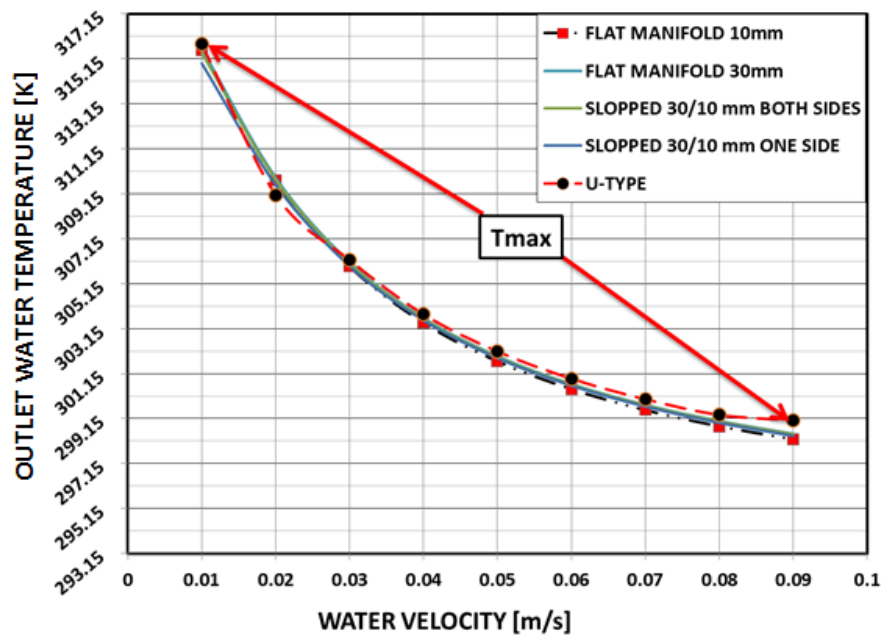


Figure 4-7 Cooling water outlet temperature at the five duct configurations and flow velocities (0.01 – 0.09 m/s)

Figure 4-8 shows the PV cells average temperature with the use of five duct configurations and different flow velocities. Also for the PV cells temperature, with all cooling duct configurations temperature decreases with the increase of flow velocity, and U-type cooling duct configuration has the lowest cells temperature among duct configurations, consequently higher heat is extracted from the system.

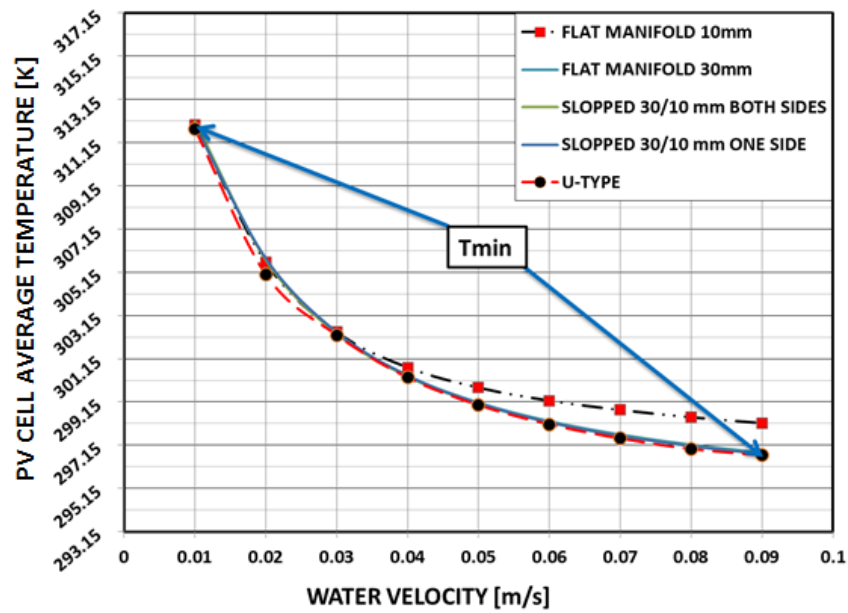


Figure 4-8 PV cells temperature with the use of five duct configurations and flow velocities (0.01 – 0.09 m/s)

From **Figure 4-6** to **Figure 4-8**, U- Type configuration demonstrates the best performance among tested configurations, in terms of cooling water temperature distribution, higher outlet temperature, consequently better heat extraction from PV cells. This configuration was chosen to be used with the CPV system in the thermal analysis.

4.4.2. PV module average temperature

4.4.2.1 PV module average temperature at different flow rates and ambient temperatures

A uniform solar flux of 1000 W/m^2 was applied to the top surface of the PV module with a cooling water temperature of 20°C and changing flow rate of cooling water from 50 mL/min to 850 mL/min, and no concentration effect. While the ambient temperature range of 15°C to 50°C and interval of 5°C was used. **Figure 4-9** shows an increase in PV module average temperature with the increase of ambient temperature, and a decrease in PV module

temperature with the decrease of flow velocity. PV module average temperature is about 53 °C when ambient temperature of 15 °C and no cooling. This temperature increased to reach about 83 °C when the ambient temperature changed to 50 °C which makes temperature difference of about 33 °C between the two cases. While using flow rate of 50 mL/min decreased the PV module temperature to about 33 °C and 42 °C when the ambient temperatures of 15 °C and 50 °C were used, respectively which decreased the difference caused by the ambient temperature to about 11 °C. Increasing the flow rate to 650 mL/min decreased the PV module temperature to about 22 °C and 23 °C, at ambient temperatures of 15 °C and 50 °C and the difference is only about 1 °C and no significant decrease with further flow rate increase.

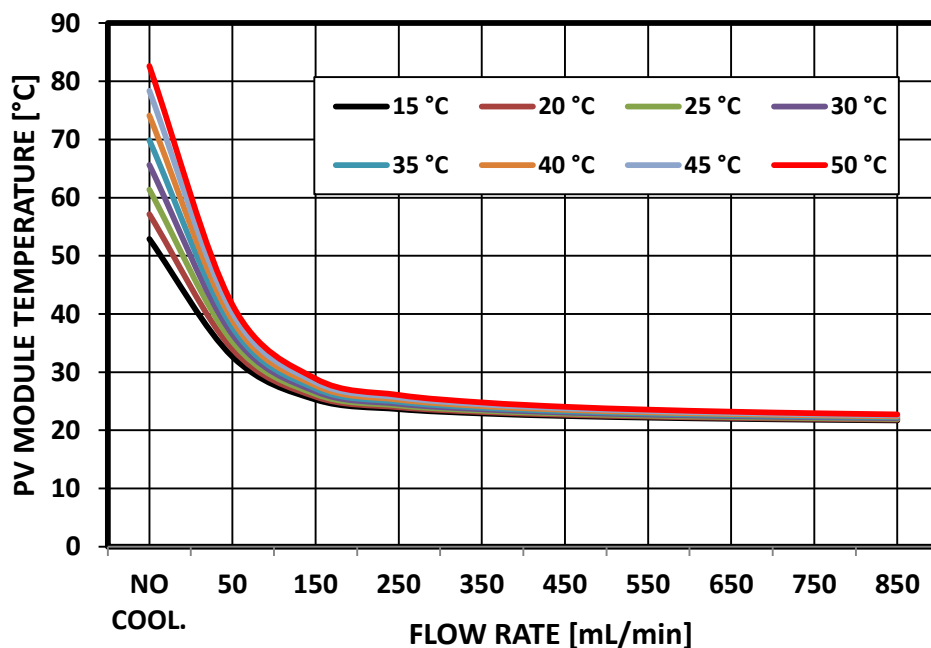


Figure 4-9 PV module average temperature at different cooling water (20 °C inlet temperature) flow rates and ambient temperatures

4.4.2.2 PV module temperature with different concentration ratios

Solar flux of three different geometric concentration ratios was imported to the CPV/T system with simulated SAC flux distribution from OPTISWORKS software. The input solar flux at the inlet aperture of SAC is 1000 W/m^2 at the concentrator inlet aperture, and SAC received flux is then imported to COMSOL software, at geometric concentration ratios of 2, 4 and 6, as well as different ambient temperature ranging from 15°C to 50°C . **Figure 4-10** shows the PV module temperature under concentration, without and with cooling flow rates ranging from 50 mL/min to 850 mL/min , and ambient temperature of 50°C . It is clear that the PV module temperature is increasing with the increase of concentration ratio, while decreasing with the increase of flow rate. At GCR 2, and no cooling PV module temperature increased to about 104°C from about 83°C for PV module without concentration. Using flow rate of 50 mL/min caused a reduction in PV module temperature to reach about 53°C . Increasing flow rate to 550 mL/min PV module temperature drops to about 25°C and no significant decrease with higher flow rates. With GCR of 4, and no cooling, the PV module temperature increased to about 138°C . Using flow rate of 50 mL/min caused a significant reduction in PV module temperature to be about 74°C . Increasing flow rate to the maximum used (850 mL/min) the PV module temperature dropped to about 27°C . For the case of GCR6, PV module temperature reached 169°C , at no cooling, while using flow rate of 50 mL/min decreased the PV module temperature to about 94°C , which is higher than the PV module maximum working temperature (85°C), and increasing flow rate to 850 mL/min decreases the PV module temperature to about 30°C .

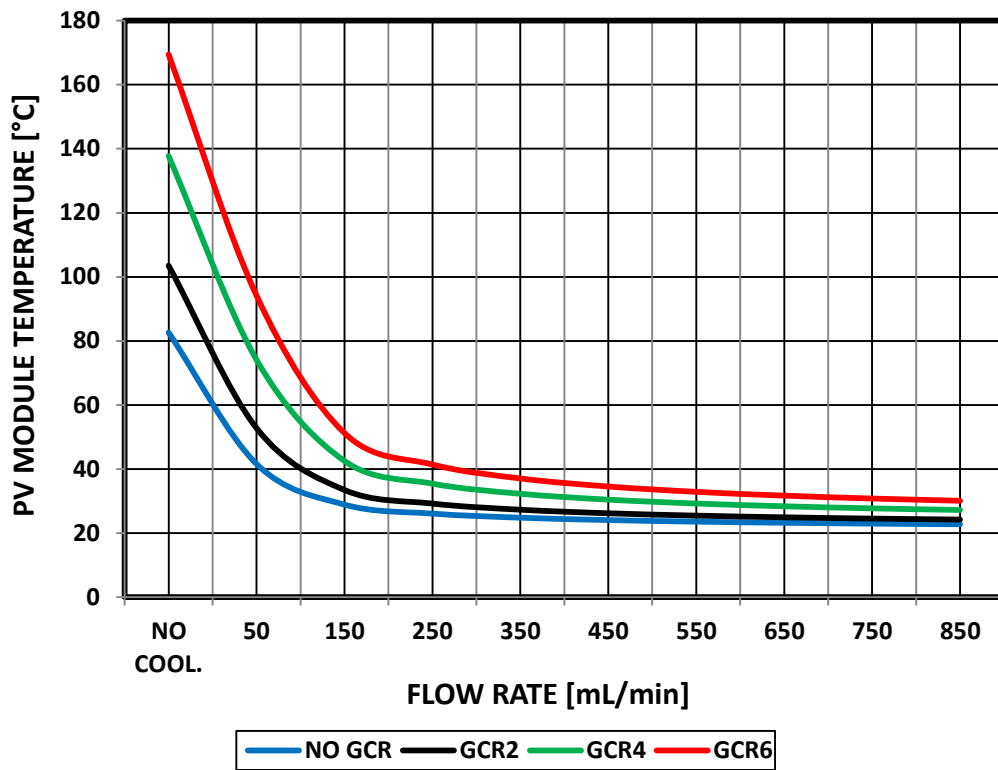


Figure 4-10 PV module temperature with different concentration ratios and cooling flow rates
($T_a = 50\text{ }^{\circ}\text{C}$)

4.4.2.3 PV module temperature distribution under concentration and different flow rate

Figure 4-11 shows the CPV/T system under simulation with geometric concentration ratio of 2, ambient temperature of $25\text{ }^{\circ}\text{C}$, without cooling and with different cooling flow rates. In **Figure 4-11-A** where no cooling is applied the temperature distribution take the flux distribution with higher temperature at the higher concentration regions and temperature difference of about $30\text{ }^{\circ}\text{C}$. Using cooling flow rate of 50 mL/min , the temperature distribution varies (**Figure 4-11-B**) from the no cooling case that takes a gradient (cold to hot) distribution where system has colder regions close to the cooling water inlet, and gets hotter as the water flows through the duct channels and the hottest region is close to the cooling duct outlet. With higher flow rates, temperature distribution gets back to the concentration distribution, but with

lower temperature difference, as shown in the cases where the flow rate was 450 mL/min and 850 mL/min the temperature difference was 14 °C and 10 °C, respectively.

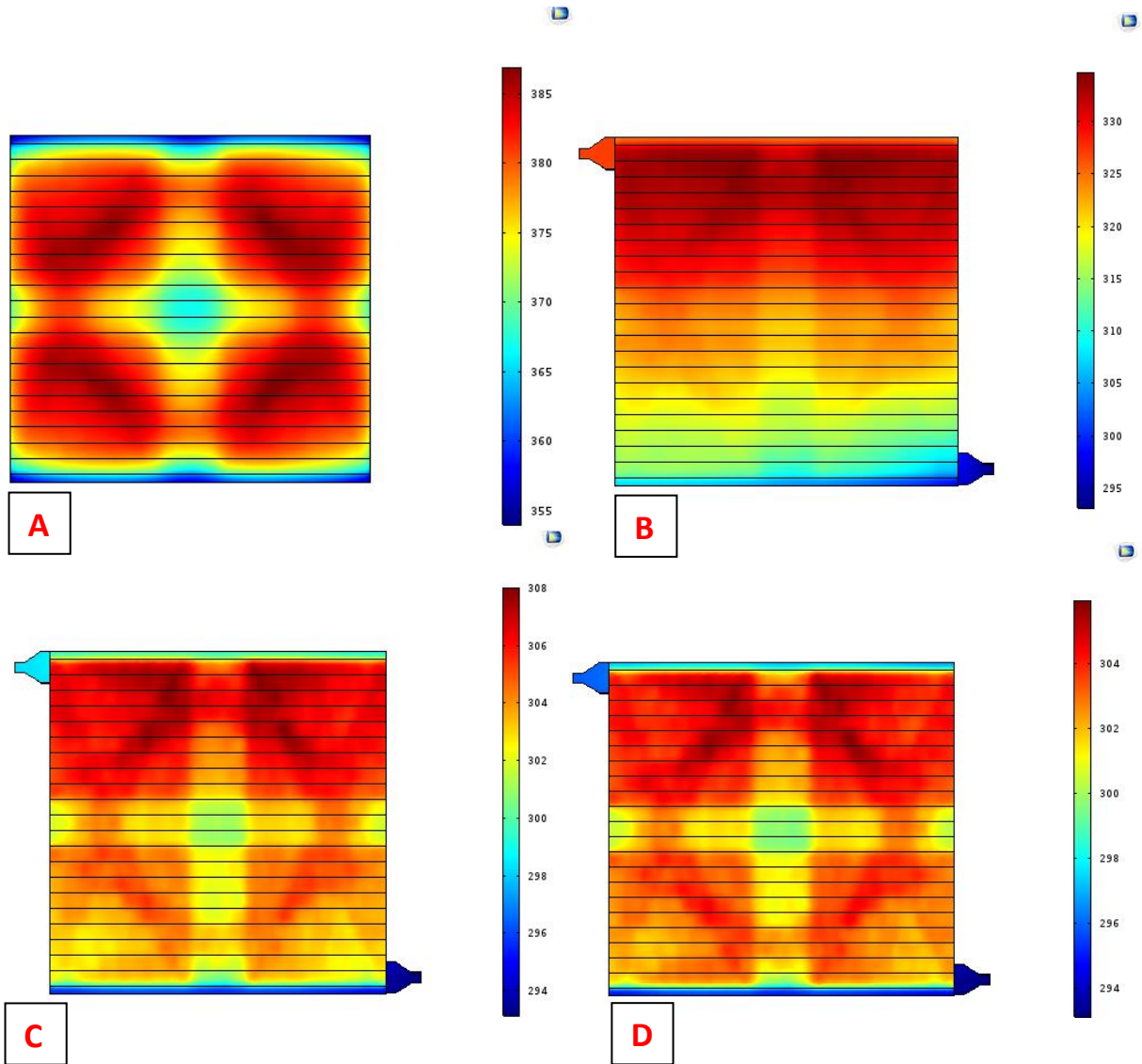


Figure 4-11 CPV/T system temperature distribution under concentration and cooling effect (GCR = 2): A- no cooling, B- flow rate of 50mL/min, C- flow rate of 450mL/min and D- flow rate of 850mL/min ($T_a = 25\text{ }^{\circ}\text{C}$)

4.4.3. Average outlet temperature of cooling water under concentration

Figure 4-12 shows the average water temperature at the cooling duct outlet, at geometric concentration ratios of 2, 4 and 6. Water cooling used at different flow rates ranging from 50 mL/min to 850 mL/min with interval of 100 mL/min, and ambient temperature of 50°C. It is clear that the average water temperature at the cooling duct outlet is also increasing with increase of geometric concentration ratio and decreasing with the increase of flow rate. Using SAC with GCR of 2, water temperature at the outlet reaches about 63 °C, at flow rate of 50 mL/min, which is higher than that of PV module without concentration (about 49 °C), while decreased to about 25 °C, at flow rate of 550 mL/min and no significant drop with higher flow rates used. Water temperature increased at the same flow rate (50 mL/min) with the use of SAC with GCR 4, to reach about 90 °C. This temperature decreased to about 26 °C at flow rate of 850 mL/min. Cooling water outlet temperature increased further using SAC with GCR 6, to reach its maximum of about 115 °C at the lowest flow velocity used (50 mL/min), and decreased till it reached about 28 °C at maximum flow rate used (850 mL/min). It is clear from **Figure 4-10** and **Figure 4-12** that the PV module temperature takes the same trend as the water cooling temperature with the change of flow rate and concentration ratio.

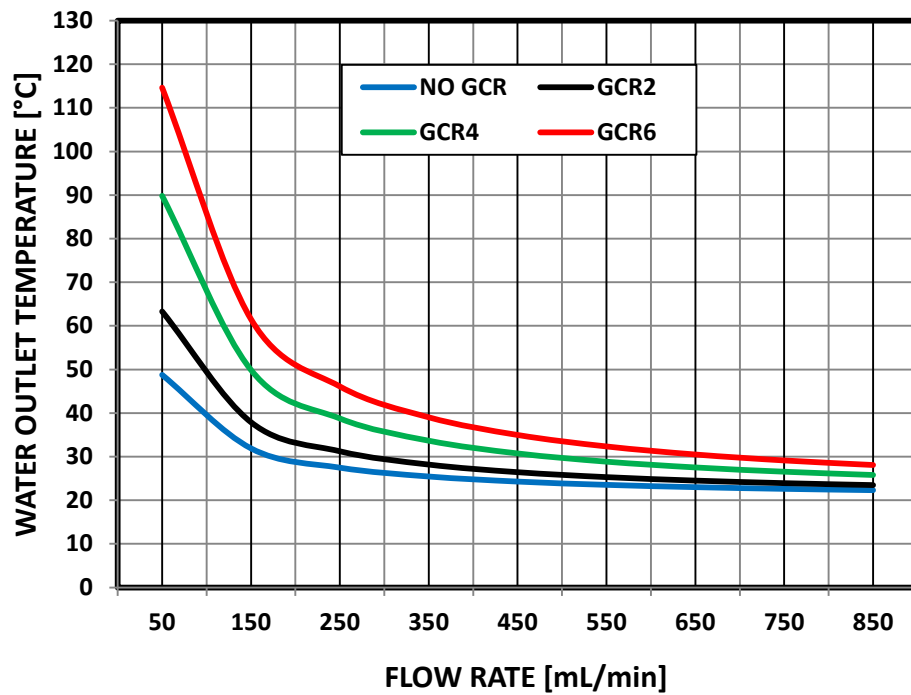


Figure 4-12 Average cooling water outlet temperature with different concentration ratios

4.4.4. CPV/T system thermal power output at different operating conditions

Figure 4-13 shows the thermal power output of the PV/T system under different ambient and flow velocity values, and where there is no concentration effect. The thermal power output of the PV/T system varies with the variation of operating conditions, where the maximum power output value achieved is about 140 W at maximum flow rate of 850 mL/min and maximum ambient temperature of 50 °C. The thermal power output decreased with the decrease of flow rate and ambient temperature to be about 59 W at minimum flow and ambient temperature used (50 mL/min and 15°C). Also it is noticed that the thermal power increased with a fixed amount with the increase of ambient temperature, while higher increase with flow rate from 50 mL/min to 150 mL/min and then the increase will be with lower amount taking the linear trend for the rest of flow rates.

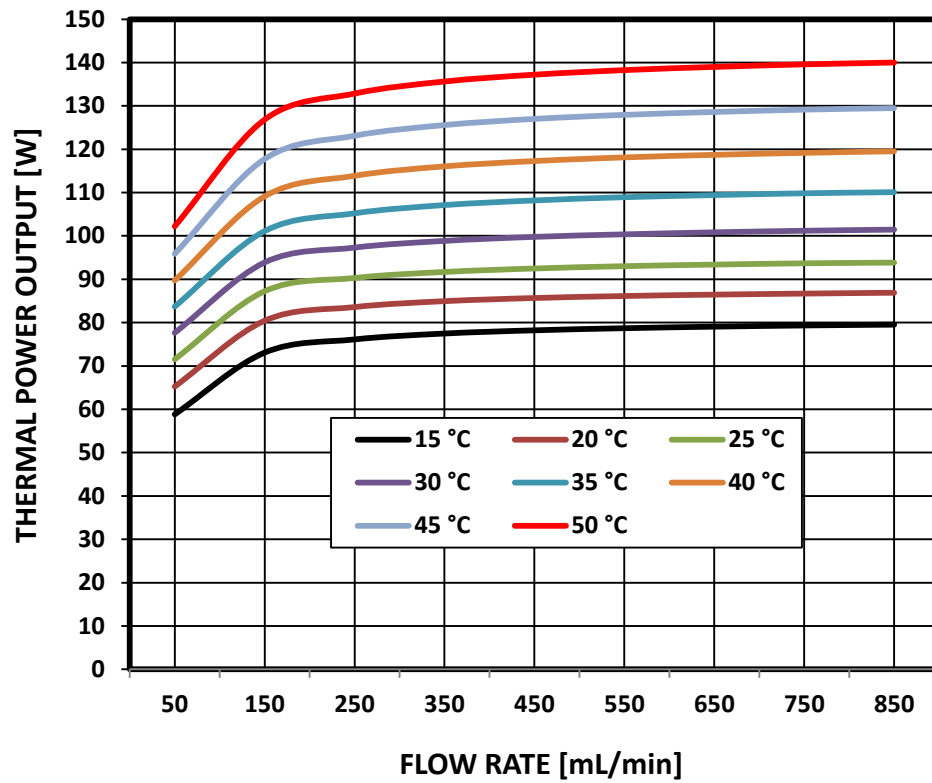


Figure 4-13 PV/T system power output at different flow rates and ambient temperatures

In **Figure 4-14**, the thermal power output of CPV/T system with different concentration ratios was compared with the PV/T system at different cooling water flow rates and ambient temperature of 25 °C. **Figure 4-14** also shows variation of thermal power output with the variation of concentration ratio where the maximum power output value is achieved at maximum flow rate (850 mL/min) and maximum concentration ratio used (GCR 6), while the minimum value is at minimum flow rate (50 mL/min) and minimum concentration ratio used (GCR 2). The thermal power achieved with low temperature could be used directly for domestic heating, while power with higher temperature is useful for other applications that require high temperatures.

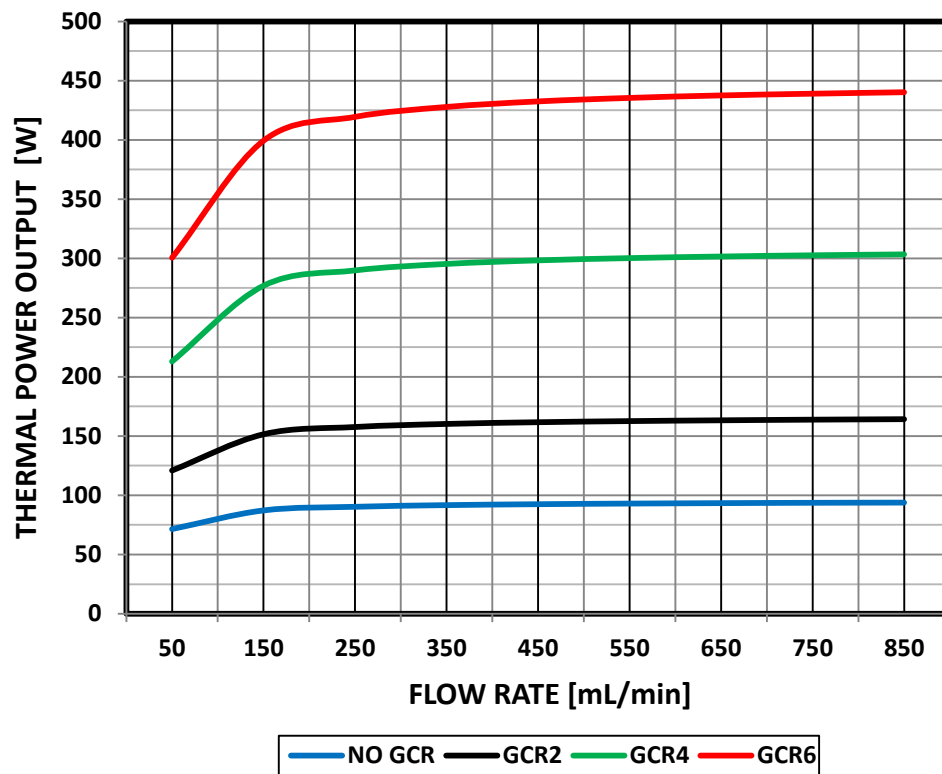


Figure 4-14 CPV/T system power output at different flow rates and ambient temperature values

4.4.5. Pumping power for different flow rates

Using water cooling to maintain PV at a desirable working temperature, needs additional power to circulate water through the cooling system. This power should be determined to know how much the system consumes, consequently determining the method of circulating the cooling water. Pressure drop in the CPV/T system at horizontal and 27.02 ° inclination orientations has been extracted from COMSOL, and then the pumping power was calculated using the following equation [197]:

$$\text{Pumping Power} = V_w * \Delta P \quad (4.11)$$

Where ΔP : is the pressure drop, which is the water pressure difference between the inlet and outlet of the cooling duct. The outlet pressure is assumed to be 1 atmospheric pressure

(1.01325×10^5 Pa) and the inlet pressure is obtained from COMSOL software. Pumping efficiency is not considered in this work. **Figure 4-15** shows the increase of pressure drop with the increase of flow rate and the corresponding pumping power required for the flow rate range used. It is clear that the pumping power required to compensate the pressure drop in the cooling system is very small even with the maximum flow rate (0.022 W) which is available in domestic use and no additional pumping arrangement is needed.

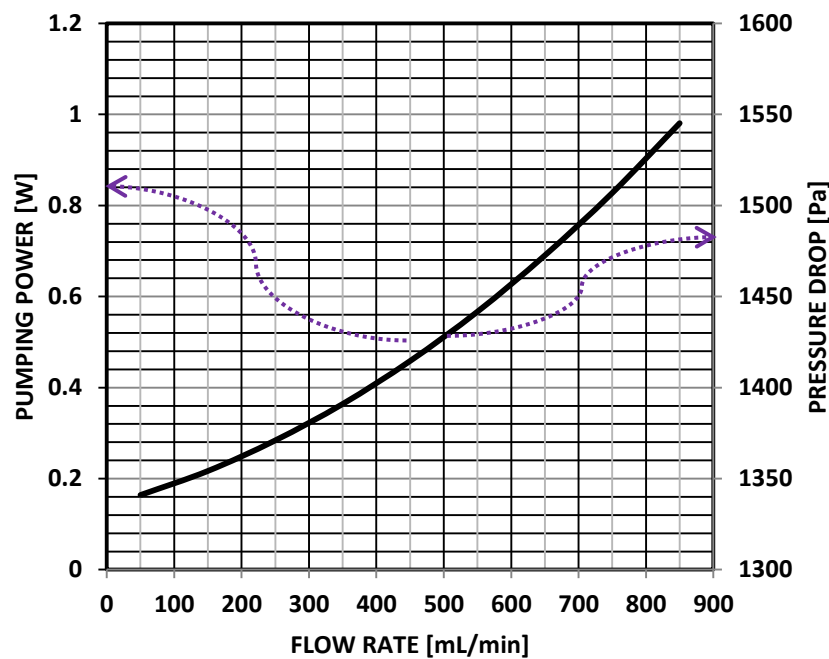


Figure 4-15 Change of pressure drop and pumping power with flow rate

4.5. Conclusions

Thermal simulation of the CPV/T system was run using COMSOL multi-physics software to investigate the system temperature under different operating conditions. These conditions include changing concentration ratio of the Squared Aperture Concentrator (SAC) to values of GCR 2, 4 and 6, changing ambient temperature in a range of 15 °C to 50 °C with an interval of 5 °C and changing cooling water flow rate in a range of 50 mL/min to 850 mL/min with an interval of 100 mL/min. Investigation was run under a solar flux of 1000 W/m² taking into

account the part of solar flux converted into electricity. Thermal investigation results show that PV module temperature significantly increased with the increase of solar flux concentration and less increased with the increase of ambient temperature. Active water cooling is very important and has a significant effect on PV module temperature that as the water flow rate increased the PV module average temperature decreased. Likewise, cooling water temperature increased with the increase of flux concentration and ambient temperature while decreased with the increase of flow rate.

The thermal power output of the PV/T system varied with the variation of operating conditions, where the maximum power output value is achieved at maximum flow rate used (850 mL/min) and maximum ambient temperature used (50 °C) within the range tested. For CPV/T system the thermal power output also varied with the variation of operating conditions that the maximum power output value is achieved at maximum flow rate (850 mL/min) and maximum concentration ratio used (GCR 6), while the minimum value is at minimum flow rate (50 mL/min) and minimum concentration ratio used (GCR 2). These values of power output generated by the this design, shows clearly the potential of such system to be tested experimentally to validate the simulation results under real operating conditions.

CHAPTER 5: EXPERIMENTAL SETUP

5.1. Introduction

In this chapter, an experimental setup for indoor and outdoor testing is presented. The indoor experimental setup was used to investigate the optical efficiency of the small scale Square Aperture Concentrators (SAC) with low GCR values of 4, 6, 8 and 10, small scale Hexagonal Aperture Concentrators (HAC) with low GCR values of 2, 4, 6, 8, 10 and the large scale Square Aperture Concentrator with GCR value of 2. The outdoor experimental setup was used to test the large scale square aperture concentrators with GCR 2, 4 and 6. The effect of geometric concentration ratio (GCR) of the small and large SAC concentrators on the electrical output of PV cell/module was investigated through measuring the radiation flux on the PV, I-V curve and electrical power output using various cooling techniques. Detailed description of the experimental setup including fabrication of the designed CPV/T system and calibration of measuring instruments are included.

5.2. Classification of indoor radiation source

The indoor radiation source is a D'Artagnan follow-spot light (10° to 25° zoom angle) with 2500W Metal Halide arc lamp. According to the Standard Specification of Solar Simulation for Photovoltaic Testing ASTM E927 – 10 [198], the radiation source to be used as a solar simulator should be within three classes namely: class A, class B and class C as shown in Table 5-1. These classes are determined using three main tests including: light spectral match, spatial non-uniformity and temporal instability. These tests were performed to classify the indoor light source.

Table 5-1 ASTM E927 – 10 classifications of solar simulators for photovoltaics [198]

Classification	Spectral Match (each interval)	Temporal Instability	Irradiance Spatial Non-Uniformity
Class A	0.75–1.25	2%	2%
Class B	0.6–1.4	5%	5%
Class C	0.4–2.0	10%	10%

To measure the spectral match of the solar simulator light, the light spectrum should be compared to the sun light spectrum by comparing the irradiance distribution as a percentage of the total irradiance through specific wavelengths defined by ASTM standards. An Ocean USB2000+ Series spectrometer shown in **Figure 5-1** was used in this work and connected to the computer. USB2000+ covers the light source spectrum that comes within the wavelength range of 200 nm to 1100 nm, and the optical resolution ranges from ~0.1 nm to 10.0 nm. The simulator light spectrum was measured at three different points, one at the centre of the spot light, one at the middle between the centre and the edge of the spot light and one at the edge of the light spot.

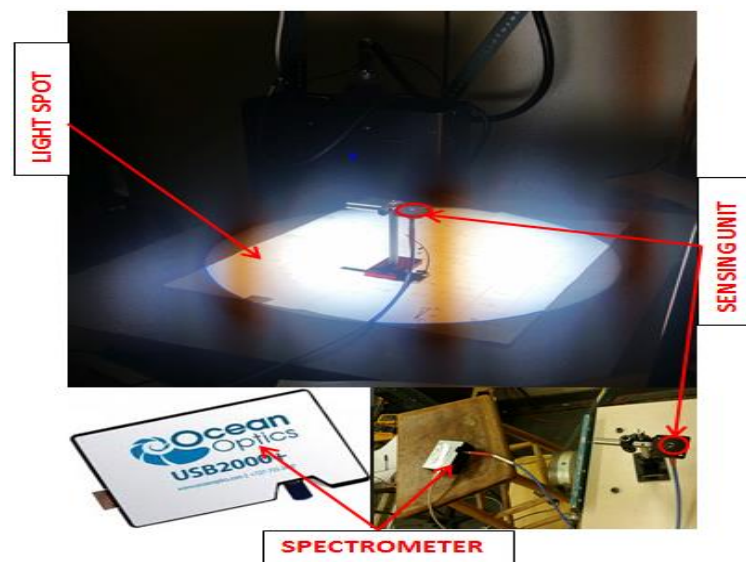


Figure 5-1 Spectral match test setup

Data was compared with standard spectrum and classification was determined to each position independently as shown in **Table 5-2 to Table 5-4**.

Table 5-2 Simulator Light spectrum distribution at the centre of the light spot and match with the standard spectrum distribution

Standard Spectrum		Simulator Light spectrum at the centre		
Wavelength (nm)	Irradiance performance	Irradiance performance	match	classification
400-500	18.4	21.68756	1.178672	A
500-600	19.9	37.64515	1.891716	C
600-700	18.4	23.88761	1.29824	B
700-800	14.9	12.6773	0.850825	A
800-900	12.5	3.458518	0.276681	out of standard
900-1100	15.9	0.643852	0.040494	out of standard
	100	100		

Table 5-3 Simulator Light spectrum distribution at the middle and match with the standard spectrum distribution

Standard Spectrum		Simulator Light spectrum at the middle		
Wavelength (nm)	Irradiance performance	Irradiance performance	match	classification
400-500	18.4	16.45083	0.894067	A
500-600	19.9	33.98701	1.70789	C
600-700	18.4	24.82123	1.34898	B
700-800	14.9	15.71736	1.054857	A
800-900	12.5	6.181769	0.494542	C
900-1100	15.9	2.841797	0.178729	out of standard
	100	100		

Table 5-4 Simulator Light spectrum distribution at the edge of the light spot and match with the standard spectrum distribution

Standard Spectrum		Simulator Light spectrum at the edge		
Wavelength (nm)	Irradiance performance	Irradiance performance	match	classification
400-500	18.4	16.36882	0.88961	A
500-600	19.9	16.87369	0.847924	A
600-700	18.4	16.77823	0.91186	A
700-800	14.9	16.68457	1.11977	A
800-900	12.5	16.63952	1.331162	B
900-1100	15.9	16.65517	1.047495	A
	100	100		

Table 5-5 lists the overall spectral match and classification of the simulator light by taking the average values of spectral match of each wavelength interval for the three measuring positions. **Table 5-5** shows that the spectral match is in class A for wavelengths 400-500, 600-700, 700-800, class B for wavelengths 800-900 and class C for wavelengths 500-600 and 900-1100 according to ASTM E927 – 10 classifications of solar simulators for photovoltaics. However, using the overall average of 0.9647, the spectral match can be classified as class A

Table 5-5 Overall spectral match and classification of the simulator light

standard	Spectral match				
Wavelength (nm)	Centre	Middle	Edge	Average	Class
400-500	1.178672	0.894067	0.88961	0.98745	A
500-600	1.891716	1.70789	0.847924	1.48251	C
600-700	1.29824	1.34898	0.91186	1.18636	A
700-800	0.850825	1.054857	1.11977	1.008484	A
800-900	0.276681	0.494542	1.331162	0.700795	B
900-1100	0.040494	0.178729	1.047495	0.422239	C

Overall Average	0.9647	A
------------------------	---------------	----------

Temporal instability of simulator light was measured according to ASTM E927 – 10 standard by taking the irradiance readings for a period of time with fixed sampling time (e.g. 1 second) and calculating the temporal instability using the following equation [198]:

$$\text{Temporal instability} = \frac{\text{max Irradiance} - \text{min Irradiance}}{\text{max Irradiance} + \text{min Irradiance}} \times 100 \quad (5.1)$$

Figure 5-2 shows the irradiance values with three different sampling times of 50 ms, 100 ms and 1 s for a period of 60 s. It is clear that there is little change in light intensity with time.

Table 5-6 shows the instability calculated by equation (5.1) for the three different sampling times. It can be seen that the maximum temporal instability is 0.9 for 50 ms sampling time. Thus the light source can be classified as A.

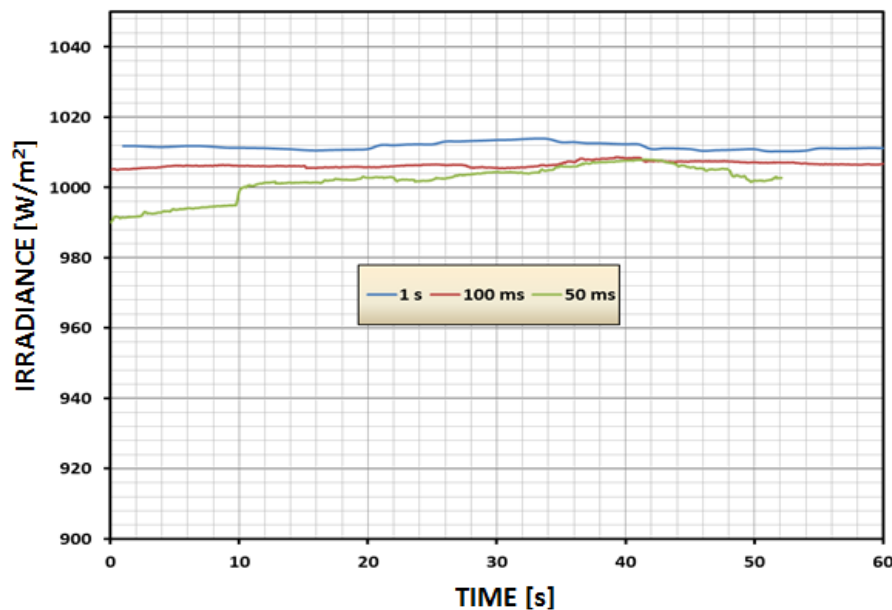


Figure 5-2 Irradiance sampling with time at three different sampling times: 1 second, 100 milliseconds and 50 milliseconds

Table 5-6 Temporal instability of simulator light at three different test sampling times

Data sampling time (1 second)			
Irradiance (W/m ²)		Temporal instability (%)	Classification
Max	1015.7964	0.46	A
Min	1006.5228		
Data sampling time (100 milliseconds)			
Irradiance (W/m ²)		Temporal instability (%)	Classification
Max	1011.4722	0.32	A
Min	1005.0142		
Data sampling time (50 milliseconds)			
Irradiance (W/m ²)		Temporal instability (%)	Classification
Max	1008.0138	0.90	A
Min	990.01672		

To measure the spatial non-uniformity, the procedure recommended by ASTM E927 – 10, was used where the measuring area should be divided into at least 36 equally sized positions and a solar sensor used to measure the light intensity (W/m²) in each position. The area of the measuring device should not be larger than the area of individual measured position and also the area of the measuring device multiplied by the number of test positions should not to be smaller than 25% of the total measured area [198]. In the current work, the measuring area was divided into 64 positions as shown in **Figure 5-3**.

After mapping light intensity of the defined area, equation (5.2) was used to evaluate the non-uniformity in percentage [198]:

$$\text{Non – uniformity} = \frac{\text{max Irradiance} - \text{min Irradiance}}{\text{max Irradiance} + \text{min Irradiance}} \times 100 \quad (5.2)$$

1	2	3	4	5	6	7	8
9	10	11	12	13	14	15	16
17	18	19	20	21	22	23	24
25	26	27	28	29	30	31	32
33	34	35	36	37	38	39	40
41	42	43	44	45	46	47	48
49	50	51	52	53	54	55	56
57	58	59	60	61	62	63	64

Figure 5-3 Measuring area for light intensity mapping

Kipp & Zenon SMP11 Pyranometer was used to map the measuring area at different levels and light spot areas. Increasing the light spot diameter decreases the total light intensity and decreasing the spot diameter increases the intensity at the same level. Different light spot diameters for the measuring areas were investigated, starting from the largest light spot diameter (65 cm), and areas within the light spot (40 cm x 40 cm, 30 cm x 30 cm and 20 cm x 20 cm) at a certain height from the light source. **Table 5-7** shows the analysis results for the spatial non-uniformity to the areas used in testing small and large concentrators.

Table 5-7 Spatial non-uniformity of the areas used in testing small and large concentrators

Measuring area (cm)	Spatial Non-Uniformity (%)	Height from source (cm)	Classification	Irradiance (W/m ²)
D = 55	40	108	Out of standard	385
20 x 20	4.09	90	B	973.5

5.3. Indoor experiment setup

The indoor experimental setup is for testing the optical efficiency of the small and large scale concentrators and PV performance under different operating conditions. **Figure 5-4** shows a schematic diagram and a picture of the test facility consisting of radiation source, concentrator, cooling and measuring devices.

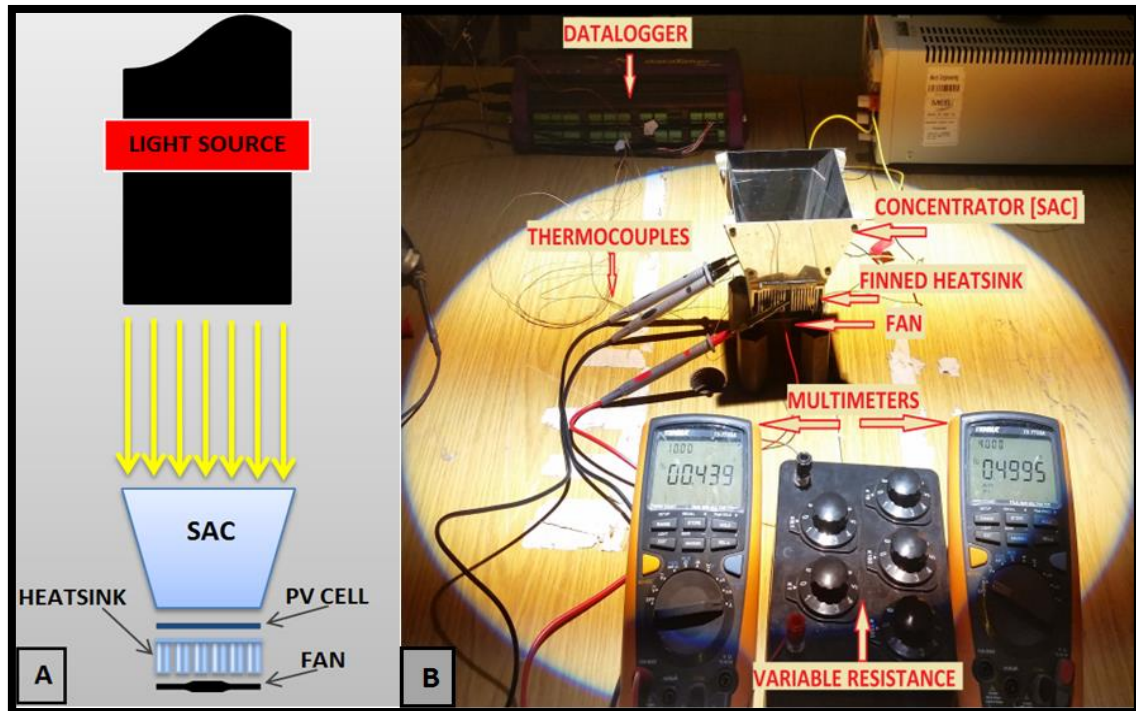


Figure 5-4 Experimental set-up for CPV system testing: A- schematic diagram, B- picture view

5.3.1. Small scale concentrator/ PV test facility

SAC and HAC concentrators are manufactured using MIRO-SUN® PV weatherproof reflective material with a surface reflectivity of 90.1 % [183], as shown pictorially in **Figure 5-6**. Dimensions of SAC and HAC at different geometric concentration ratios are illustrated in **Table 5-8**.

Table 5-8 SAC and HAC dimensions at different geometric concentration ratios

GCR	Inlet aperture area [cm²]	Exit aperture area [cm²]
2	50	25
4	100	25
6	150	25
8	200	25
10	250	25

To have accurate size of the designed concentrators and the true concentrator height (H), and material height (slant height H_s) the fabrication was based on the development method of truncated square (for SAC) and hexagonal (for HAC) pyramids which is used in engineering drawing, and illustrated in **Figure 5-5**. After fabrication of concentrators, the dimensions were measured and compared with the modelled ones, and they were the same with ± 0.5 mm.

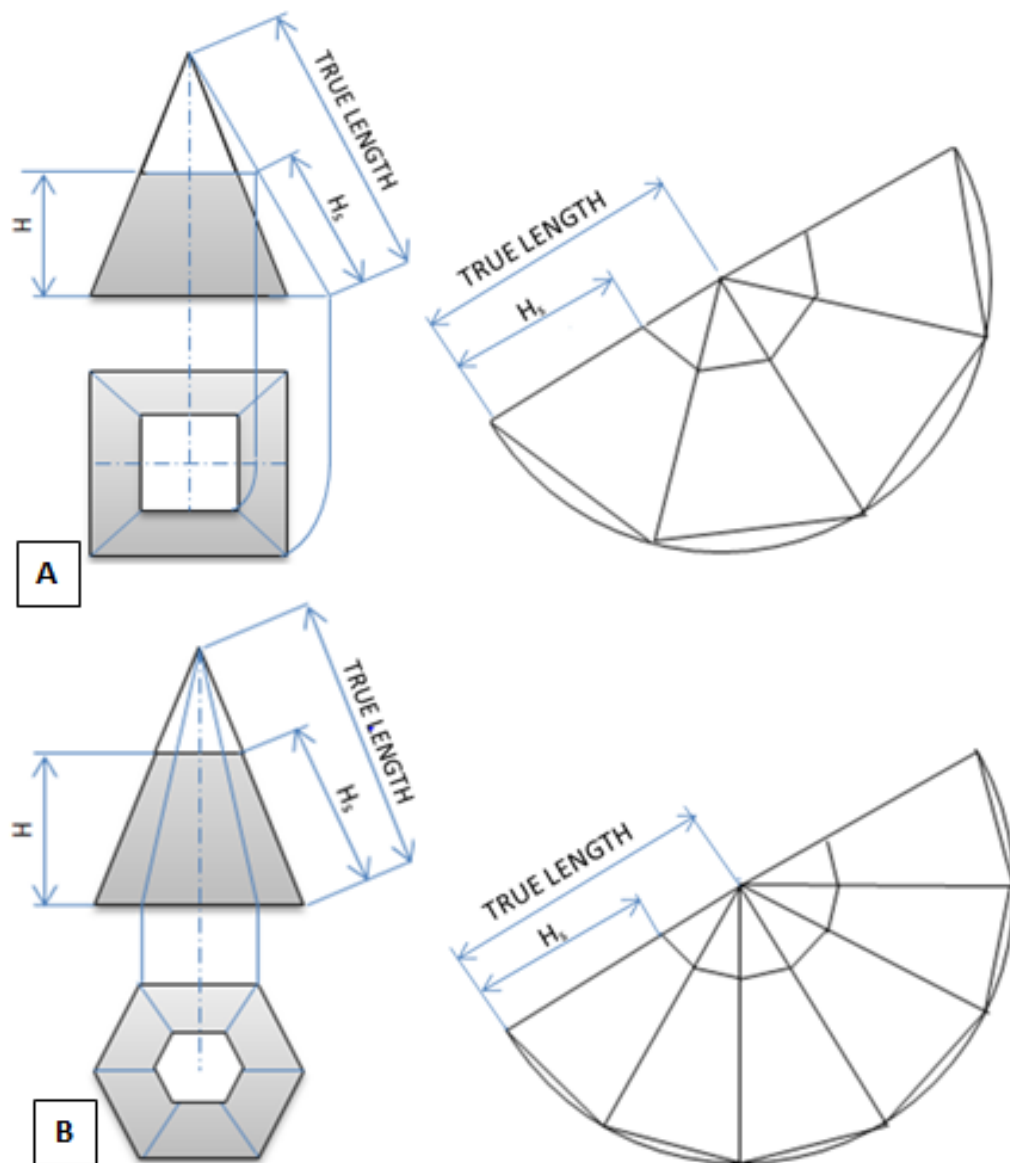


Figure 5-5 Concentrator development: A- SAC and B- HAC

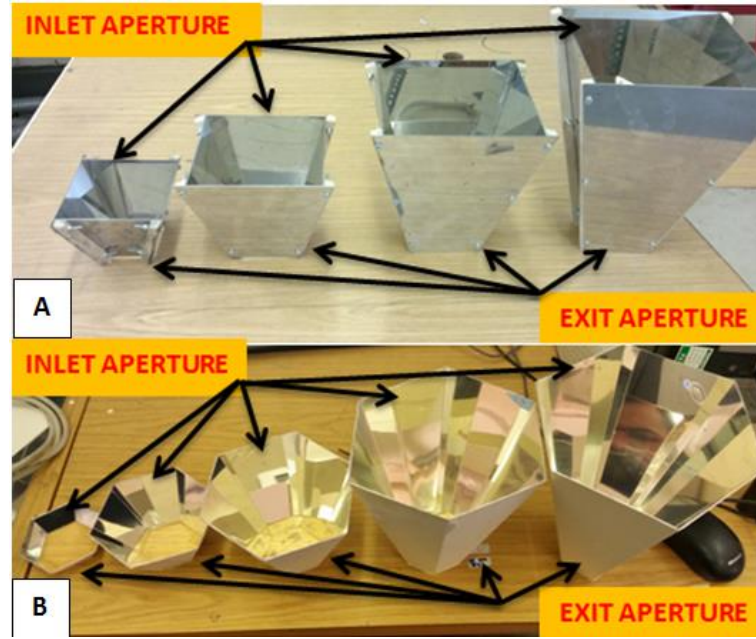


Figure 5-6 A: SAC and B: HAC with exit aperture area of 25 cm² and GCR =2-10

Concentrator input and output flux was mapped using 5mm x 5mm flux sensors (S1 and S2) with high sensitivity (0.114 $\mu\text{V}/\text{W}/\text{m}^2$) from Captec Enterprise[®] (**Figure 5-7**). The inlet aperture and receiver areas were divided into many regions as recommended by ASTM standards [198] and flux measurements were taken in each region to evaluate the flux distribution and uniformity of all the concentrators used.

The geometric concentration ratio, actual concentration ratio (ACR) and optical efficiency for the investigated concentrators were evaluated using equations 5.3-5:

$$GCR = \frac{A_{in}}{A_{out}} \quad (5.3)$$

$$ACR = \frac{q_{out}}{q_{in}} \quad (5.4)$$

$$\eta_{opt} = \frac{ACR}{GCR} \times 100 \quad (5.5)$$

Where A_{in} and A_{out} are the inlet and exit areas of the concentrators, q_{in} and q_{out} are the radiation flux at inlet and exit areas of the concentrators and η_{opt} is the optical efficiency of the concentrator [21].

The PV cell used in this work is a polycrystalline silicon cell with an area of 50 mm X 50 mm.

Figure 5-7 shows a schematic diagram of the measurement setup using devices for measuring the output current and voltage, radiation and temperature.

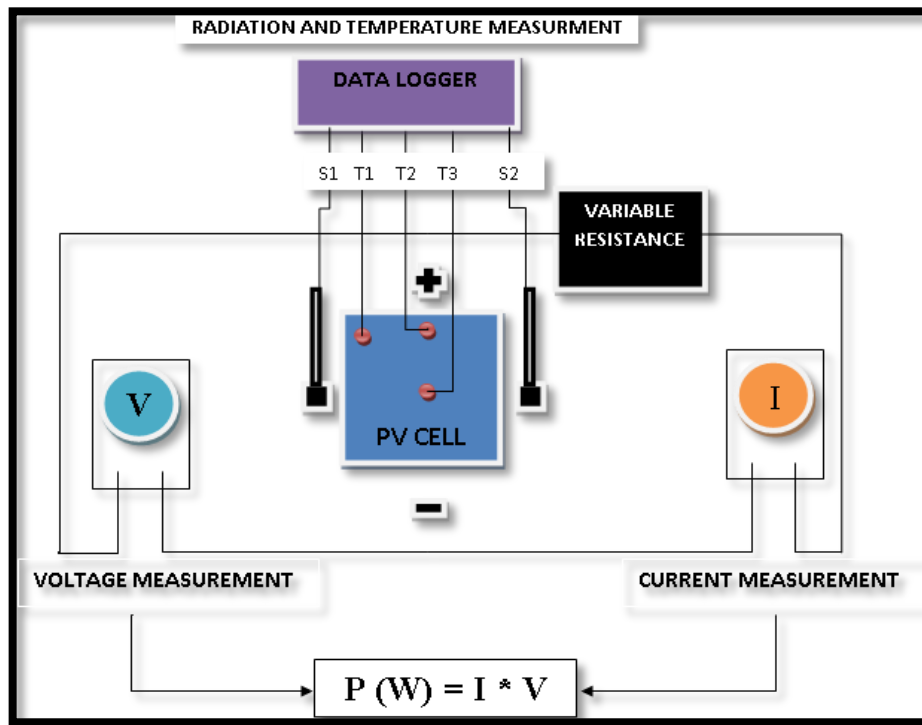


Figure 5-7 Schematic diagram of the system output measurements

The electrical power output was measured using two logging multi-meters (TENMA 72-7732A), with accuracy of $\pm 0.1\%$ for DC current and $\pm 0.025\%$ for DC voltage and connected to a computer; one to measure the current and another for the voltage and a variable resistance box ($0.005\ \Omega - 9999\ \Omega$) used as a variable load to obtain the PV cell I-V curves.

The maximum power point was calculated using equation 5.6 [199]:

$$P_{max}(W) = I_m(A) \times V_m(V) \quad (5.6)$$

Where, P_{max} is the maximum output power produced by the system (with and without concentration), I_m is the current at maximum power point and V_m is the Voltage at maximum power point. The CPV electrical conversion efficiency is calculated using equation 5.7 [199]:

$$\eta_e = \frac{P_{max}}{P_{in}} \times 100 \quad (5.7)$$

Where: P_{in} is the input power calculated by multiplying the average measured flux and the area of the PV cell (50mm X 50mm).

For the temperature measurement, T-type surface thermocouples with a diameter of 0.13 mm and length of 1000mm (Omega, model number: 5TC-TT-TI-36-1M) T1, T2 and T3 (**Figure 5-7**) were fitted at the back of the PV cell using Aluminium Foil Tape and thermal paste was used to ensure good thermal contact; one at the centre, one at the side and one in the corner of the PV cell. These thermocouples were connected to a data logger (Data Taker DT85), monitored using PC and have an error of ± 0.5 °C (0.4 %) [200].

Experiments were carried out using irradiance of 651 W/m^2 at the PV cell (without concentration) or at the concentrator aperture for concentration ratios 4, 6, 8 and 10 with no cooling applied. As preliminary testing of, experiments were carried out with heatsink attached to the PV cell with fan operating (active cooling) and without the fan operating (passive cooling) to investigate the effect of cooling PV output. I-V curves, irradiance and temperature were all measured. A CPU cooler (SAN ACE MC) that has an aluminium heatsink and fan (specifications are in **Table 5-9**) was attached to the PV cell.

Table 5-9 Technical specifications of cooling element

Model No.	Rated voltage [V]	Rated current [A]	Speed [RPM]
109X7612H1176	12	0.1	3900

5.3.2. Large scale concentrator PV/T testing

For the large scale SAC, indoor measurements of the electrical output for the PV module carried out with SAC, was only for GCR = 2. This is due to the limitation of the light spot area where the maximum diameter can be used is 55cm and this covers the inlet aperture of the GCR =2 concentrator. The same indoor setup was used with both small and large scale SAC concentrator, but with the addition of the developed cooling duct design fitted underneath the PV module. The cooling system shown in **Figure 5-9** is a U type duct, which was fabricated using rectangular cross-section aluminium tube (10 mm × 30 mm × 1.5 mm) , glued using a very high thermally conductive filled silicone adhesive (OMEGATHERM® 201) to produce the continuous U shape. To ensure good conduction and no gap between the PV module and the cooling duct, a highly thermal conductive non-curing heat transfer paste HTSP (specification of HTSP listed in **Table 5-10**) was used as a thermal interface material. Two Resistance Thermometer Detector Platinum100 (RTDPt100) were connected to the water inlet and exit of the cooling duct.

Table 5-10 Technical specification of highly thermally conductive heat transfer paste HTSP

Colour	Base	Thermal Conductivity (W/m.K)	Density at 20°C (g/ml)	Viscosity (Pa.s)	Temperature Range (°C)
Pale	Silicone	3.0	3.0	42-48	-50 to +200

For PV module temperature measurement, the same calibrated T type surface thermocouples (model number; 5TC-TT-TI-36-1M) as those used with the small scale test rig were used where five thermocouples were fitted using Aluminium Foil Tape at the back side of the PV module; one the centre of the PV module and four at the centres of the four PV cells of the module. Then, the back side PV module was pressed to the top surface of the cooling duct, to ensure good contact. **Figure 5-8** shows schematic diagram for the cooling system attached to the PV module.



Figure 5-8 schematic diagram for the cooling system

Figure 5-9 shows the parts of cooling duct, thermocouples positions and process of assembly with PV module.

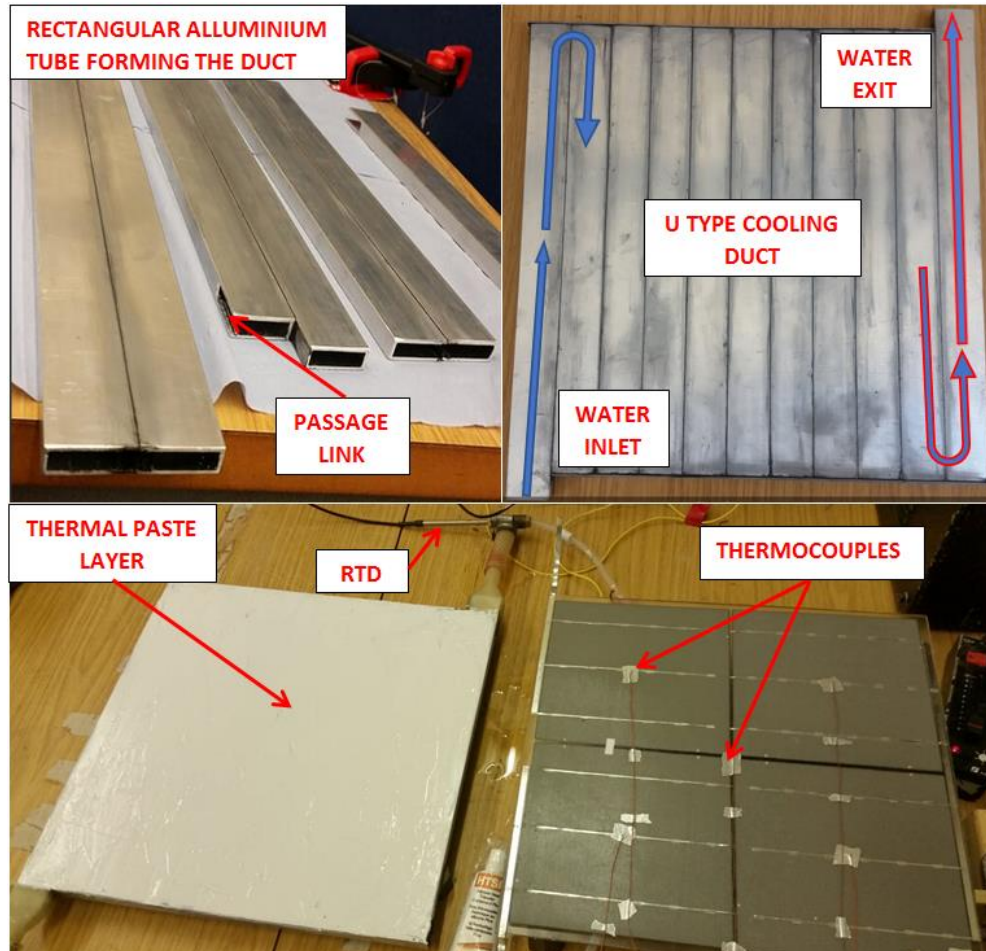


Figure 5-9 Parts of cooling facility, thermocouples positions and process of assembling with PV module

5.4. Outdoor experimental setup

The outdoor experimental setup is for testing the optical efficiency of large scale SAC concentrators and the whole CPV/T performance, which cannot be tested by the indoor setup for size limitations. PV module performance was tested under different operating conditions with and without concentration as well as with and without cooling. Flow rate was controlled using valve and Platon flow meter and different flow rates were used (ranging from 50 mL/min to 700 mL/min) depending on the PV module temperature which should be cooled up to or close to the inlet water temperature to see the maximum system power output can be

obtained. The incoming solar radiation, current/ voltage (I-V) and Power/voltage (P-V) curves for the PV module were measured using PVA-1000S PV Analyzer Kit from Solmetric, which is an I-V tracer with advanced wireless irradiance, temperature and tilt sensing (Specifications are in **Table 5-11**). **Figure 5-10** shows a picture of the outdoor test facility used in the experiments, and **Figure 5-11** shows schematic diagram for test facility connections and data acquisition.

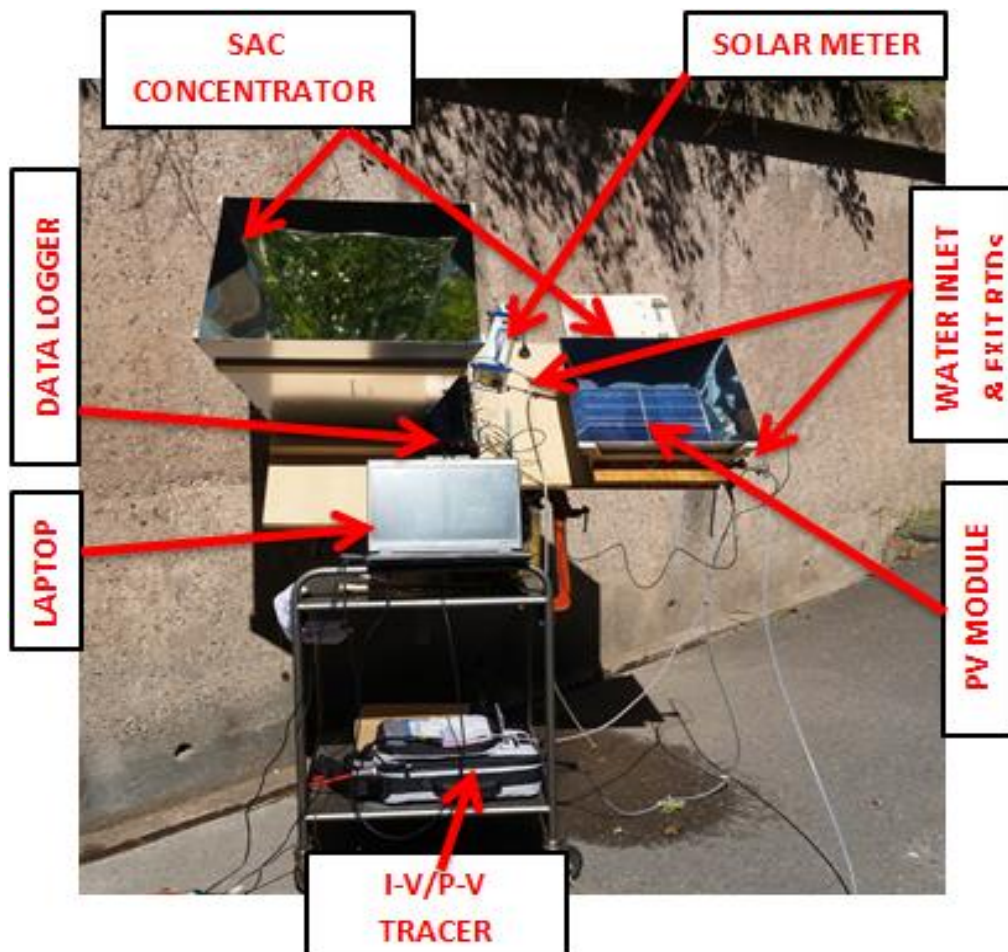


Figure 5-10 CPV/T outdoor test facility

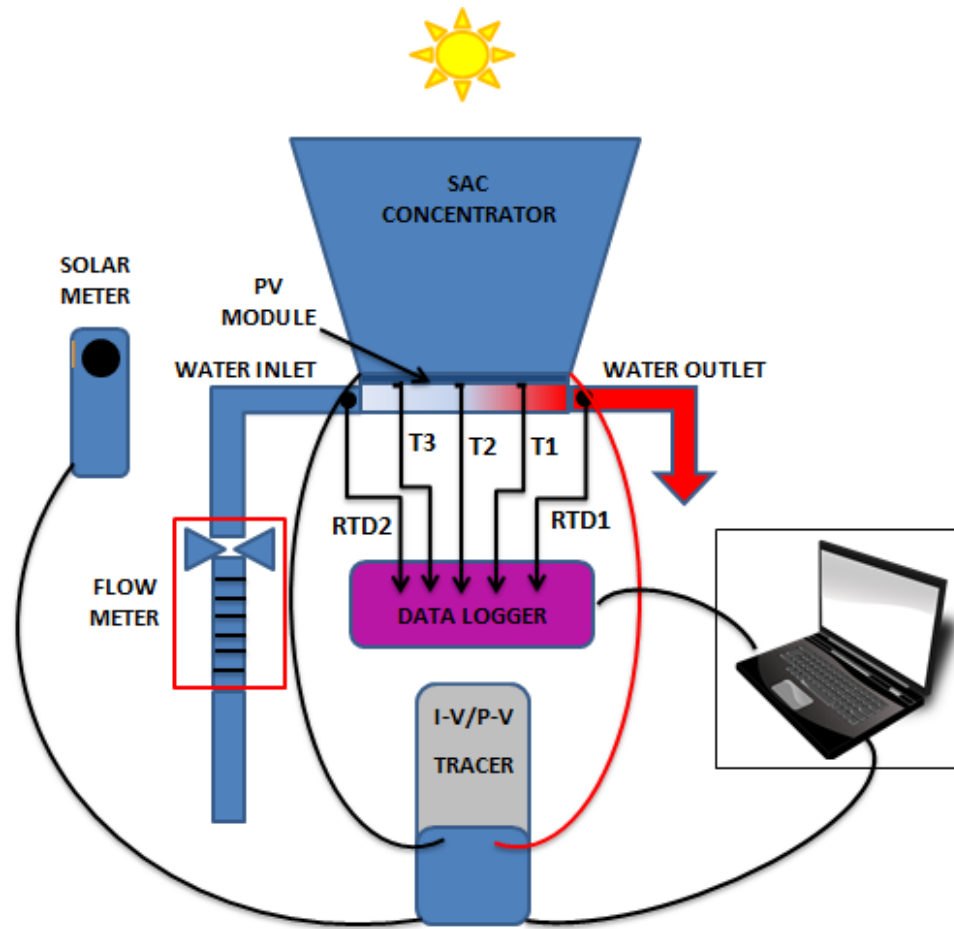


Figure 5-11 Schematic diagram of CPV/T outdoor test facility

Table 5-11 PVA-1000S PV Analyzer Kit technical specifications

Parameter	Value
PV voltage	0–1000 V
PV Current	0-30 A
Voltage accuracy	0 to 55°C $\pm 0.5\% \pm 0.25$ V
Current accuracy	0 to 55°C $\pm 0.5\% \pm 0.04$ A
Voltage resolution	25 mV
Current resolution	2 mA
Measurement duration	4s
I-V sweep duration	0.05 - 2s
I-V trace points	100 or 500
Operating temp	-10 to +65°C

5.5. Calibration of measuring devices

To evaluate the uncertainty of measured data, measuring instruments are calibrated. The following subsections describe the calibration of the thermocouples used to measure the temperature and the flow meter used to measure the cooling water flow rate.

5.5.1. Calibration of thermocouples

The thermocouples used in the experiment were calibrated using adjustable temperature water heater shown in **Figure 5-12** and liquid-in-glass thermometer. The ends of thermocouples were held together around the thermometer sensing end at the same level, and inserted in the water heater. Thermocouples were connected to the DataTaker DT85 channel to record temperature readings, simultaneously with thermometer readings.

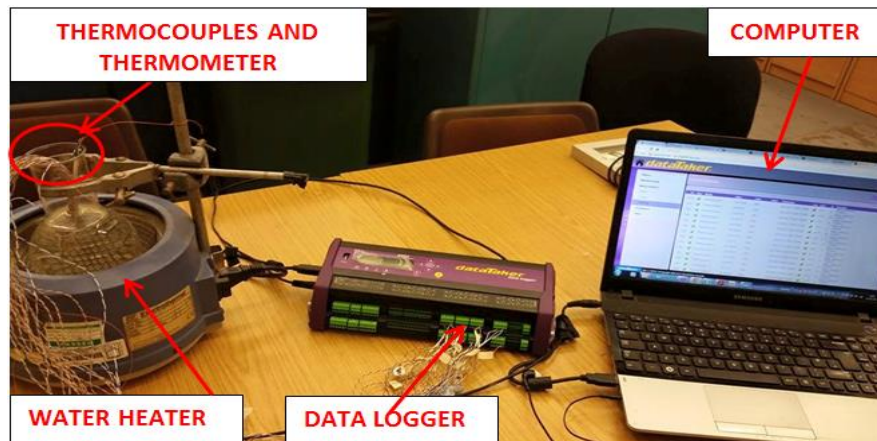


Figure 5-12 Calibration setup for thermocouples

Figure 5-13 shows one of the thermocouples readings versus thermometer readings. A linear fitting using the equation (5.8) with R^2 of 0.999 was used to calculate the value of curve fit (\bar{x}), consequently used to determine thermocouple uncertainty as described below.

$$\bar{x} = 0.9961x + 0.3272 \quad (5.8)$$

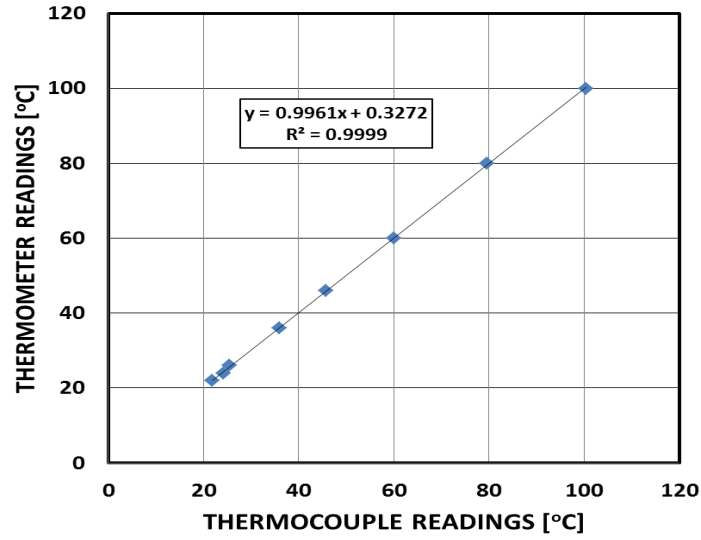


Figure 5-13 Relation between thermometer and thermocouple readings

Other thermocouples readings have similar behaviour as presented in **Appendix B**. The uncertainty of the thermocouples was calculated using equation (5.9) [201]:

$$U'_{\text{thermocouple}} = \sqrt{(U'_{st})^2 + (U'_{\text{curve-fit}})^2} \quad (5.9)$$

Where U'_{st} uncertainty of the standard thermometer, $U'_{\text{curve-fit}}$ is the uncertainty of the curve fit and $U'_{\text{thermocouple}}$ is the uncertainty of the thermocouples. The uncertainty of the curve fit is calculated by equation (5.10) [201]:

$$(5.10)$$

$$U'_{\text{curve-fit}} = t_{n-1,95\%} S_{\bar{x}}$$

$$S_{\bar{x}} = \frac{\sigma}{\sqrt{n}} \quad (5.11)$$

$$\sigma = \sqrt{\frac{1}{n-1} \sum_{i=1}^n (x_i - \bar{x})^2} \quad (5.12)$$

Where; $t_{n-1,95\%}$ is the student distribution value at a degree of freedom $n-1$ and confidence level **95%**, n is the number of data points, $S_{\bar{x}}$ is standard deviation of the mean, and σ the standard deviation. Calculation of thermocouple uncertainty was carried out and details are shown in **Table 5-12**. The uncertainty of thermometer was assumed negligible as good agreement of thermometer reading against the ice temperature test (0 °C). Therefore, the uncertainty of thermocouples was considered the same as the curve fit uncertainty. Two Resistance Thermometer Detector Platinum100 (RTDPt100) were used to measure the water temperature at the cooling duct inlet and exit positions. RTDs were calibrated using ice temperature measurements and results showed that RTD readings are very close to 0 (-0.2 °C) as shown in **Figure 5-14**.

Table 5-12 Calculations of thermocouple reading uncertainty

Data points	Thermometer readings (x_i)	Thermocouple readings	Curve fit equation (\bar{x}) $T = 0.9961x + 0.3272$	Deviation ($x_i - \bar{x}$) ²
1	22	21.75	22	1.22E-05
2	24	24.23	24.46	0.21
3	26	25.42	25.65	0.125
4	36	35.89	36.08	0.006
5	46	45.72	45.87	0.017
6	60	59.96	60.06	0.003
7	80	79.55	79.57	0.188
8	100	100.37	100.31	0.096
Sum ($\sum_{i=1}^n (x_i - \bar{x})^2$) = 0.646		Degree of freedom (n-1) = 7		
Standard deviation (σ) =		Standard deviation of mean ($S_{\bar{x}}$) = 0.107		
$t_{n-1,95\%} = 2.365$		Uncertainty of the thermocouple ($U'_{\text{curve-fit}}$) = 0.25K		

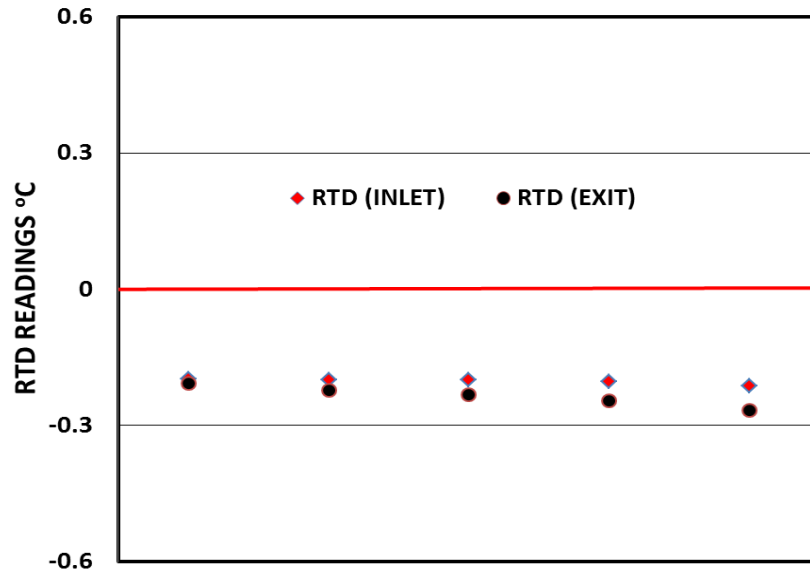


Figure 5-14 RTD ice temperature readings

Table 5-13 lists the curve fit equations and uncertainty calculation results of all calibrated thermocouples.

Table 5-13 Curve fit equations and uncertainty calculation results of thermocouples

Thermocouple	Curve fit equation (\bar{x})	Uncertainty (K)
T1	$T = 0.9961x + 0.3272$	0.25
T2	$T = 0.9976x + 0.3512$	0.18
T3	$T = 0.9975x + 0.3972$	0.22
T4	$T = 0.9963x + 0.2944$	0.22
T5	$T = 0.9978x + 0.3046$	0.18
T6	$T = 0.9979x + 0.0739$	0.21
T7	$T = 0.9961x + 0.2254$	0.19
T8	$T = 0.9972x + 0.2417$	0.18
T9	$T = 0.9957x + 0.3398$	0.16
T10	$T = 0.9938x + 0.3191$	0.29
T11	$T = 0.9955x + 0.1837$	0.18
T12	$T = 0.9958x + 0.2211$	0.193649

5.5.2. Calibration of water flowmeter

Figure 5-15 shows the flow meter calibration setup, which includes a CT Platon flow meter (50 – 800 cm³/min (mL/min)), graduated glass cylinder (500mL) and stopwatch.

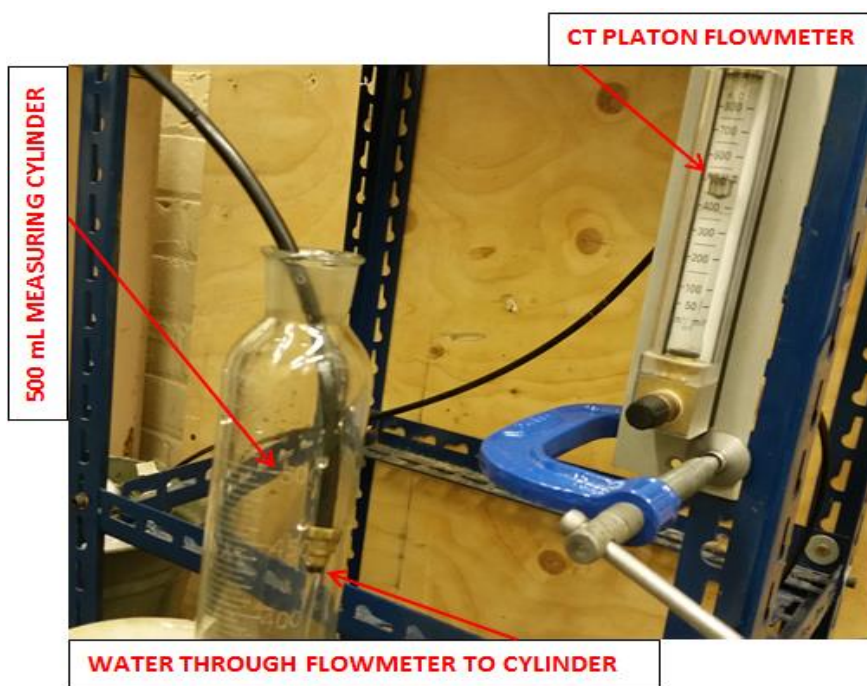


Figure 5-15 Flow meter calibration setup

Seven flow rate points were taken (50 mL/min and 100, 200 to 600 mL/min) and flow rate (V_w) was calculated using equation (5.13). **Figure 5-16** shows the measured values against the Platon flow meter readings.

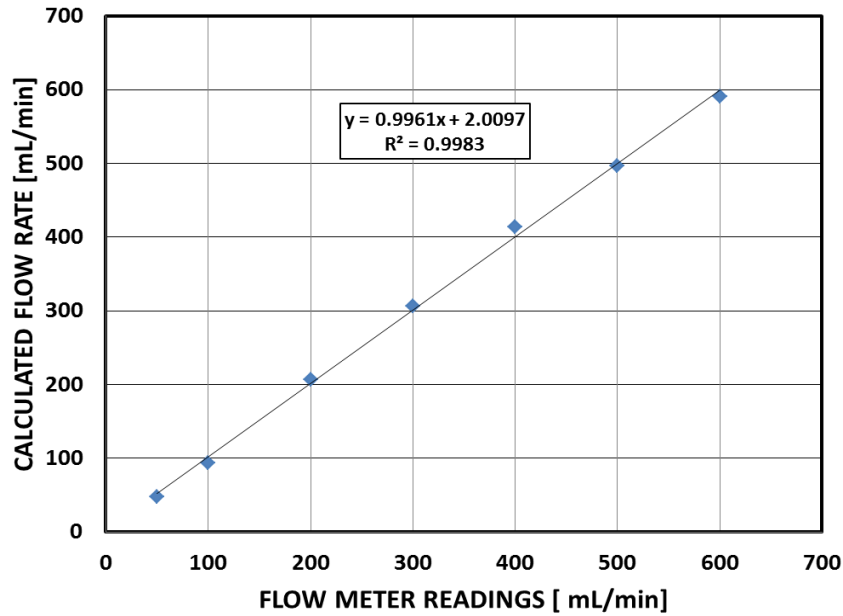


Figure 5-16 Relation between calculated flow rate using cylinder and flowmeter readings

Based on the calculated uncertainty using curve fitting equation (5.14) ($U'_{curve-fit}$) and uncertainty of the calibration method (U'_{vc}), the uncertainty of the Platon flow meter (U'_{fm}) was calculated using equation (5.15).

$$V_w = \frac{\text{collected volume}(V_f)}{\text{collection time}(t)} \quad (5.13)$$

$$\bar{x} = 0.9961x + 2.0097 \quad (5.14)$$

$$U'_{fm} = \sqrt{(U'_{vc})^2 + (U'_{curve-fit})^2} \quad (5.15)$$

U'_{vc} is the uncertainty of the graduated cylinder volume as given by equation (5.16).

$$U'_{vc} = \sqrt{\left(\frac{\partial V_w}{\partial V_f} \Delta V\right)^2 + \left(\frac{\partial V_w}{\partial t} \Delta t\right)^2} \quad (5.16)$$

Where V_f is the total collecting cylinder volume (in mL), ΔV is the error in measuring the volume which is equal to the step in the graduating scale of the measuring cylinder (± 2.5 mL), Δt is the minimum time that can be counted when cylinder is filling with water ($\frac{1}{60}$ min) and t is time in seconds. The calibration method uncertainty can be estimated using equation (5.17).

$$U'_{vc} = \sqrt{\left(\frac{1}{t} \Delta V\right)^2 + \left(\frac{V_f}{t^2} \Delta t\right)^2} \quad (5.17)$$

From equation (5.17) U'_{vc} is ± 8.7 mL/min, and the uncertainty calculations for the flow rate measurement (U'_{fm}) is detailed in **Table 5-14**.

Table 5-14 Calculations of flow rate measurement uncertainty

Data points n	Flow meter readings (x_i)	Calculated flow rate	Curve fit equation (\bar{x}) T = 0.9961x + 0.3272	Deviation ($x_i - \bar{x}$) ²
1	50	47.61905	51.8147	3.293136
2	100	93.72071	101.6197	2.623428
3	200	206.8252	201.2297	1.512162
4	300	306.2787	300.8397	0.705096
5	400	414.0787	400.4497	0.20223
6	500	496.5243	500.0597	0.003564
7	600	590.5512	599.6697	0.109098
Sum ($\sum_{i=1}^n(x_i - \bar{x})^2$) = 8.449		Degree of freedom (n-1) = 6		
Standard deviation (σ) = 1.187		Standard deviation of mean ($S_{\bar{x}}$) = 0.4485		
t_{n-1,95%} = 2.447		Uncertainty of curve fit (U'_{curve-fit}) = 1.0975 mL/min		
Uncertainty of the flow rate (U'_{fm}) = 8.8 mL/min				

5.6. Conclusions

In this chapter, the experimental setup to investigate the performance of concentrator photovoltaic/ thermal (CPV/T) system was described. The setup involves classifying the indoor light according to the Standard Specification of Solar Simulation for Photovoltaic Testing ASTM E927 – 10, in terms of light spectral match, spatial non-uniformity and temporal instability. Also setup includes preparing the CPV/T system by fabricating the selected design of concentrators, fabricating the cooling duct, aligning the PV module to the cooling duct with the thermocouples and RTDs. Acquiring data from indoor experiments was done with different devices including data logger to take temperature and indoor radiation measurements and CT Platon flow meter (flow rate ranges from 50 mL/min to 800 mL/min). Data from outdoor experiment was acquired using PVA-1000S PV Analyzer Kit from Solmetric to measure the incoming solar radiation, current/ voltage (I-V) and Power/voltage (P-V) curves for the CPV/T system and flow rate using the same flow meter. Thermocouples, RTDs and flow meter were calibrated before use, and uncertainty of thermocouples did not exceed 0.25 K, while ice test for RTDs show temperature readings close to 0 °C (-0.2 °C) and calculated uncertainty of flow meter using cylinder method was 8.8 mL/min.

CHAPTER 6: EXPERIMENTAL RESULTS AND VALIDATION

6.1. Introduction

The first part of this chapter includes the optical validation of SAC (developed in chapter three) in terms of optical efficiency and received flux distribution using three different geometric concentration ratios and different concentrator material surface reflectivity. Secondly, indoor thermal validation CPV/T system is presented by the comparison of simulation (SIM) and experimental (EXP) work of the CPV/T system with concentration ratio of 2 using the cooling duct designed in chapter 4. Thermal validation includes the PV module temperature and outlet cooling water temperature. Thirdly, CPV/T system electrical power output under indoor conditions is presented for both small and large scale SAC. Fourthly, CPV/T system power output under outdoor conditions is presented, including electrical power output, thermal power output and CPV/T system total power output at different operating conditions such as different concentration ratios and different cooling water flow rates.

6.2. Optical validation

In this section the optical simulation (SIM) results in terms of the concentrator optical efficiency and the flux distribution on the receiver (PV cell) obtained using OPTISWORKS software will be compared to the experimental (EXP) results at the same conditions. The percentage deviation of the optical simulation results compared to experimental results are calculated using equation (6.1) [202].

$$Dev(\%) = \left| \frac{EXP - SIM}{EXP} \right| * 100 \quad (6.1)$$

6.2.1. Large scale SAC concentrator optical efficiency

Optical simulation of the large scale SAC presented in chapter 3 was experimentally validated in terms of optical efficiency at different geometric concentration ratios, received flux distribution and surface reflectivity. **Figure 6-1** compares the simulation and outdoor experimental results of SAC concentrator optical efficiency, for three different geometric concentration ratios of 2, 4 and 6 using Miro-Sun PV reflector material 90.1%. It can be seen that good agreement in the SAC optical efficiency with maximum deviation of 9.13 % at geometric concentration ratio of 4, while minimum deviation of 0.37 % is achieved at geometric concentration ratio of 2. Deviation could be attributed to concentrator geometry error due to fabrication.

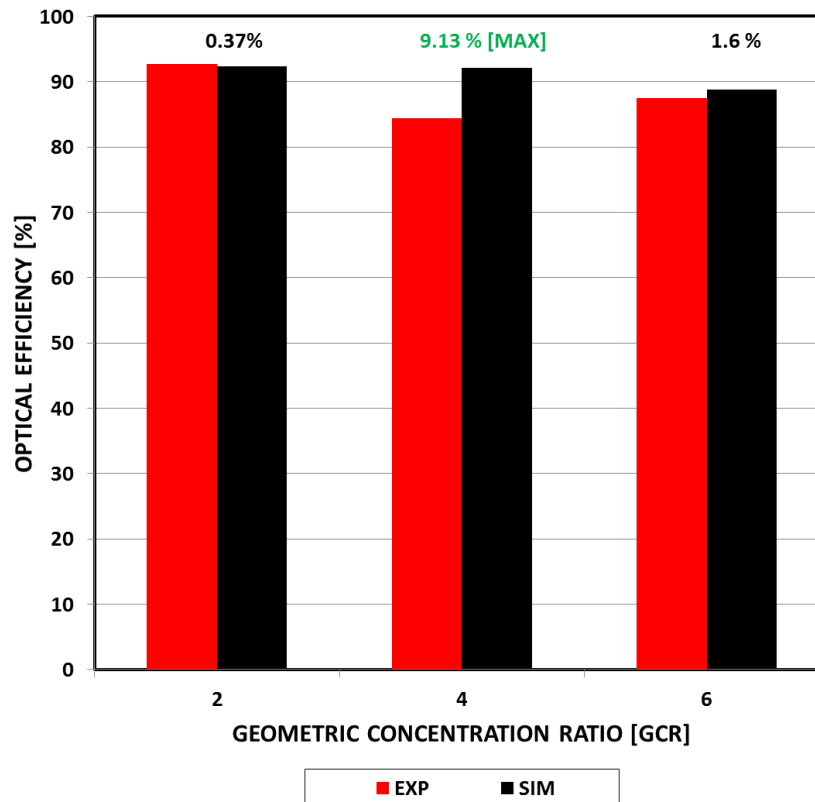


Figure 6-1 SAC optical efficiency (reflectivity of 90.1 %)

This can also be seen from **Figure 6-2** which compares the predicted actual concentration ratios to those obtained experimentally. It can be seen that the maximum difference between actual and simulation values for the concentrator with geometric concentration ratio of 4 where an actual concentration ratio of about 3.69 predicted by simulation and 3.38 from experimental measurements. While concentrator with geometric concentration ratio of 2 shows an actual concentration ratio of about 1.855 predicted by simulation and 1.848 obtained from experimental measurements.

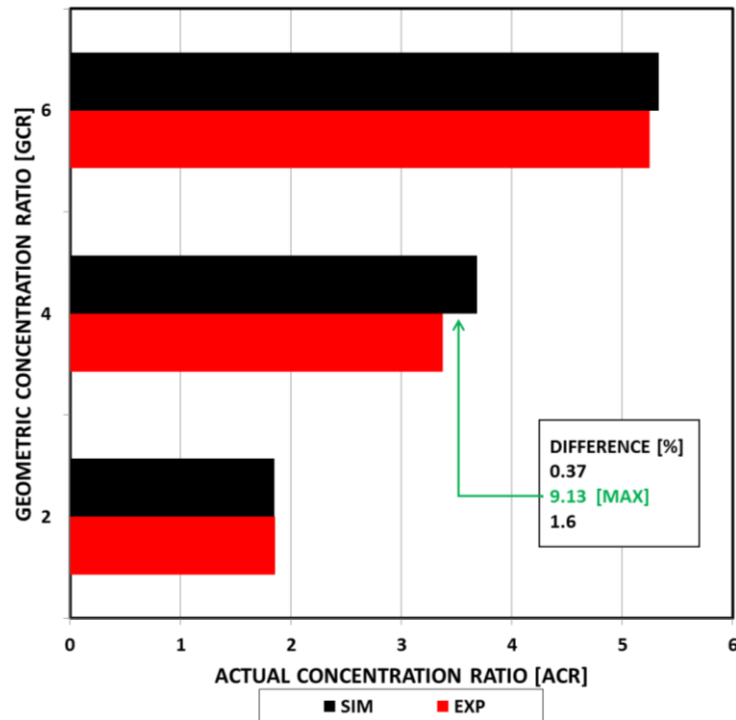


Figure 6-2 SAC actual concentration ratio

6.2.2. SAC concentrator flux distribution

Experimental flux distribution was measured at 36 positions equally spaced at the exit aperture (receiver) of each large SAC using radiation sensor with an area of 5 mm x 5 mm. Similar positions were selected from simulation results at the receiver for comparison purpose with the experimentally measured values at the same input irradiance. **Figure 6-3** compares the predicted and experimentally measured flux distribution at geometric concentration ratios of 2, 4 and 6. About 85 % of points calculated deviation values are between 0% (full agreement) and ± 20 %. Good agreement was achieved between simulation and experimental results with an average deviation of ± 12 % to ± 14 % for the compared concentration ratios.

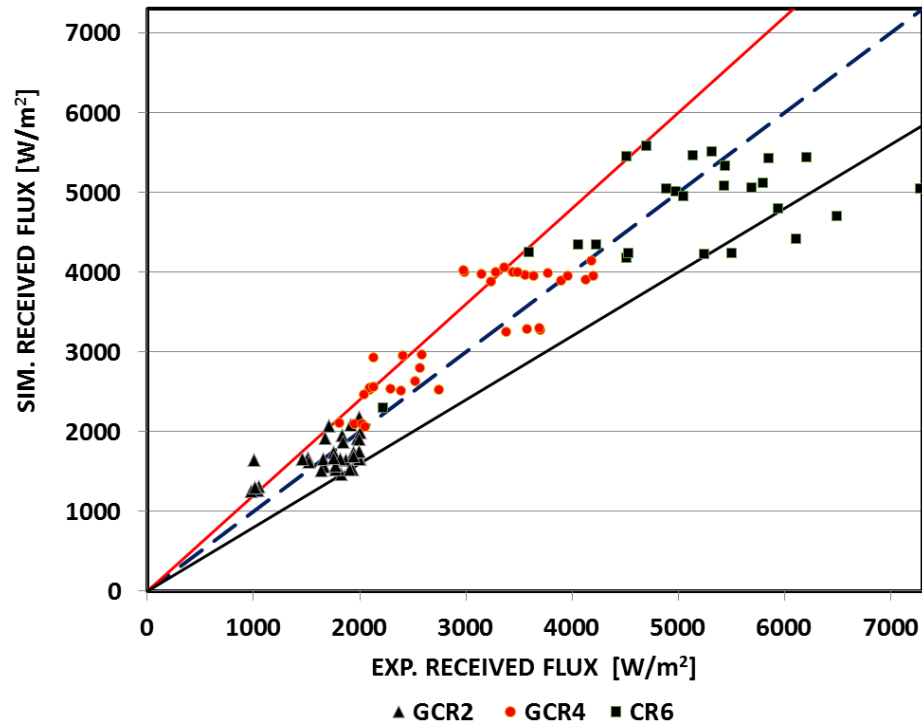


Figure 6-3 Simulated and experimentally measured flux distribution at geometric concentration ratios of 2, 4 and 6 with $\pm 20\%$ deviation.

Figure 6-4 shows pictorial flux distribution from outdoor experiment and simulated flux distribution for SAC with geometric concentration ratio of 2. As observed in **Figure 6-4**, real and simulated flux distributions show a cross like shape with low concentration regions at the centre of the cross, while the corners have higher concentration regions. Also the diagonal flux distribution shows lower concentration at the centre and higher concentration at the corner regions

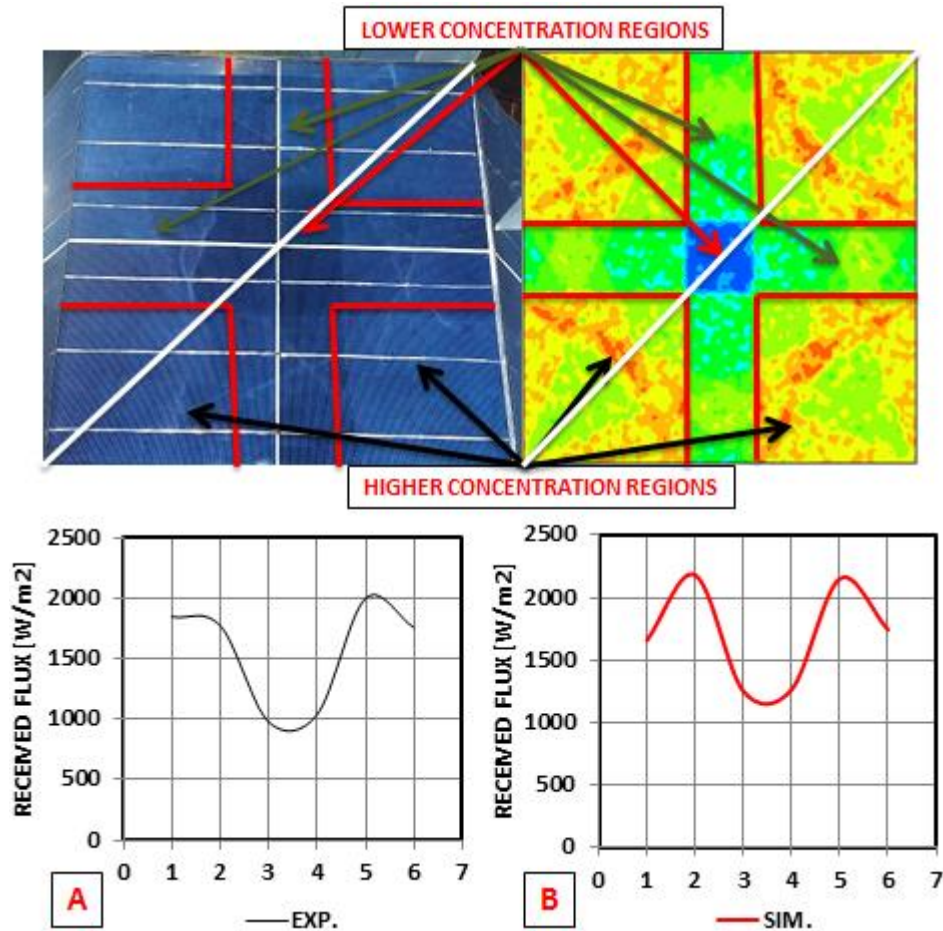


Figure 6-4 Pictorial flux distribution from outdoor experiment (A) and simulated (B) flux distribution for large SAC with geometric concentration ratio of 2.

6.2.3. Small scale concentrators optical performance

6.2.3.1. Effect of material surface reflectivity on optical efficiency

Figure 6-5 shows validation results for the effect of concentrator material surface reflectivity on the optical efficiency. A comparison between simulation and experimental results of the concentrator optical efficiency for three different values of surface reflectivity shows good agreement with maximum deviation of 11.5% with the use of 316 polished stainless steel (Ref. = 55.35%) and minimum deviation of 1.97% with the use of mirror (Ref. = 72.95%).

This indicates the increase of concentrator optical efficiency with the increase of material surface reflectivity.

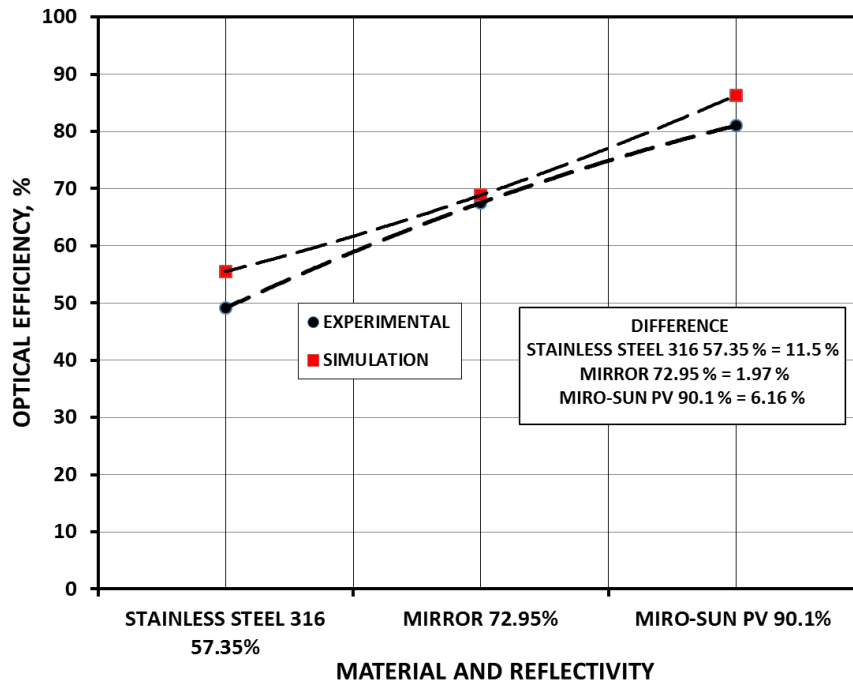


Figure 6-5 Validation for the effect of surface reflectivity on concentrator optical efficiency

6.2.3.2. Optical efficiency of small scale SAC and HAC concentrators

The experimental indoor testing results for Hexagonal Aperture Concentrator (HAC) optical efficiency is shown in **Figure 6-6**. The HAC was manufactured from Miro-Sun PV reflector material 90.1% with different geometric concentration ratios. Three GCRs of 2, 4 and 6 for HAC were tested experimentally to investigate the optical efficiency of the concentrator. HAC with GCR2 has achieved an optical efficiency of about 83%, where HAC with GCR4 has an optical efficiency of 84% and HAC with GCR6 has achieved an optical efficiency of about 76%. **Figure 6-7** shows the optical efficiency of HAC and SAC, and it can be seen that both concentrator geometries are comparable in terms of efficiency, where at GCR4 the measured optical efficiency of SAC is about 83% and HAC at the same GCR is about 85%. On the other hand, the optical efficiency of both SAC and HAC at GCR 6 is about 76%. This

highlights the feasibility of such geometries to be used in CPV systems, with the SAC advantage of better flux distribution and simplicity of fabrication.

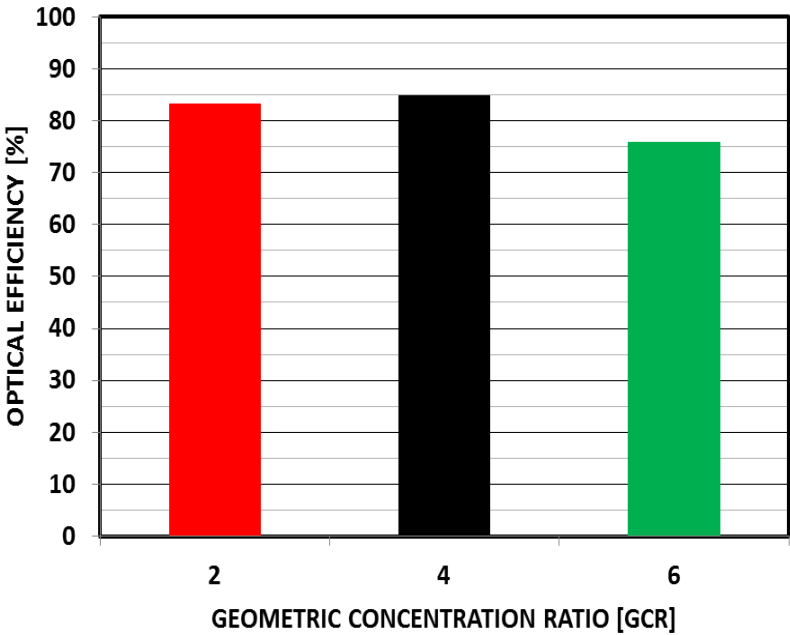


Figure 6-6 HAC concentrator optical efficiency

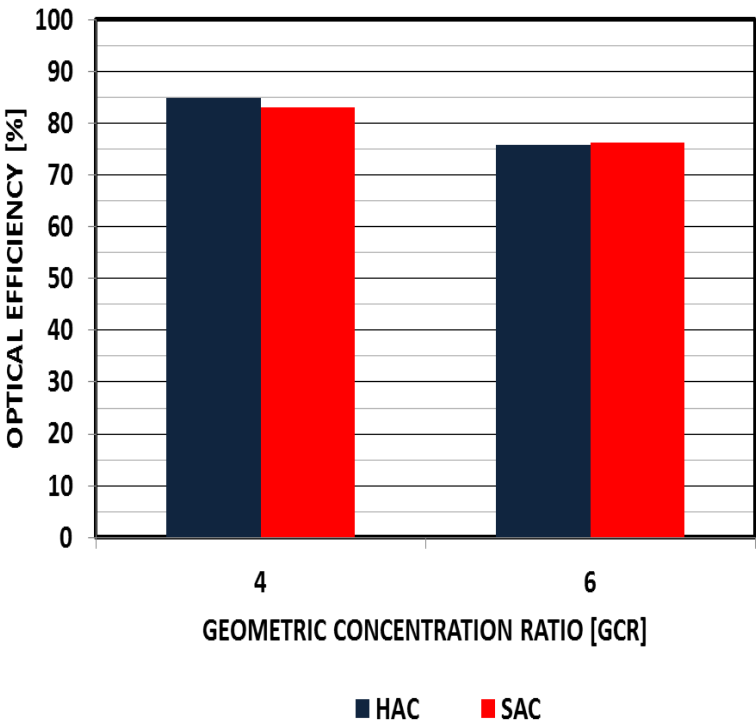


Figure 6-7 Optical efficiency of HAC and SAC

6.3. Thermal validation of CPV/T system

In this section a comparison of simulation (SIM) and indoor experimental (EXP) thermal results of the CPV/T system with concentration ratio of 2 using the cooling duct developed in chapter 4 is presented. This includes comparing the PV module temperature, and the outlet water temperature as predicted using COMSOL Multi-physics software to those measured experimentally (EXP) at the same conditions. The percentage deviation for the thermal simulation results compared to experimental results is calculated using equation (6.1).

Figure 6-8 shows the simulation and experimental results of the PV module temperature (T_c) at various water flow rates where good agreement between simulation and experimental results with maximum deviation of 5.86% at water flow rate of 50mL/min, while a minimum deviation of 1.01% at flow rate of 250 mL/min were achieved.

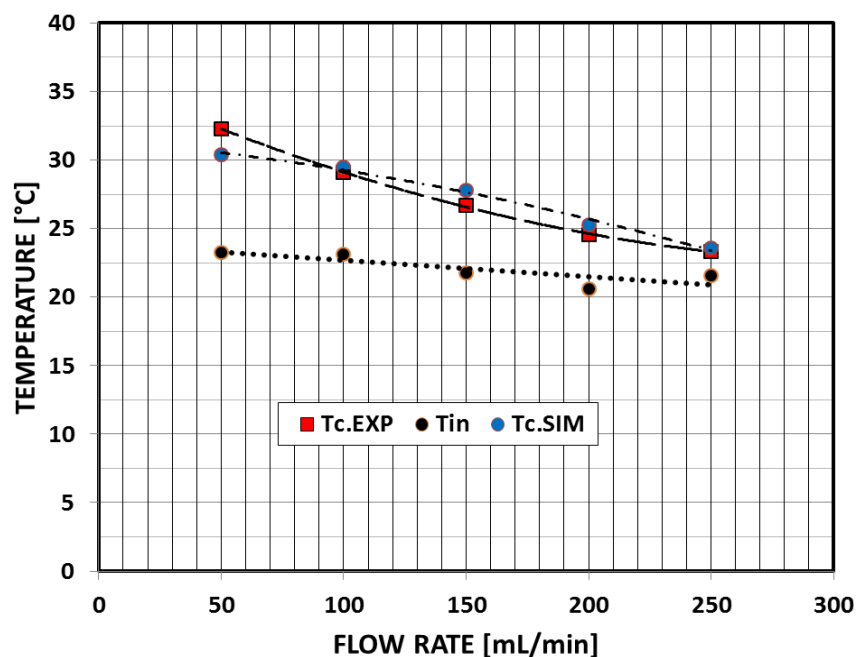


Figure 6-8 Validation of the change in PV module temperature with water flow rate

It is clear from **Figure 6-8** that the PV module temperature decreases with the increase of water flow rate where at lowest flow rate used (50 mL/min) the PV module temperature is

about 32 °C under irradiance of 385 W/m², ambient temperature (T_a) of 22 °C and inlet water temperature (T_{in}) of 23 °C but decreases to reach about 23 °C, at flow rate of 250 mL/min and T_{in} of 21 °C. Here it is worth noting that the simulation was carried out at water inlet conditions (temperature and flow rate) and input radiation equal to those measured experimentally.

Figure 6-9 shows the variation in cooling water temperature at the outlet (T_{out}) with the change of flow rate as predicted by simulation and measured experimentally. It is clear that there is a good agreement between simulation and experimental results where maximum deviation of 7.07% at water flow rate of 250mL/min, while a minimum deviation of 0.6% at flow rate of 50 mL/min. Temperature difference between inlet and outlet cooling water (ΔT) decreases with the increase of flow rate from 8.7 °C at flow rate of 50 mL/min to about 1.5 °C at flow rate of 250 mL/min.

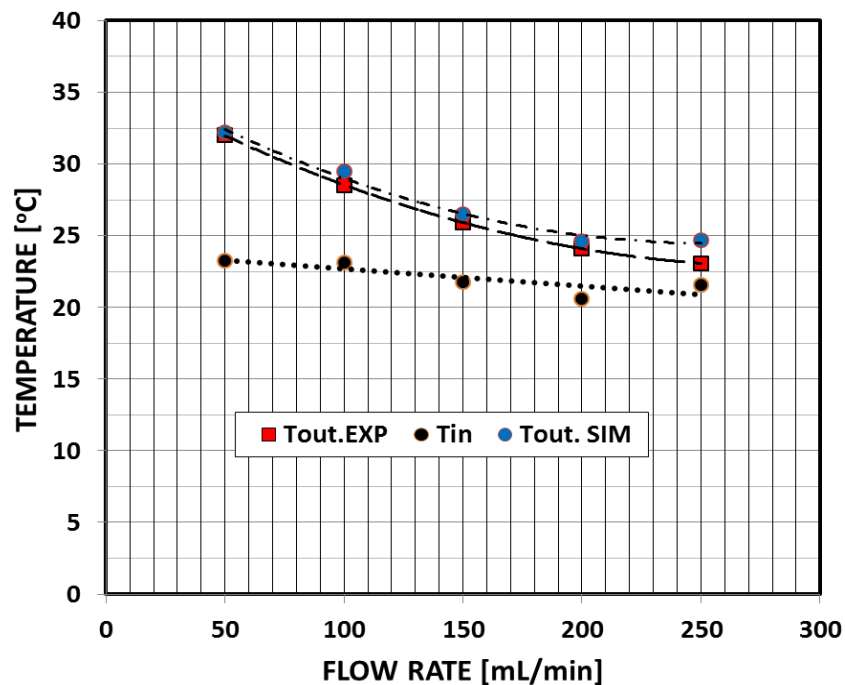


Figure 6-9 Validation of the change in cooling water temperature at the outlet with flow rate

6.4. Power output of CPV/T system under indoor conditions

6.4.1. Indoor power output of small scale CPV system

Figure 6-10 shows the measured I-V curves for PV cell with input irradiance of 651 W/m^2 without concentration using three different cooling methods namely no cooling, passive cooling (heatsink) and active cooling (heatsink with fan). It can be seen that the open circuit voltage, V_{oc} has increased from 0.522 V with no cooling to 0.554 V using passive cooling and 0.582 V under active cooling, while no significant change in short circuit current, I_{sc} . This increase in voltage is due to the decrease in cell temperature by cooling from about 51.6°C to 34.63°C using passive cooling and 19.97°C with active cooling that uses a fan with heatsink.

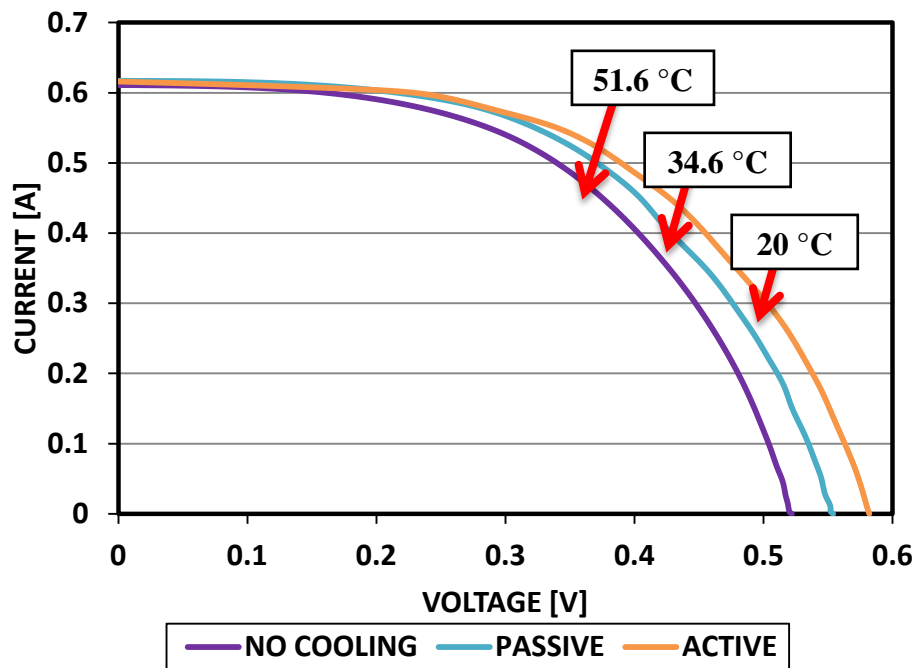


Figure 6-10 I-V curves for the PV cell under different cooling methods

Figure 6-11 to Figure 6-13 show the I-V curves of the PV cell output under various geometric concentration ratios 4, 6, 8 and 10 using various cooling mechanisms namely no cooling, passive cooling and active cooling and **Figure 6-14** shows the corresponding measured PV

cell temperature. **Figure 6-11** shows the PV cell I-V curves under various concentrations with no cooling where an increase in short circuit current from 0.611 A with no concentration to 1.71 A, 1.87 A, 1.94 A and 2.22 A as concentration ratio increases to 4, 6, 8 and 10, respectively can be observed. In contrast, the open circuit voltage dropped with the increase in concentration from 0.522 V with no concentration to 0.496 V, 0.491 V, 0.445 V and 0.435 V with concentration ratio of 4, 6, 8 and 10, respectively. This drop is due to the increase in PV cell temperature from about 51.6 °C with no concentration to about 134.6 °C with concentration ratio of 10 (**Figure 6-14**).

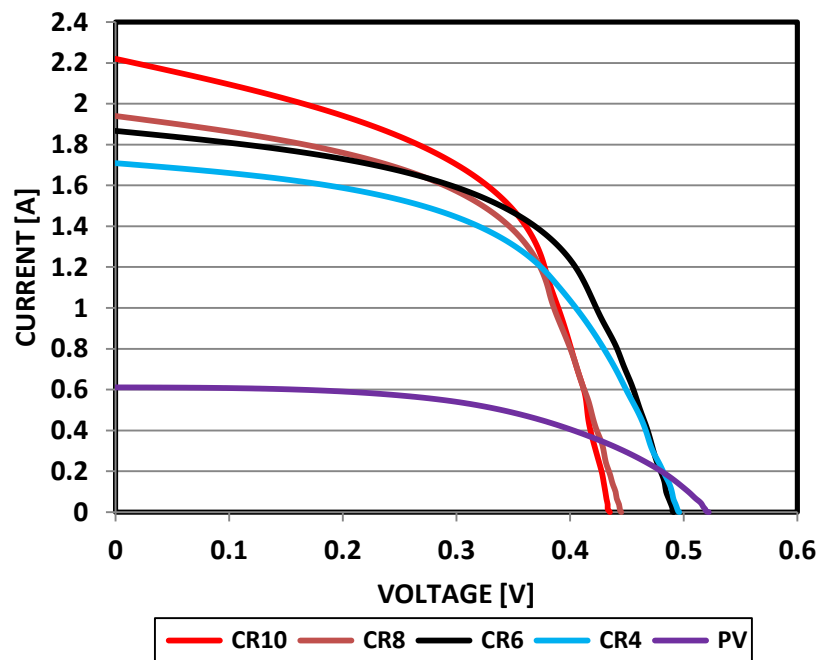


Figure 6-11 PV output with concentration and no cooling

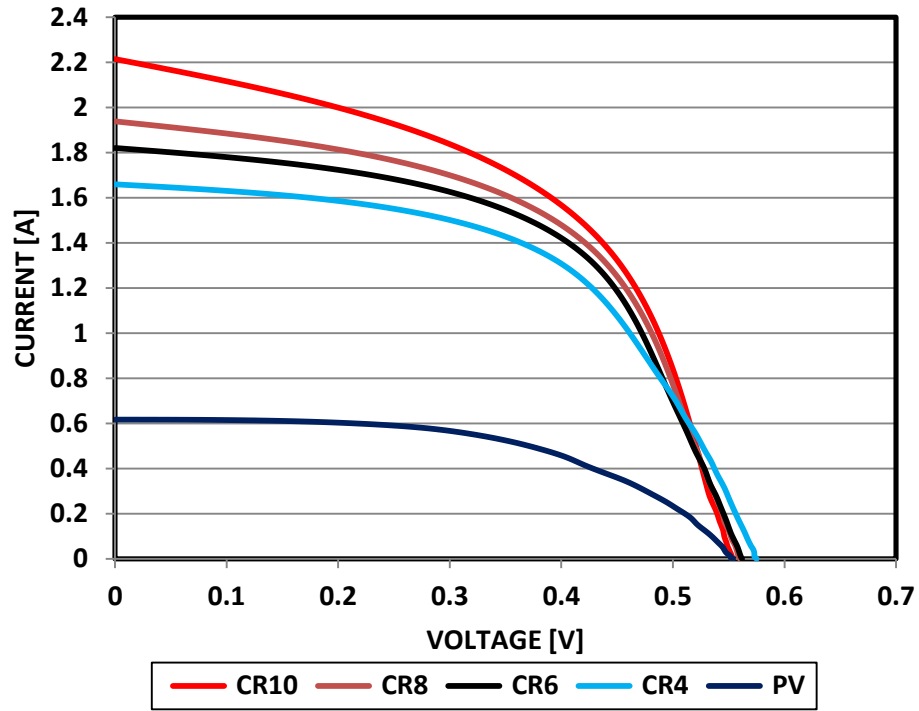


Figure 6-12 PV output with concentration and passive cooling

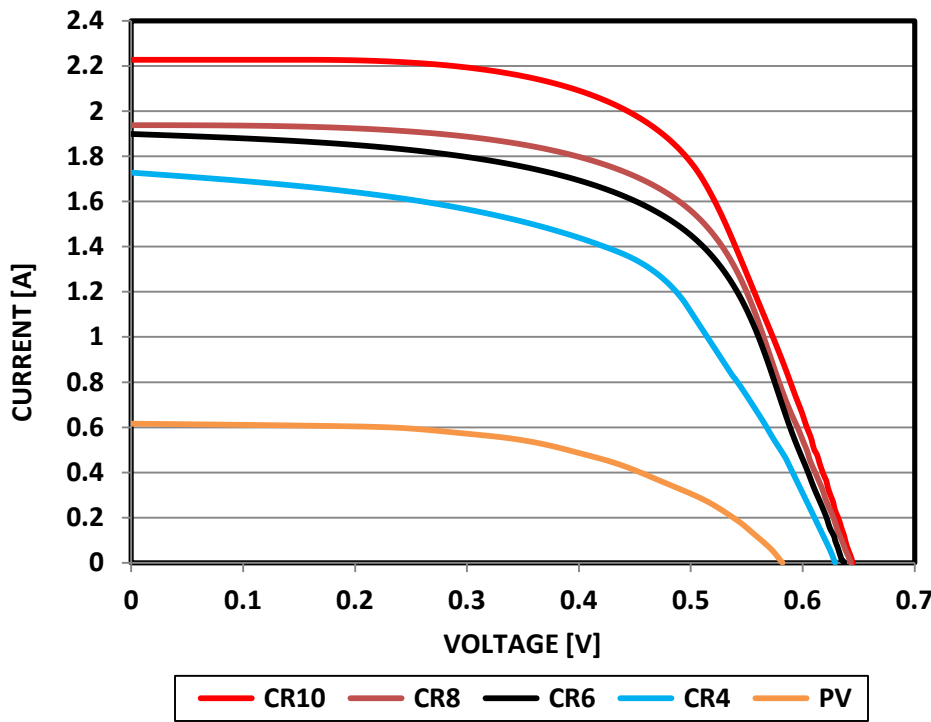


Figure 6-13 PV output with concentration and active cooling

Figure 6-12 shows the PV cell output with passive cooling under geometric concentration ratios of 4, 6, 8 and 10. It can be seen that no significant difference in the short circuit current compared to the case of no cooling shown in **Figure 6-11**, but the open circuit voltage has improved from 0.496 V, 0.491 V, 0.445 V and 0.435 V with no cooling to 0.575 V, 0.562 V, 0.56 V and 0.53 V at GCR 4, 6, 8 and 10, respectively. The PV cell temperature has decreased from 51.6 °C with no cooling to 34.63 °C with the use of passive cooling and no concentration, and from 134.6 °C with no cooling to 75.63 °C in the case of concentration ratio of 10 with the use of passive cooling, but this reduction in cell temperature is still relatively not sufficient when compared with the normal operating cell temperature of 42 °C to 46 °C [199]. Also although an increase in open voltage values with passive cooling was achieved, this voltage decreased with the increase in concentration, highlighting the need for further cooling enhancement. **Figure 6-13** shows the effect of using fan with the finned heatsink (active cooling) on the PV cell output under various concentration ratios. I-V curves show that the short circuit current remains similar to those shown in **Figure 6-11** and **Figure 6-12**, but the open circuit voltage was significantly improved. With concentration, open circuit voltage has increased from 0.629 V to 0.637 V, 0.643 V and 0.645 V as the concentration ratio increased from 4 to 6, 8 and 10 respectively. This improvement in voltage is due to the significant decrease in the cell temperature from 51.6 °C with no cooling to about 20 °C with active cooling and no concentration, and from 134.6 °C with no cooling to about 25.4 °C with active cooling at GCR of 10, which is close to the cell temperature used in standard tests [203].

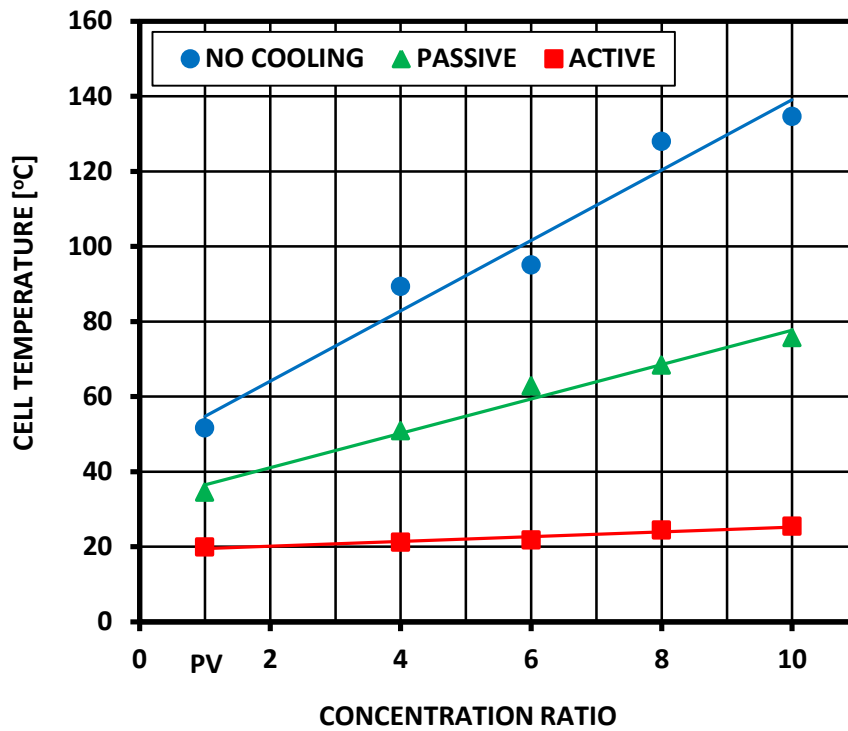


Figure 6-14 PV cell temperature under various operating conditions

Figure 6-15 shows the PV cell maximum power output as calculated by equation 5.6 under the three cases of cooling and four cases of concentration ratios. It is clear from this figure that with no cooling the power output increases, from about 0.17 W with no concentration to about 0.52 W with increasing the concentration ratio to 6. Then no significant increase in power at GCRs of 8 and 10 due to the high PV cell temperature (**Figure 6-14**) which increased from 95 °C at GCR 6 to 127.97°C and 134.6 °C at GCRs 8 and 10 respectively, which reduces the voltage and consequently decreases the power output.

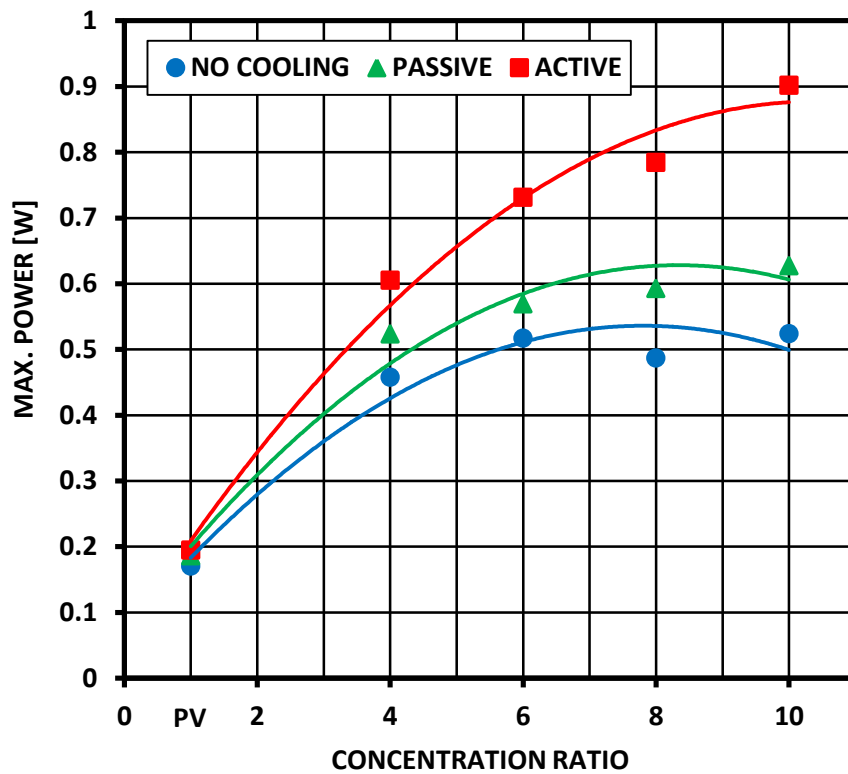


Figure 6-15 PV cell maximum power output at different operating conditions

Using passive cooling, the PV cell maximum power output has improved significantly from about 0.186 W with no concentration to 0.523 W with concentration ratio of 4, then continued to improve but at a lower rate to reach 0.569 W, 0.593 W and 0.627 W with the use of concentration ratios of 6, 8 and 10, respectively (**Figure 6-15**). This improvement is due to the decrease in PV cell temperature (**Figure 6-14**) from 51.6 °C to 34.5 °C for the PV with no cooling and from 134.6 °C to 75.633 °C for the PV with concentration ratio of 10. Active cooling has improved the PV cell power output significantly at all concentration ratios from about 0.195 W with no concentration to 0.605 W, 0.731 W, 0.784 W and 0.902 W with concentration ratios of 4, 6, 8 and 10, respectively (**Figure 6-15**). This improvement can be related to the significant decrease in PV cell temperature (**Figure 6-14**) at all concentration ratios to less than 25.4 °C. For instance, at maximum concentration ratio used (GCR=10), the

PV cell power output increased by about 90 % with active cooling from the case where no cooling is used. The electrical efficiency was calculated using equation (5.7). **Figure 6-16** shows the variation of PV cell electrical efficiency with concentration ratio using no, passive and active cooling. **Figure 6-16** shows that the PV cell efficiency decreased from 10.48 % for the PV cell with no concentration to 5.26 % with concentration ratio of 10 for the no cooling case. An increase in cell efficiency can be seen with the use of passive and active cooling to be 11.40 % and 11.97 % with no concentration and 6.32 % and 9.04 % with concentration ratio of 10, respectively.

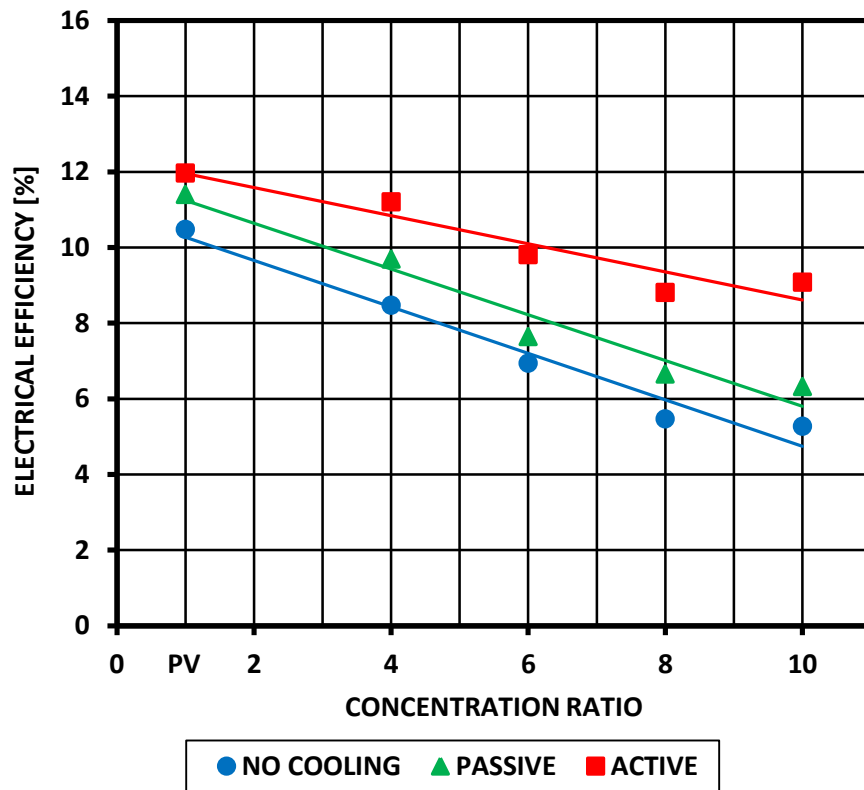


Figure 6-16 PV cell electrical conversion efficiency

Figure 6-17 shows the percentage improvement in the PV electrical efficiency due to the passive and active cooling at various concentration ratios compared to no cooling. It can be seen that the PV electrical efficiency improved by 9% using passive cooling and 14% using

active cooling compared to the PV cell efficiency under no cooling and no concentration, while about 20% improvement with passive cooling and about 72% improvement has been achieved with active cooling at concentration ratio of 10.

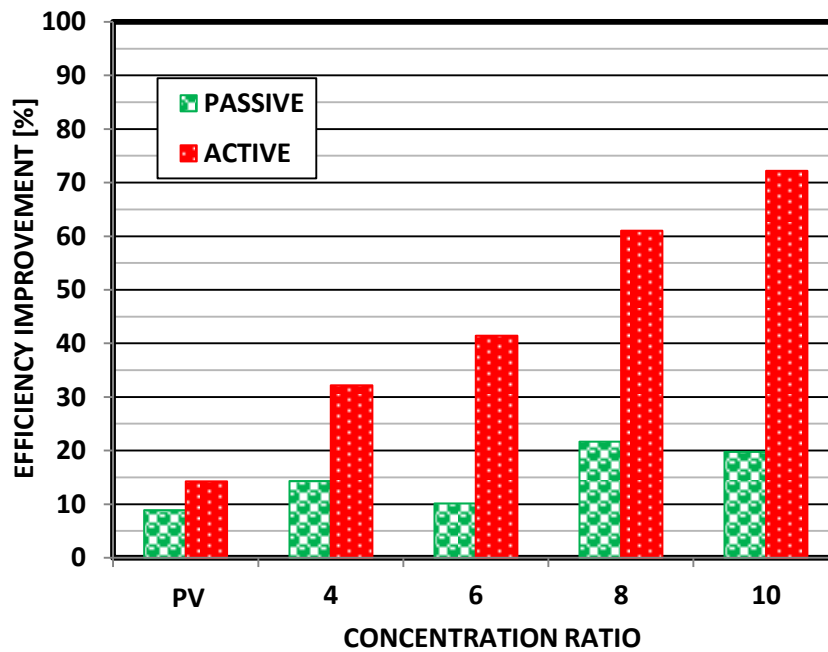


Figure 6-17 PV electrical efficiency improvement with cooling enhancement

The different values of efficiency improvement highlight the importance of choosing the appropriate cooling method to improve PV cell's electrical conversion efficiency at certain concentration ratio. For instance, there is little difference in the improvement of the PV cell with no concentration and of the PV under GCR 6 using passive cooling, while using active cooling, the improvement in efficiency increased by about three times that of passive cooling.

The percentage power gain of a Concentrator Photovoltaic (CPV) system determines the percentage output power increase compared to the reference power output with no concentration and no cooling. The percentage power gain is calculated using equation (6.2):

$$\text{Percentage Power Gain (\%)} = \frac{P_{CR} - P_{ref}}{P_{ref}} \times 100 \quad (6.2)$$

Where P_{CR} is the maximum power produced by the PV cell using concentrators, and P_{ref} is the maximum power output produced by the PV cell without concentrators and no cooling.

This increase in power gain will reduce the PV cell material that should be used in an application. This reduction can be calculated using equation (6.3):

$$\text{Material reduction (\%)} = \left(1 - \frac{P_{ref}}{P_{CR}}\right) \times 100 \quad (6.3)$$

The increase in power gain as calculated by the equation (6.2) is illustrated in **Figure 6-18**. With no cooling, PV cell power under GCRs 4, 6, 8 and 10 has increased by about 168.41%, 203.15 %, 185.61 % and 207.11%, respectively, more than PV cell with no concentration. This power gain is further enhanced when applying passive cooling to the PV cell to be about 181.89 %, 206.66 %, 219.22 % and 237.91%, for the same concentration ratios. With active cooling, the power gain is significantly higher than with no cooling and with passive cooling to be about 210.58 %, 275.27 %, 302.55 % and 362.85 %, indicating the potential of increasing CPV power gain using active cooling techniques.

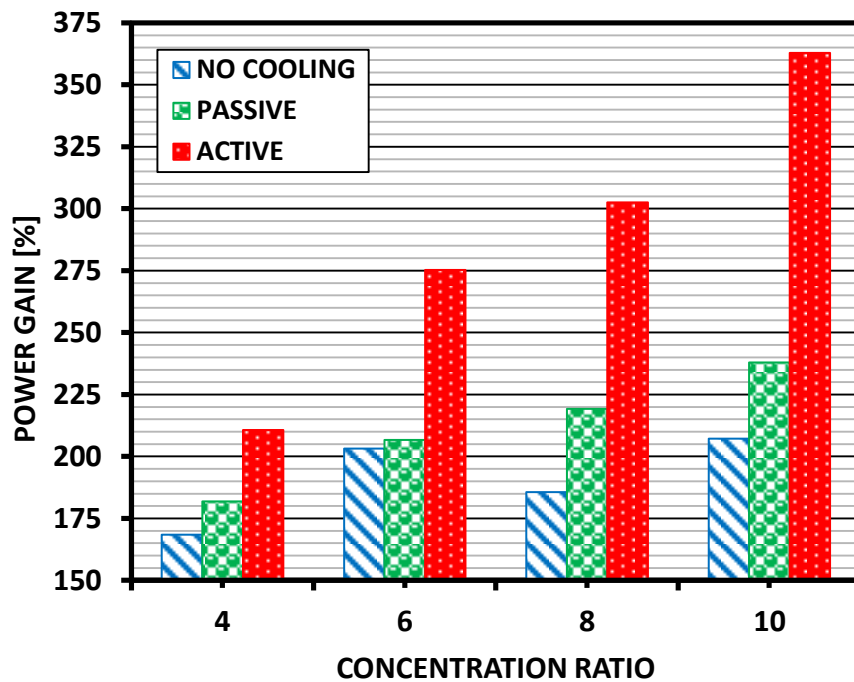


Figure 6-18 Increase in power gain using SAC at various cooling methods

From **Figure 6-18** it can be concluded that significant improvement in PV cell power output is possible using different concentration ratios and cooling methods. This will reduce the amount of PV material as illustrated in **Figure 6-19**. It is noticeable that under no cooling the use of concentration will reduce the PV material by about 62.74 %, 67.01 %, 64.99 % and 67.44 % at concentration ratios of 4, 6, 8 and 10, respectively to achieve the same power output as that produced by the PV cell with no concentration. Using passive cooling, the reduction in PV material is enhanced to reach 64.53 %, 67.39 %, 68.67 % and 70.41 % with the same concentration ratios. The most significant reduction in PV cell material occurred with the use of active cooling, where the PV material decreased by about 67.80 %, 73.35 %, 75.16 % and 78.39 % for the same concentration ratios (4, 6, 8 and 10). The cooling technique should be chosen carefully, especially at GCR 6 where it can be seen that no significant material reduction (67.01 to 67.39) between no cooling and passive cooling. On the other hand, there is significant increase (67.01 to 73.35) when active cooling was used.

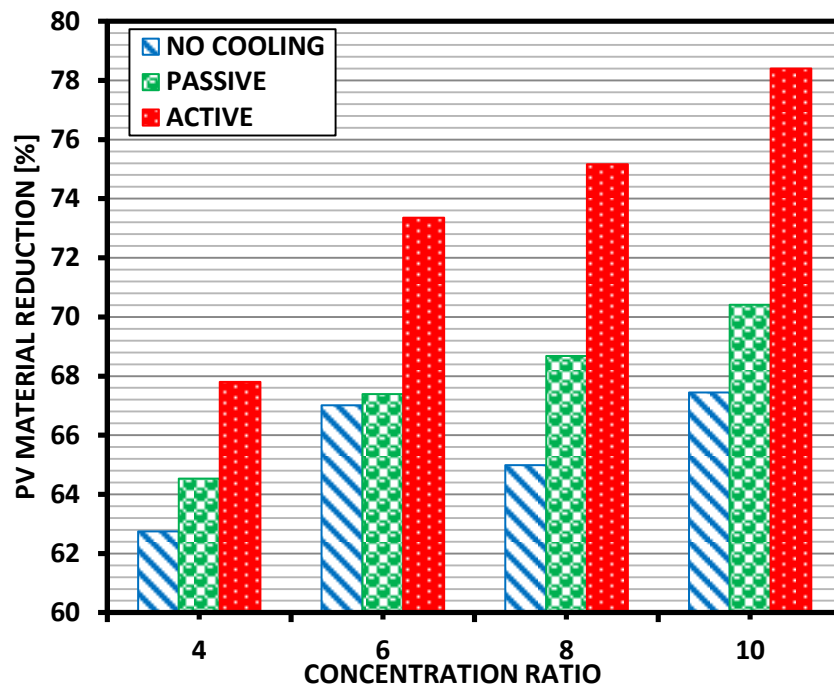


Figure 6-19 PV material reduction using SAC with cooling effect

6.4.2. Indoor power output of CPV/T system

The electrical output power of the CPV/T system with large scale SAC was tested indoor with geometric concentration ratio of 2 at different cooling conditions (with and without cooling). **Figure 6-20** shows the PV module power output and average temperature under no concentration and with concentration of 2 without cooling (natural convection) and with the use of water cooling at 50 mL/min flow rate. It is clear that both concentration and cooling flow rate have a significant effect on the PV module power output where the maximum power has increased without cooling from about 4.7 W to 6.45 W by the use of GCR2 concentrator and PV module temperature has increased from 40 °C to 49 °C under irradiance of 385 W/m². On the other hand, using cooling with concentrator has increased the power output to 6.76 W and decreased PV module temperature from 49 °C under natural convection to 32 °C using water cooling at flow rate of only 50 mL/min.

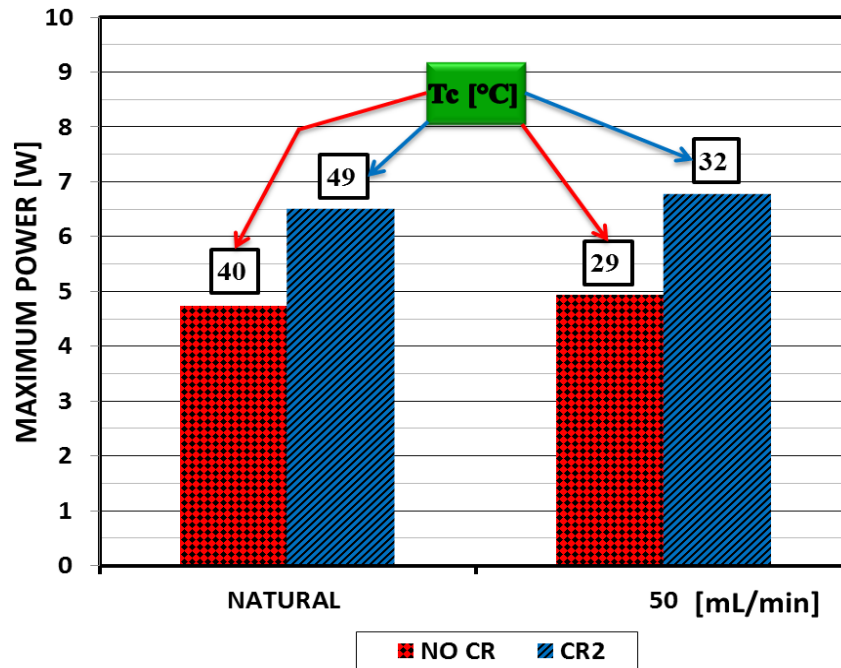


Figure 6-20 Effect of concentration cooling on PV module power output

Figure 6-21 shows the variation of CPV/T system maximum power output with the change of module temperature using water cooling at different flow rates (from 50 mL/min to 250 mL/min). PV module maximum power increases with the decrease of PV module temperature where it increased from about 6.5 W when module temperature is 49 °C under natural convection cooling to reach about 7.2 W when module temperature is 23.35 °C using water cooling at flow rate 250 mL/min. This clearly shows the positive effect of water cooling on the PV module electrical power output.

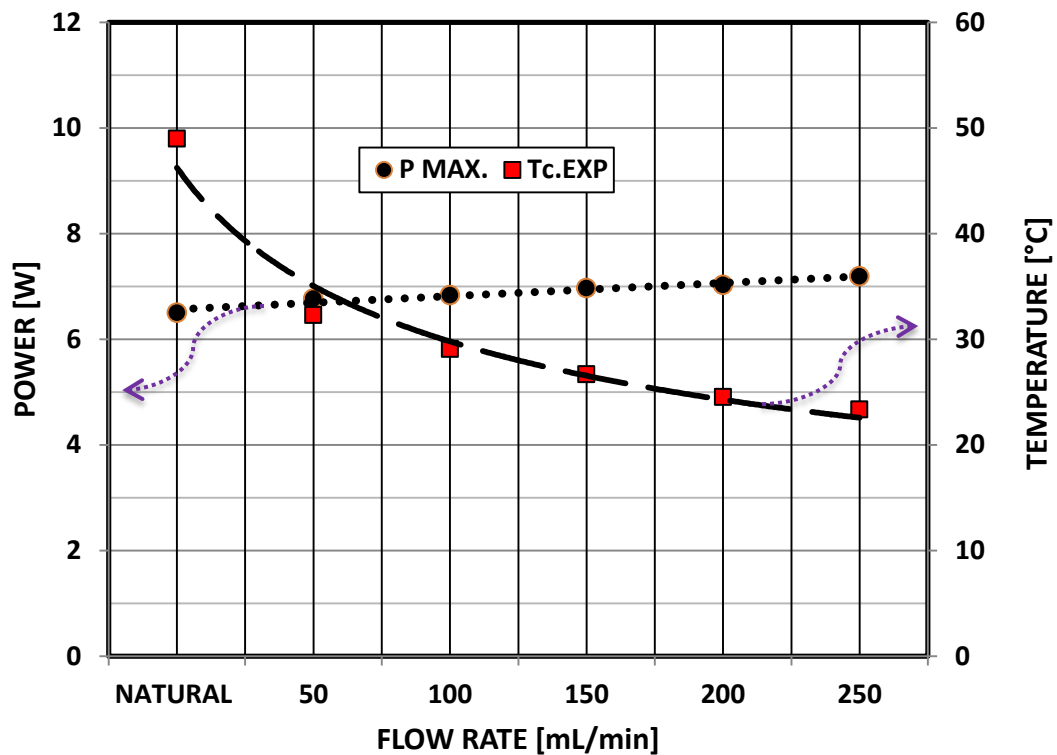


Figure 6-21 Change of CPV/T power output (large SAC with GCR2) with water cooling flow rate

6.4.3. Indoor and outdoor PV module power output comparison

Figure 6-22 shows I-V curves, which were taken during outdoor and indoor testing to the PV module. PV module was tested outdoor under irradiance of about 684 W/m^2 producing short circuit current of about 5.89A, and then tested indoor under light source under irradiance that produces similar short circuit current (5.92A). The indoor irradiance over PV module was mapped and the average irradiance value was very close to the outdoor irradiance (699 W/m^2) with a deviation of 2.2 % from the outdoor measured irradiance.

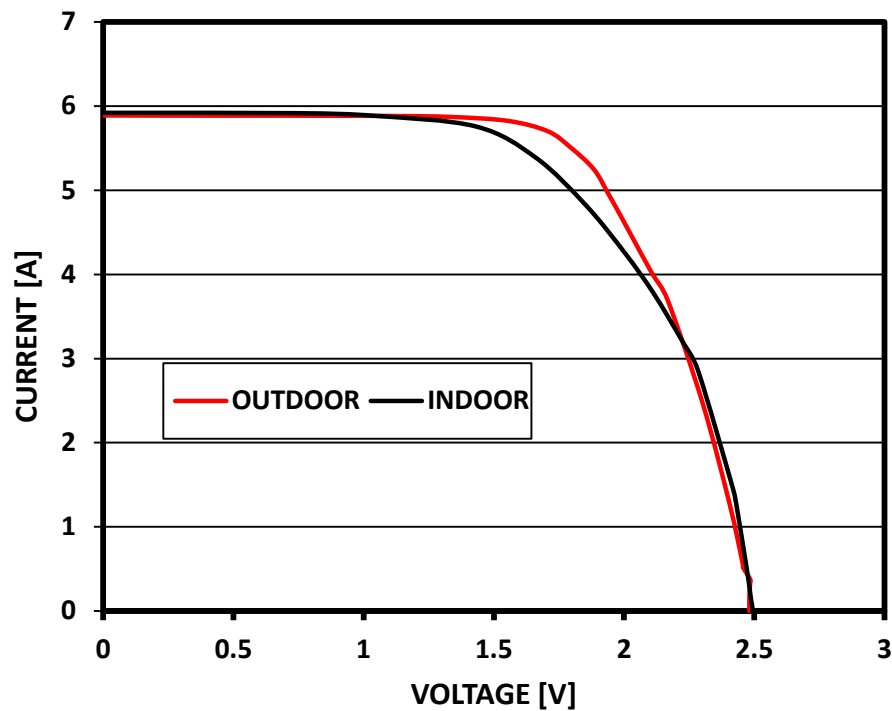


Figure 6-22 Outdoor and indoor I-V curve experimental measurements

This irradiance produced about the same open circuit voltage ($\approx 2.49\text{V}$) as the one generated by the PV module when tested outdoor. Also, the P-V curves taken during outdoor and indoor PV module testing as shown in **Figure 6-23** show close maximum output power values of 9.89 W and 8.95 W, respectively with a deviation of 9.5%. This indicates good agreement of indoor and outdoor generated current and power output which reflects the good light characteristics of the indoor solar simulator compared to the outdoor light.

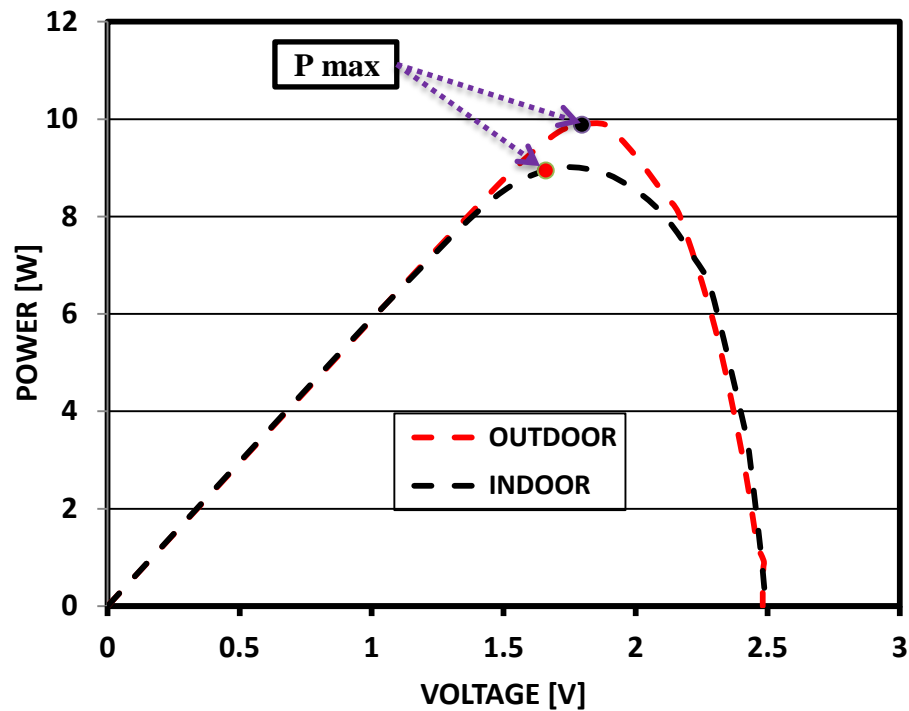


Figure 6-23 Outdoor and indoor P-V curve experimental measurements

6.5. Power output of CPV/T system under outdoor testing conditions

In this section, outdoor experimental results of the CPV/T system power output (electrical and thermal) using SAC with geometric concentration ratios of 2, 4 and 6 are presented. Testing of CPV/T was conducted on a clear sky day (18/ 08/2016) with irradiance ranging from 940 to 995 W/m², with and without cooling and manual sun tracking.

6.5.1. CPV/T electrical power output

Figure 6-24 shows the CPV/T module maximum electrical power output under no concentration and with concentration ratios of 2, 4 and 6, without cooling (natural convection) and with the use of water cooling. GCR 6 was not tested without cooling for the reason of high PV temperature that may damage the PV module. From **Figure 6-24** it is clear that PV module at all concentration ratios tested is performing better with than without cooling. Also it is noticed that the power output difference between cooling and no cooling increases with

the increase of concentration where in the case of no concentration the difference in output power between cooling and no cooling is about 1.36 W representing an increase by about 12 % from the case of no cooling. This increases further to about 25.3 % and 63.58 % in the cases of GCR2 and GCR4, respectively.

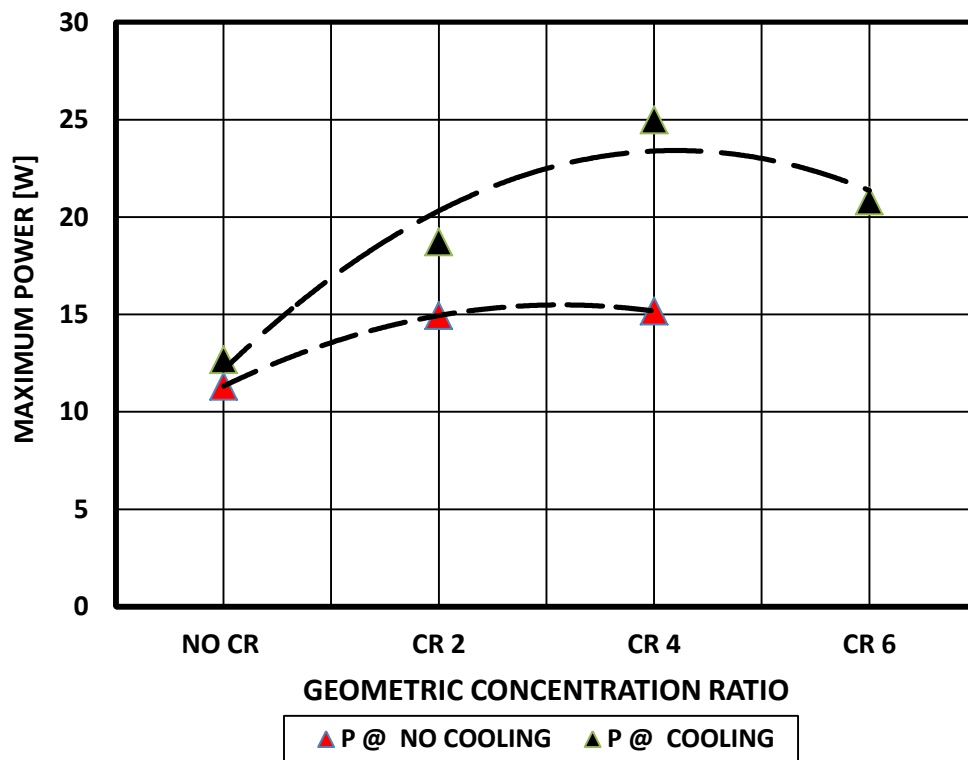


Figure 6-24 Power output of CPV/T system at different Geometric concentration ratios (cooling and no cooling, and flux of 940 -995 W/m²)

Figure 6-25 shows the PV module temperature (T_c) under no concentration and with concentration ratios of 2, 4 and 6, with no cooling (natural convection) and with the use of water cooling. Increasing the concentration increases the module temperature to reach about 112 °C with no cooling at geometric concentration ratio of 4. This PV module temperature is higher than the maximum working temperature of 90 °C and close to the temperature limit of destruction of 120 °C for PV module as reported by Kern [204]. Therefore, cooling is

necessary to maintain the PV cell temperature as low as possible, where using cooling water flow rate of 750 mL/min reduced the PV module temperature to about 25 °C.

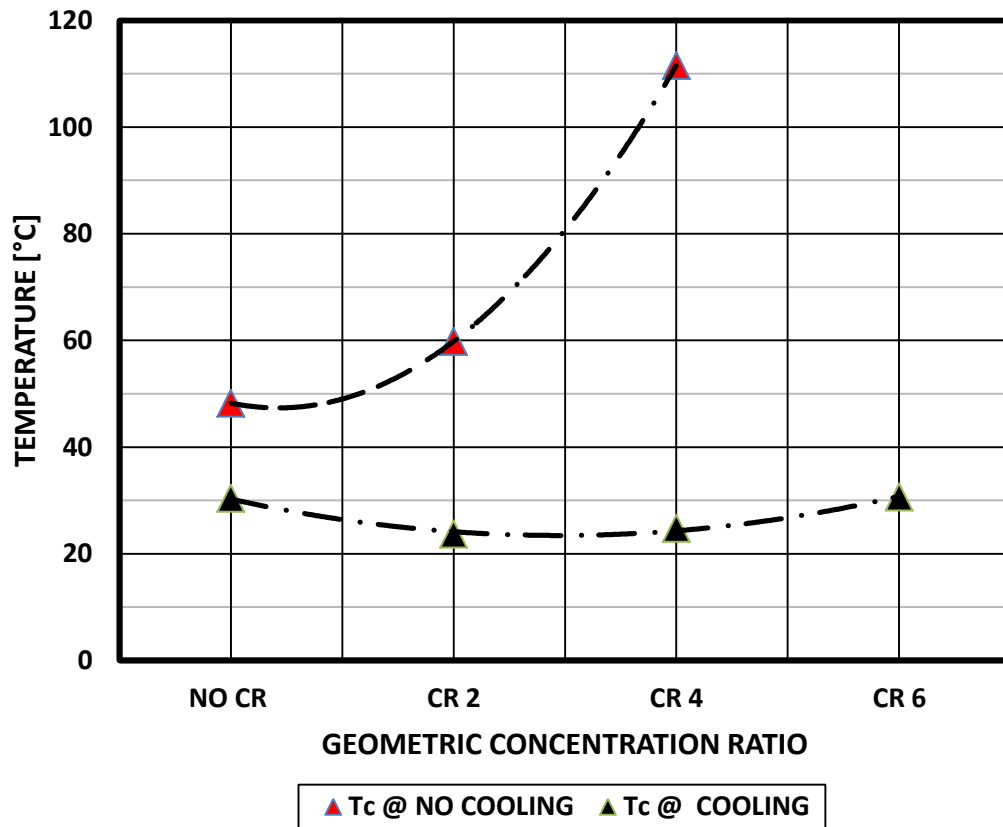


Figure 6-25 PV module temperature under no concentration and at different concentration ratios with and with no cooling (940 – 995 W/m²)

Figure 6-26 to **Figure 6-28** shows the effect of water cooling on the CPV/T electrical power output at different flow rates for geometric concentration ratios of 2, 4 and 6. It is clear that the power output is increasing with increasing the flow rate that decreases the module temperature (T_c) with the presence of concentration effect. Using SAC with geometric concentration ratio of 2, the maximum power increased from 17.166 W at flow rate of 50 mL/min to 18.725 W at the highest flow rate of 550 mL/min due to the decrease in the PV module temperature from about 37 °C to 24 °C.

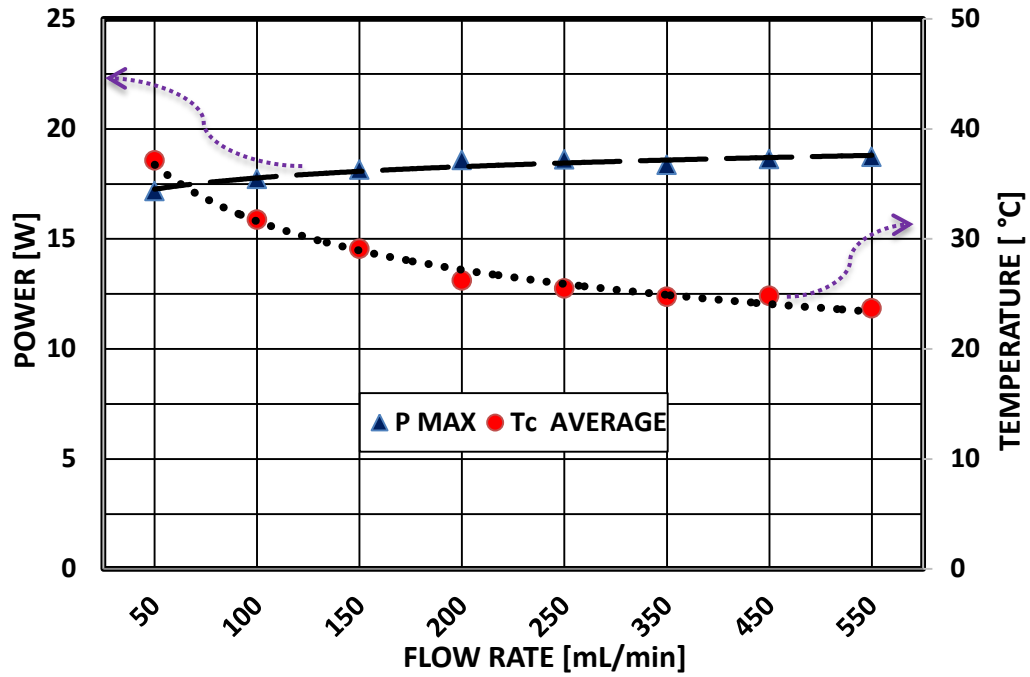


Figure 6-26 Effect of flow rate on CPV/T system electrical power output and module temperature at GCR 2 and average flux of 980 W/m²

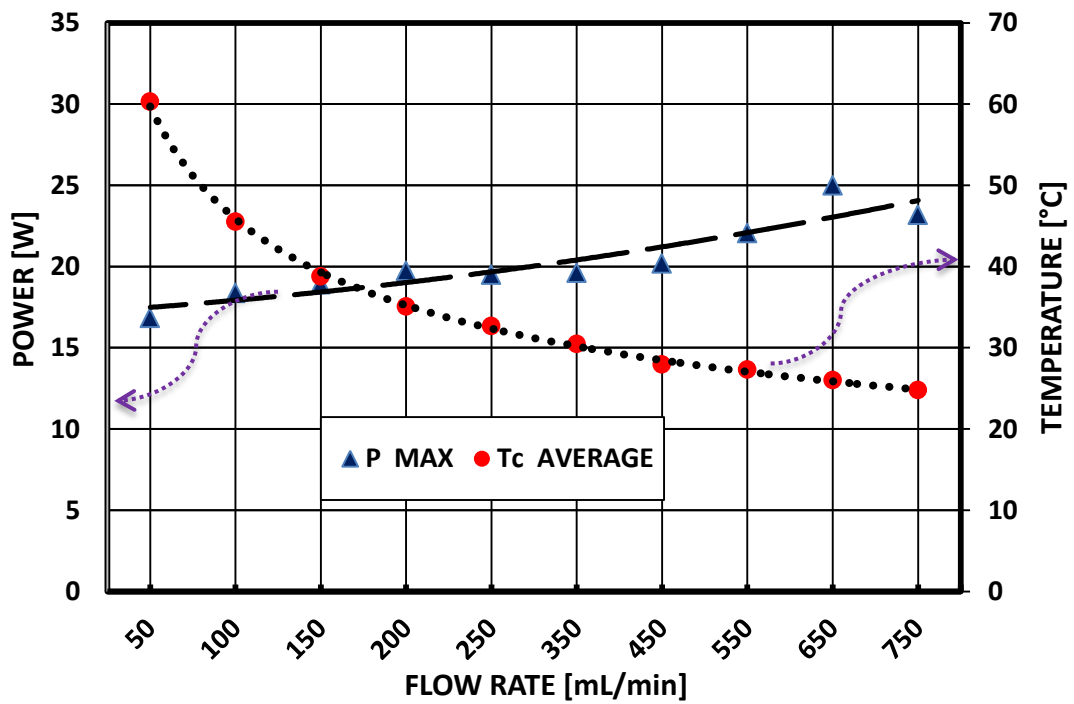


Figure 6-27 Effect of flow rate on CPV/T system electrical power output and module temperature at GCR 4 and average flux of 956 W/m²

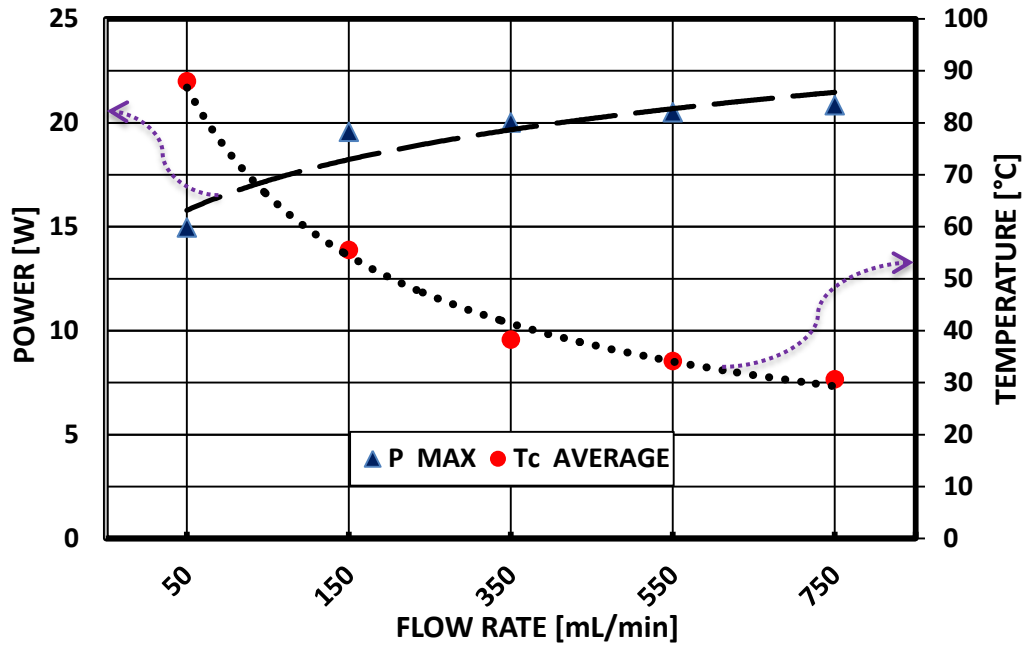


Figure 6-28 Effect of flow rate on CPV/T system electrical power output and module temperature at GCR 6 and average flux of 941 W/m^2

Using SAC with geometric concentration ratio of 4 the highest maximum power is 25 W at flow rate 650 mL/min that lowered the PV module temperature to about 25 °C compared to 16.84 W at flow rate 50 mL/min that kept the PV module temperature at about 60 °C (**Figure 6-27**). On the other hand, for SAC with geometric concentration ratio of 6 the highest maximum power is only 21 W at flow rate 750 mL/min that lowers the PV module temperature to about 31 °C compared to 15 W at flow rate 50 mL/min, which maintained the PV module temperature at about 88 °C (**Figure 6-28**).

6.5.2. CPV/T thermal output

The thermal output power (Q) of the CPV/T system was tested outdoor with geometric concentration ratios of 2, 4 and 6, at different water cooling flow rates. **Figure 6-29** shows the CVP/T system cooling water outlet temperature at different concentration ratios and flow rates. It can be seen that the outlet water temperature is highest at low flow rate and decreases

with increasing the flow rate. Using SAC with concentration ratio of 2 produces hot water with temperature (T_{out}) of 39.2 °C at 50 mL/min flow rate and inlet water temperature (T_{in}) of 24 °C. As the flow rate increases the outlet temperature decreases till reaching 27.5 °C, at flow rate of 550 mL/min. When SAC with concentration ratio of 4 is used, the water outlet temperature (T_{out}) is 63.8 °C at 50 mL/min flow rate and inlet water temperature (T_{in}) of about 29 °C. As the flow rate increases the water outlet temperature decreases to be 30.2 °C, at flow rate of 550 mL/min and T_{in} of 23.8 °C. Increasing the water flow rate to 750 mL/min lowers T_{out} to 28.1 °C, at T_{in} of 23.3 °C. As the concentration increased to GCR 6, the water outlet temperature increases to be 91.6 °C at 50 mL/min flow rate and inlet water temperature (T_{in}) of 27.6 °C. Increasing the flow rate to 550 mL/min and 750 mL/min, decreases the water outlet temperature to 33 °C and 30.6 °C, at T_{in} of 24.1 °C and 22.9 °C, respectively.

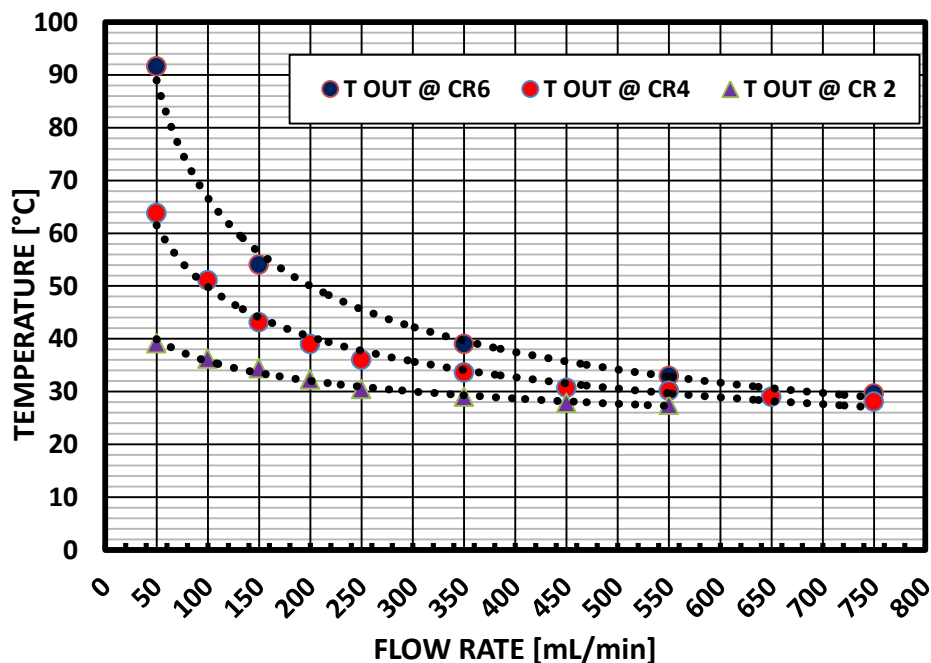


Figure 6-29 CPV/T system outlet water temperature under different concentration ratios and flow rates (flux of 940 to 995 W/m²)

Figure 6-30 shows the CVP/T system thermal output power (Q) and corresponding temperature difference (ΔT) of cooling water between inlet and outlet, at geometric concentration ratios of 2, 4 and 6 and different flow rates. The lowest flow rate produces highest temperature difference and lowest thermal power, while highest flow rate produces lowest temperature difference and highest thermal power. For the SAC with geometric concentration ratio of 2, the generated thermal power increased from about 54 W to 151 W with increasing flow rate from 50 mL/min to 550 mL/min which decreased the temperature difference from about 15 K to 4 K, respectively. At geometric concentration ratio of 4 the generated thermal power increased from about 124 W to 260 W with increasing the flow rate from 50 mL/min to 750 mL/min, which decreased the temperature difference from about 35 K to 5 K, respectively. This is 1.72 times the generated thermal power produced by SAC with concentration ratio of 2. Using SAC with concentration ratio of 6, the generated thermal power increased from about 228 W to 362 W with increasing the flow rate from 50 mL/min to 750 mL/min, which decreased the temperature difference from about 64 K to 7 K, respectively. This is also 1.4 times the generated thermal power produced by SAC with concentration ratio of 4.

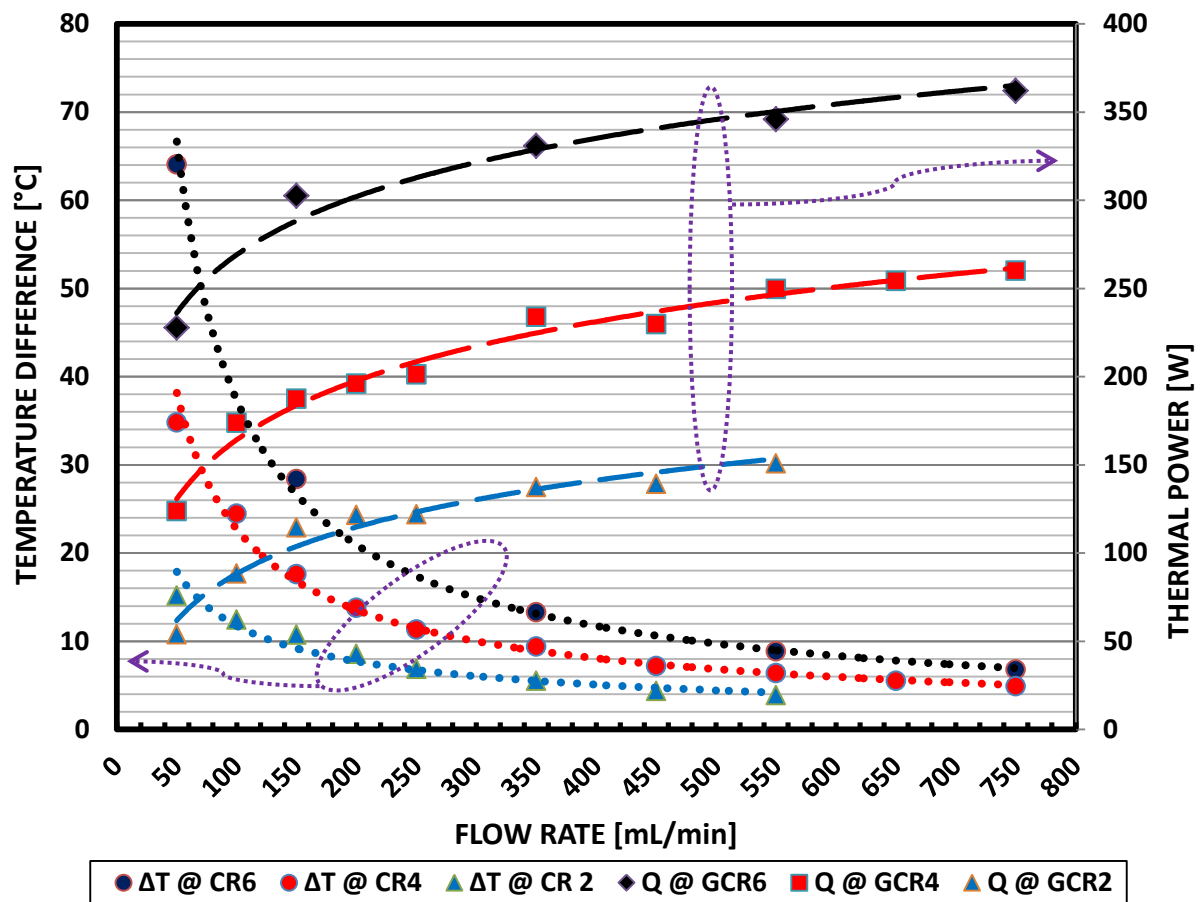


Figure 6-30 CVP/T system thermal output power and temperature difference at different geometric concentration ratios

6.5.3. Total CPV/T output

The total useful CPV/T system output energy comprises of the electrical output power and the extracted thermal energy under certain irradiance / concentration and water cooling flow rate.

Figure 6-31 shows the CPV/T system total output energy at geometric concentration ratios of 2, 4 and 6, and different water cooling flow rates. Although, the electrical power did not increase with the use of SAC with geometric concentration ratio of 6 compared to that generated by SAC with geometric concentration ratio of 4 (**Figure 6-26** to **Figure 6-28**), the total power generated by SAC of 6 is significantly higher than that generated by SAC of 4.

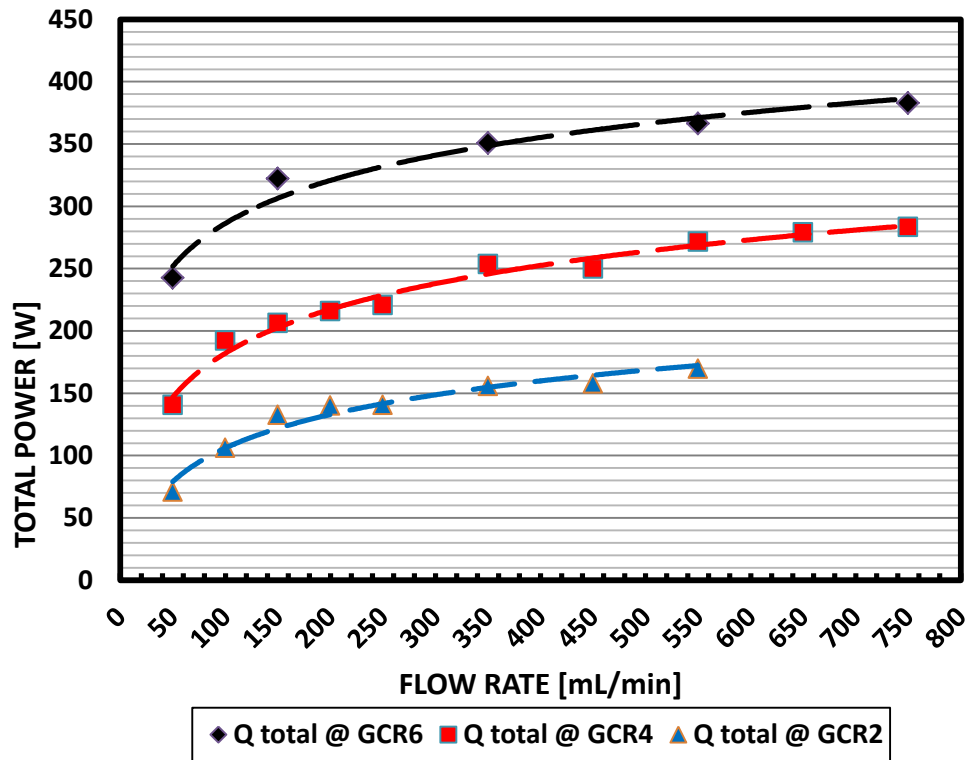


Figure 6-31 CVP/T system total output power at different geometric concentration ratios and flow rates (flux of 940 -995 W/m²)

6.5.4. CPV/T system power gain

The increase in electrical power gain as calculated by equation (6.2) is shown in **Figure 6-32**. With no cooling, PV module electrical power under GCRs of 2 and 4 has increased by about 32% and 34%, respectively, compared to PV module electrical power with no concentration. This power gain is further enhanced when applying water cooling to the PV module with different flow rates, ranging from 50 mL/min to 750 mL/min. At flow rate of 50 mL/min, the electrical power gain has increased to about 52 %, 49 % and 32 % for GCRs 2, 4 and 6, respectively. While at flow rate of 550 mL/min, the electrical power gain was further enhanced to be about 65%, 95% and 81% for the same GCRs, respectively. The decrease in electrical power gain with the increase of concentration ratio is due to the increase in PV

module temperature with higher concentration and cooling water flow rate still not sufficient to lower PV module temperature. Increasing flow rate at GCR 4 and 6 to 750 mL/min increased the power gain to 105% and 84% respectively, showing limited improvement in the electrical power generated by the CPV/T system with increasing concentration effect.

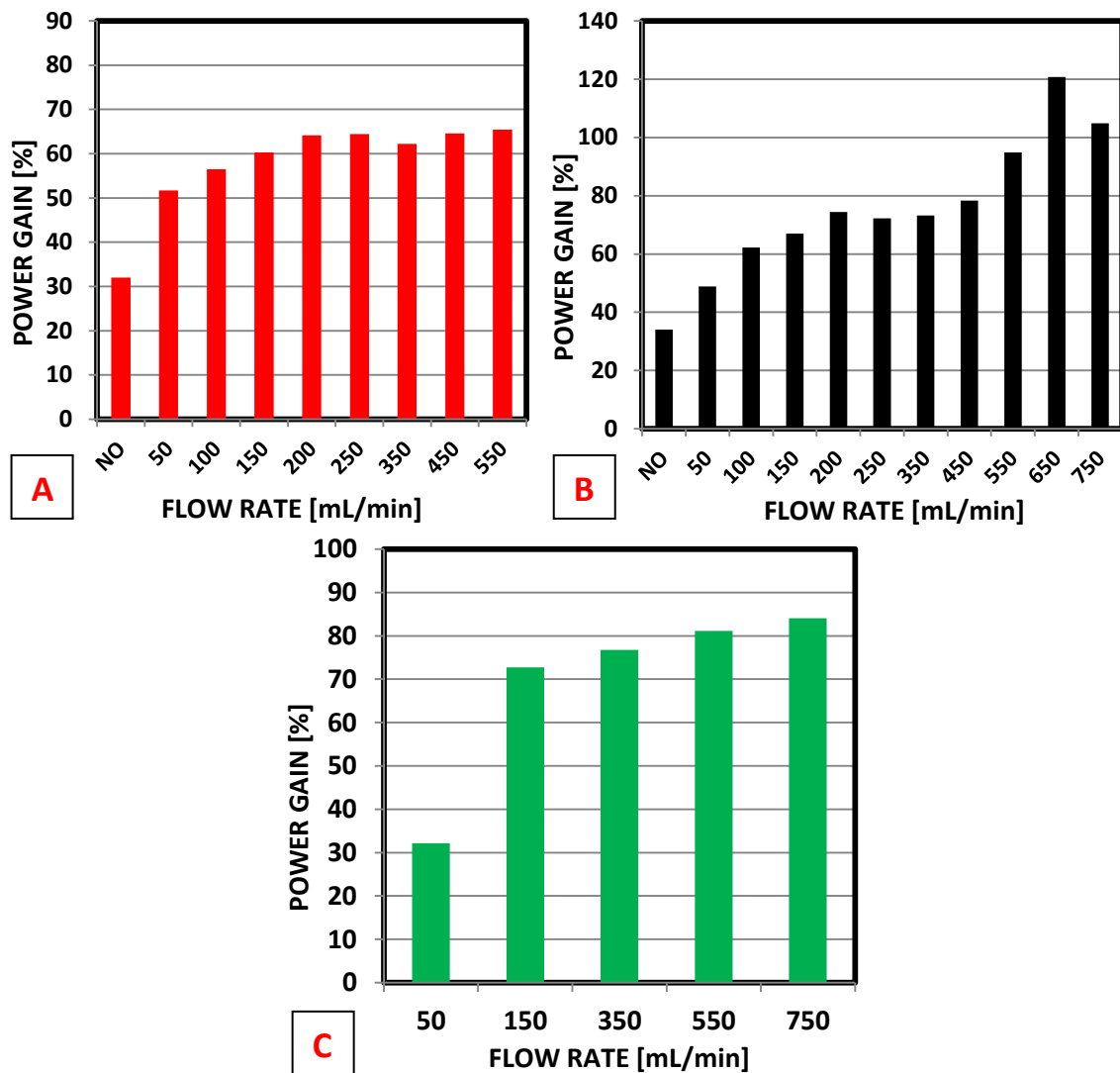


Figure 6-32 CPV/T system electrical power gain at different water flow rates: A- GCR2, B- GCR4 and C- GCR6 (940 – 995 W/m²)

The CPV/T system produces thermal power in addition to the PV module electrical power. The increase in thermal power gain is shown in **Figure 6-33**, where it is compared with the

PV module at no concentration and no cooling electrical output only with cooling and concentration effects are applied. At water cooling flow rate 50 mL/min, the thermal power gain achieved under GCRs of 2, 4 and 6 is significant, which is increased by about 379%, 1000% and 1924%, , respectively. This thermal power gain is further enhanced when applying higher cooling water flow rate of 550 mL/min to be about 1330%, 2119% and 2975%, for the same GCRs, respectively. As mentioned, at GCR of 2 there was no significant increase after this flow rate as the module temperature is close to the inlet cooling water temperature. While for GCRs 4 and 6, increasing the flow rate to 750mL/min enhanced the thermal power gain to be 2213% and 3119%, respectively.

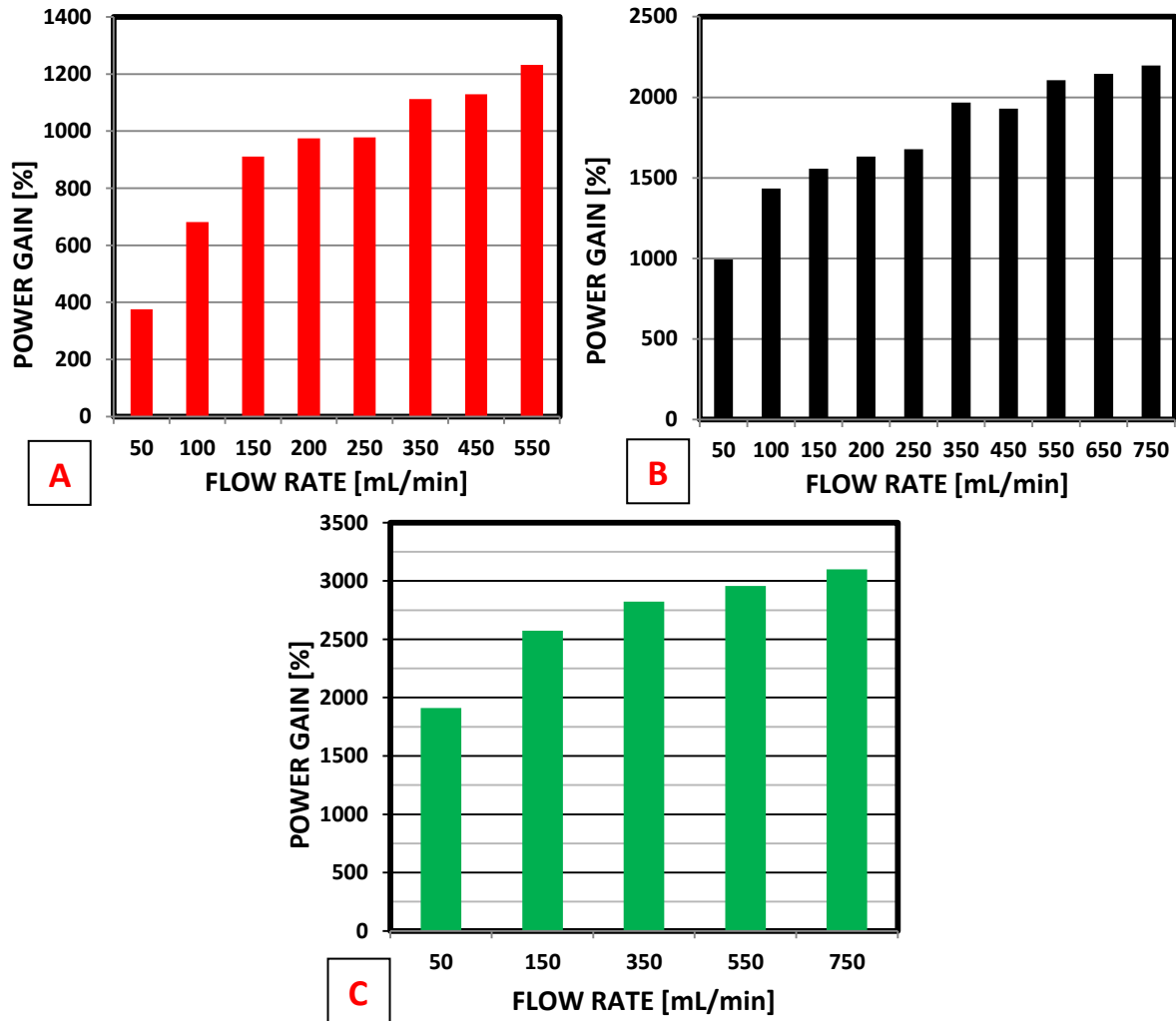


Figure 6-33 CPV/T system thermal power gain at different water flow rates: A- GCR2, B- GCR4 and C- GCR6 (940 – 995 W/m²)

The total power gain using different concentration ratios with and without cooling is presented in **Figure 6-34**. The total power gain using SAC with GCR2 is about 32% without cooling, which is only the electrical power from CPV system with no cooling, and no useful thermal power is extracted from the system, while the module temperature has reached 60 °C. A total power gain of 1398 % is achieved using water cooling at maximum flow rate used of 550 mL/min where module temperature decreased to be close to the inlet water temperature (≈ 24 °C). The total power gain has increased using SAC with GCR4 to about 34% with no

cooling and the module temperature reached about 112 °C, while enhancement of 2403% using water cooling at maximum flow rate of 750 mL/min and a decrease in module temperature to about 25 °C. Increasing SAC GCR to 6, increased the total power gain to 2044% at cooling water flow rate 50 mL/min and module temperature reached about 88 °C, while with cooling flow rate of 750 mL/min the total power gain has increased to 3283%, which is a result of reducing the module temperature to about 30 °C. Also it is noticed from **Figure 6-34** that the total power gain has increased with a constant value ($\approx 850\%$) with the variation of concentration ratio especially with higher cooling flow rates.

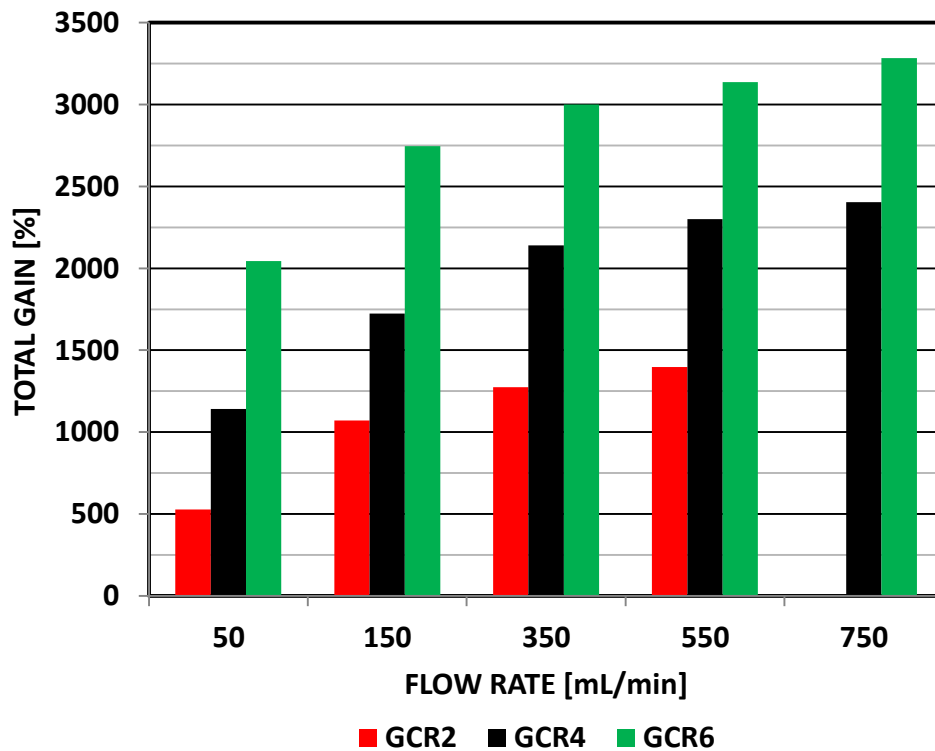


Figure 6-34 CPV/T system thermal power gain at different water flow rates and GCRs of 2, 4 and GCR6 (940 – 995 W/m²)

6.5.5. CPV/T System efficiency

The experimental testing results of the CPV/T system total performance with geometric concentration ratios of 2, 4 and 6, and different cooling water flow rates is shown in **Figure 6-35**. It is clear that the system efficiency is at its lowest value with the lowest cooling water flow rate and the lowest concentration ratio, where the total efficiency of the CPV/T system is about 40 %, 44 % and 50 % at geometric concentration ratios of 2, 4 and 6, respectively. But with the increase of flow rate the total efficiency increased to be the highest at the highest flow rate, but with lowest geometric concentration ratio where the total efficiency of the CPV/T system reached about 95 %, 88 % and 78 % at geometric concentration ratios of 2, 4 and 6, respectively.

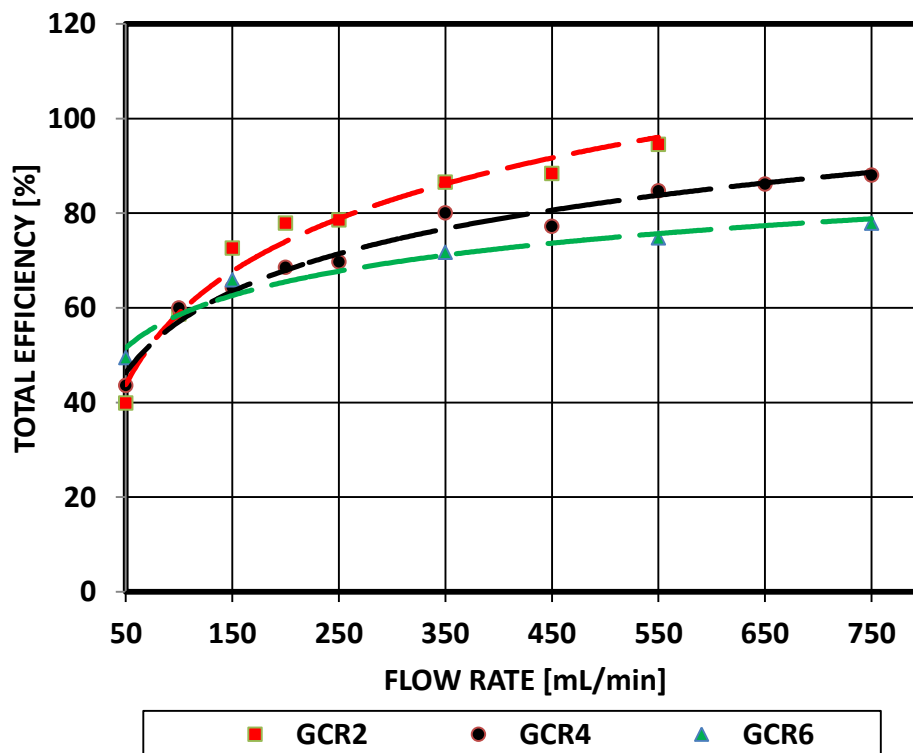


Figure 6-35 CPV/T system total efficiency (940 – 995 W/m²)

6.6. Conclusion

The optical validation results of SAC showed good agreement between experimental and simulation using OptisWorks software for the concentrator optical efficiency, and received flux distribution at various concentrator material surface reflectivity. Using geometric concentration ratios (GCR) of 2, 4 and 6, the maximum deviation in optical efficiency of 9.13 %, which is at GCR 4. The deviation in received flux distribution for most of flux values are within deviation $\pm 20\%$ and with an average of $\pm 12 - \pm 14 \%$ for the tested concentration ratios. Regarding the effect of concentrator reflective material on the efficiency, maximum deviation from experiment is 11.5 % with GCR6 using Stainless steel 315 (ref. = 57.35 %).

Indoor thermal experimental testing and simulation using Comsol multi-physics for the PV module temperature (T_c) using SAC with GCR2 and different cooling water flow rates shows maximum deviation of 5.86% at water flow rate of 50mL/min, while validation results for outlet water temperature, the maximum deviation is 7.07% at water flow rate of 250mL/min.

Three GCRs of 2, 4 and 6 for HAC were tested experimentally to investigate the optical efficiency of the concentrator showing optical efficiencies of about 83%, 84% and 76%, respectively. Comparing HAC with SAC at the same geometric concentration ratios, both concentrators have similar optical efficiency with no significant difference and highlighting the feasibility of such geometry to be used in CPV systems.

PV module indoor and outdoor testing showed a good agreement of maximum power output values (8.95 W and 9.89 W, respectively) with a deviation of 9.5%. CPV/T system electrical power output under indoor conditions of both small and large scale SAC was tested and power output results showed a significant increase in PV cell power output with concentration, especially when active cooling is applied. A significant improvement was

observed in small scale CPV system electrical conversion efficiency with the use of active cooling reaching up to 72%, and the power gain by 362.85 %, while the PV cell material was reduced by 78.39 %, at GCR10. Large scale CPV/T system shows also an improvement in electrical power output with the increase of cooling water flow rate that contributes to decreasing module temperature under indoor testing conditions. Testing CPV/T system power output under outdoor conditions and cooling effect, showed an enhancement in both electrical and thermal power output, and consequently the generated total power output, with the increase of concentration ratio and flow rate.

The main advantage of this CPV/T system is that a higher total power output (by module area) compared with flat PV module which produces only electrical power. For instance, CPV/T with geometric concentration ratio of 2 (area of two PV modules) has a total power output (thermal and electrical) of about 180 W, compared with a total power output of two modules of about 23W, which results in an increase of more than 8 times the flat PV. Increasing the concentration to 6 increases the total power to about 385 W resulting in an increase of 7 times the flat PV consisting of 6 flat PV modules with output of 68 W. The total efficiency of the CPV/T system reached about 95 %, 88 % and 78 % at geometric concentration ratios of 2, 4 and 6, respectively at highest flow rate. These results highlight the benefits of such system in generating both electrical and thermal power for domestic use as one useful package of energy.

CHAPTER 7: CONCLUSIONS AND RECOMMENDATIONS FOR FUTURE WORKS

7.1. Introduction

Use of renewable energy sources is receiving significant interest worldwide to provide energy for human life social and industrial development. Today's world is facing problems related to the excessive burning of conventional fossil fuel energy sources by the industrial developed nations such as global warming, air pollution and climate change, while developing nations still in need for sufficient energy generation and supply. The best available solution for these problems is to harnessing renewable energy sources, as planned by many countries, such as solar, wind, geothermal and nuclear energy.

Although clean and reliable solar (photovoltaic and thermal) energy is likely to be a good alternative to conventional sources, which expected with wind energy to be 60% of total energy produced by 2040, this technology is not meeting the world needs as well as it has low systems' efficiency and higher initial costs. This leads to the need for more research into solar energy systems including development, optimization and performance enhancement of new solar systems.

Although Middle Eastern and North African countries enjoy high levels of direct solar radiation, the total electricity generated from renewable sources is not more than 4% of total electricity generated in the area due to its high cost, and to the availability of conventional fossil fuel energy sources like oil and natural gas in this area.

Libya has a total area of 1,759,540 km² and a large part of the country is located in the Sahara desert, and enjoys high rate of solar radiation with high beam component of a maximum average annual direct normal solar irradiance reaching 3000 kWh/m² per annum. The consumption of electrical energy (kWh/capita) in Libya has increased, by more than 111% in the period from 2000 to 2012, due to the development of all life sectors as a result of the quick economic improvement of living standards. The total installed capacity of renewable energy is only about 0.06 % of the total produced, while 99.94 % uses fossil fuel. The lack of development in solar energy systems in Libya is due to many factors involving the relatively high cost compared with the conventional available sources (oil and gas), absence of encouragement and awareness by the authorities, as well as the lack of sufficient research and the war that has erupted in 2011, which also affected the quality of energy provided to the public consumption.

In this research project, an investigation was conducted to enhance the performance of a low concentrating photovoltaic thermal (CPV/T) system using 3D flat sided (V-trough like) concentrator with different concentrators' geometry configurations and effective cooling facility. The optical investigation took into account different design parameters that affect the optical performance of the system; amount of radiation available, optical design parameters like concentrator's side angle, concentrator material reflectivity, gap distance between concentrator and receiver and incidence angle and their effect on the optical efficiency and received flux distribution. The thermal investigation includes design of cooling facility, which was carried out by simulating five different flow configurations of the cooling duct. The choice of optimum design was through the minimum PV module temperature and maximum outlet water temperature, where all duct geometries are designed in a way to provide good contact surface with the PV module back surface. Then, thermal investigation was carried out to the PV module

under solar flux of 1000 W/m^2 , with and without cooling, at different ambient temperature values ranging from 15°C to 50°C , and with cooling flow rate ranging from 50 mL/min to 850 mL/min . this is to investigate the effect of both variables (ambient temperature and flow rate) on PV operating temperature. Then the received flux of three different geometric concentration ratios of SAC exported from OPTISWORKS optical software was imported with the real distribution to COMSOL multi-physics software to study the effect of different operating conditions on the CPV/T system thermal performance, and indicate the optimum cooling flow rate that makes the PV module working within the Nominal Operating Cell Temperature (NOCT) ranges of 42°C to 46°C .

7.2. Theoretical and experimental investigation conclusions

Comprehensive, optical, electrical and thermal investigations on the CPV/T system using 3D flat sided concentrator were conducted.

7.2.1. Conclusions from optical modelling and experimental work

Four different 3D flat sided concentrators were mathematically modelled; Squared Aperture concentrator (SAC), Hexagonal Aperture Concentrator (HAC), Octagonal Aperture Concentrator (OAC) and Circular Aperture Concentrator (CAC) for photovoltaic application. Mathematical modelling results were compared to those obtained using OptisWorks software. Conclusion regarding the optical performance involves the following:

- Novel mathematical optical model was generated, to the HAC geometry to calculate the geometrical concentration ratio (GCR_{HAC}) and actual concentration ratio (ACR_{HAC}) by the inlet aperture area (A_{in}) a function of aperture width (W_{in}) and number of reflections (n),

and material reflectivity (ρ) and at any concentrator side angle (ψ), consequently the optical performance.

- Novel mathematical optical model was generated, to calculate the geometrical concentration ratio (GCR_{OAC}) and actual concentration ratio (ACR_{OAC}) by the inlet aperture area (A_{in}) a function of aperture width (W_{in}), number of reflections (n) and material reflectivity (ρ) of the Octagonal Aperture Concentrator at any concentrator side angle (ψ), consequently the optical performance.
- Good agreement between results of the mathematical models and the optical simulation results for the optical efficiency of the four geometries with an average deviation of 5.1 %, 2.4 %, 2.1 % and 0.67 % for the SAC, HAC, OAC and CAC geometries, respectively.
- The optimum concentrator side angle was chosen depending on the highest optical efficiency and the lowest concentrator height consequently less material used in fabricating the concentrator.
- The optimum concentrator side angle (ψ) of the four geometries with the same GCR has the same value, and the optimum concentrator angle decreases with the increase of concentration ratio.
- Optimum concentrator side angles for GCR of 2, 4, 6, 8 and 10 are 35°, 30°, 20°, 20° and 15°, respectively. Also concentrator height increases with the decrease of side angle.
- Good agreement between simulation and experimental results of the SAC optical efficiency using Miro-Sun PV reflector material 90.1% for three different GCRs of 2, 4 and 6 with a maximum deviation of 9.13 % at GCR 4, and a minimum at GCR 2 with a deviation of 0.37 % from experimentally measured optical efficiency.

- Optical efficiency is increasing with the increase of surface reflectivity, and good agreement between simulation and experimental results of the SAC using three different concentrator material reflectivity values with maximum deviation of 11.5% with the use of 316 polished stainless steel (Ref. = 55.35%) and minimum deviation of 1.97% with the use of mirror (Ref. = 72.95%).
- Received flux distribution generated by the four geometries was evaluated using Standard Deviation (σ) and Coefficient of Variance (CV), where lower value represents better flux uniformity. σ and CV calculation results showed that the best uniformity among the four geometries is SAC with $\sigma = 629 \text{ W/m}^2$ and $\text{CV} = 0.16$, followed by HAC with $\sigma = 1246 \text{ W/m}^2$ $\text{CV} = 0.29$ and OAC with $\sigma = 1418 \text{ W/m}^2$ $\text{CV} = 0.34$.
- CAC generates the worst case of received flux distribution with $\sigma = 4582 \text{ W/m}^2$ and $\text{CV} = 1.1$, which is a result of highly concentrated flux at the center and little flux is distributed on the rest of receiver area.
- Good agreement between simulation and experimental results regarding flux distribution validation using SAC geometry, with an average deviation of 12 -14 % for the compared concentration ratios, where the calculated deviation of most points is between 0% (full agreement) and ± 20 %.

7.2.2. Conclusions from thermal modelling and experimental work

The thermal modelling was conducted using COMSOL Multi-physics software to characterize the thermal performance of the CPV/T system. Conclusions are summarized in the following points:

- For better performance of cooling facility, the selected U-type cooling duct configuration provides best performance, in which highest outlet cooling water temperature and lowest PV module average temperature among the modelled configurations were achieved.
- Indoor experimental validation of the CPV/T system was conducted with different cooling water flow rates ranging from 50 mL/min to 250 mL/min under GCR of 2. Validation results for the PV module temperature (T_c) showed good agreement between simulation and modelling with maximum deviation of 5.86% at water flow rate of 50mL/min, while a minimum deviation of 1.01% at flow rate of 250 mL/min.
- Validation results for the outlet cooling water temperature (T_{out}) showed good agreement between simulation and modelling with maximum deviation of 7.07% at water flow rate of 250mL/min, while a minimum deviation of 0.6% at flow rate of 50 mL/min.
- The comprehensive thermal modelling results showed that in the worst case where there is no cooling, ambient temperature (T_a) is 50 °C and GCR 6, PV module temperature reaches very high average temperature exceeding 169 °C that is about 125 K higher than the Nominal Operating Cell Temperature range (NOCT = 42- 46 °C).
- Using cooling flow rate of 250 mL/min reduces PV module temperature to about 42 °C, consequently reduces the concentration effect and makes the PV system works at the normal temperature. Apart from GCR6, other GCRs used and PV without concentration, the flow rate that limits PV module temperature to the NOCT ranges between 50 and 150 mL/min.

- From thermal simulation and experimental work at all conditions with and without concentration, increasing flow rate decreases PV cell/module temperature, hence increasing system electrical and thermal performance.
- This system can be used in various applications, depending on the outlet water temperature generated. For instance, for low temperature ($> 30\text{ }^{\circ}\text{C}$) the system could be used for swimming pool water heating [205], and this temperature can be achieved from the system with concentration ratios of 2, 4 and 6. While for medium temperature ($30\text{ }^{\circ}\text{C} - 100\text{ }^{\circ}\text{C}$) the system can be used for domestic hot water and space heating using concentration ratio of 4 and 6.
- Using the thermal output of the system for residential applications that run at temperature range of $20\text{--}90\text{ }^{\circ}\text{C}$, can reduce the consumption of fuel by about 50 %-70 % for hot water and by 30 % - 60 % for space heating applications [206].

7.2.3. Conclusions from electrical experimental work

- A comparison was made for the light source and its effect on PV module electrical output by using metal halide arc lamp for indoor and sun light for outdoor experimental work. PV module testing showed a good agreement for the maximum power output values (8.95 W and 9.89 W, respectively) with a deviation of 9.5%.
- CPV/T system electrical power output under indoor conditions to both small and large scale SAC was tested and power output results showed a significant increase in PV cell/module power output with concentration, especially more enhanced when active cooling is applied.

- A significant improvement was observed in small scale CPV system electrical conversion efficiency with the use of active cooling reaching up to 72%, and the electrical power gain by 362.85 % while PV cell material can be reduced by 78.39 %, at GCR10.
- Large scale CPV/T system showed also an improvement in electrical power output with the increase of cooling water flow rate that contributes to decreasing the module temperature under indoor testing conditions.

7.2.4. Total power output from experimental work using large scale SAC concentrator

The main benefit of this CPV/T system is that a higher total power output (by module area) compared with flat PV cell/module which produces only electrical power. Conclusions are summarized in the following points:

- Testing CPV/T system power output under outdoor conditions and cooling effect, showed an enhancement in both electrical and thermal power output, and consequently the total generated power output, with the increase of concentration ratio and flow rate.
- CPV/T with geometric concentration ratio of 2 has a total power output of about 180W, compared with a total power output of two modules of about 23W, consequently an increase of more than 8 times the flat PV module.
- Increasing the concentration to 6 increases the total power to about 385 W compared with the total power output of 6 flat PV modules of about 68W which results in an increase of 7 times the flat PV.

- The maximum total efficiency of the designed CPV/T system with the use of SAC with GCRs of 2, 4 and 6, at maximum used flow rates is about 95 %, 88 % and 78 %, respectively.

These results highlight the benefit and feasibility of using the developed system in generating both enhanced electrical and thermal power for domestic use as one useful package of energy with high performance compared with the flat PV modules which generate only electrical power and susceptible to the effect of higher temperature in the absence of effective cooling system.

7.3. Future works

Based on the development process, the electrical and thermal concentrating photovoltaic (CPV/T) system results show an encouraging highly efficient device, that can provide a combination of electrical and thermal energy output suitable for various applications including domestic usage with many times higher than flat PV systems or Concentrated PV systems efficiencies. On the other hand, the present project offers models and results, for work that can be conducted in the future to enhance the developed system further. Recommendations highlighted from this project for future work are listed in the following points:

Detailed investigation of the feasibility of using the novel HAC and OAC geometry in façade integrated systems using mathematical modelling experimental testing is recommended.

From design point of view, the SAC geometry is suitable for CPV/T system using tracking system, while changing the square sides to a rectangular with side ratio of 1:4 will increase the daily performance; as a result the design can be used as static concentrator and experimental work to validate the optical simulation is recommended.

The thermal modelling of the CPV/T system using COMSOL Multi-physics was carried out using steady heat transfer model, which gives results when the model reaches the steady state, while more detailed behaviour of the system can be gained using a transient model to study the system performance at different solar hour angles.

Testing of a complete array for the CPV/T system under real conditions for building water heating should be conducted. A comparison for the array output should be carried out, with two system connecting methods (series and parallel connections) including evaluation of the electrical and thermal power output.

REFERENCES

1. CRES, *Energy Outlook of Greece*. 2009.
2. IEA, *World Energy Outlook 2016 Executive Summary*. 2016.
3. IEA, *Technology Roadmap: Solar Photovoltaic Energy*. 2010.
4. IEA, *Technology Roadmap: Solar Photovoltaic Energy*. 2014.
5. Sarasa-Maestro, C.J., R. Dufo-López and J.L. Bernal-Agustín, *Photovoltaic remuneration policies in the European Union*. Energy Policy, 2013. **55**: p. 317-328.
6. Bank, W., *Renewable electricity output (% of total electricity output)*. 2013.
7. WorldBank, *Electric power consumption*, W.D. Indicators, Editor. 2000 - 2012.
8. Ahwide, F. and Y. Aldali, *The Current Situation and Perspectives of Electricity Demand and Estimation of Carbon Dioxide Emissions and Efficiency*. International Journal of Environmental, Ecological, Geological and Geophysical Engineering, 2013. **Vol:7**(12).
9. (RCREEE), R.C.f.R.E.a.E.E., *Energy Supply and Demand – Current Trends*. 2012.
10. WorldBank, *CO2 emissions*, W.D. Indicators, Editor. 2000 - 2012.
11. Mohamed, A.M.A., A. Al-Habaibeh and H. Abdo, *An investigation into the current utilisation and prospective of renewable energy resources and technologies in Libya*. Renewable Energy, 2013. **50**: p. 732-740.
12. Buhawa, Z.M., *Modelling of Electric Power Networks with Renewable Power Sources in Faculty of Electrical Engineering*. 2012, Pilsen: Pilsen. p. 102.
13. Tiwari, G.N., *Solar energy: fundamentals, design, modelling and applications*. 2002: Alpha Science Int'l Ltd.
14. Whitfield, G.R., R.W. Bentley, C.K. Weatherby, A. Hunt, H.-D. Mohring, F.H. Klotz, P. Keuber, J.C. Miñano and E. Alarte-Garvi, *The development and testing of small concentrating PV systems*. Solar Energy, 1999. **67**(1): p. 23-34.
15. Llorente, J., J. Ballestrín and A.J. Vázquez, *A new solar concentrating system: Description, characterization and applications*. Solar Energy, 2011. **85**(5): p. 1000-1006.
16. Zahedi, A., *Review of modelling details in relation to low-concentration solar concentrating photovoltaic*. Renewable and Sustainable Energy Reviews, 2011. **15**(3): p. 1609-1614.
17. Sangani, C.S and Solanki, *Experimental evaluation of V-trough (2 suns) PV concentrator system using commercial PV modules*. 2007, Elsevier B.V. p. 453–459.
18. Guiqiang, L., P. Gang, Y. Su, Z. Xi and J. Jie, *Preliminary study based on building-integrated compound parabolic concentrators (CPC) PV/thermal technology*. Energy Procedia, 2012. **14**(0): p. 343-350.
19. Zhu, L., R.F. Boehm, Y. Wang, C. Halford and Y. Sun, *Water immersion cooling of PV cells in a high concentration system*. Solar Energy Materials and Solar Cells, 2011. **95**(2): p. 538-545.
20. Garcia-Botella, A., A.A. Fernandez-Balbuena, D. Vázquez and E. Bernabeu, *Ideal 3D asymmetric concentrator*. Solar Energy, 2009. **83**(1): p. 113-117.
21. Leutz, R. and A. Suzuki, *Nonimaging Fresnel Lenses*. 2001: Springer, UK.
22. Lorenzo, E. and A. Luque, *Fresnel lens analysis for solar energy applications*. Applied Optics, 1981. **20**(17): p. 2941-2945.
23. Matthew J. Parry-Hill, R.T.S.a.M.W.D. *Solar Cell Operation*. 2015 [24/01/2017]; Available from: <http://micro.magnet.fsu.edu/primer/java/solarcell/>.

REFERENCES

24. Jäger-Waldau, A., *PV Status Report 2014*. 2014, European Union, 2014: Luxembourg: Publications Office of the European Union, 2014.
25. Green, M.A., K. Emery, Y. Hishikawa, W. Warta and E.D. Dunlop, *Solar cell efficiency tables (Version 45)*. Progress in Photovoltaics: Research and Applications, 2015. **23**(1): p. 1-9.
26. Warmuth, B.B.K.K.C.K.S.N.S.P.R.P.J.R.T.S.G.S.-H.G.W.H.W.I.B.A.H.W., *PHOTOVOLTAICS REPORT*. 2016, Fraunhofer Institute for Solar Energy Systems: Freiburg.
27. Khan, F., S.N. Singh and M. Husain, *Effect of illumination intensity on cell parameters of a silicon solar cell*. Solar Energy Materials and Solar Cells, 2010. **94**(9): p. 1473-1476.
28. Bagnall, D.M. and M. Boreland, *Photovoltaic technologies*. Energy Policy, 2008. **36**(12): p. 4390-4396.
29. Shiao, M., *PV Balance of Systems 2015: Technology Trends and Markets*. 2015.
30. Law, D.C., R.R. King, H. Yoon, M.J. Archer, A. Boca, C.M. Fetzer, S. Mesropian, T. Isshiki, M. Haddad, K.M. Edmondson, D. Bhusari, J. Yen, R.A. Sherif, H.A. Atwater and N.H. Karam, *Future technology pathways of terrestrial III–V multijunction solar cells for concentrator photovoltaic systems*. Solar Energy Materials and Solar Cells, 2010. **94**(8): p. 1314-1318.
31. Yamaguchi, M., T. Takamoto, K. Araki and N. Ekins-Daukes, *Multi-junction III–V solar cells: current status and future potential*. Solar Energy, 2005. **79**(1): p. 78-85.
32. Cotal, H., C. Fetzer, J. Boisvert, G. Kinsey, R. King, P. Hebert, H. Yoon and N. Karam, *III-V multijunction solar cells for concentrating photovoltaics*. Energy & Environmental Science, 2009. **2**(2): p. 174-192.
33. *New world record for solar cell efficiency at 46%, in French-German cooperation confirms competitive advantage of European photovoltaic industry*. 2014, Fraunhofer Institute for Solar Energy Systems ISE: Freiburg, Germany.
34. Green, M.A., K. Emery, Y. Hishikawa, W. Warta and E.D. Dunlop, *Solar cell efficiency tables (version 47)*. Progress in Photovoltaics: Research and Applications, 2016. **24**(1): p. 3-11.
35. Simon P. Philipps, A.W.B., Kelsey Horowitz, Sarah Kurtz, *Current Status of Concentrator Photovoltaic (CPV) Technology*. 2016, Fraunhofer Institute for Solar Energy Systems ISE and National Renewable Energy Laboratory NREL: Washington, D.C. :.
36. Tabor, H., *Stationary mirror systems for solar collectors*. Solar Energy, 1958. **2**(3–4): p. 27-33.
37. Fraidenraich, N., *Design procedure of V-trough cavities for photovoltaic systems*. Progress in Photovoltaics: Research and Applications, 1998. **6**(1): p. 43-54.
38. Rabl, A., *Comparison of solar concentrators*. Journal Name: Sol. Energy; (United States); Journal Volume: 18:2, 1976: p. Medium: X; Size: Pages: 93-111.
39. Fraidenraich, N. and G.J. Almeida, *Optical properties of V-trough concentrators*. Solar Energy, 1991. **47**(3): p. 147-155.
40. Maiti, S., N. Sarmah, P. Bapat and T.K. Mallick, *Optical analysis of a photovoltaic V-trough system installed in western India*. Applied Optics, 2012. **51**(36): p. 8606-8614.
41. Solanki, C.S., C.S. Sangani, D. Gunashekar and G. Antony, *Enhanced heat dissipation of V-trough PV modules for better performance*. Solar Energy Materials and Solar Cells, 2008. **92**(12): p. 1634-1638.
42. Kostic, L.T., T.M. Pavlovic and Z.T. Pavlovic, *Influence of reflectance from flat aluminum concentrators on energy efficiency of PV/Thermal collector*. Applied Energy, 2010. **87**(2): p. 410-416.
43. Shaltout, M.A.M., A. Ghetas and M. Sabry, *Solar Electricity: Photovoltaics and WindV-trough concentrator on a photovoltaic full tracking system in a hot desert climate*. Renewable Energy, 1995. **6**(5): p. 527-532.

REFERENCES

44. Butler, B.A., E.E. van Dyk, F.J. Vorster, W. Okullo, M.K. Munji and P. Booysen, *Characterization of a low concentrator photovoltaics module*. Physica B: Condensed Matter, 2012. **407**(10): p. 1501-1504.
45. Qin, L., Y. Wang, M. Vivar, Q. Huang, L. Zhu, M. Fuentes and Z. Wang, *Comparison of photovoltaic and photocatalytic performance of non-concentrating and V-trough SOLWAT (solar water purification and renewable electricity generation) systems for water purification*. Energy, 2015. **85**: p. 251-260.
46. Maiti, S., S. Banerjee, K. Vyas, P. Patel and P.K. Ghosh, *Self regulation of photovoltaic module temperature in V-trough using a metal–wax composite phase change matrix*. Solar Energy, 2011. **85**(9): p. 1805-1816.
47. Bione, J., O.C. Vilela and N. Fraidenraich, *Comparison of the performance of PV water pumping systems driven by fixed, tracking and V-trough generators*. Solar Energy, 2004. **76**(6): p. 703-711.
48. Tina, G.M. and P.F. Scandura, *Case study of a grid connected with a battery photovoltaic system: V-trough concentration vs. single-axis tracking*. Energy Conversion and Management, 2012. **64**: p. 569-578.
49. Künnemeyer, R., T.N. Anderson, M. Duke and J.K. Carson, *Performance of a V-trough photovoltaic/thermal concentrator*. Solar Energy, 2014. **101**: p. 19-27.
50. Su, Z., S. Ding, Z. Gan and X. Yang, *Analysis of a photovoltaic-electrolyser direct-coupling system with a V-trough concentrator*. Energy Conversion and Management, 2016. **108**: p. 400-410.
51. Abella, M.A., F. Chenlo, P. Valera, J. Enrile and R. Osuna. *Operation of standard PV modules in V-trough concentrators*. in *Photovoltaic Specialists Conference, 2005. Conference Record of the Thirty-first IEEE*. 2005. IEEE.
52. Bahaidarah, H., B. Tanweer, P. Gandhidasan and S. Rehman, *A Combined Optical, Thermal and Electrical Performance Study of a V-Trough PV System—Experimental and Analytical Investigations*. Energies, 2015. **8**(4): p. 2803.
53. García, M., L. Marroyo, E. Lorenzo and M. Pérez, *Experimental energy yield in 1· 5× and 2× PV concentrators with conventional modules*. Progress in Photovoltaics: Research and Applications, 2008. **16**(3): p. 261-270.
54. Wu, Y., *Thermal management of concentrator photovoltaics*. 2009, University of Warwick.
55. Guiqiang, L., P. Gang, Y. Su, Z. Xi and J. Jie, *Preliminary study based on building-integrated compound parabolic concentrators (CPC) PV/thermal technology*. Energy Procedia, 2012. **14**: p. 343-350.
56. Xu, G., X. Zhang and S. Deng, *Experimental study on the operating characteristics of a novel low-concentrating solar photovoltaic/thermal integrated heat pump water heating system*. Applied Thermal Engineering, 2011. **31**(17–18): p. 3689-3695.
57. Bernardo, L.R., B. Perers, H. Håkansson and B. Karlsson, *Performance evaluation of low concentrating photovoltaic/thermal systems: A case study from Sweden*. Solar Energy, 2011. **85**(7): p. 1499-1510.
58. Sarmah, N., B.S. Richards and T.K. Mallick, *Design, development and indoor performance analysis of a low concentrating dielectric photovoltaic module*. Solar Energy, 2014. **103**: p. 390-401.
59. Sharma, S., A. Tahir, K.S. Reddy and T.K. Mallick, *Performance enhancement of a Building-Integrated Concentrating Photovoltaic system using phase change material*. Solar Energy Materials and Solar Cells, 2016. **149**: p. 29-39.
60. Sarmah, N. and T.K. Mallick, *Design, fabrication and outdoor performance analysis of a low concentrating photovoltaic system*. Solar Energy, 2015. **112**: p. 361-372.

REFERENCES

61. Nilsson, J., H. Håkansson and B. Karlsson, *Electrical and thermal characterization of a PV-CPC hybrid*. Solar Energy, 2007. **81**(7): p. 917-928.
62. Poulek, V., A. Khudysh and M. Libra, *Innovative low concentration PV systems with bifacial solar panels*. Solar Energy, 2015. **120**: p. 113-116.
63. Su, Y., S.B. Riffat and G. Pei, *Comparative study on annual solar energy collection of a novel lens-walled compound parabolic concentrator (lens-walled CPC)*. Sustainable Cities and Society, 2012. **4**: p. 35-40.
64. Su, Y., G. Pei, S.B. Riffat and H. Huang, *A Novel Lens-Walled Compound Parabolic Concentrator for Photovoltaic Applications*. Journal of Solar Energy Engineering, 2012. **134**(2): p. 021010-021010-7.
65. Irshid, M.I. and M.O. Othman, *V-troughs with high concentration ratios for photovoltaic concentrator cells*. Solar Cells, 1988. **23**(3): p. 159-172.
66. Paul, D.I., *Theoretical and Experimental Optical Evaluation and Comparison of Symmetric 2D CPC and V-Trough Collector for Photovoltaic Applications*. International Journal of Photoenergy, 2015. **2015**.
67. Singh, H., M. Sabry and D.A.G. Redpath, *Experimental investigations into low concentrating line axis solar concentrators for CPV applications*. Solar Energy, 2016. **136**: p. 421-427.
68. Strong S.J., M.A.J., Manasse F.K. *A novel mildly concentrating photovoltaic/thermal total energy system*. in *Sun II; Proceedings of the Silver Jubilee Congress*. 1979. Atlanta, Ga.
69. Mammo, E.D., N. Sellami and T.K. Mallick, *Performance analysis of a reflective 3D crossed compound parabolic concentrating photovoltaic system for building façade integration*. Progress in photovoltaics: research and applications, 2013. **21**(5): p. 1095-1103.
70. Baig, H., N. Sellami, D. Chemisana, J. Rosell and T.K. Mallick, *Performance analysis of a dielectric based 3D building integrated concentrating photovoltaic system*. Solar Energy, 2014. **103**: p. 525-540.
71. Baig, H., N. Sellami and T.K. Mallick, *Trapping light escaping from the edges of the optical element in a Concentrating Photovoltaic system*. Energy Conversion and Management, 2015. **90**: p. 238-246.
72. Sellami, N. and T.K. Mallick, *Optical efficiency study of PV Crossed Compound Parabolic Concentrator*. Applied Energy, 2013. **102**: p. 868-876.
73. Muhammad-Sukki, F., S.H. Abu-Bakar, R. Ramirez-Iniguez, S.G. McMeekin, B.G. Stewart, N. Sarmah, T.K. Mallick, A.B. Munir, S.H. Mohd Yasin and R. Abdul Rahim, *Mirror symmetrical dielectric totally internally reflecting concentrator for building integrated photovoltaic systems*. Applied Energy, 2014. **113**: p. 32-40.
74. Abu-Bakar, S.H., F. Muhammad-Sukki, R. Ramirez-Iniguez, T.K. Mallick, A.B. Munir, S.H. Mohd Yasin and R. Abdul Rahim, *Rotationally asymmetrical compound parabolic concentrator for concentrating photovoltaic applications*. Applied Energy, 2014. **136**: p. 363-372.
75. Abu-Bakar, S.H., F. Muhammad-Sukki, D. Freier, R. Ramirez-Iniguez, T.K. Mallick, A.B. Munir, S.H. Mohd Yasin, A. Abubakar Mas'ud and N. Md Yunus, *Performance analysis of a novel rotationally asymmetrical compound parabolic concentrator*. Applied Energy, 2015. **154**: p. 221-231.
76. Abu-Bakar, S.H., F. Muhammad-Sukki, D. Freier, R. Ramirez-Iniguez, T.K. Mallick, A.B. Munir, S.H. Mohd Yasin, A. Abubakar Mas'ud and N.A. Bani, *Performance analysis of a solar window incorporating a novel rotationally asymmetrical concentrator*. Energy, 2016. **99**: p. 181-192.
77. Sellami, N. and T.K. Mallick, *Design of nonimaging static solar concentrator for window integrated photovoltaic*. AIP Conference Proceedings, 2012. **1477**(1): p. 106-109.

REFERENCES

78. Schuetz, M.A., K.A. Shell, S.A. Brown, G.S. Reinbolt, R.H. French and R.J. Davis, *Design and Construction of a Low-Concentration Photovoltaic System Based on Compound Parabolic Concentrators*. IEEE Journal of Photovoltaics, 2012. **2**(3): p. 382-386.
79. Lu, Z.H., Q. Song, S.Q. Li, Q. Yao and A. Othman, *The Effect of Non-Uniform Illumination on the Performance of Conventional Polycrystalline Silicon Solar Cell*, in *Proceedings of ISES World Congress 2007 (Vol. I – Vol. V): Solar Energy and Human Settlement*, D.Y. Goswami and Y. Zhao, Editors. 2009, Springer Berlin Heidelberg: Berlin, Heidelberg. p. 1445-1448.
80. Bahaidarah, H.M.S., A.A.B. Baloch and P. Gandhidasan, *Uniform cooling of photovoltaic panels: A review*. Renewable and Sustainable Energy Reviews, 2016. **57**: p. 1520-1544.
81. Baig, H., K.C. Heasman and T.K. Mallick, *Non-uniform illumination in concentrating solar cells*. Renewable and Sustainable Energy Reviews, 2012. **16**(8): p. 5890-5909.
82. Franklin, E. and J. Coventry, *Effects of highly non-uniform illumination distribution on electrical performance of solar cells*. 2002.
83. Chong, K.K., T.K. Yew, C.W. Wong and S.L. Lau, *Study of image quality of mirror via solar flux distribution measurement using a high speed optical scanner*. Applied Optics, 2011. **50**(25): p. 4927-4935.
84. Muneer, T., *Solar radiation and daylight models*. 2004, Amsterdam; Paris: Elsevier Butterworth Heinemann.
85. Rahimi, M., P. Valeh-e-Sheyda, M.A. Parsamoghadam, M.M. Masahi and A.A. Alsairafi, *Design of a self-adjusted jet impingement system for cooling of photovoltaic cells*. Energy Conversion and Management, 2014. **83**: p. 48-57.
86. Royne, A., C.J. Dey and D.R. Mills, *Cooling of photovoltaic cells under concentrated illumination: a critical review*. Solar Energy Materials and Solar Cells, 2005. **86**(4): p. 451-483.
87. Al-Shohani, W.A.M., A. Sabouri, R. Al-Dadah, S. Mahmoud and H. Butt, *Experimental investigation of an optical water filter for Photovoltaic/Thermal conversion module*. Energy Conversion and Management, 2016. **111**: p. 431-442.
88. Al-Shohani, W.A.M., R. Al-Dadah and S. Mahmoud, *Reducing the thermal load of a photovoltaic module through an optical water filter*. Applied Thermal Engineering, 2016. **109**, Part A: p. 475-486.
89. Valeh-e-Sheyda, P., M. Rahimi, A. Parsamoghadam and M.M. Masahi, *Using a wind-driven ventilator to enhance a photovoltaic cell power generation*. Energy and Buildings, 2014. **73**: p. 115-119.
90. Natarajan, S.K., T.K. Mallick, M. Katz and S. Weingaertner, *Numerical investigations of solar cell temperature for photovoltaic concentrator system with and without passive cooling arrangements*. International Journal of Thermal Sciences, 2011. **50**(12): p. 2514-2521.
91. Jian, S. and S. Mingheng. *Experimental Study on A Concentrating Solar Photovoltaic/Thermal System*. in *Power and Energy Engineering Conference (APPEEC), 2010 Asia-Pacific*. 2010. IEEE.
92. Tarabsheh, A.A., S. Voutetakis, A.I. Papadopoulos, P. Seferlis, I. Etier and O. Saraereh, *Investigation of temperature effects in efficiency improvement of non-uniformly cooled photovoltaic cells*, in *Chemical Engineering Transactions*. 2013. p. 1387-1392.
93. Sun, J. and M. Shi, *Numerical study on optical and electric-thermal performance for solar concentrating PV/T air system*. Science in China Series E: Technological Sciences, 2009. **52**(12): p. 3514-3520.
94. Xu, X., M.M. Meyers, B.G. Sammakia and B.T. Murray. *Thermal modeling of hybrid concentrating PV/T collectors with tree-shaped channel networks cooling system*. in *Thermal and*

REFERENCES

- Thermomechanical Phenomena in Electronic Systems (ITherm)*, 2012 13th IEEE Intersociety Conference on. 2012. IEEE.
95. Xuetao, C., X. Xianghua and L. Xingang, *Analysis of a Concentrating Photovoltaic/Thermal Solar System*, in *Proceedings of ISES World Congress 2007 (Vol. I – Vol. V): Solar Energy and Human Settlement*, D.Y. Goswami and Y. Zhao, Editors. 2009, Springer Berlin Heidelberg: Berlin, Heidelberg. p. 1386-1390.
 96. Hedayatzadeh, M., Y. Ajabshirchi, F. Sarhaddi, A. Safavinejad, S. Farahat and H. Chaji, *Thermal and Electrical Assessment of an Integrated Solar Photovoltaic Thermal (PV/T) Water Collector Equipped with a Compound Parabolic Concentrator (CPC)*. International Journal of Green Energy, 2013. **10**(5): p. 494-522.
 97. Huang, B.J., T.H. Lin, W.C. Hung and F.S. Sun, *Performance evaluation of solar photovoltaic/thermal systems*. Solar Energy, 2001. **70**(5): p. 443-448.
 98. Brogren, M., P. Nostell and B. Karlsson, *Optical efficiency of a PV–thermal hybrid CPC module for high latitudes*. Solar Energy, 2001. **69**, **Supplement 6**: p. 173-185.
 99. Brogren, M. and B. Karlsson. *Low-concentrating water-cooled PV-thermal hybrid systems for high latitudes*. in *Conference Record of the Twenty-Ninth IEEE Photovoltaic Specialists Conference*, 2002. 2002.
 100. Davidsson, H., B. Perers and B. Karlsson, *Performance of a multifunctional PV/T hybrid solar window*. Solar Energy, 2010. **84**(3): p. 365-372.
 101. Stropnik, R. and U. Stritih, *Increasing the efficiency of PV panel with the use of PCM*. Renewable Energy, 2016. **97**: p. 671-679.
 102. Browne, M.C., B. Norton and S.J. McCormack, *Heat retention of a photovoltaic/thermal collector with PCM*. Solar Energy, 2016. **133**: p. 533-548.
 103. Ceylan, İ., A.E. Gürel, A. Ergün and A. Tabak, *Performance analysis of a concentrated photovoltaic and thermal system*. Solar Energy, 2016. **129**: p. 217-223.
 104. Tina G, Cosentino F and N. G. *Effect of Thermal Gradient on Electrical Efficiency of Hybrid PV/T*. in *the 26th European Photovoltaic Solar Energy Conference*. 2010. Spain.
 105. Smith, D.R.B., K. L.; Pritchard, D. A., *Combined photovoltaic thermal collector testing*, in *IEEE Photovoltaic Specialists Conference*. 1978: Washengton D.C.
 106. Lambarski, T.J., *Electrical design guidelines for photovoltaic/thermal systems*. 1984. Medium: X; Size: Pages: 1045-1050.
 107. De Vries, D.W., *Design of a photovoltaic/thermal combi-panel*. PhD report, EUT, 1998. 1998, Eindhoven University of Technology EUT Eindhoven.
 108. Xuetao, C., X. Xianghua and L. Xingang. *Analysis of a concentrating photovoltaic/thermal solar system*. in *Proceedings of ISES World Congress 2007 (Vol. I–Vol. V)*. 2008. Springer.
 109. Zhao, J., Y. Song, W.-H. Lam, W. Liu, Y. Liu, Y. Zhang and D. Wang, *Solar radiation transfer and performance analysis of an optimum photovoltaic/thermal system*. Energy Conversion and Management, 2011. **52**(2): p. 1343-1353.
 110. Sharan, S.N. and T.C. Kandpal, *Testing of a prototype combined photovoltaic-thermal linear fresnel concentrator-receiver system*. Energy Conversion and Management, 1992. **33**(1): p. 37-39.
 111. Otanicar, T., I. Chowdhury, P.E. Phelan and R. Prasher, *Parametric analysis of a coupled photovoltaic/thermal concentrating solar collector for electricity generation*. Journal of Applied Physics, 2010. **108**(11): p. 114907.

REFERENCES

112. Garg, H.P., R.K. Agarwal and J.C. Joshi, *Experimental study on a hybrid photovoltaic-thermal solar water heater and its performance predictions*. Energy Conversion and Management, 1994. **35**(7): p. 621-633.
113. Ricardo, B., D. Henrik, G. Niko, G. Christian, C. Luis and M. Chabu, *Measurements of the electrical incidence angle modifiers of an asymmetrical photovoltaic/thermal compound parabolic concentrating-collector*. Engineering, 2013. **5**(01): p. 37.
114. Iurevych, O., S. Gubin and M. Dudeck. *Combined receiver of solar radiation with holographic planar concentrator*. in *IOP conference series: materials science and engineering*. 2012. IOP Publishing.
115. Xu, Y., C.Y. Wang, Y.M. Hua and Y.M. Zhang. *Studies on a low concentration photovoltaic/thermal system with constant volume refrigeration*. in *Key Engineering Materials*. 2012. Trans Tech Publ.
116. Proell M., R.M., Schoelkopf W., Hauer A., *Maximum efficiency of low concentrating PV-T collectors and optical boundary conditions*. Proceedings of the ISES solar world congress 2011, 2011.
117. Abu-Bakar, S.H., F. Muhammad-Sukki, R. Ramirez-Iniguez, D. Freier, T.K. Mallick, A.B. Munir, S.H.M. Yasin, A.A. Mas' ud and N.A. Bani, *Novel optical concentrator technology for building integrated photovoltaic systems*. 2016.
118. AL-Hamdani, A.H., B.D. Blawa and S. AL-Ani, *Parabola Dish and Cassegrain Concentrators to Improve Solar Cell Conversion Efficiency*.
119. Visa, I., M.D. Moldovan, M. Comsit and A. Duta, *Improving the renewable energy mix in a building toward the nearly zero energy status*. Energy and Buildings, 2014. **68, Part A**: p. 72-78.
120. Hughes, B.R., N.P.S. Cherisa and O. Beg, *Computational study of improving the efficiency of photovoltaic panels in the UAE*. World Academy of Science, Engineering and Technology, 2011. **73**: p. 278-287.
121. Lovegrove, K. and W. Stein, *Concentrating solar power technology : principles, developments and applications*. 2012.
122. Bode, S.-J. and P. Gauché. *Review of optical software for use in concentrating solar power systems*. in *1st South African Solar Energy Conference*. 2012.
123. Meller, Y. and A. Kribus, *Kaleidoscope homogenizers sensitivity to shading*. Solar Energy, 2013. **88**: p. 204-214.
124. Falcone, P.K., *A handbook for solar central receiver design*. 1986, Sandia National Labs., Livermore, CA (USA).
125. Roccia, J.P., B. Piaud, C. Coustet, C. Caliot, E. Guillot, G. Flamant and J. Delatorre, *SOLFAST, a Ray-Tracing Monte-Carlo software for solar concentrating facilities*. Journal of Physics: Conference Series, 2012. **369**(1): p. 012029.
126. Blanco, M., A. Mutuberria, A. Monreal and R. Albert, *Results of the empirical validation of Tonatiuh at Mini-Pegase CNRS-PROMES facility*. Proc SolarPACES, 2011.
127. Belhomme, B., R. Pitz-Paal, P. Schwarzbözl and S. Ulmer, *A new fast ray tracing tool for high-precision simulation of heliostat fields*. Journal of Solar Energy Engineering, 2009. **131**(3): p. 031002.
128. Riveros-Rosas, D., M. Sánchez-González and C.A. Estrada, *Three-dimensional analysis of a concentrated solar flux*. Journal of Solar Energy Engineering, 2008. **130**(1): p. 014503.
129. Schwarzbözl, P., R. Pitz-Paal and M. Schmitz. *Visual HFLCAL-A software tool for layout and optimisation of heliostat fields*. in *Proceedings*. 2009.
130. Leonardi, E. and B. D'Aguanno, *CRS4-2: a numerical code for the calculation of the solar power collected in a central receiver system*. Energy, 2011. **36**(8): p. 4828-4837.

REFERENCES

131. Wei, X., Z. Lu, W. Yu and Z. Wang, *A new code for the design and analysis of the heliostat field layout for power tower system*. Solar Energy, 2010. **84**(4): p. 685-690.
132. Noone, C.J., M. Torrilhon and A. Mitsos, *Heliostat field optimization: A new computationally efficient model and biomimetic layout*. Solar Energy, 2012. **86**(2): p. 792-803.
133. Winston, R. and R.C. Gee, *Nonimaging light concentrator with uniform irradiance*. 2003, Google Patents.
134. Segev, G. and A. Kribus, *Performance of CPV modules based on vertical multi-junction cells under non-uniform illumination*. Solar Energy, 2013. **88**: p. 120-128.
135. Sze, J.R. and A.-C. Wei, *Achromatic Solar Concentrator based on Planar Structure*. in *Solid-State and Organic Lighting*. 2015. Optical Society of America.
136. Freier, D., F. Muhammad-Sukki, S.H. Abu-Bakar, R. Ramirez-Iniguez, A. Abubakar Mas'ud, R. Albarracín, J.A. Ardila-Rey, A.B. Munir, S.H. Mohd Yasin and N.A. Bani, *Software simulation and experimental characterisation of a rotationally asymmetrical concentrator under direct and diffuse solar radiation*. Energy Conversion and Management, 2016. **122**: p. 223-238.
137. Kistler, B.L., *A user's manual for DELSOL3: a computer code for calculating the optical performance and optimal system design for solar thermal central receiver plants*. Sandia National Laboratories, Sandia Report No. SAND86-8018, 1986.
138. Lipps, F.W. and L.L. Vant-Hull, *A cellwise method for the optimization of large central receiver systems*. Solar Energy, 1978. **20**(6): p. 505-516.
139. Garcia, P., A. Ferriere and J.-J. Bezier, *Codes for solar flux calculation dedicated to central receiver system applications: a comparative review*. Solar Energy, 2008. **82**(3): p. 189-197.
140. Wendelin, T., A. Dobos and A. Lewandowski, *SolTrace: A ray-tracing code for complex solar optical systems*. Contract, 2013. **303**: p. 275-3000.
141. Craig, K.J., M.A. Moghimi, A.E. Rungasamy, J. Marsberg and J.P. Meyer, *Finite-volume ray tracing using Computational Fluid Dynamics in linear focus CSP applications*. Applied Energy, 2016. **183**: p. 241-256.
142. *OPTISWORKS: Your Project*. 2016 [11/01/2017]; Available from: <http://www.optis-world.com/Your-Project/Energy-Suite>.
143. Sellami, N., T.K. Mallick and D.A. McNeil, *Optical characterisation of 3-D static solar concentrator*. Energy Conversion and Management, 2012. **64**: p. 579-586.
144. Kerrouche, A., D. Hardy, D. Ross and B. Richards, *Luminescent solar concentrators: from experimental validation of 3D ray-tracing simulations to coloured stained-glass windows for BIPV*. Solar Energy Materials and Solar Cells, 2014. **122**: p. 99-106.
145. Abdullahi, B., R. Al-dadah and S. Mouhmd, *Optical Performance of Double Receiver Compound Parabolic Concentrator*. Energy Procedia, 2014. **61**: p. 2625-2628.
146. Sarmah, N., K. Shank, L. Micheli, K. Reddy and T.K. Mallick, *Design and Optical Performance Analysis of a Reflective Type High Concentrating Photovoltaic System*.
147. Mouzouris, M., L. Roberts and M. Brooks, *Thermal performance of a high-flux solar concentrating system*. R & D Journal of the South African Institution of Mechanical Engineering, 2010. **27**: p. 10-22.
148. Sellami, N. and T. Mallick, *Optical Performances of Refractive Crossed Compound Parabolic Concentrator CCPC*.
149. Al-Shohani, W.A., R. Al-Dadah, S. Mahmoud and A. Algareu, *Optimum design of V-trough concentrator for photovoltaic applications*. Solar Energy, 2016. **140**: p. 241-254.

REFERENCES

150. Algarue, A., S. Mahmoud and R. Al-Dadah, *Optical Performance of Low Concentration Ratio Reflective and Refractive Concentrators for Photovoltaic Applications*. Energy Procedia, 2014. **61**: p. 2375-2378.
151. Ali, I., K. Reddy and T.K. Mallick. *Optical performance of circular and elliptical 3-D static solar concentrators*. in *National Solar Conference, American Solar Energy Society*. 2010.
152. Reddy, K., I. Saleh Ali, T. Mallick and T. O'Donovan, *An optical analysis of a static 3-D solar concentrator*. 2013.
153. Ali, I.M.S., T.K. Mallick, P.A. Kew, T.S. O'Donovan and K. Reddy. *Optical performance evaluation of a 2-D and 3-D novel hyperboloid solar concentrator*. in *World Renewable Energy Congress XI*. 2010.
154. Sellami, N. and T.K. Mallick, *Optical characterisation and optimisation of a static Window Integrated Concentrating Photovoltaic system*. Solar Energy, 2013. **91**: p. 273-282.
155. Daabo, A.M., S. Mahmoud and R.K. Al-Dadah, *The optical efficiency of three different geometries of a small scale cavity receiver for concentrated solar applications*. Applied Energy, 2016. **179**: p. 1081-1096.
156. Daabo, A.M., S. Mahmoud, R.K. Al-Dadah and A. Ahmad, *Numerical investigation of pitch value on thermal performance of solar receiver for solar powered Brayton cycle application*. Energy, 2017. **119**: p. 523-539.
157. Daabo, A.M., S. Mahmoud and R.K. Al-Dadah, *The effect of receiver geometry on the optical performance of a small-scale solar cavity receiver for parabolic dish applications*. Energy, 2016. **114**: p. 513-525.
158. Arnaoutakis, G.E., J. Marques-Hueso, T.K. Mallick and B.S. Richards, *Coupling of sunlight into optical fibres and spectral dependence for solar energy applications*. Solar energy, 2013. **93**: p. 235-243.
159. Aldossary, A., A. Algarue, S. Mahmoud and R. AL-Dadah, *Performance of Multi Junction Photovoltaic Cells with High Concentration Ratio*. Energy Procedia, 2014. **61**: p. 2258-2261.
160. Sendhil Kumar, N., K. Matty, E. Rita, W. Simon, A. Ortrun, C. Alex, W. Roland, G. Tim and M. Tapas Kumar, *Experimental validation of a heat transfer model for concentrating photovoltaic system*. Applied Thermal Engineering, 2012. **33–34**: p. 175-182.
161. TRANSYS 17.1. 2017 [13/01/2017]; Available from: <http://sel.me.wisc.edu/trnsys/features/>.
162. Al-Alili, A., Y. Hwang, R. Radermacher and I. Kubo, *A high efficiency solar air conditioner using concentrating photovoltaic/thermal collectors*. Applied Energy, 2012. **93**: p. 138-147.
163. Buonomano, A., F. Calise and A. Palombo, *Solar heating and cooling systems by CPVT and ET solar collectors: a novel transient simulation model*. Applied energy, 2013. **103**: p. 588-606.
164. Eicker, U., A. Colmenar-Santos, L. Teran, M. Cotrado and D. Borge-Diez, *Economic evaluation of solar thermal and photovoltaic cooling systems through simulation in different climatic conditions: An analysis in three different cities in Europe*. Energy and Buildings, 2014. **70**: p. 207-223.
165. Bosco, N., T.J. Silverman and S. Kurtz, *Modeling Thermal Fatigue in CPV Cell Assemblies*. IEEE Journal of Photovoltaics, 2011. **1**(2): p. 242-247.
166. Bosco, N., C. Sweet, T. Silverman and S. Kurtz. *CPV cell infant mortality study*. in *7th International Conference on Concentrating Photovoltaic Systems (CPV-7)*. 2011.
167. Micheli, L., N. Sarmah, X. Luo, K.S. Reddy and T.K. Mallick, *Design of A 16-Cell Densely-packed Receiver for High Concentrating Photovoltaic Applications*. Energy Procedia, 2014. **54**: p. 185-198.

REFERENCES

168. Micheli, L., E.F. Fernandez, F. Almonacid, K. Reddy and T.K. Mallick, *Enhancing ultra-high CPV passive cooling using least-material finned heat sinks*. CPV-11, 2015.
169. Oliverio, L., G. Timò, A. Minuto and P. Gropelli, *Thermal simulations of a CPV point focus module using Comsol Multiphysics*. Solar Energy Technology, 2010: p. 55-64.
170. Fontenault, B.J. and E. Gutierrez-Miravete. *Modeling a Combined Photovoltaic-Thermal Solar Panel*. in *Comsol Conference, Boston, MA*. 2002.
171. Cellura, M., V.L. Brano and A. Marvuglia, 582. *A Photovoltaic panel coupled with a phase changing material heat storage system in hot climates*. 2008.
172. Aldossary, A., S. Mahmoud and R. Al-Dadah, *Technical feasibility study of passive and active cooling for concentrator PV in harsh environment*. Applied Thermal Engineering, 2016. **100**: p. 490-500.
173. Fontenault, B., *Active Forced Convection Photovoltaic/Thermal Panel Efficiency Optimization Analysis*. 2012, Rensselaer Polytechnic Institute.
174. Baig, H., N. Sarmah, K.C. Heasman and T.K. Mallick, *Numerical modelling and experimental validation of a low concentrating photovoltaic system*. Solar Energy Materials and Solar Cells, 2013. **113**: p. 201-219.
175. Ota, Y., T. Sueto, H. Nagai, K. Araki and K. Nishioka, *Reduction in Operating Temperature of 25 Series-Connected 820X Concentrator Photovoltaic Module*. Japanese Journal of Applied Physics, 2013. **52**(4S): p. 04CR03.
176. Chemisana, D., M. Ibáñez and J.I. Rosell, *Characterization of a photovoltaic-thermal module for Fresnel linear concentrator*. Energy Conversion and Management, 2011. **52**(10): p. 3234-3240.
177. Chemisana, D. and J.I. Rosell, *Electrical performance increase of concentrator solar cells under Gaussian temperature profiles*. Progress in Photovoltaics: Research and Applications, 2013. **21**(4): p. 444-455.
178. Hollands, K.G.T., *A concentrator for thin-film solar cells*. Solar Energy, 1971. **13**(2): p. 149-163.
179. Kiatgamolchai, S. and E. Chamni, *Theory and experiment of a two-dimensional cone concentrator for sunlight*. Solar Energy, 2008. **82**(2): p. 111-117.
180. Burkhard, D.G., G.L. Strobel and D.R. Burkhard, *Flat-sided rectilinear trough as a solar concentrator: an analytical study*. Applied Optics, 1978. **17**(12): p. 1870-1883.
181. Chaves, J., *Introduction to nonimaging optics*. 2008: CRC Press.
182. Schmidt-Kloiber, H. and H. Schoeffmann, *Metallic hollow cones as light concentrators*. Applied Optics, 1986. **25**(2): p. 252-257.
183. *MIRO-SUN® PV weatherproof reflective 90*, A. Solar, Editor. 2010, Alanod Solar.
184. Chenlo, F. and M. Cid, *A linear concentrator photovoltaic module: analysis of non-uniform illumination and temperature effects on efficiency*. Solar Cells, 1987. **20**(1): p. 27-39.
185. Montgomery, D.C. and G.C. Runger, *Applied statistics and probability for engineers*. 2014.
186. Rice, J.A., *Mathematical statistics and data analysis*. Vol. Duxbury advanced series. 2007, Belmont, Calif: Thomson Brooks/Cole.
187. Saleh Ali, I.M., T.S. O'Donovan, K.S. Reddy and T.K. Mallick, *An optical analysis of a static 3-D solar concentrator*. Solar Energy, 2013. **88**(0): p. 57-70.
188. Jones, A.D. and C.P. Underwood, *A thermal model for photovoltaic systems*. Solar Energy, 2001. **70**(4): p. 349-359.
189. Çengel, Y.A., J.M. Cimbala and R.H. Turner, *Fundamentals of thermal-fluid sciences*. 2012, Boston: McGraw-Hill Higher Education.
190. Theristis, M. and T.S. O'Donovan, *Electrical-thermal analysis of III-V triple-junction solar cells under variable spectra and ambient temperatures*. Solar Energy, 2015. **118**: p. 533-546.

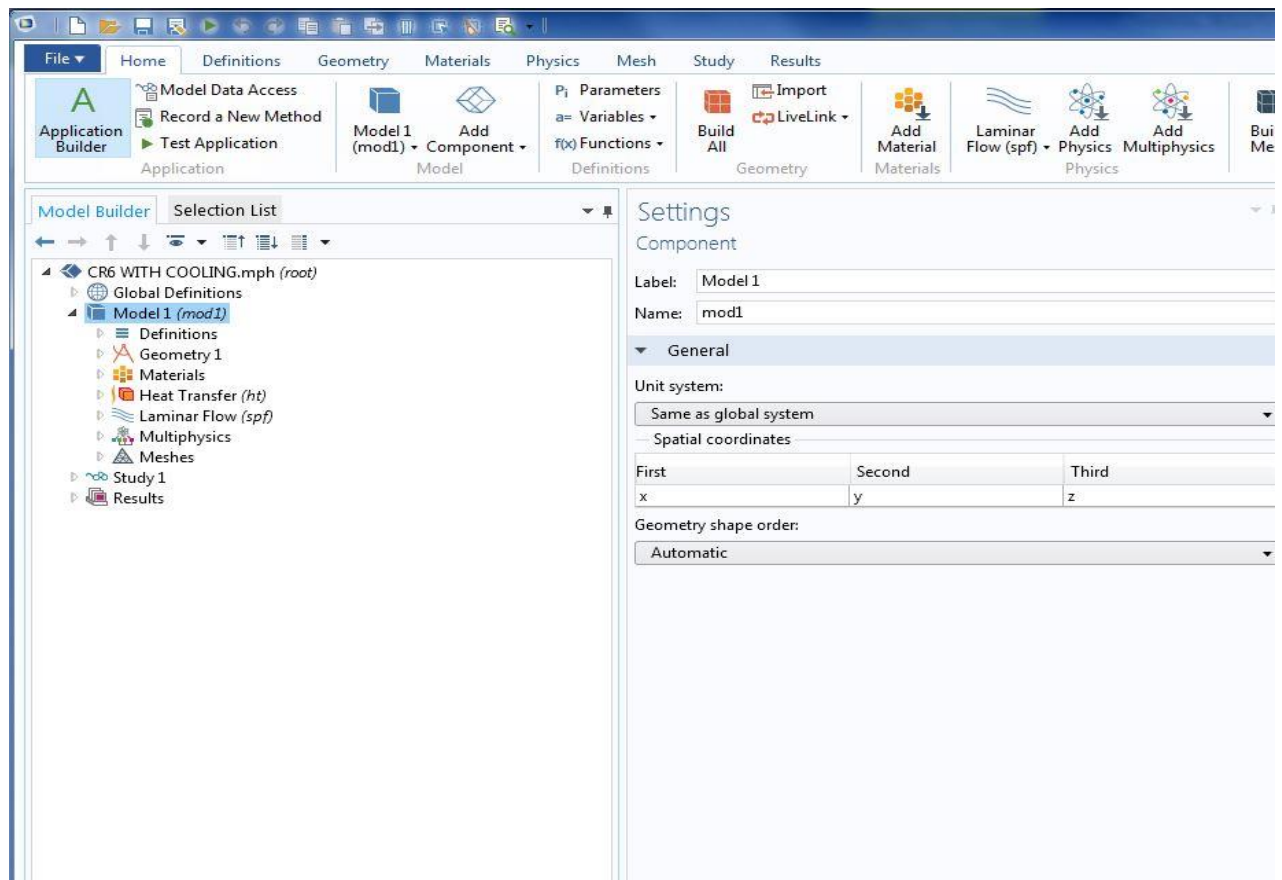
REFERENCES

191. Theristis, M., N. Sarmah, T.K. Mallick and T.S. O'Donovan, *Design and numerical analysis of enhanced cooling techniques for a high concentration photovoltaic (HCPV) system*. School of Engineering & Physical sciences, Herriot-Watt University Edinburgh, United Kingdom, 2012.
192. Bocchi, F. *How to calculate mass conservation and energy balance*. 2015 [26-01-2017]; Available from: <http://www.comsol.com/blogs/author/fabio-bocchi/>.
193. Teo, H.G., P.S. Lee and M.N.A. Hawlader, *An active cooling system for photovoltaic modules*. Applied Energy, 2012. **90**(1): p. 309-315.
194. Skoplaki, E. and J.A. Palyvos, *On the temperature dependence of photovoltaic module electrical performance: A review of efficiency/power correlations*. Solar Energy, 2009. **83**(5): p. 614-624.
195. Kerzmann, T. and L. Schaefer, *System simulation of a linear concentrating photovoltaic system with an active cooling system*. Renewable Energy, 2012. **41**: p. 254-261.
196. Frei, W. *Solutions to Linear Systems of Equations: Direct and Iterative Solvers*. 2013 [29-01-2017]; Available from: <https://www.comsol.com/blogs/solutions-linear-systems-equations-direct-iterative-solvers/>.
197. Cengel, Y.A., J.M. Cimbala and M. Kanoğlu, *Fluid mechanics, fundamentals and applications*, 2006. McGraw Hill, New York.
198. E927-10, A., *Standard Specification for Solar Simulation for Photovoltaic Testing*. 2015. p. 5.
199. Tomas Markvart . Wiley, C., ed. *Solar Electricity*. second edition ed. 2001, John Wiley & Sons,LTD.
200. OMEGA, *ANSI and IEC Color Codes for Thermocouples, Wire and Connectors*. 11/07/2016.
201. Embaye, M., *ENHANCEMENT OF PANEL RADIATOR BASED HYDRONIC CENTRAL HEATING SYSTEM USING FLOW PULSATION* in *Engineering and Physical Sciences*. 2016, University of Birmingham. p. 277.
202. Embaye, M., R.K. Al-Dadah and S. Mahmoud, *Thermal performance of hydronic radiator with flow pulsation – Numerical investigation*. Applied Thermal Engineering, 2015. **80**: p. 109-117.
203. Fraas, L.M. and L.D. Partain, *Solar cells and their applications*. Vol. 236. 2010: John Wiley & Sons.
204. Kern, G., *SunSine{trademark}300: Manufacture of an AC Photovoltaic Module; Final Report Phases I & II; 25 July 1995-30 June 1998*, in *Other Information: PBD: 22 Mar 1999*. 1999. p. Medium: ED; Size: vp.
205. Organization, W.H., *Guidelines for safe recreational water environments. Volume 2: Swimming pools and similar environments*. 2006: World Health Organization.
206. FANINGER, G., *The potential of Solar Heat in the future energy system*. IFF-University of Klagenfurt, Austria, 2010.

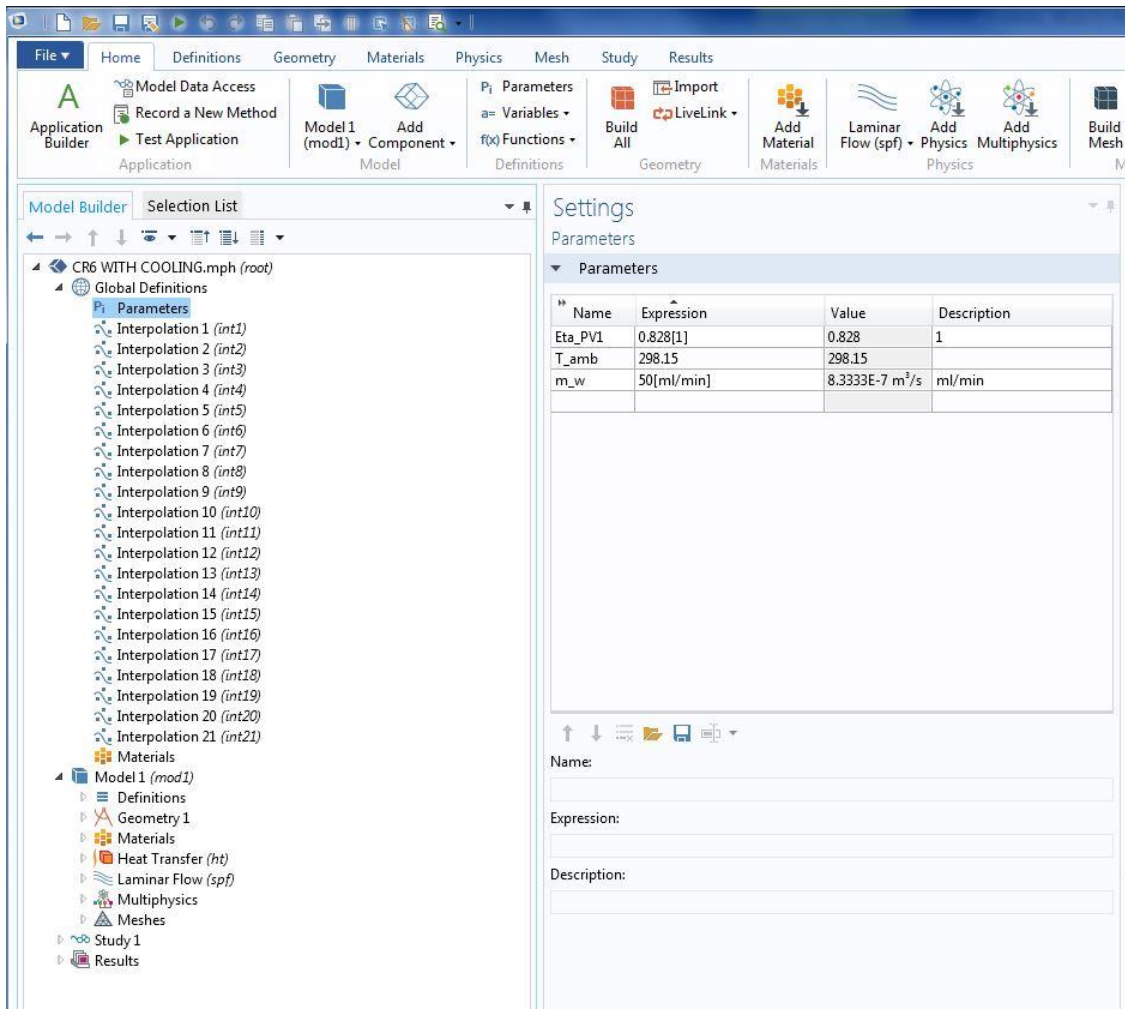
APPENDIX-A

Appendix A includes pictorial steps of CPV/T system thermal model setup using COMSOL Multi-physics 5.2a. The setup includes the detailed definitions of CPV/T system geometry, materials and the conjugate heat transfer model as well as the boundary conditions used in the thermal model. Also the definition of the heat flux which was imported from OptisWorks software as it is distributed after concentration to COMCOL using interpolation function in parameters under global definitions. More details are listed below:

1- Model



2- Global Definitions -Parameters



The screenshot displays the COMSOL Multiphysics software interface. The top menu bar includes File, Home, Definitions, Geometry, Materials, Physics, Mesh, Study, and Results. The left pane shows the 'Model Builder' tree with 'Global Definitions' expanded, listing 21 interpolation parameters (int1 to int21). The right pane shows the 'Parameters' settings panel, which includes a table of parameters.

Name	Expression	Value	Description
Eta_PV1	0.828[1]	0.828	1
T_amb	298.15	298.15	
m_w	50[ml/min]	8.3333E-7 m³/s	ml/min

Below the table, there are input fields for Name, Expression, and Description.

3- Global Definitions- interpolation of flux

The screenshot displays the ANSYS Workbench software interface. The 'Model Builder' tree on the left shows the project structure, including 'Global Definitions' and 'Model 1 (mod1)'. The 'Settings' panel on the right is configured for an interpolation function named 'int1'.

Global Definitions

- Parameters
 - Interpolation 1 (int1)
 - Interpolation 2 (int2)
 - Interpolation 3 (int3)
 - Interpolation 4 (int4)
 - Interpolation 5 (int5)
 - Interpolation 6 (int6)
 - Interpolation 7 (int7)
 - Interpolation 8 (int8)
 - Interpolation 9 (int9)
 - Interpolation 10 (int10)
 - Interpolation 11 (int11)
 - Interpolation 12 (int12)
 - Interpolation 13 (int13)
 - Interpolation 14 (int14)
 - Interpolation 15 (int15)
 - Interpolation 16 (int16)
 - Interpolation 17 (int17)
 - Interpolation 18 (int18)
 - Interpolation 19 (int19)
 - Interpolation 20 (int20)
 - Interpolation 21 (int21)
- Materials
- Model 1 (mod1)
 - Definitions
 - Geometry 1
 - Materials
 - Heat Transfer (ht)
 - Laminar Flow (spf)
 - Multiphysics
 - Mesher
 - Study 1
 - Results

Settings

Interpolation

Plot Create Plot

Label: Interpolation 1

Definition

Data source: Local table

Function name: int1

t	f(t)
6	3252.68
7.583	3242.46
9.166	3227.24
10.749	3176.87
12.332	3085.64
13.915	2995.52
15.497	2977.29
17.08	3058.99
18.663	3151.1
20.246	3178.8
21.829	3132.37
23.412	3080.86
24.995	3074.27
26.578	3127.35
28.161	3212.3

Define primitive function

Primitive function name: int1_prim

Define inverse function

Inverse function name: int1_inv

Interpolation and Extrapolation

Interpolation: Linear

Extrapolation: Constant

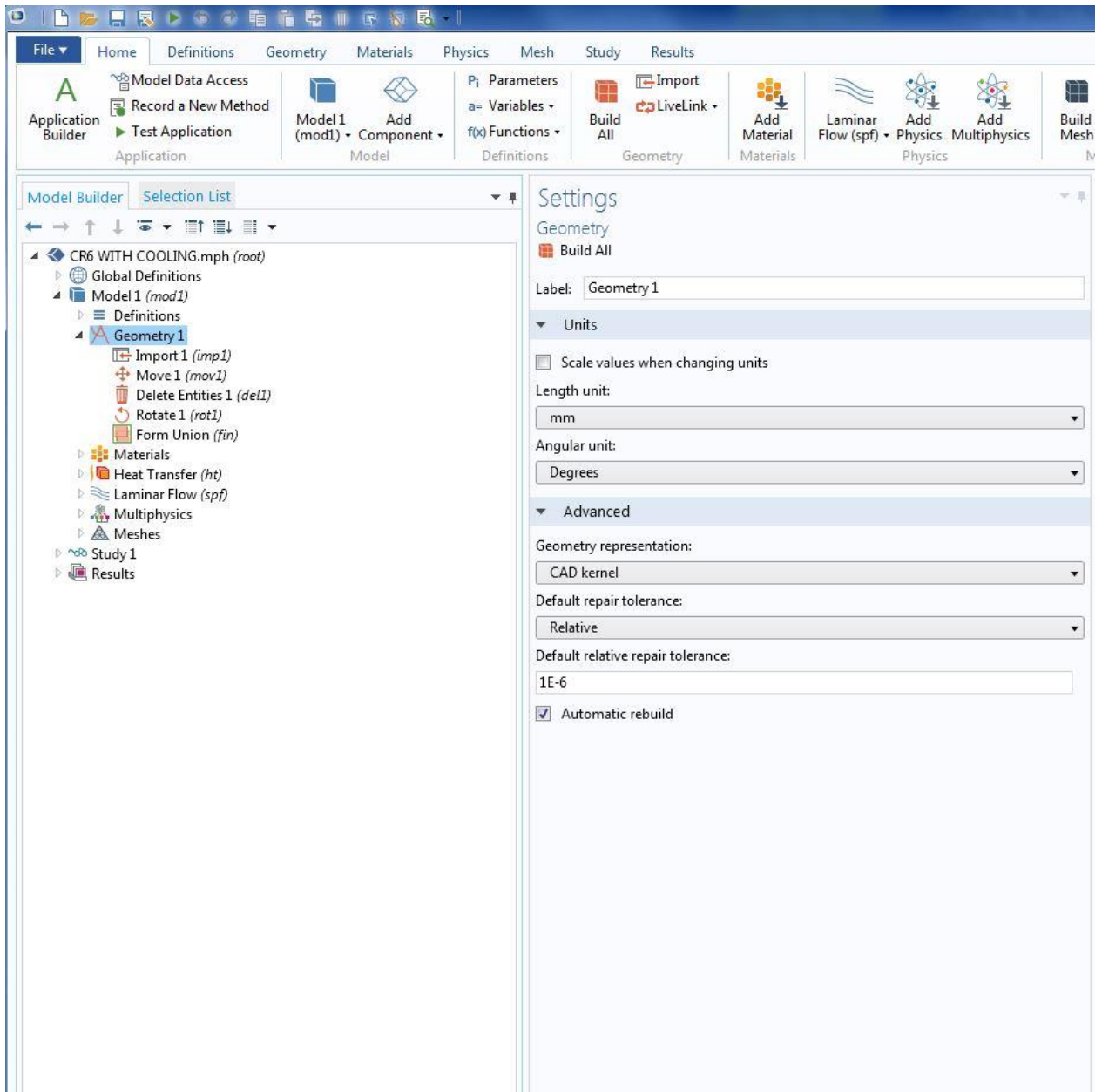
Units

Arguments: mm

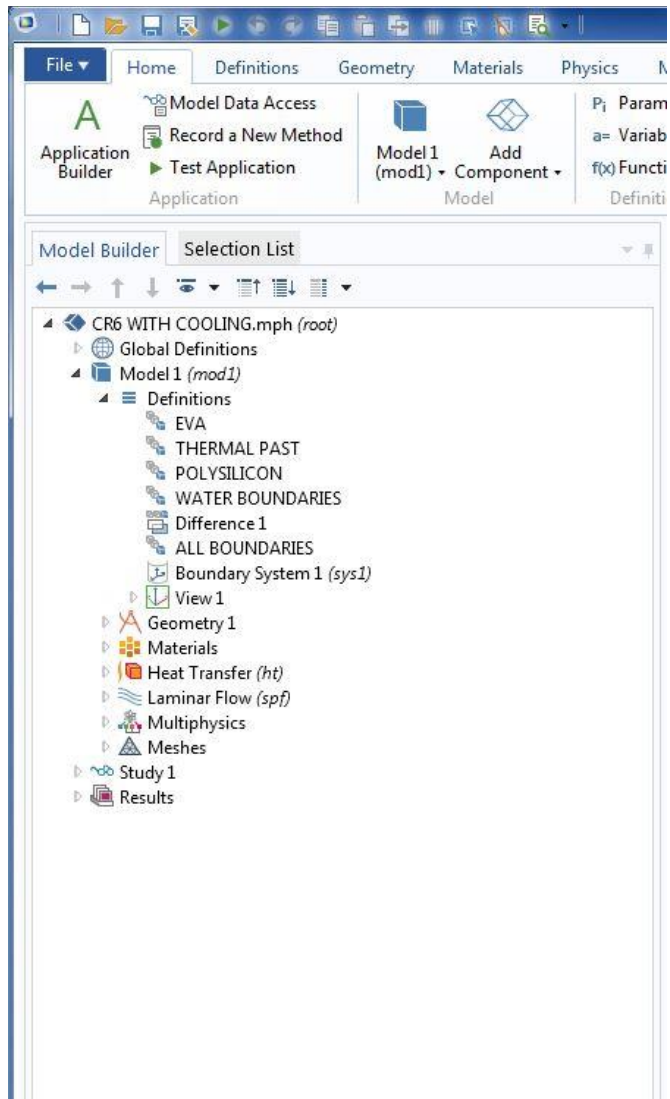
Function: W/m^2

Random Sampling

4- Geometry



5- Definitions for material selections



6- EVA – Properties

The screenshot shows the COMSOL Multiphysics interface with the 'Materials' tab selected. The 'Model Builder' tree on the left shows the hierarchy: CR6 WITH COOLING.mph (root) > Global Definitions > Model 1 (mod1) > Materials > EVA (mat5). The 'Settings' pane on the right shows the 'Basic' property group for the selected material. The 'Output Properties and Model Inputs' section is expanded, showing a table of output properties.

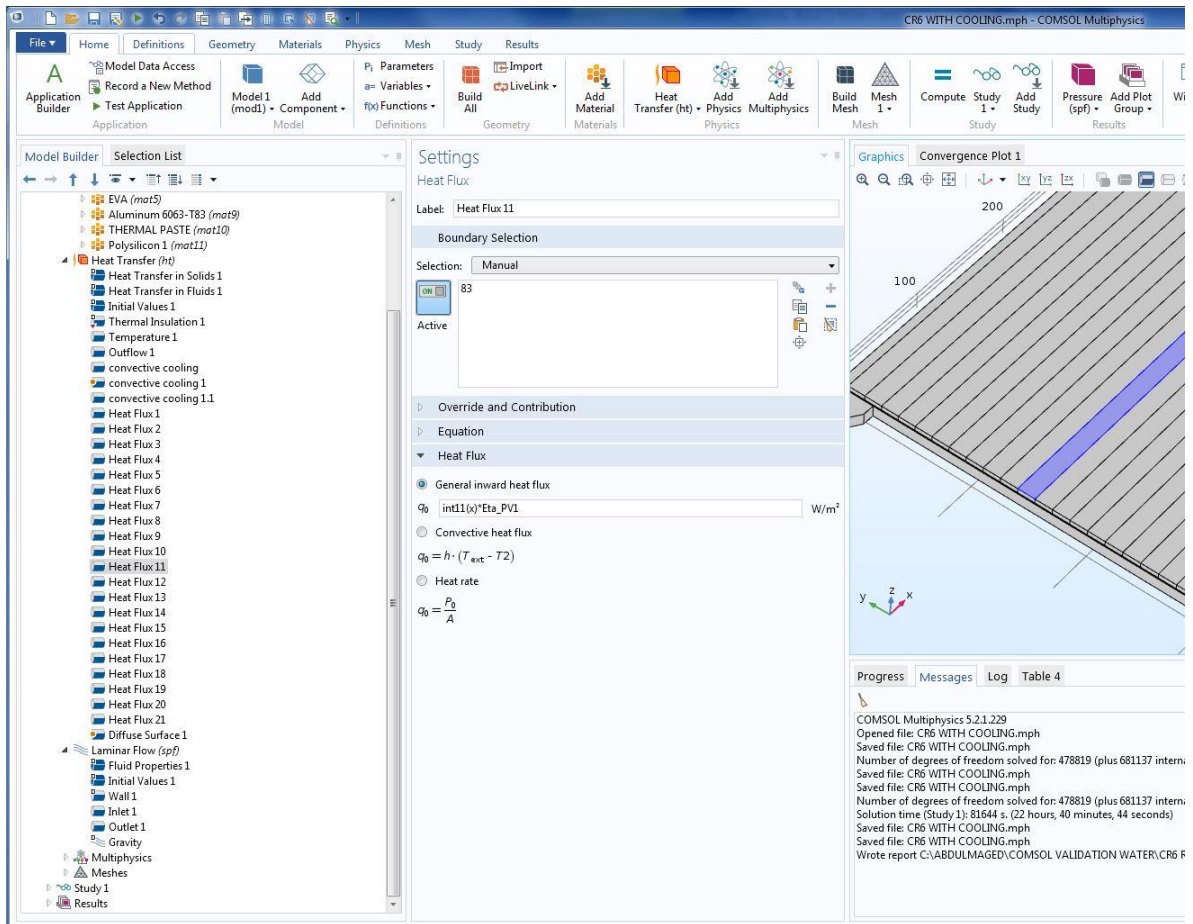
Property	Variable	Expression	Unit	Size
Thermal conductivity	k; kii = k _{...}	0.34	W/(m·K)	3x3
Density	rho	950	kg/m ³	1x1
Heat capacity at cons...	Cp	1400	J/(kg·K)	1x1
Surface emissivity	epsilon_r...	0.85	1	1x1

7- Thermal paste-Properties

The screenshot shows the COMSOL Multiphysics interface with the 'Materials' tab selected. The 'Model Builder' tree on the left shows the hierarchy: CR6 WITH COOLING.mph (root) > Global Definitions > Model 1 (mod1) > Materials > THERMAL PASTE (mat10). The 'Settings' pane on the right shows the 'Basic' property group for the selected material. The 'Output Properties and Model Inputs' section is expanded, showing a table of output properties.

Property	Variable	Expression	Unit	Size
Thermal conductivity	k; kii = k _{...}	3	W/(m·K)	3x3
Density	rho	3000	kg/m ³	1x1
Heat capacity at cons...	Cp	1000	J/(kg·K)	1x1
Surface emissivity	epsilon_r...	0.85	1	1x1

8- Heat transfer- Heat flux



9- Heat transfer- Convective cooling [Horizontal plate Upside]

The screenshot displays the COMSOL Multiphysics 5.2.1.229 interface for a heat transfer simulation. The left pane shows the Model Builder with a tree of components including Heat Transfer (ht) and various heat fluxes. The center pane shows the Settings for 'convective cooling 1', including boundary selection, equation type (Convective heat flux), and material properties (Air). The right pane shows a 3D plot of the plate geometry and a convergence plot.

Model Builder Selection List:

- EVA (mat5)
- Aluminum 6063-T83 (mat9)
- THERMAL PASTE (mat10)
- Polysilicon 1 (mat11)
- Heat Transfer (ht)
 - Heat Transfer in Solids 1
 - Heat Transfer in Fluids 1
 - Initial Values 1
 - Thermal Insulation 1
 - Temperature 1
 - Outflow 1
 - convective cooling
 - convective cooling 1**
 - convective cooling 1.1
 - Heat Flux 1
 - Heat Flux 2
 - Heat Flux 3
 - Heat Flux 4
 - Heat Flux 5
 - Heat Flux 6
 - Heat Flux 7
 - Heat Flux 8
 - Heat Flux 9
 - Heat Flux 10
 - Heat Flux 11
 - Heat Flux 12
 - Heat Flux 13
 - Heat Flux 14
 - Heat Flux 15
 - Heat Flux 16
 - Heat Flux 17
 - Heat Flux 18
 - Heat Flux 19
 - Heat Flux 20
 - Heat Flux 21
 - Diffuse Surface 1
- Laminar Flow (spf)
 - Fluid Properties 1
 - Initial Values 1
 - Wall 1
 - Inlet 1
 - Outlet 1
 - Gravity
- Multiphysics
- Mesher
- Study 1
- Results

Settings: Heat Flux

Label: convective cooling 1

Boundary Selection

Selection: Manual

Active: 39, 43, 47, 51, 55, 59, 63, 67

Override and Contribution

Equation

Heat Flux

☐ General inward heat flux

☒ Convective heat flux

$q_0 = h \cdot (T_{\text{ext}} - T_2), \quad h = h_{\text{air}}(L, p_A, T_{\text{ext}})$

Heat transfer coefficient:

External natural convection

Horizontal plate, upside

Plate diameter (area/perimeter):

L 0.23335 m

Fluid:

Air

Absolute pressure:

p_A User defined

1[atm]

External temperature:

T_{ext} User defined

T_{amb} K

☐ Heat rate

$q_0 = \frac{P_0}{A}$

Graphics: Convergence Plot 1

Progress Messages Log Table 4

COMSOL Multiphysics 5.2.1.229

Opened file: CR6 WITH COOLING.mph

Saved file: CR6 WITH COOLING.mph

Number of degrees of freedom solved for: 47881

Saved file: CR6 WITH COOLING.mph

Saved file: CR6 WITH COOLING.mph

Number of degrees of freedom solved for: 47881

Solution time (Study 1): 81644 s. (22 hours, 40 m)

Saved file: CR6 WITH COOLING.mph

Saved file: CR6 WITH COOLING.mph

Wrote report C:\ABDULMAGED\COMSOL VALID

10- Heat transfer- Convective cooling [Horizontal plate Downside]

The screenshot displays the COMSOL Multiphysics 5.2.1.229 interface for a model titled "CR6 WITH COOLING.mph". The left pane shows the "Model Builder" tree with the following structure:

- EVA (mat5)
- Aluminum 6063-T83 (mat9)
- THERMAL PASTE (mat10)
- Polysilicon 1 (mat11)
- Heat Transfer (ht)
 - Heat Transfer in Solids 1
 - Heat Transfer in Fluids 1
 - Initial Values 1
 - Thermal Insulation 1
 - Temperature 1
 - Outflow 1
 - convective cooling
 - convective cooling 1
 - convective cooling 1.1
 - Heat Flux 1
 - Heat Flux 2
 - Heat Flux 3
 - Heat Flux 4
 - Heat Flux 5
 - Heat Flux 6
 - Heat Flux 7
 - Heat Flux 8
 - Heat Flux 9
 - Heat Flux 10
 - Heat Flux 11
 - Heat Flux 12
 - Heat Flux 13
 - Heat Flux 14
 - Heat Flux 15
 - Heat Flux 16
 - Heat Flux 17
 - Heat Flux 18
 - Heat Flux 19
 - Heat Flux 20
 - Heat Flux 21
- Diffuse Surface 1
- Laminar Flow (spf)
 - Fluid Properties 1
 - Initial Values 1
 - Wall 1
 - Inlet 1
 - Outlet 1
 - Gravity
- Multiphysics
- Mesher
- Study 1
- Results

The right pane shows the "Settings" for the "Heat Flux" feature, specifically for "convective cooling 1.1". The "Boundary Selection" is set to "Manual" with 3 boundaries selected. The "Equation" section is expanded, showing the "Convective heat flux" option selected. The governing equation is:

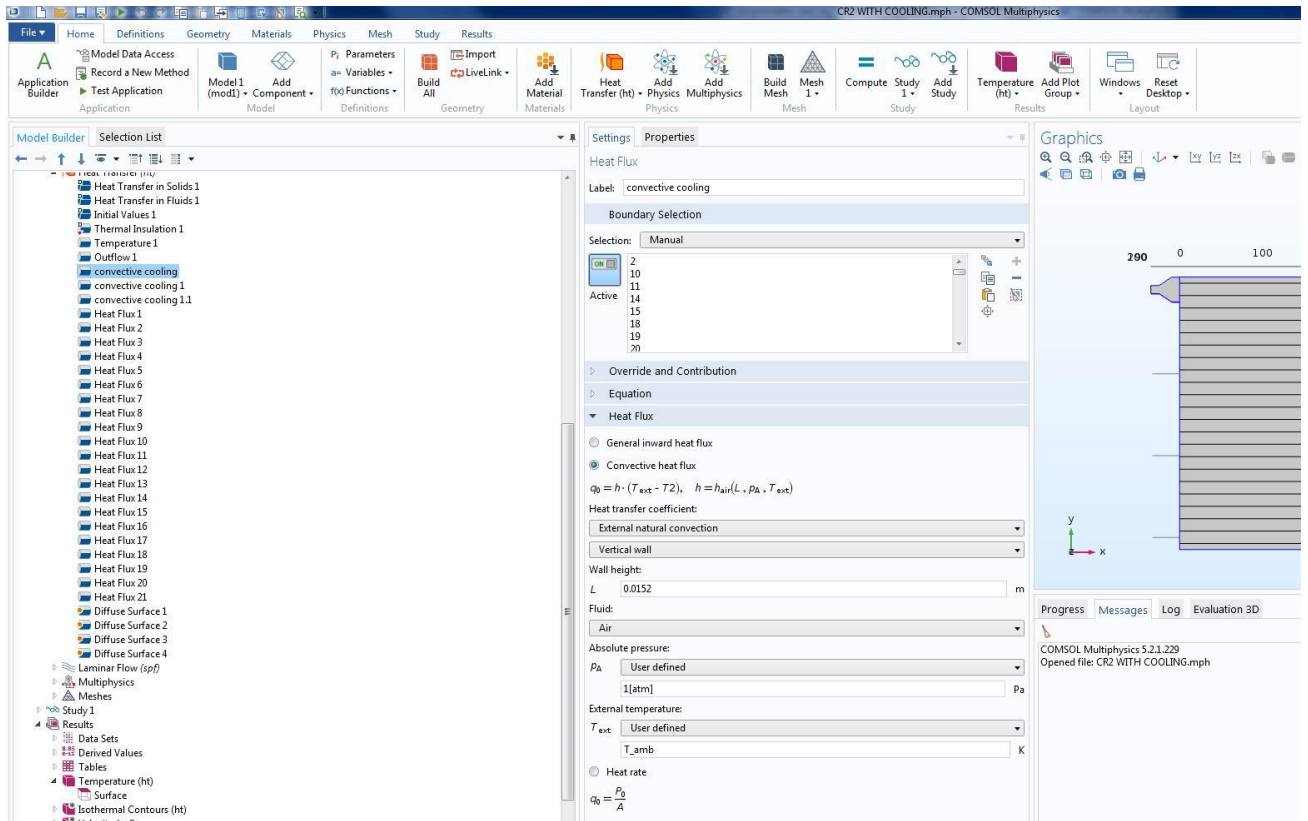
$$q_0 = h \cdot (T_{ext} - T_2), \quad h = h_{air}(L, p_A, T_{ext})$$

The "Heat transfer coefficient" is set to "External natural convection" with the sub-option "Horizontal plate, downside". The "Plate diameter (area/perimeter)" is defined as $L = 0.23335$ m. The "Fluid" is set to "Air". The "Absolute pressure" is set to $p_A = 1$ [atm]. The "External temperature" is set to $T_{ext} = T_{amb}$ K. The "Heat rate" equation is shown as $q_0 = \frac{P_0}{A}$.

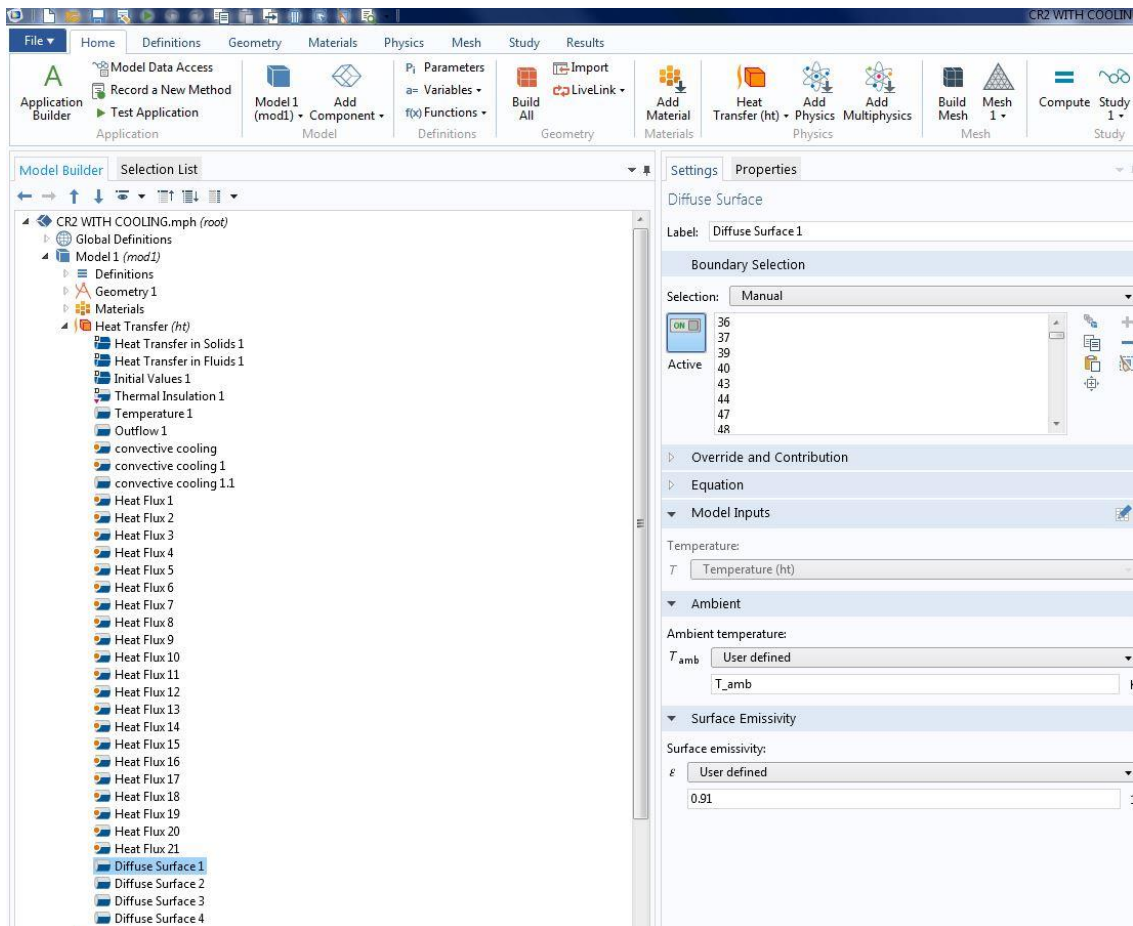
The "Graphics" pane on the far right shows a "Convergence Plot 1" with a plot of the solution. The bottom right pane shows the "Progress" tab with the following information:

COMSOL Multiphysics 5.2.1.229
 Opened file: CR6 WITH COOLING.mph
 Saved file: CR6 WITH COOLING.mph
 Number of degrees of freedom solved for: 4;
 Saved file: CR6 WITH COOLING.mph
 Saved file: CR6 WITH COOLING.mph
 Number of degrees of freedom solved for: 4;
 Solution time (Study 1): 81644 s. (22 hours, 41 minutes)
 Saved file: CR6 WITH COOLING.mph
 Wrote report C:\ABDULMAGED\COMSOL V\

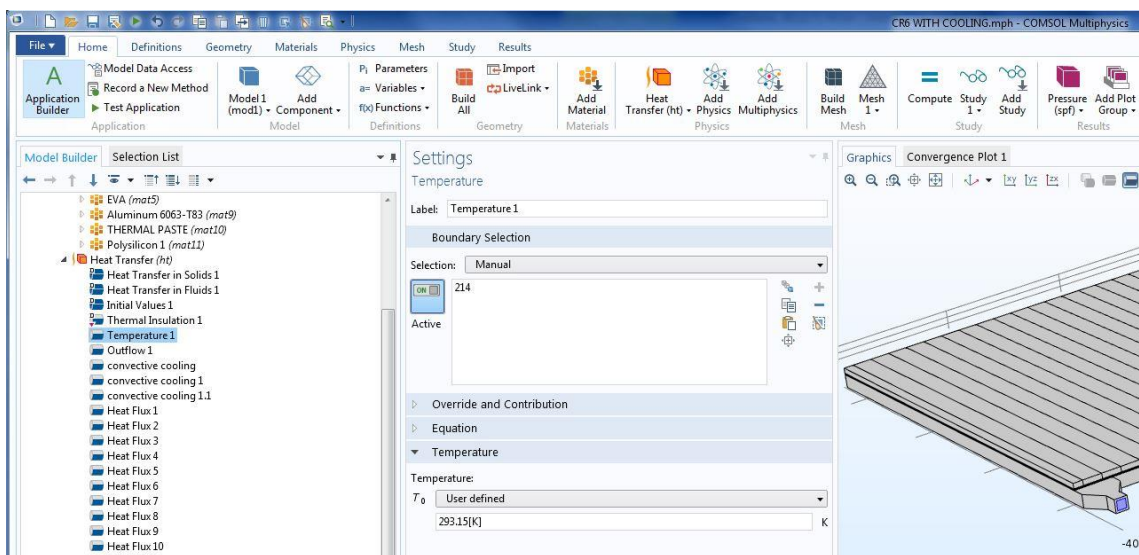
11- Heat transfer- Convective cooling [Vertical walls]



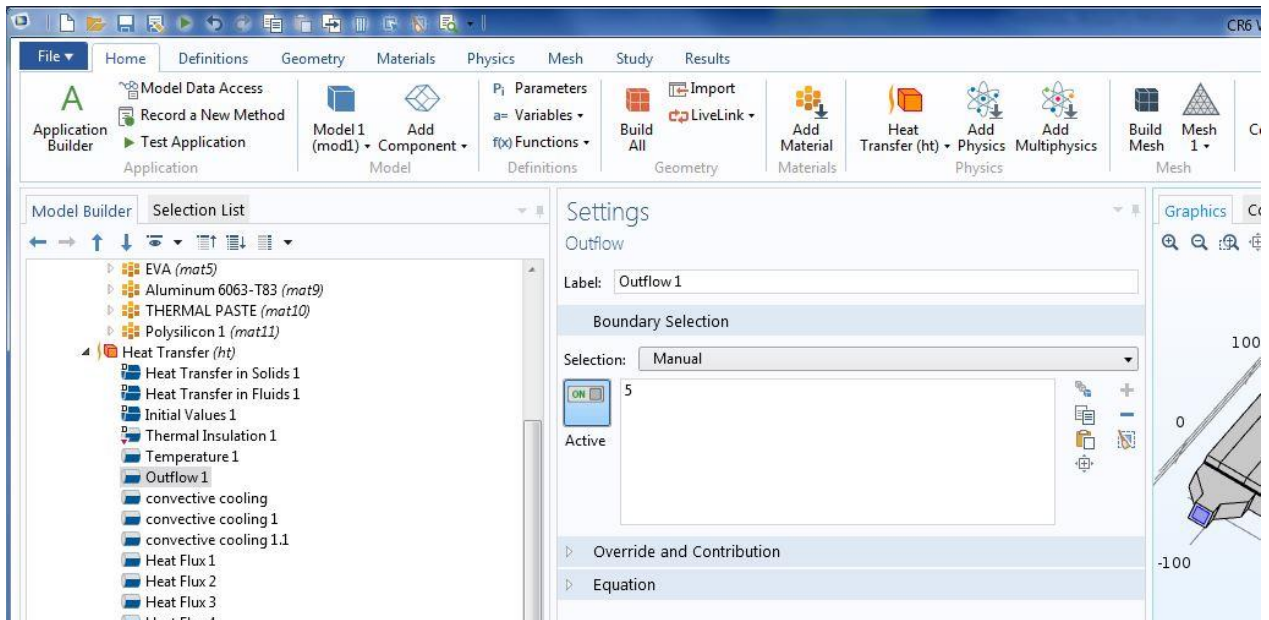
12- Heat transfer – Diffuse Surface



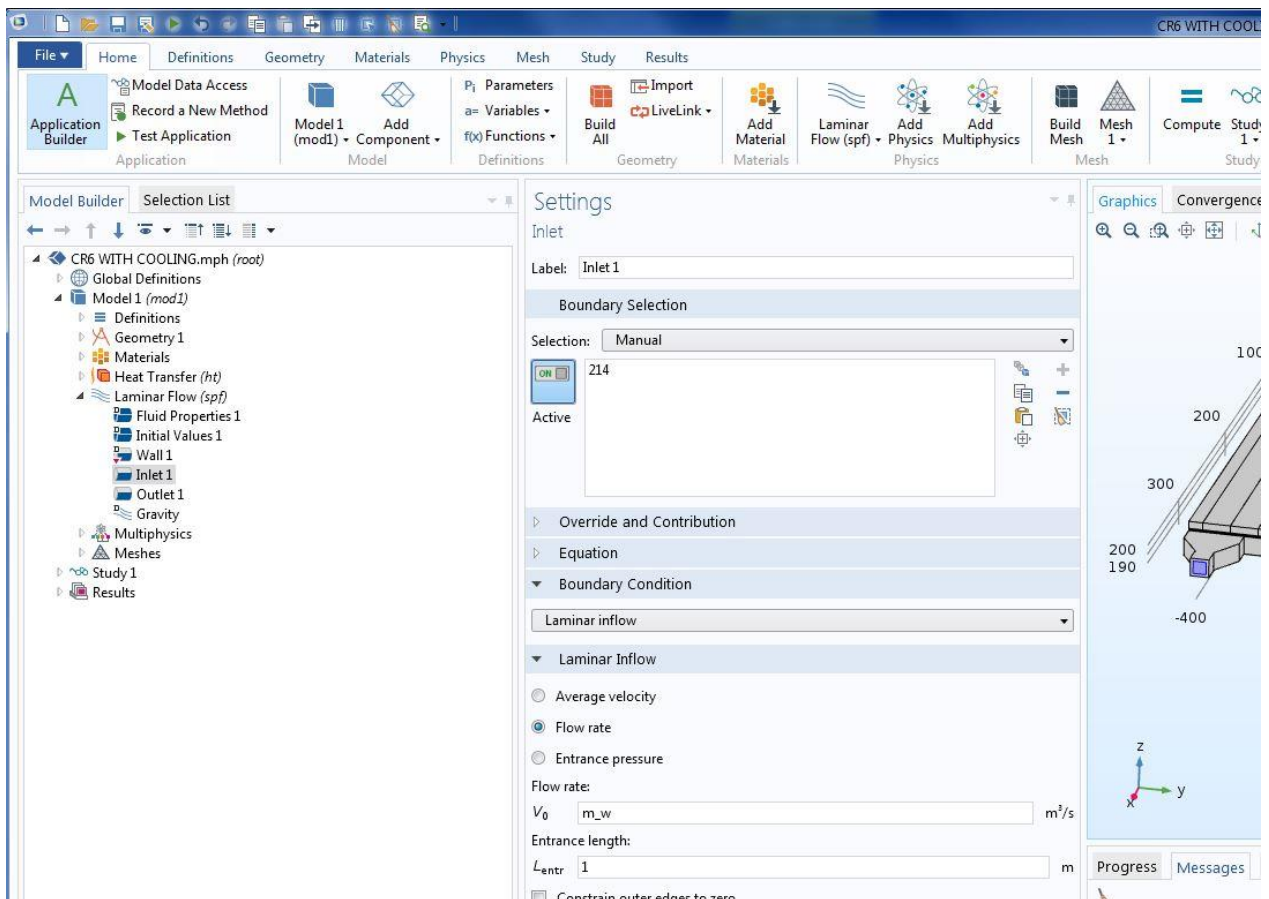
13- Heat transfer – inlet water temperature



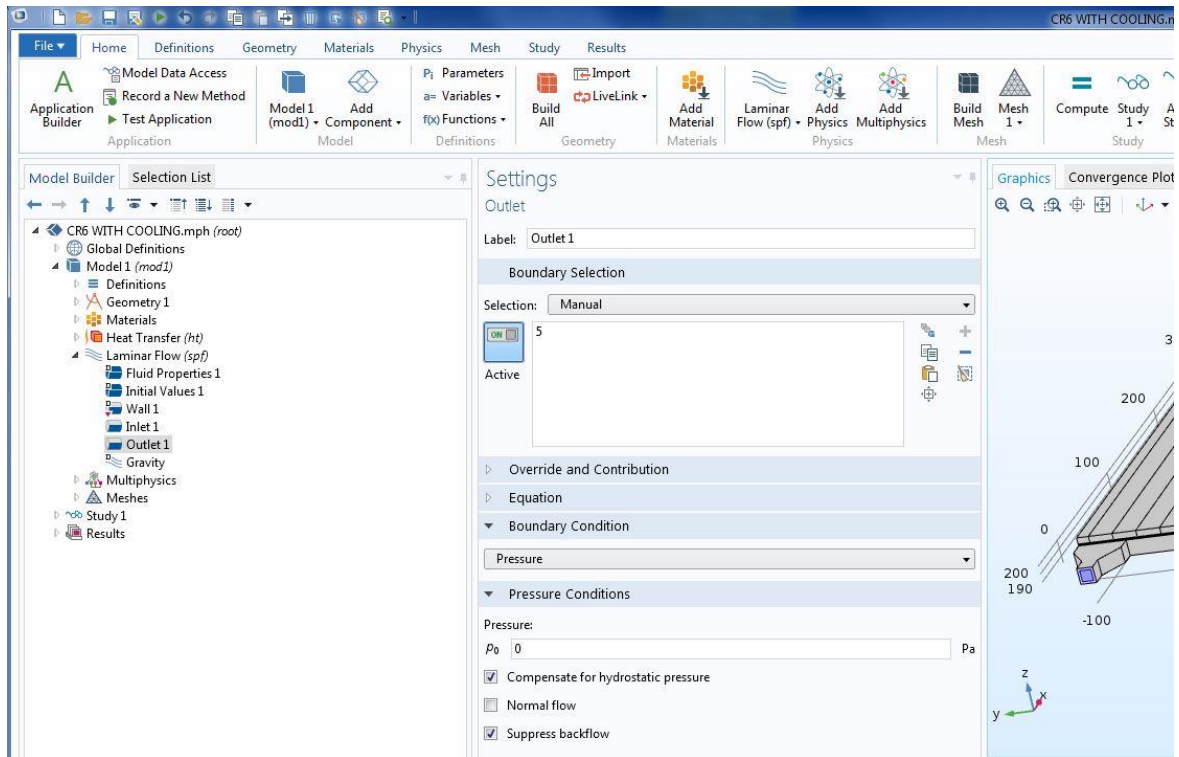
14- Heat transfer – water outflow



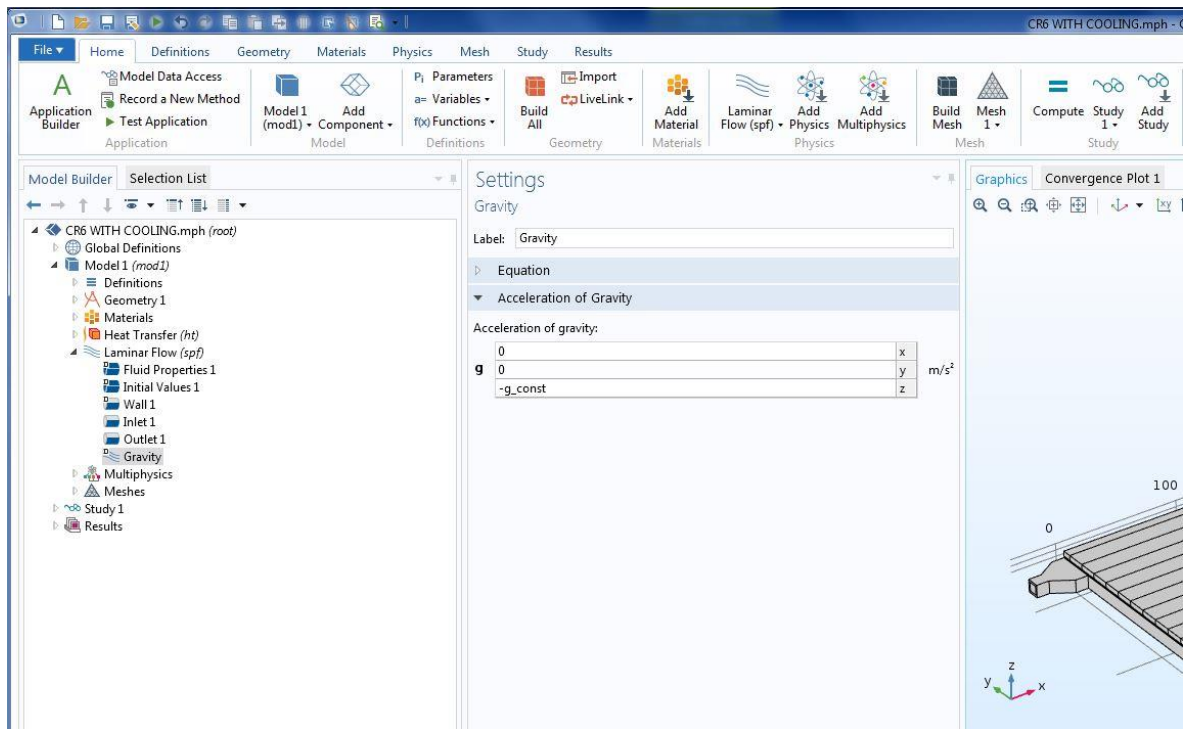
15- Laminar flow – Inlet



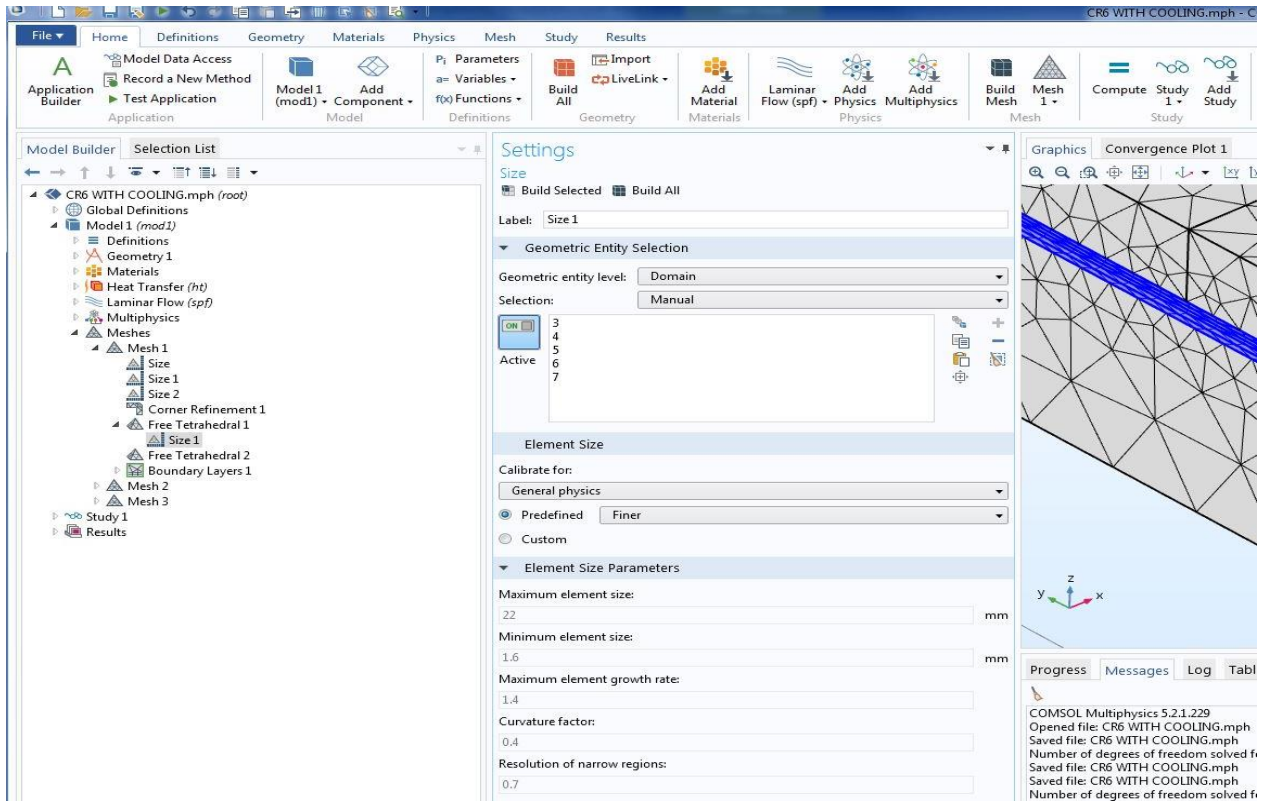
16- Laminar flow – Outlet



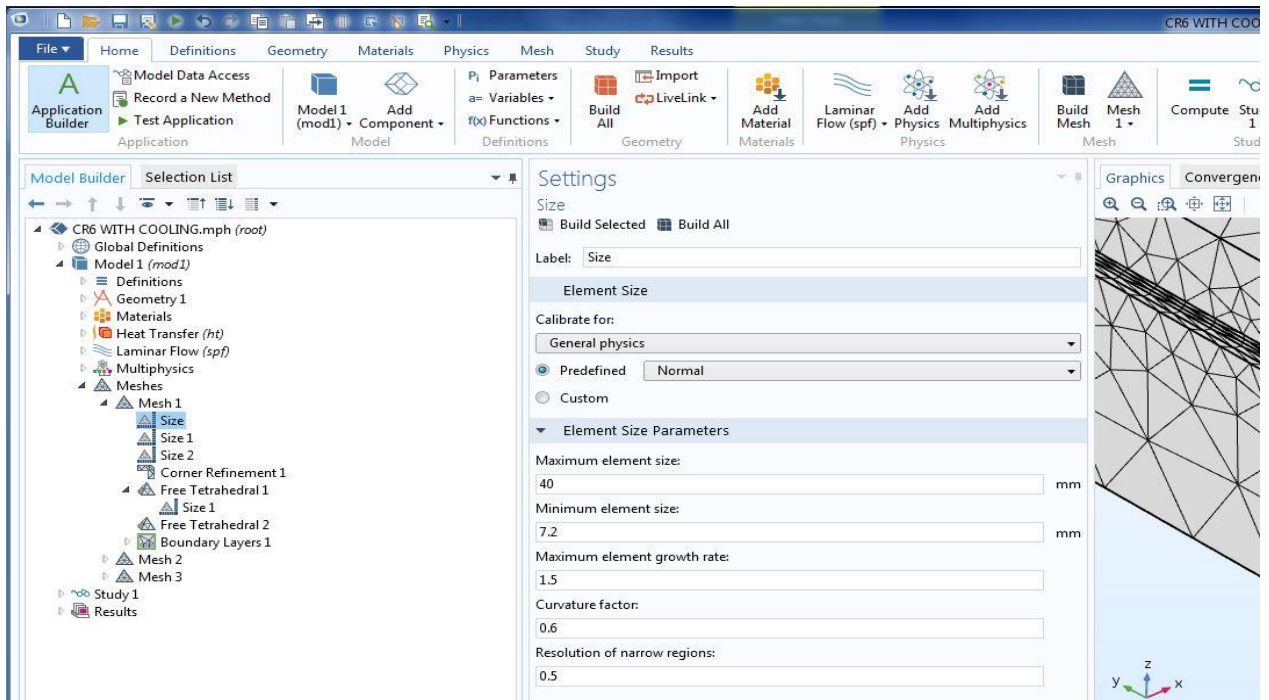
17- Laminar flow-Gravity



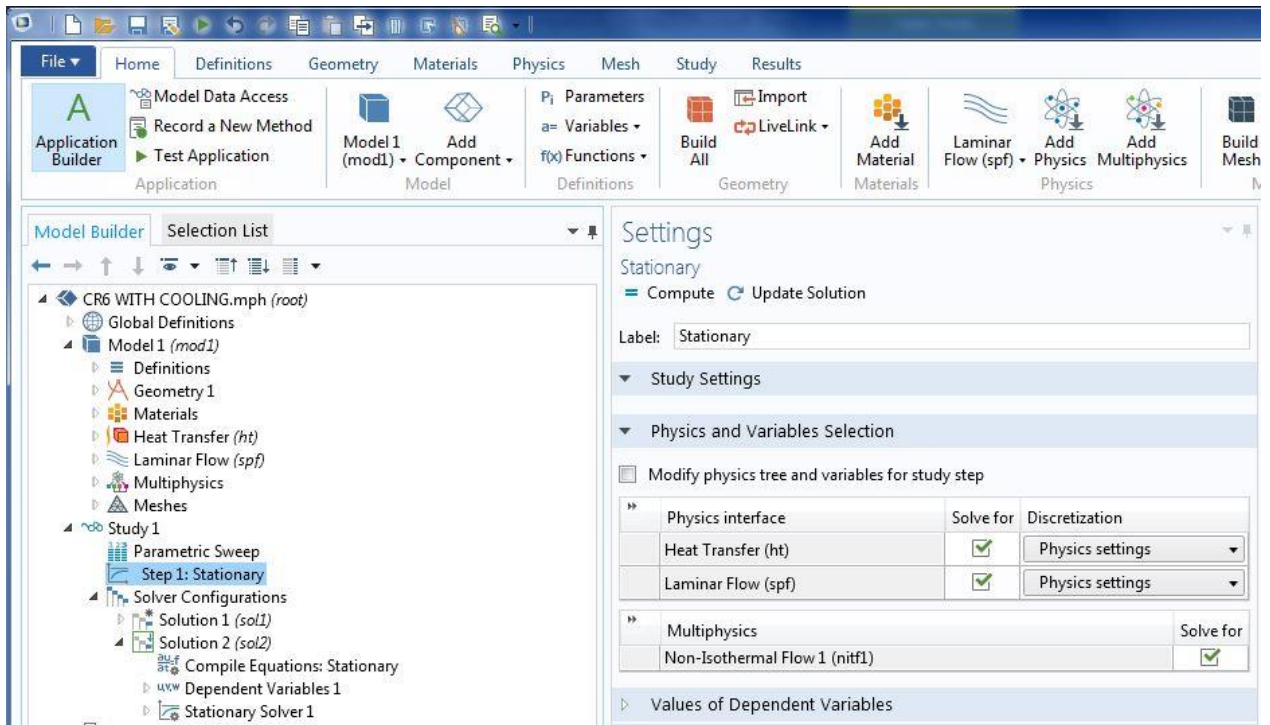
18- Mesh- PV cells, EVA, Back sheet and Thermal paste



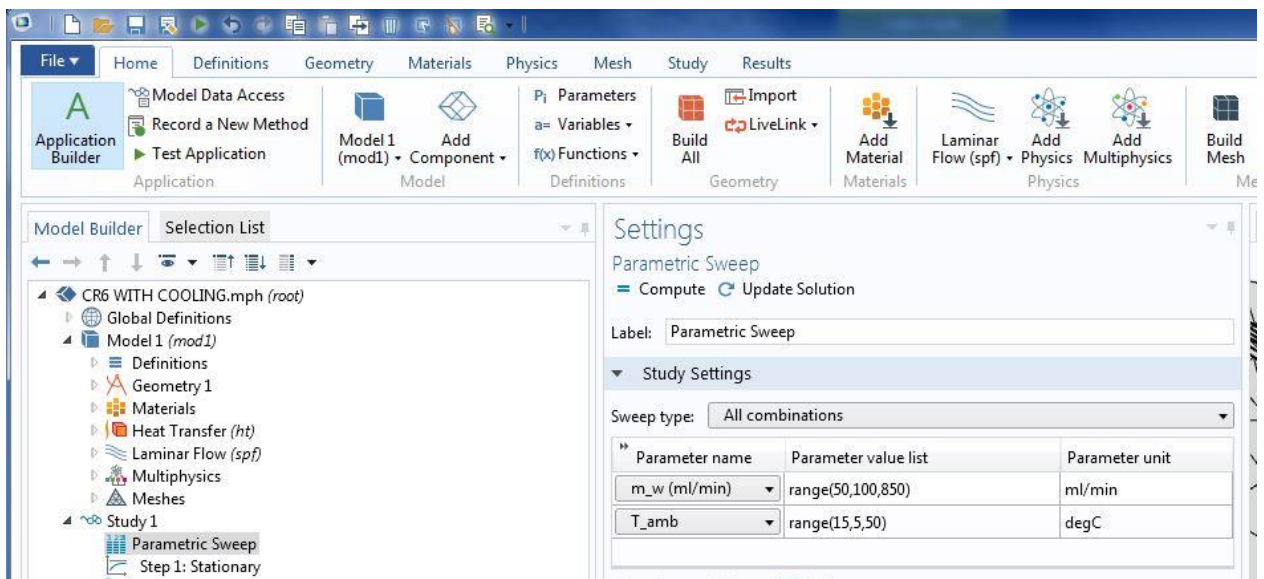
19- Mesh- remaining



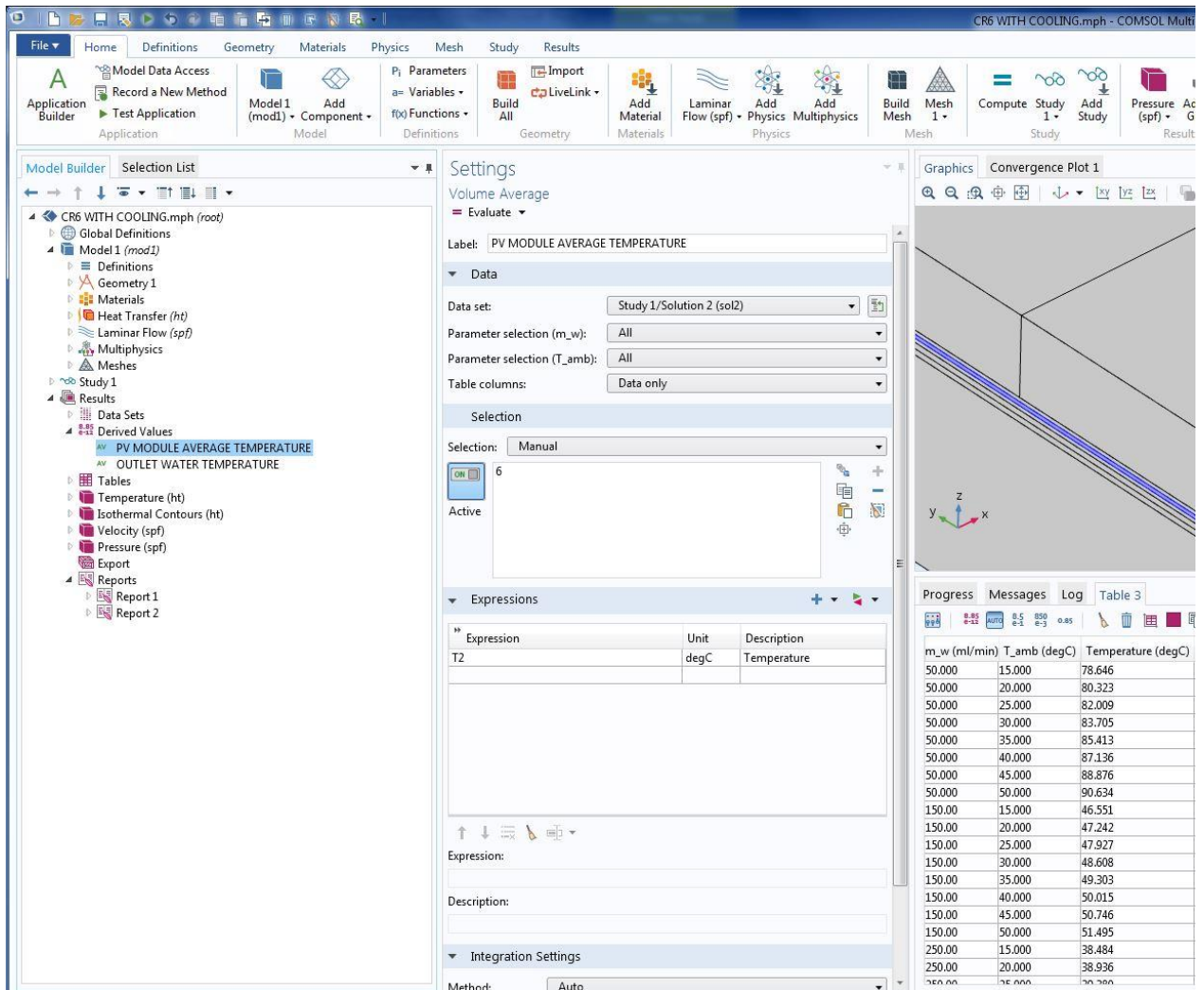
20- Study – stationary



21- Study – Parametric Sweep



22- Results



APPENDIX-B

Appendix B presents the calibration procedure for the thermocouples used in PV temperature measurements. **Figures B1** and **B 2** show the temperature readings for 12 thermocouples versus the temperature readings of the thermometer that taken simultaneously with thermocouples, which are details of calibration procedure presented in chapter 5, section 5.5.1.

